The Formation of Early-Type Galaxies

Mark Anderson Norris

A Thesis presented for the degree of
Doctor of Philosophy

Extragalactic Astronomy
Department of Physics
University of Durham
England

July 2008

Dedicated to

My family

The Formation of Early-Type Galaxies

Mark Anderson Norris

Submitted for the degree of Doctor of Philosophy
July 2008

Abstract

This Thesis examines the formation and evolution of early-type elliptical and S0 galaxies. In order to shed light on the key processes which lead to the formation of elliptical and S0 galaxies a range of techniques have been employed.

The kinematics and stellar populations of the major and minor axes of the nearby edge-on S0 galaxy NGC 3115 have been examined through deep Gemini-GMOS longslit spectroscopy. The behaviour of the radial profiles of the line strength indices is found to be well explained by a simple model where NGC 3115 is composed of two components; an older classical spheroidal component, which displays a negative (decreases outwards) metallicity gradient and is enhanced in α-elements relative to the solar value together with a younger, constant metallicity disc which displays close to solar [α/Fe]. The kinematics and stellar populations of the integrated light of NGC 3115 are compared to those previously found for its globular cluster (GC) system. The GCs are found to rotate in a manner consistent with the galaxy as a whole and the red GC sub-population is found to have ages, metallicities and [α/Fe] abundance indistinguishable from those displayed by the spheroid of NGC 3115 at 2 effective radii. This study provides strong support to the theory that the GC systems of galaxies are closely linked to galaxy spheroid formation.

The formation and evolution of S0 galaxies is further examined through the study of 18 edge-on S0 galaxies observed in a manner identical to that presented for NGC 3115. These galaxies are all found to display significant stellar discs and to present regular disc kinematics. In several cases signatures of kinematic substructure such as inner discs or bars are found. Ionised gas emission is observed at a low level in 72% of the sample; the kinematics of this ionised gas is highly variable, with examples of regular disc-like kinematics, confused counter-rotation and streams not aligned with any axis observed. The kinematic data has been utilised to produce a B-band Tully-Fisher relation (TFR) for S0

galaxies. The S0 TFR is observed to be offset to fainter magnitudes from the TFR for local spirals, an observation which can crudely be explained by the formation of S0s through the truncation of star formation (and subsequent disc fading) in normal spiral galaxies. The offset from the spiral TFR for each galaxy is shown to correlate well with both disc and central age, in the correct sense, and with the correct magnitude, such that the large observed scatter in the S0 TFR can be explained as being due to the different times at which the progenitor spirals ceased forming stars and hence the different amounts they have faded up to the present.

Multi-object spectroscopic observations of the GC system of the shell elliptical NGC 3923 are presented, as well as a novel technique for examining the spectra of the integrated light of galaxies at the same time as observing their GC system. The observations are used to demonstrate that neither the integrated light nor the GC system of NGC 3923 shows evidence for significant rotation. The stellar populations of the red GCs are again found to be consistent in age, metallicity and [α/Fe] with that displayed by the integrated light of the spheroid of NGC 3923 at large radii ($> 2R_e$). The velocity dispersion profile of the integrated light and GC system of NGC 3923 are both observed to be flat at larger radii, a finding indicative of the presence of significant amounts of Dark Matter. Using the GC kinematic data, a simple spherical isotropic dynamical model is presented which demonstrates that a significant increase in mass-to-light (M/L) ratio is required to explain the observed constant velocity dispersion profile. The M/L profile determined is in good agreement with that measured independently from X-ray observations.

Declaration

The work in this thesis is based on research carried out at the Extragalactic Astronomy Group, the Department of Physics, Durham University, England. No part of this thesis has been submitted elsewhere for any other degree or qualification and it is all my own work unless referenced to the contrary here or in the text. Some of this work has, however, been published in the following papers (in chronological order):

"GMOS spectroscopy of the S0 galaxy NGC 3115". Norris, Mark A.; Sharples, Ray M.; Kuntschner, Harald, 2006, Monthly Notices of the Royal Astronomical Society, 367, 815

"Gemini/GMOS spectroscopy of the spheroid and globular cluster system of NGC 3923" Norris, Mark A.; Sharples, Ray M.; Bridges, Terry; Gebhardt, Karl; Forbes, Duncan A.; Proctor, Robert; Raul Faifer, Favio; Carlos Forte, Juan; Beasley, Michael A.; Zepf, Stephen E.; Hanes, David A. , 2008, Monthly Notices of the Royal Astronomical Society, 385, 40

Acknowledgements

I would first like to thank my supervisor, Ray Sharples for all of his invaluable advice and encouragement, as well as for allowing me the freedom to explore avenues often at first glance only tangentially connected to the task at hand. Out of such diversions emerged a much deeper understanding of the process of research and also, occasionally, something of interest. Others within the department also deserve special note for generously giving up their time to educate me in the ways of astronomy, programming or both, so thank you John Lucey, Russell Smith and Mark Swinbank. Thanks also go to Lydia Heck and Alan Lotts for somehow managing to keep the computer systems running.

Outside of Durham my thanks must go to those who were involved in my various collaborative endeavours, first and foremost to Harald Kuntschner who has been an invaluable guide through the subtleties of studying stellar populations. Also Mike Beasley, Terry Bridges, Favio Faifer, Duncan Forbes, Juan Carlos Forte, Karl Gebhardt, Dave Hanes, Michael Pierce, Robert Proctor and Stephen Zepf, all receive my gratitude for their patient help through the minefields of telescope proposals, Phase II and paper writing.

I would also like to thank PPARC/STFC for providing me with enough money to put a roof over my head during the completion of this PhD. The good people at the Gemini Observatories also deserve my endless gratitude for supplying me with large amounts of exceptional data, without which this PhD would be impossible. I also thank the ESO Directors Discretionary Fund for providing me with financial support for a collaborative visit to Garching during the completion of this Thesis.

A special thank you must be extended to the many housemates who made Ferens Park such a memorable place to live, thank you Rob Crain, Hugh Dickinson, Jim Geach, Gareth Jones, Maud Michaud, Shelly O'Mahony and George Mountricas.

The list of those responsible for providing a social life for postgrads and postdocs at Durham during my stay is long and distinguished, even if the list of drinking establish-

ments frequented was not, thank you: Raul Angulo, Kris Beckwith, Phil Bett, Rich Bielby, Craig Booth, Jaeil Cho, Kristen Coppin, Rob Crain, Neil Crighton, Greg Davies, Hugh Dickinson, Andreea Font, Bill Frith, Jim Geach, Andy Goulding, Juan Gonzalez, Mark Harrison, John Helly, Bret Lehmer, Noam Libeskind, Matt Middleton, Ian McCarthy, Jim Mullaney, David Radburn-Smith, Tim Rawle, Nic Ross, John Stott, Chiara Tonini, Dave Wake, Julie Wardlow and Rich Whitaker. Thank you all for playing football, sitting in the Market Tavern or losing your money playing poker with me, I am eternally grateful. Special thanks go to Ruth who has put up with much to support my dream and without whose support this Thesis would never have been completed.

Finally I would like to thank my family for their constant faith and support over the many years it has taken to get to this point.

Contents

List of Figures

List of Tables

The diversity of the phenomena of Nature is so great, and the treasures hidden in the heavens are so rich, precisely in order that the human mind shall never be lacking in fresh nourishment.

Johannes Kepler (1571-1630)

Chapter 1

Introduction

The disciplines of Cosmology and Extragalactic Astronomy seek to answer the very greatest of questions, how did the Universe come to take its current appearance? Both have had significant successes in recent times, often approaching the same question from different directions, with cosmology tending to focus on the large scale physics which dominates the evolution of the Universe as a whole, while extragalactic astronomy attempts to build up a picture of the formation and evolution of galaxies on the smallest scales, and the great agglomerations of galaxies on the largest. The combination of the fruits of both these endeavours has lead to the emergence of a consistent picture of the evolution of the Universe since its formation over 13 Gyr ago. From studies of the Cosmic Microwave Background radiation (e.g. WMAP (Spergel et al., 2007)) in combination with studies of the clustering of galaxies at lower redshift (e.g. 2dFGRS (Cole et al., 2005), SDSS (Tegmark et al., 2006)) it has proven possible to determine the overall parameters which govern the evolution of the Universe. These parameters which describe the amounts of baryonic (i.e. normal) and dark matter (non-baryonic matter), the energy density of the relic radiation left over from the big bang epoch, the expansion rate (the Hubble constant) and the acceleration in the expansion rate of the Universe (due to the dark energy component), can be used to build up an understanding of the framework in which galaxy formation and evolution occurs.

An example of this process can be seen in the work done to simulate the distribution of dark matter within the Universe, Figure 1.1 demonstrates one such attempt, the so called "Millennium Run" (Springel et al., 2005). This is an N-body simulation of 1 billion dark matter particles, evolved from a redshift of 127 to the current epoch. The input initial conditions are based on the concordance cosmology described above, with the

original input consisting of dark matter distributed smoothly except for the influence of small density perturbations following a Gaussian random field. The random density perturbations are thought to have been seeded by quantum mechanical effects during a brief period of exponential growth in the Universe just after the Big Bang, the so called inflationary era. For the sake of simplicity the effects of the baryons are omitted in the Millenium Simulation. As the baryons provide only a small fraction of the mass relative to the dark matter this simplification is justified if the baryons trace the DM accurately. As many sets of observations from the galaxy scale (the detection of DM in spiral galaxies due to their observed rotation velocities), through cluster scale (through observations of gravitational lensing due to the cluster potential) and up to the very largest scales of the filaments and superclusters (through the measurement of bulk motions of galaxies and clusters) detect a close correspondence between DM and baryons this assumption seems robust. Omitting the baryons also makes the simulation process much simpler, as the dark matter itself only interacts through gravity. An examination of the structures formed by the DM shows that slight overdensities present at the epoch of the CMB radiation (due to the input Gaussian random field) grow through gravitational collapse to form the structures seen in the present day, for example in the distribution of galaxies observed in local redshift surveys (see Figure 1.2), where very close agreement between theoretical and observational measurements now exist. The growth of these structures tends not to be entirely smooth; in fact structures are generally built up in a hierarchical manner, with smaller structures tending to merge gradually over time to form larger and larger agglomerations.

This dark matter structure of filaments, clusters and voids (the "cosmic web") therefore forms the envelope within which the baryonic matter resides. Hence the modern synthesis has arrived at a point where the overarching behaviour of the Universe is well understood, with the DM providing the stage onto which the baryonic matter interacts to form galaxies. What is not fully understood at present is how the baryonic matter evolves to form the myriad of structures seen within the Universe. Mostly this is due to the fact that baryonic interactions are considerably more complicated than DM ones, with baryons interacting through several other forces not experienced by DM. In particular it is the interaction of baryonic matter with electromagnetic radiation which leads to many processes which are extremely important in galaxy formation.

In most scientific endeavours the first step towards an understanding is classification.

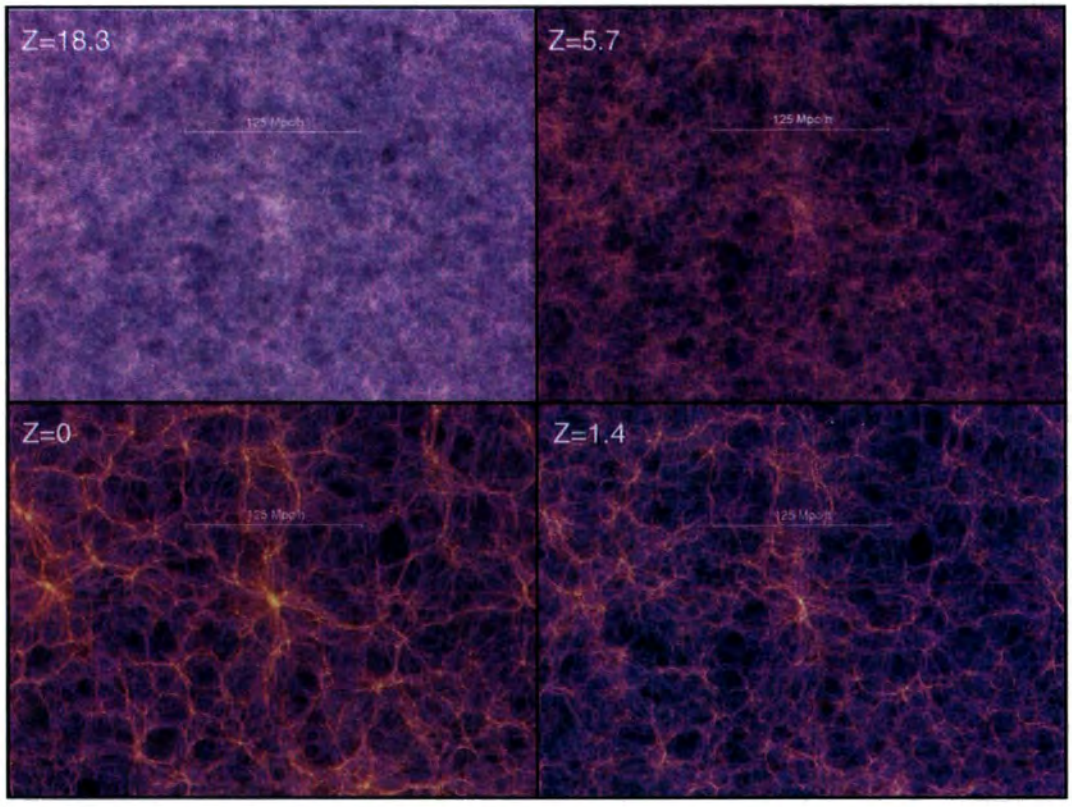

Figure 1.1: The Millennium Simulation. Representation of the density of dark matter at 4 redshifts in the Millennium simulation, demonstrating the growth of structure in the Universe (from Springel et al. (2005)).

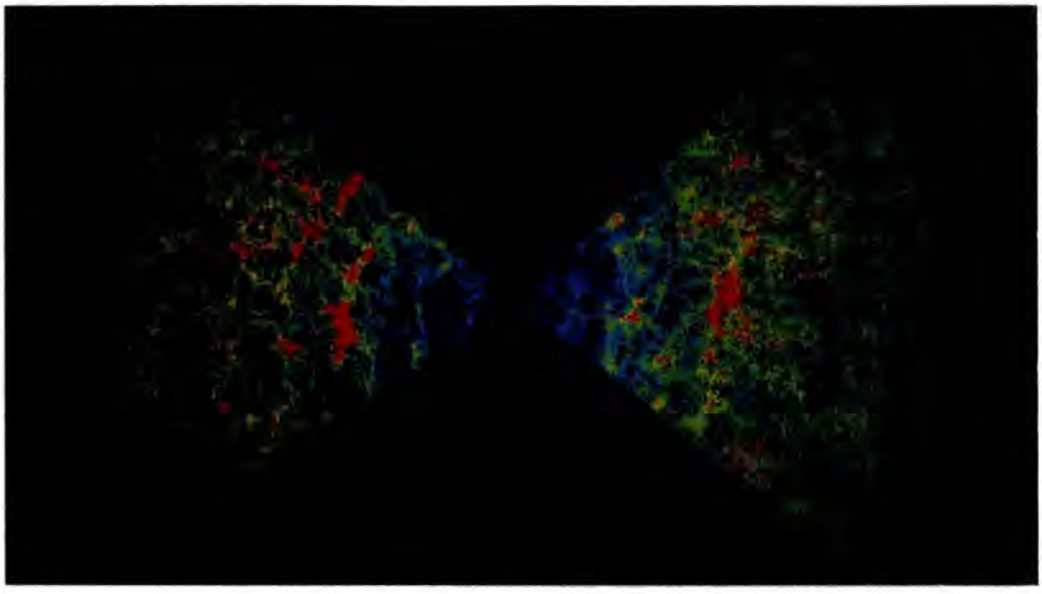

Figure 1.2: The position of galaxies as determined by the 2dF galaxy redshift survey (Colless, 1999). Red indicates higher density regions. A comparison with the z=0 panel of Figure 1.1 shows good qualitative agreement in the types of structures found both in the simulations and the nearby Universe.

In this respect the study of galaxy formation is no different and it was Edwin Hubble himself who presented one of the first classification schemes for galaxies (seen in Figure 1.3), the so called Hubble tuning fork diagram (Hubble, 1936). Hubble believed that his diagram represented a sequence of evolution with galaxy types on the left changing into the types on the right with time, an idea now known to be incorrect. If anything the evolutionary sequence presented by this diagram tends to be in the other direction, with it now known that the merger of equal mass spirals is likely to result in the formation of an elliptical galaxy, and also that it is possible through secular evolution to turn later type spirals into earlier spirals types (i.e. Sc to Sa). Even today the terms used to separate galaxies into two broad classes reflect this misunderstanding on the part of Hubble, with the galaxies to the left termed early-type (Ellipticals and S0s) due to their supposed antiquity, and the galaxies to the right termed Late-type (Spirals and Irregulars) due to their supposed recent formation from the early types. In the present understanding the Late-type galaxies are known to be currently forming stars and to be rich in cold gas and dust. In contrast the early-type galaxies are generally not currently forming significant quantities of stars and usually have smooth structures with little cold gas and dust present. Until recently early-type galaxies were generally thought to be a fairly uniform

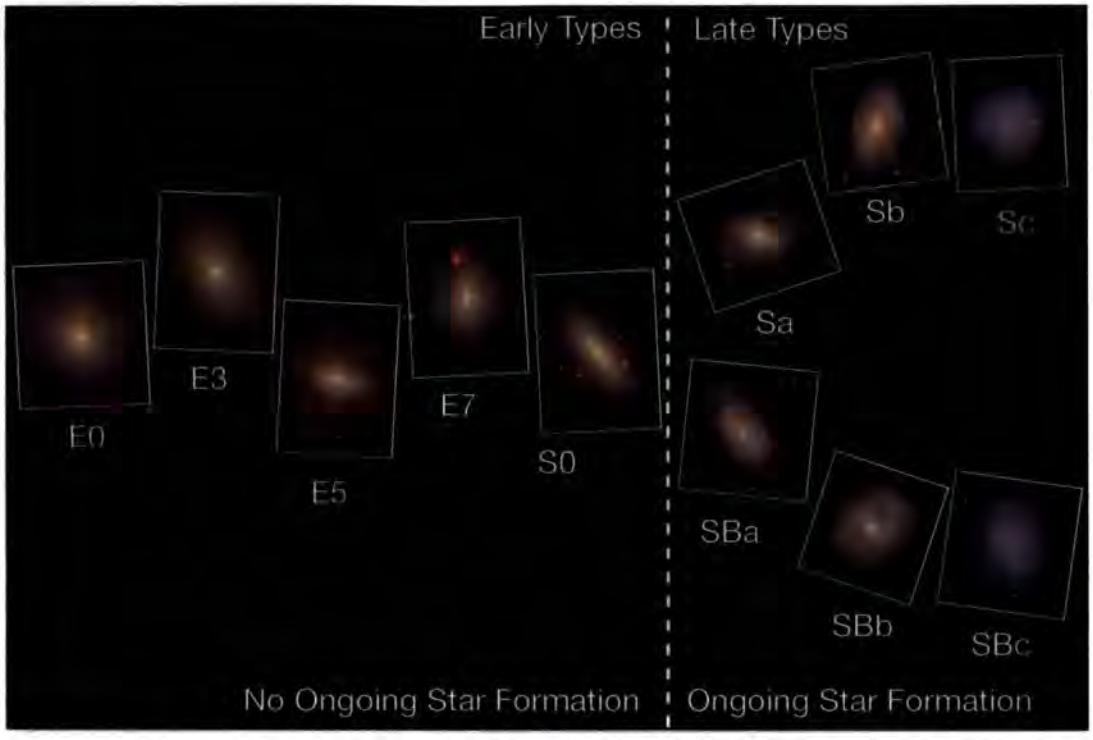

Figure 1.3: The Hubble Sequence. The galaxy classification scheme presented by Hubble (1936) separates galaxies into early type (smooth and generally featureless) and late type (complicated structure, dusty and gas rich) galaxies. The late-type spirals are separated into barred and unbarred varieties, Irregular galaxies are omitted for clarity. Galaxy images are from the Sloan Digital Sky Survey (Adelman-McCarthy et al., 2008).

class of objects, composed of older stars formed early in the history of the Universe in a single monolithic collapse of a large gas cloud. This picture is however at odds with the theoretical framework set out previously which predicts that galaxies are built from smaller substructures over time. As will be explained later observational data collected in recent decades has also largely discounted this picture.

The main topic of this Thesis is the study of the formation and evolution of early-type galaxies through an examination of their kinematics and stellar populations, with the aim of reconciling observations of early-type galaxies with the predictions of cosmology. To aid the following presentation the current understanding of the properties of early-type galaxies and their implications for the formation mechanisms are presented in Section 1.1. In Section 1.1 and in Section 1.2 the outline of this Thesis will be provided.

1.1. The Properties of Early-Type Galaxies

Early-type galaxies (ETGs) contain a significant fraction of the total mass found in stars in the Universe: 22% for true ellipticals rising to ~75% if spiral bulges are included (Fukugita et al., 1998). Hence any complete understanding of the formation of galaxies must include the formation of ETGs. Two main hypotheses have traditionally been presented to explain the formation and evolution of ETGs. The first is the Monolithic Collapse model (Eggen et al., 1962; Larson, 1975; Arimoto & Yoshii, 1987), in which ETGs form from the collapse of a single large gas cloud at early epochs, this collapse leads to a starburst and the rapid conversion or expulsion of all the gas, leaving the galaxy to passively evolve to the present. The second model, the Hierarchical Merging model (Toomre, 1977; White & Rees, 1978) is more in tune with the cosmological underpinnings described above, as ETGs (and galaxies in general) are formed by the repeated merging of subcomponents.

In recent years the apparent disagreement between these two scenarios has somewhat weakened, with observations showing the merging of multiple gas-rich star forming fragments at large redshift, in a manner which appears hierarchical, but which can lead to results similar to those predicted by a monolithic collapse. An example of such behaviour is found in the case of the so called Spiderweb galaxy (Miley et al., 2006), a collection of around 10 merging star forming clumps seen at a redshift of 2.2 (see Figure 1.4). These objects are currently thought to be forming the precursor to a cD galaxy. Theoretically there still remains some work to be done to understand entirely the required conditions to allow ETGs to form by such mergers at such early epochs. In the main this is simply due to the inherent difficulty of modelling such complicated systems with realistic gas physics and feedback processes at the required resolution, although more recent efforts are now beginning to reach the required thresholds (e.g. Pipino et al. (2007); Martínez-Serrano et al. (2008)).

An examination of the properties of ETGs can be instructive in helping to determine where the galaxy formation process fits within the overarching cosmology, and in what follows the main observational constraints on the ETG formation process are presented.

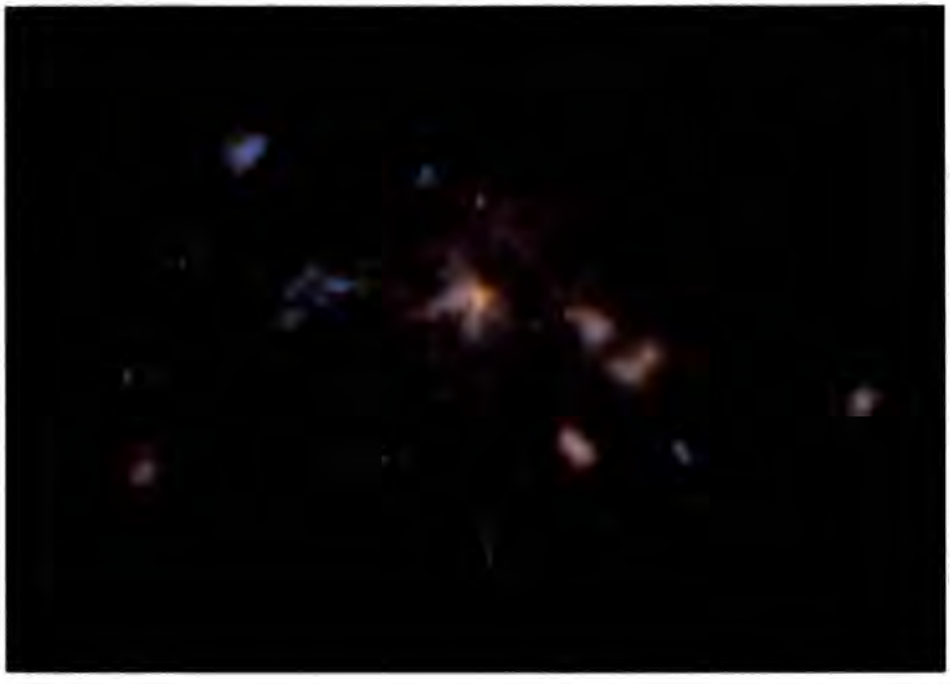

Figure 1.4: The Spiderweb galaxy (Miley et al., 2006), a merging group of gas rich star forming clumps observed at z=2.2. It is perhaps from events such as these that many ETGs are created.

The ETG Fossil Record

There are basically two approaches to studying the formation of ETGs, the apparently most straightforward approach would simply be to examine ETGs at increasing redshift and watch the formation process as it proceeds. Notable successes have been made this way, in particular studies of the morphology density relation have shown that the numbers of Elliptical galaxies in clusters remain relatively constant since at least z=1 (Dressler, 1980; Dressler et al., 1997; Smith et al., 2005; Postman et al., 2005), with the number of S0 galaxies increasing and the number of spirals decreasing towards z=0, a result indicative of some transformation process (such as ram pressure stripping leading to the end of star formation) changing spirals into S0s. The downside with such studies of galaxy formation at high redshift is simply the observational difficulties that are inherent in studying high redshift objects, the objects become progressively smaller and fainter making any rigourous analysis of individual objects challenging, and selection effects which lead to different biases in the high and low redshift samples.

The second approach to studying the formation of ETGs is the one utilised in this Thesis in which nearby examples of the galaxy types of interest are studied in great detail

and clues to their formation found in the "fossil record" of their stellar populations and kinematics. This approach has the benefit of allowing very detailed analysis of individual galaxies, but at the expense of having the added complexity of necessarily having to account for evolution since the epochs of interest. Below are described some of the main conclusions from various lines of study into the formation of ETGs.

Colour-Magnitude Relation and the Fundamental Plane

Part of the reason ETGs were originally thought to have formed via a relatively uniform monolithic collapse was the observation that ETGs display several tight correlations between their physical parameters. One of the first to be noticed was the observation that ETGs located in a variety of environments follow an extremely tight colour-magnitude relation (Baum, 1959; Visvanathan & Sandage, 1977; Sandage & Visvanathan, 1978a,b; Terlevich et al., 1999), with the implication that both ellipticals and S0s must have been passively evolving for at least 1 Gyr (see Figure 1.5 for an example of the C-M relation for the Coma Cluster). Further examination of the slope of the colour-magnitude relation by Bower et al. (1998) found that the bulk of the stellar population of the ETGs must have formed before z=1 and that the subsequent amount of merging since the formation of the ETGs was small, with the stars forming in objects no less than half the mass of the objects they currently reside in.

Another interesting discovery was the observation by Bower et al. (1992) that the intrinsic scatter in the colour-σ (where σ is the central velocity dispersion) relation was even smaller, and that if this scatter was purely due to an age dispersion it could be used to place limits on the epoch of formation. In this case the preferred conclusion was that ellipticals in the Virgo and Coma clusters formed the majority of their stars before z=2.

A further set of clues to ETG formation comes from the study of the Fundamental Plane of ETGs, this is the observation that the observable quantities of central velocity dispersion σ, effective radius R_e and luminosity are closely related in ETGs. Dressler et al. (1987) and Djorgovski & Davis (1987) demonstrated that when examined in the 3 dimensional space of R_e, σ and I_e (the intensity within R_e) galaxies tend to lie close to a plane, the so called Fundamental Plane (FP). Various projections of this plane had previously been discovered as the Faber-Jackson (Faber & Jackson, 1976), and Kormendy relations (Kormendy, 1977). Figure 1.6 displays a recent example of the Fundamental Plane from Bernardi et al. (2006).

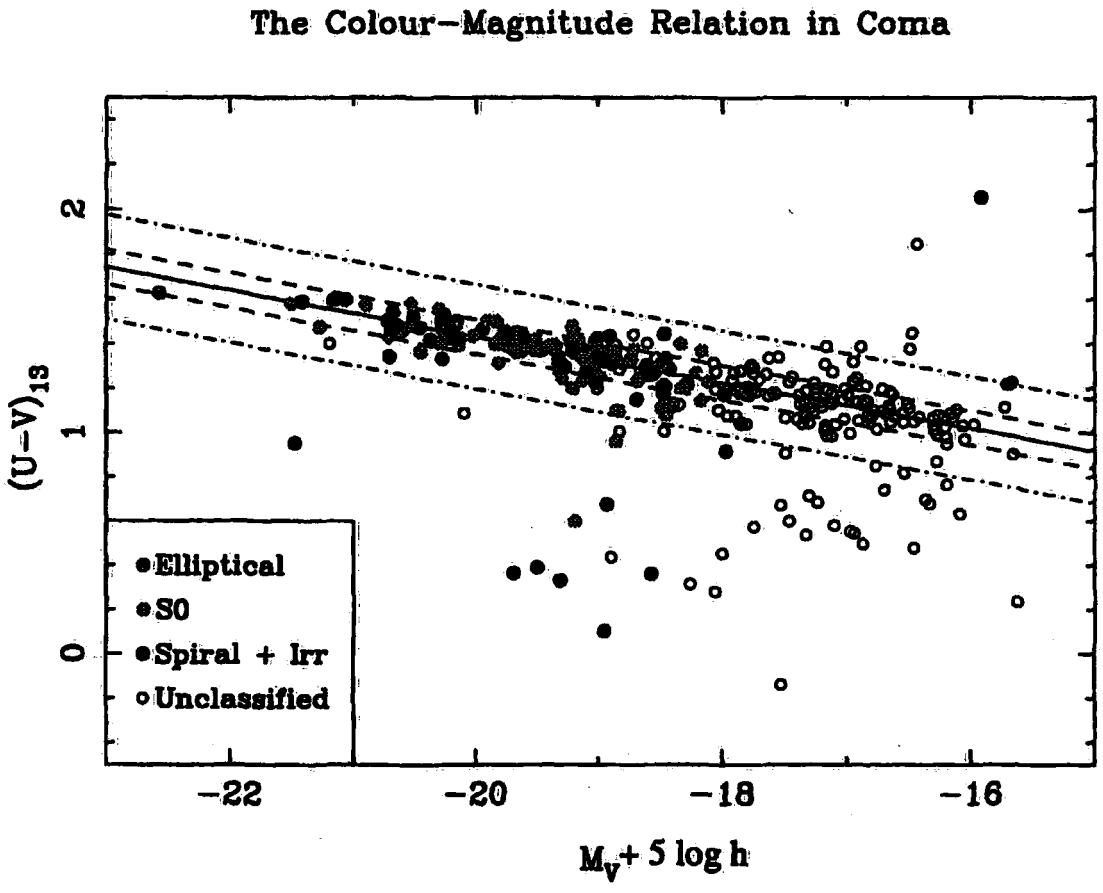

Figure 1.5: Figure 2 from Bower et al. (1999), the colour-magnitude diagram for spectroscopically confirmed members of the Coma cluster, data from Terlevich et al. (1999). Objects which are located significantly below the mean relation are also found to be discrepant in their Balmer indices, in the sense expected if they harbour younger stellar components. These objects have therefore undergone non-negligible amounts of recent star formation which has lead to their bluer colours.

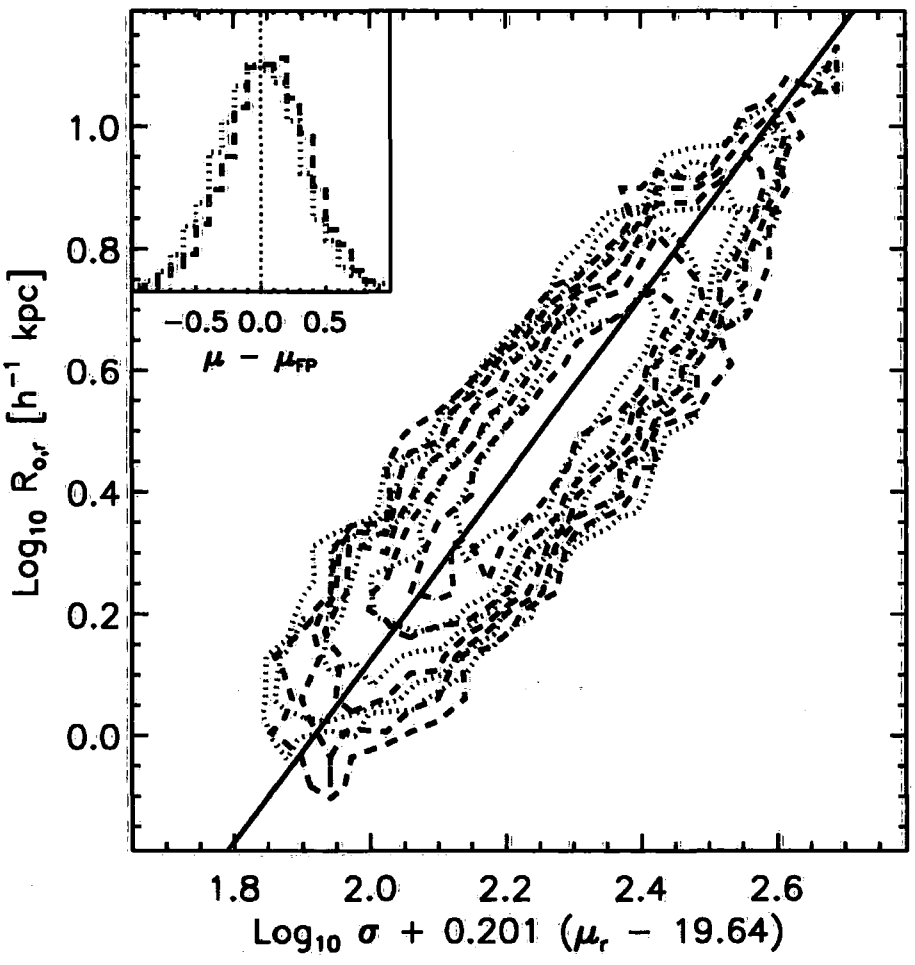

Figure 1.6: Figure 3 from Bernardi et al. (2006) - The r band Fundamental Plane for 40,000 SDSS galaxies. The dashed and dotted lines represent subsamples which populate over and under-dense regions respectively. Galaxies in dense regions are ~0.08 mag fainter on average.

The existence of the FP has been used to make several inferences about the formation of ETGs. Bender et al. (1992) found that the small scatter in the FP of the Virgo and Coma clusters implied a very small (<12%) dispersion in the value of M/L ratio at any point in the plane. They also found that the tilt of the FP implies a variation in the M/L ratio along the plane, with an increase by a factor of 3, at the same time that the mass is increasing by a factor of 100. Renzini & Ciotti (1993) found that the small scatter in the FP, if due to an age dispersion, was consistent with that predicted by the results of studies of the colour-magnitude and colour-σ relations. Later work by various authors (e.g. Pahre et al. (1998); Mobasher et al. (1999); Trujillo et al. (2004)) found that the tilt in the FP cannot be simply explained and is probably due to a combination of stellar population variation along the plane (in the sense that the oldest galaxies are most metal rich) and a systematic trend away from structural homology. Finally, an examination of 40,000 SDSS galaxies by Bernardi et al. (2003, 2006) found small differences between galaxies located in over-dense and under-dense regions, in the sense that galaxies located in higher density regions were around 1 Gyr older than those in the field. These studies again confirmed that ETGs followed a FP which was consistent with a formation epoch of around 9 Gyr ago, followed by passive evolution up to the present.

Out of these three lines of inquiry a consistent picture can therefore be seen to have emerged. The stars in ETGs appear to have formed relatively early in the lifetime of the Universe (before z=2) and to have evolved relatively passively since that time. At first glance this picture seems more in tune with a monolithic collapse scenario, although as already described a hierarchical merging formation is also permitted as long as the majority of the merging (at least any merging which leads to new star formation) occurs before a redshift of 2. It could prove to be the case that the epoch of star formation and the epoch when those stars were assembled into the ETGs observed today may be different. One further observation which is more in tune with the hierarchical picture is the observation that galaxies in lower density environments are slightly younger than those in high density environments.

Line Strength Indices of Galaxies

One of the most powerful methods of examining the formation and evolution of galaxies is to examine the stellar populations of the galaxies directly. Ideally this can be done, as it is in the Milky Way and nearby galaxies, by directly examining the resolved stellar

populations of the galaxies. Using the Hertzsprung-Russell diagram it becomes possible to accurately determine the age and metallicity of the stellar populations, the presence of features such as several main sequence turnoffs can also be used to determine the various periods of star formation. In practice this approach is limited to the nearest galaxies and for the majority of galaxies only the integrated properties of large ensembles of stars, with presumably variable formation histories, can be studied. Early attempts at this type of study focussed on the study of the integrated colours of galaxies, with the observation that the mean colours of ETGs are generally consistent with G-K dwarfs, as would be expected if the stellar populations were old. Study of the gradients in galaxy colours also revealed that ETGs generally become bluer with radius (Franx et al., 1989; Peletier et al., 1990), an effect which could be due to either age or metallicity gradients. In fact the study of integrated colours has several drawbacks, not least of which is the degeneracy between the effects of age and metallicity on the colours (Li & Han, 2008).

In recent decades the improved sensitivity of spectroscopic instrumentation has allowed the study of the spectra of integrated stellar populations to flourish. The strength and appearance of absorption lines in the integrated spectra is determined by factors such as the ages and chemical make up of the stars comprising the stellar population, and their internal kinematics. In addition the relative strengths of different absorption lines can be used to partly circumvent the age-metallicity degeneracy found in the broad band optical colours.

One of the first attempts to exploit this sensitivity to age and metallicity was introduced by Burstein et al. (1984) and augmented subsequently by several authors (Worthey, 1994; Worthey & Ottaviani, 1997; Trager et al., 1998). This system, known as the Lick/IDS system, is based on a set of absorption line indices chosen to be mostly sensitive to age (e.g. Hγ, Hδ and Hβ), iron abundance (e.g. Fe5270, Fe5335) or an alpha-element such as magnesium (e.g. Mgb). Early discoveries using this system included the observation by González (1993) that in his sample of 40 nearby ellipticals, the central stellar population was found to have a wide range of mean ages, from 2 Gyr up to 17 Gyr. González (1993) also confirmed the findings of several previous studies that the abundance ratios of Mg to Fe in ellipticals, especially the most massive ones are considerably different from those found in the solar neighbourhood (O'Connell, 1976; Peletier, 1989; Gorgas et al., 1990; Worthey et al., 1992). The generally accepted implication of this finding is that the apparent α-element overabundances are caused by very short star formation timescales

(Thomas et al. (2005a) found using a simple closed box model that for [α/Fe] > 0.2 the formation timescale must be less than 1 Gyr); most of the stars are thought to form rapidly so that only the products of the prompt Type II supernovae are produced quickly enough to become incorporated into new stars before the star formation event ceases. The star formation event is thought to have ended before the first stars have undergone the required binary evolution to create the Type Ia supernovae responsible for creating much of the Fe found in the Universe, hence the stars formed in such a rapid event are somewhat Fe deficient relative to the amount of α-elements they are observed to have. Such α-element enhancements do not sit particularly well with either of the formation scenarios presented. The monolithic collapse would predict that large galaxies would have longer star formation timescales, due to their larger potentials being capable of holding more material during the formation event. In the hierarchical picture, which at least initially was thought to predict many ETGs should form from the merger of spirals, the observed α-element enhancement was also problematic. This is due to the fact that the majority of stars found in the ETG would have formed in the progenitor spirals over a long period prior to the merger event, the overall α-element enhancement should therefore be lower than observed.

More recent studies have built on this earlier work, including the effect that the α-enhancement can have on the measured ages and metallicities of the stellar populations (Thomas et al., 2003, 2004), and attempting to correct for the fact that the observed errors in the line strength indices lead to an apparent anti-correlation of age and metallicity (Trager et al., 2000; Kuntschner et al., 2001). Work by Thomas et al. (2005a) on the central stellar populations of 124 ETGs found that all three stellar population parameters, age, metallicity and [α/Fe], correlate with σ, that the bulk of ETGs formed their stars mainly between z= 5 and 2 and that in lower density environments the end of star formation was delayed by around 2 Gyr. Similar results were found by Nelan et al. (2005) for a larger sample of 4000 red sequence (those observed to lie on the tight colour-magnitude sequence observed in clusters, i.e. in Figure 1.5) galaxies. One possible complication is that the behaviour of the horizontal branch stars can have a significant influence on the measured Hβ index and hence the implied age; at present it is not clear whether or not such stellar types cause significant problems in typical ETGs.

Broadly speaking the result of studies into the line strength indices of ETGs can be seen to support the conclusions of investigations of the colour-magnitude, colour-σ and

Fundamental Plane of ETGs, in the sense that ETGs are generally found to have formed the majority of their stars at very early epochs, and that there appear to be slight differences in the epoch of the last significant star formation dependent on the environment in which the ETG resides. Some complications are however apparent. Studies which focus only on the central regions of ETGs can be biased by the presence of small amounts of young stars formed in recent minor merger or accretion events, a situation seen in several ETGs with observed strong positive age gradients, such that the inner regions appear much younger than the bulk of the galaxy (e.g. Proctor et al. (2005); Sánchez-Blázquez et al. (2007); Reda et al. (2007)). It may be that these young ages found in the inner regions of ETGs may in fact be the fingerprint of hierarchical growth, with the majority of the galaxy forming at early times only for small amounts of gas to be accreted at later times. More substantial studies of the radial behaviour of line strengths of the types now being undertaken (e.g. Sánchez-Blázquez et al. (2007); Reda et al. (2007); Loubser et al. (2007); Brough et al. (2007); Spolaor et al. (2008)) will help to settle this matter.

The Connection between Early type Galaxies and their Globular Cluster systems

One extremely powerful probe of the galaxy formation process not discussed so far involves the study of the Globular Cluster (GC) systems of galaxies. Globular star clusters (see Figure 1.7) are among the oldest stellar systems found in the Universe and as such they can allow an examination of the very earliest periods of galaxy formation (or even periods of star formation before the epoch of galaxy assembly). GCs themselves are also unusually simple systems, being a gravitationally bound system of 10^4 to 10^6 stars, all of which were formed at the same time from the same initial cloud of gas and dust. Although some MW GCs are observed to display multiple main sequences possibly indicative of several star formation periods (see for example D'Antona et al. (2005) for the case of NGC 2808), but this behaviour appears to be rare and can be explained in some cases as being due to the fact the objects are not bona fide GCs but in fact the stripped remains of a dwarf galaxy nucleus. The inherent simplicity of the stellar populations of GCs makes them ideal Simple Stellar Populations (SSPs), as they are composed of stars which formed at the same time and with the same chemical abundances. The changes in their integrated properties with time are therefore considerably simpler to understand than the composite stellar populations of galaxies. When this fact is combined with the observation that GCs appear to be formed in fixed proportion to the total mass of stars

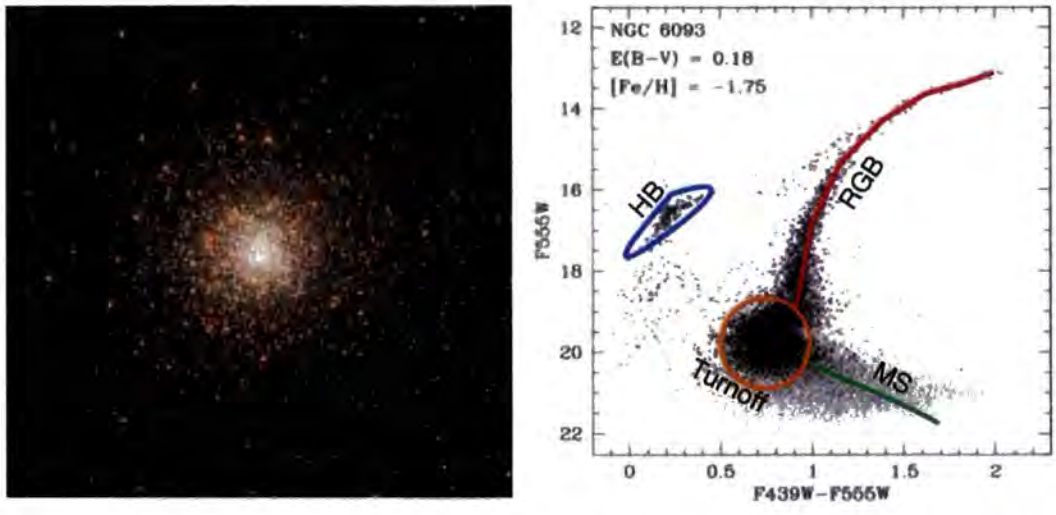

Figure 1.7: **Left Panel** : The Milky Way Globular Cluster NGC 6093 as observed by the Hubble Space Telescope. **Right Panel** : The corresponding colour-magnitude diagram for NGC 6093 stars as observed by the HST and presented in Piotto et al. (2002). Overplotted are the positions of the Main Sequence, Main Sequence Turnoff, Horizontal Branch and Red Giant branch. The positions of these features are determined by the age and metallicity of the stellar population. In GCs with only one population these features are well defined, in composite stellar populations it becomes difficult to define the position of these features making it impossible to place strong constraints on the age and metallicity of the stellar populations present.

formed in a star formation event (McLaughlin, 1999), the true power of studying the GC systems of galaxies becomes apparent. If it is assumed that the GCs which survive to the present are in no way special, at least compared to other stars which formed in unbound star clusters during the same star formation event, or from subsequently disrupted clusters then the age and metallicity distributions of the GC system of a galaxy directly trace that of the diffuse stellar population of that galaxy, quantities which are extremely difficult to tease from integrated light studies.

As with studies of galaxies, the first significant investigations of the GC systems of galaxies involved the photometric examination of the GCs, the most interesting finding being that the GC systems of almost all galaxies display bimodal colour distributions (Peng et al., 2006). This observation which was first hinted at in the early 1990's (Zepf & Ashman, 1993) has subsequently been confirmed for all massive ellipticals by Hubble Space Telescope (HST) surveys of many dozens of galaxies (Larsen et al., 2001; Kundu &

Whitmore, 2001a,b; Peng et al., 2006). Such an observed colour bimodality has traditionally been explained as being primarily due to an underlying metallicity bimodality (the ages of the two sub-populations are found to be the same within the (~2 Gyr) errors).

Several models were therefore suggested for the formation of ETGs which would naturally result in the formation of two distinct subpopulations of GCs. In the major merger scenario (Ashman & Zepf, 1992; Zepf & Ashman, 1993) the blue (metal-poor) GCs are hypothesised to have formed in spiral galaxies which subsequently merge, red (metal-rich) GCs are formed from the enriched gas present during the merger event. Forbes et al. (1997) presented several problems with the major merger scenario and went on to suggest their own evolution of models based on a multiphase dissipational collapse. In this scenario blue GCs form in gaseous fragments at high redshift, a brief cessation of star formation would then occur, possibly due to events such as cosmic reionization, followed by subsequent merging of the gaseous fragments and red GC formation. The third scenario is the accretion model of Côté et al. (1998, 2000, 2002) in which the red GCs form contemporaneously with the massive galaxies and the blue GCs are accreted later from nearby lower mass galaxies. All three scenarios have some strengths and some weaknesses, however from a practical point of view they are also generally interchangeable. By varying the redshifts at which certain events occur, each scenario can be made equivalent. Before reading too much into such scenarios it should also be noted that in recent times the existence of such distinct metallicity subpopulations has been called into question, with several authors claiming evidence for significant non-linearity in the colour-to-metallicity transformation, either from observational (Peng et al., 2006; Richtler, 2006) or theoretical (Yoon et al., 2006; Cantiello & Blakeslee, 2007) arguments. Such non-linearities in the transformation can cause a unimodal metallicity distribution to project onto a bimodal colour distribution; only the determination of a significant number of spectroscopically confirmed GC metallicities will settle this debate. To date this has only been achieved for the Milky Way (Armandroff & Zinn, 1988) and NGC 5128 (Beasley et al., 2008), both of which do indeed display multi-modal metallicity distributions.

One further discovery made via the photometric examination of GC systems was found through the examination of the numbers of GCs per unit galaxy diffuse stellar mass. The idea of a specific frequency S_N was introduced by Harris & van den Bergh (1981) and later adapted into the quantity T by Zepf & Ashman (1993), where T is the number of GCs per $10^9 M_\odot$ of galaxy stellar mass. Various studies have probed the re-

lationship between S_N/T and galaxy type, with Forbes et al. (2001b) suggesting that the bulge GCs found in spirals are similar to the metal rich GCs found in ETGs, and that when normalised only to the bulge luminosity the metal rich GCs of spirals and ETGs both have $S_N \sim 1$. This finding was confirmed by Goudfrooij et al. (2003) for a sample of 7 edge-on spirals examined with HST WFPC2 imaging, and would seem to indicate a similar formation mechanism for both the bulges of ETGs and spiral galaxies.

As in studies of the integrated properties of galaxies, there has recently been an expansion in the spectroscopic study of GCs, despite the difficulty of examining relatively faint objects at extragalactic distances. To date such observations are still in the process of building up large unbiased samples of GC spectra, but first indications are that this type of study will do much to illuminate the galaxy formation process. The main highlights of the multi-object spectroscopic examination of the GC systems of galaxies studied so far include the fact that the vast majority of GCs examined are found to be old (>9 Gyr) and that the GC subpopulations are found to be essentially coeval (and old) within the measured errors. The magnitude of the age uncertainties of typically 1-3 Gyr combined with the relatively small number of clusters examined per galaxy means that a similar uncertainty exists on the spread of cluster ages both within the a galaxy and between galaxies. Only significantly improved statistics will enable the measurement of age differences between subpopulations and between the GC systems of different galaxies.

To date studies have examined many GC systems of various galaxy types, e.g. ellipticals (NGC 1399 (Forbes et al., 2001a), NGC 3379 (Pierce et al., 2006a), NGC 4649 (Pierce et al., 2006b), NGC 5128 (Beasley et al., 2008)), S0s (NGC 524 (Beasley et al., 2004b), NGC 3115 (Kuntschner et al., 2002; Puzia et al., 2005), NGC 1380 (Puzia et al., 2005)), Spirals (M81 (Puzia et al., 2005), NGC 4594 (Larsen et al., 2002)) and Dwarf galaxies (NGC 147, 185, 205 (Sharina et al., 2006), KK84, KK211, KK221 (Puzia & Sharina, 2008)). Two meta-analyses have been completed, pulling together much of the high S/N data accumulated over the past decade, the first by Strader et al. (2005) confirming that the extragalactic GC subpopulations had ages at least as old, if not older than those measured for the MW GCs. The second analysis by Puzia et al. (2006) also confirmed this finding, but in addition discovered a significant population of extremely α-enhanced GCs associated with elliptical galaxies, a population which was not observed in either S0 or spiral galaxies.

Taken together these findings would tend to support the suggestion that ETG formation (including spiral bulges) occurred before a redshift of 2. The finding that the GCs of

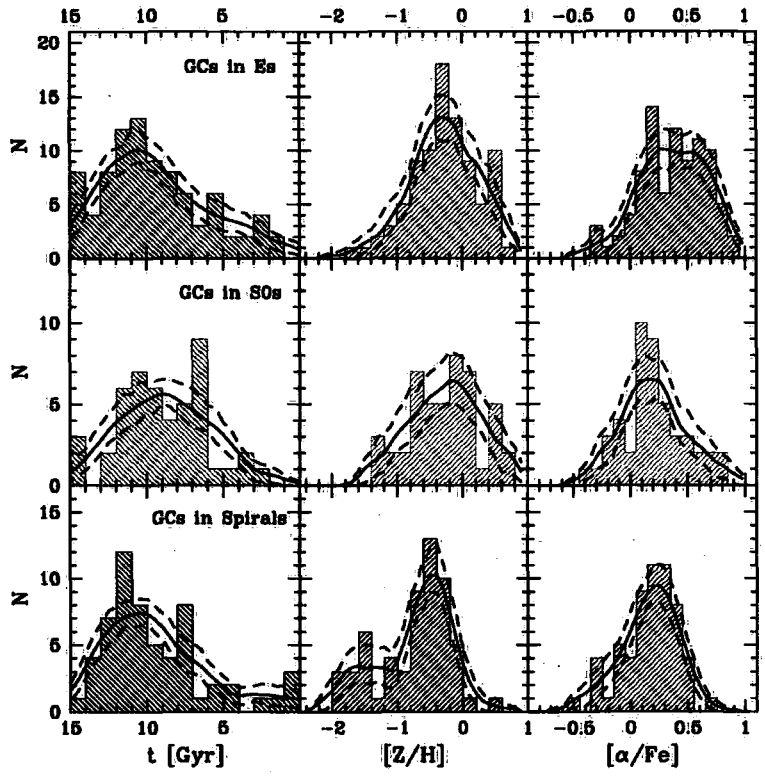

Figure 1.8: Figure 2 from Puzia et al. (2006) demonstrating the observed distribution of age, metallicity and [α/Fe] for their sample of extragalactic GCs. Of particular interest is the population of extremely α-enhanced GCs found only in the elliptical sample.

ellipticals are significantly α-enhanced would also tend to support the idea that the formation process was extremely rapid. The small number of younger GCs found in some of these studies could then be associated with more recent smaller accretion events, which could lead to the formation of a "frosting" of young stars found in the inner regions of some early types. At present samples of only 10-20 GCs per galaxy have been collected and much larger samples of 100-200 will be required to determine the formation histories of galaxies (at least the spheroidal components) on the few per cent level.

S0 Galaxies

Up to this point ETGs have generally been discussed as if they are a single galaxy type formed through a similar process. However early-type galaxies can also be broken down into two subgroups, ellipticals, and S0 galaxies. There are notable differences between ellipticals and S0s, the most obvious being the observation that S0 galaxies have significant stellar discs whereas ellipticals do not. Also, as previously discussed, evidence from the morphology-density relation shows that the number of S0 galaxies in clusters has increased since a redshift of 1, while the number of ellipticals has remained the same, strongly pointing to different formation routes for these two galaxy types. When the increase in the S0 population since z=1 is combined with the observation that there is a corresponding decrease in the number of spiral galaxies, a scenario in which S0s are the converted remains of spiral galaxies becomes obvious.

This presumed relationship between S0s and Spirals has grown more secure in recent years with work from the Nottingham group attacking the problem from a series of directions. First in Aragón-Salamanca et al. (2006) and then Barr et al. (2007) it was shown that the GC specific frequency of a sample of S0 galaxies increased with the spectroscopically derived age of the central region of the S0 (See Figure 1.9). The magnitude of the increase in S_N was found to match that expected from simple fading of the disc of the galaxy since star formation ended, assuming that spirals and S0s start with the same GC systems and no GCs are formed in the conversion process, an assumption that seems relatively secure given that the age, metallicity and [α/Fe] distributions of spirals and S0s were found to be very similar by Puzia et al. (2006) (See Figure 1.8). A second study by Bedregal et al. (2006a) found that the Tully-Fisher relation for S0 galaxies was systematically offset to fainter magnitudes than that found for spirals (See Figure 1.10). For a subset of their data comprising 7 galaxies located in the Fornax cluster the amount of offset was correlated

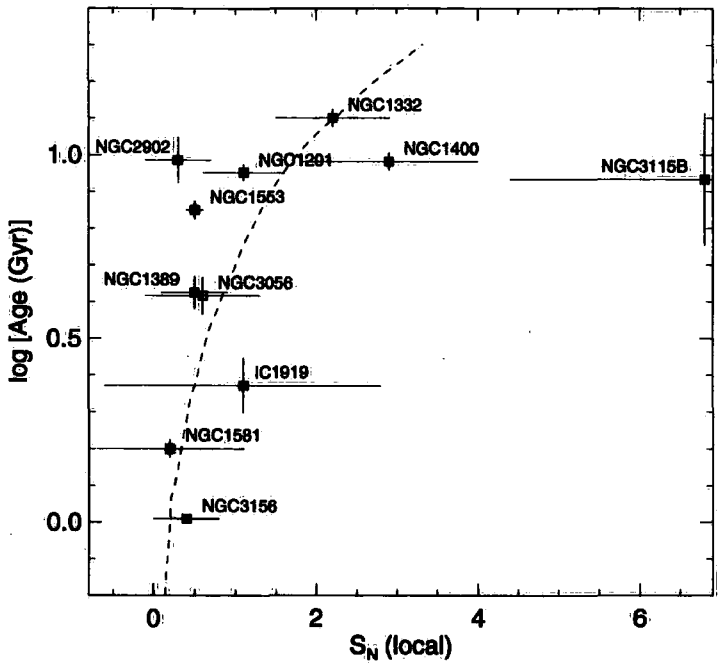

Figure 1.9: Figure 4 from Barr et al. (2007). The log(Age) of the host galaxy versus GC specific frequency. The dashed line shows the track followed by a fading spiral which started with $S_N = 0.4$, from the stellar population models of Bruzual & Charlot (2003).

with the spectrscopically determined age of the S0, again providing strong support to the idea that S0s are the passively evolving descendants of spirals which ceased forming stars at some point in the past.

One commonly cited objection to this picture is the observation that simple bulge-to-disc decompositions indicate that S0s have significantly larger Bulge-to-Total ratios (~0.6) than spirals (<0.2) (Simien & de Vaucouleurs, 1986). To fit into the simple fading spiral scenario this would require unfeasible amounts of bulge growth during the transformation. However in recent years this commonly accepted picture of S0s being dominated by large classical $r^{\frac{1}{4}}$ bulges has been challenged, most notably by Laurikainen et al. (2007) who found S0s to have B/T ratios of between 0.2 and 0.3. The large difference in measured B/T is due to the application of more sophisticated models which allowed the value of the Sérsic index to vary (previously it was held to 4) and allowed for the presence of other structures such as discs, bars or ovals which could contribute to the light of the bulge. A lower value of B/T for S0s such as that seen by Laurikainen et al. (2007) is much more readily understood in terms of a simple spiral to S0 transformation, with any increase in bulge luminosity being of the order explainable by bar driven star formation,

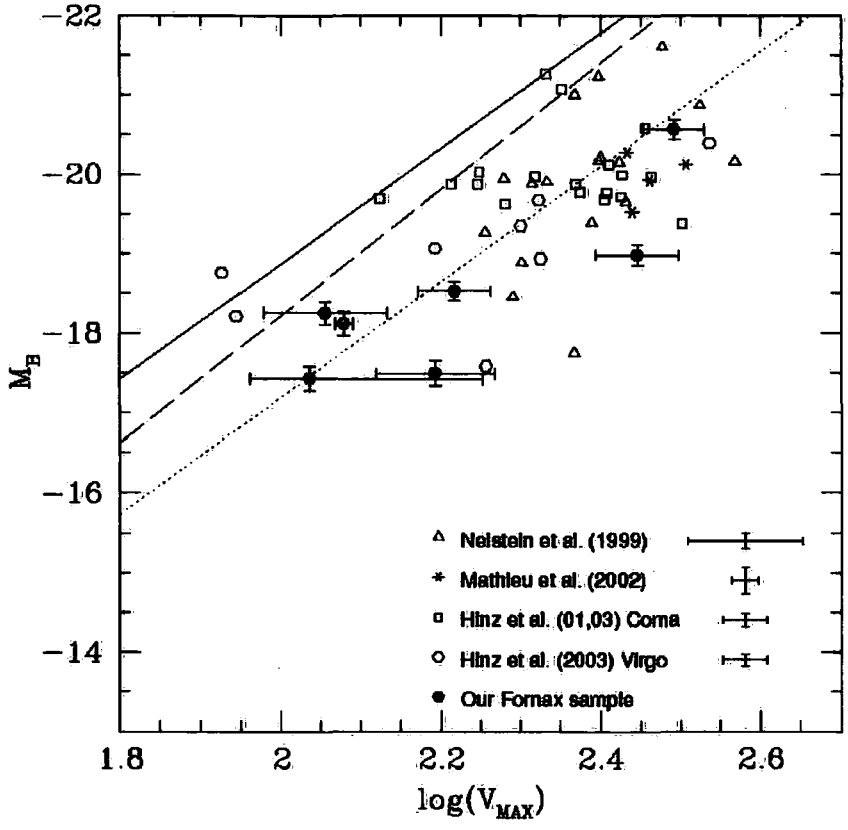

Figure 1.10: Figure 1 from Bedregal et al. (2006a). The B-band Tully-Fisher Relation for S0 galaxies. Solid and dashed lines are the local spiral TFR from Tully & Pierce (2000) and Sakai et al. (2000) respectively. The dotted line shows the best fit S0 TFR when using the slope from Tully & Pierce (2000).

or potentially through star formation in gas driven to the centre of the galaxy during the transformation event.

There exists at present a number of plausible explanations for the transformation of a star forming spiral into a quiescent S0 in a cluster environment, all of which rely on the truncation of star formation in the galaxy disc, however it remains to be seen if these mechanisms are applicable to non-cluster environments. The most common explanation for the truncation of star formation is that during infall into the cluster the cold star forming gas found in the spiral disc is stripped by the ram pressure of the hot intracluster medium, leading to a rapid shutdown of star formation (Gunn & Gott, 1972; Abadi et al., 1999). In variations of this model it is not the cold gas of the disc which is stripped but the hot gas reservoir which surrounds the galaxy and which is believed to replenish the disc as it cools. In this picture, generally called the strangulation model, star formation

continues in the disc until such time as the cold gas is depleted, the cluster medium then prevents further gas cooling onto the galaxy, ending star formation (Bekki et al., 2002; McCarthy et al., 2008). Simulations suggest that this method of quenching may be more effective in group environments where the ICM is not dense enough to strip the cold gas of the galaxy via ram pressure stripping (Kawata & Mulchaey, 2008). It is also possible that a short term enhancement of star formation, or even a starburst, is possible due to the collapse of giant molecular clouds under the external pressure of the ICM (Bekki & Couch, 2003). The observation of galaxies currently undergoing ram pressure stripping in nearby large clusters lends strong support to this explanation for at least some S0s (Vollmer et al., 2001; Vollmer, 2003; Chung et al., 2007).

A further suggested truncation mechanism involves a merger event between a spiral galaxy and a smaller galaxy. If the mass ratio is below 3:1 simulations show that it is possible to keep overall disc structure while stopping star formation through the rapid conversion of all of the gas into stars Bekki (1998). A variant of this mechanism involves the combined effects of many high-speed near misses between cluster galaxies, the so-called harassment scenario (Moore et al., 1998). The multiple close interactions lead to a heating of the disc component, leading to an increase in the velocity dispersion, and to the sinking of the gas in the disc to the inner regions where it would produce a starburst.

At present observations which truly begin to separate the most likely of these (and other) formation scenarios are in somewhat short supply. Current observations are often better at ruling out other scenarios rather than discriminating between the ones described, for example it was once though that S0s could possibly be the result of a major merger event with subsequent disc regrowth. However the kinematics of S0 galaxies show that very few exhibit counter rotating co-spatial stellar discs of the kind expected from the re-accretion of gas debris from a merger event (e.g Kuijken et al. (1996)). What is required, and is currently under construction (see Chapter 3) is a large sample of spectroscopy of S0 galaxies located in a range of environments. Through the careful study of the stellar populations of the bulge and disc components of S0 galaxies, it will be possible to probe for any evidence of an environmental dependence of the transformation mechanism using their fossil record.

1.2. Outline of this thesis

This Thesis is structured as follows:

- Chapter 2 presents the longslit spectroscopy of the major and minor axes of the nearby edge-on S0 galaxy NGC 3115. The kinematics and stellar populations of this galaxy are compared to those found in previous studies of the GC system of NGC 3115.

- Chapter 3 presents preliminary results from a large survey devoted to the spectroscopic study of the kinematics and stellar populations of edge-on S0 galaxies. This data is used to examine the Tully-Fisher relation for S0 galaxies and to examine its implication for S0 formation scenarios.

- Chapter 4 presents spectroscopy of the GC system of the shell elliptical galaxy NGC 3923. This data is used to examine the stellar populations of the GC system of NGC 3923 and to compare those populations with that found for the integrated light of NGC 3923 at $\sim 3R_e$.

- Chapter 5 presents additional nod-and-shuffle spectroscopy of NGC 3923 GCs. This data is used in conjunction with that presented in Chapter 4 to constrain the Dark Matter content of this galaxy.

- Chapter 6 provides some concluding remarks and suggestions for further extension of the work presented here.

- The Appendix provides Tables and Figures considered too large for the main body of this Thesis.

Chapter 2

GMOS Spectroscopy of the S0 Galaxy NGC 3115

2.1. Abstract

This chapter presents Gemini GMOS longslit spectroscopy of the isolated S0 galaxy NGC 3115. This data has been used to determine kinematic properties and Lick/IDS absorption line-strength indices for the major axis out to 9 kpc and for the minor axis out to 5 kpc (around 2 effective radii (R_e)). Making use of stellar population models which include the effects of variable [α/Fe] ratios the metallicities, abundance ratios and ages for the stellar population of NGC 3115 have been measured. It is observed that [α/Fe] remains fairly constant with increasing radius at [α/Fe] = 0.17 for the major axis but increases rapidly for the minor axis to [α/Fe] = 0.3. To first order this behaviour can be explained by a simple spheroid + disc model, where the spheroid has [α/Fe] = 0.3 and the disc shows close to solar abundance ratios. The disc also appears considerably younger than the spheroid, having an age of around 6 Gyr compared to 12 Gyr for the spheroid. These results are compared to those previously presented by Kuntschner et al. (2002) for the globular cluster system of NGC 3115.

2.2. Introduction and Previous Work

Globular clusters (GCs) are among the simplest stellar systems. The stellar content of individual clusters forms primarily at one epoch and location and so they are remarkably uniform in terms of metallicity, age and chemical abundances (as evidenced by their extremely tight colour magnitude diagrams e.g. Pulone et al. (2003), Clem et al. (2008)). Because GC's are believed to form preferentially during the major star forming and mass accumulation epochs, a careful examination of the GC population of a galaxy can shed light on these periods of a galaxy's development. This however relies on the assumption that GC's act as good tracers of the properties of the overall stellar population formed at the same epoch. For a more thorough discussion of why this is believed to be the case see Puzia et al. (2005). It is the aim of the present work to test this hypothesis in detail for one well studied galaxy.

NGC 3115 is one of the closest and most studied S0 galaxies. Its GC system has been extensively investigated, using both photometric (Kavelaars, 1998; Kundu & Whitmore, 1998; Puzia et al., 2002), and spectroscopic (Kuntschner et al., 2002; Puzia et al., 2004) techniques. These studies find two GC sub populations of mean metallicities [Fe/H] $\simeq$ -0.37 and [Fe/H] $\simeq$ -1.36. Kuntschner et al. (2002) find that both GC sub populations have ages which are consistent with a single epoch of formation about 12 Gyr ago. The observations of Kundu & Whitmore (1998) and Kavelaars (1998) are consistent with the metal-rich clusters being associated with a rapidly rotating thick disc system and the slower rotating metal-poor clusters being associated with the halo of NGC 3115. The stellar population of the galaxy itself has also been examined, notably by Fisher et al. (1996) who measured the line strengths and their gradients out to a radius of 40" along the major axis, Trager et al. (1998) also examined the absorption line indices of the galaxy nucleus. Elson (1997) found evidence for a bimodal distribution of metallicities with [Fe/H] $\simeq$-0.7 and [Fe/H] $\simeq$-1.3 in the resolved stellar population of the halo located 8.5′ east of the centre and 5′ from the major axis, although Kundu & Whitmore (1998) suggested that this might be due to an instrumental effect in the metallicity calibration. Taken together these observations lead to the possibility that the metal poor sub-population formed 12 - 13 Gyr ago, with the metal rich population forming several Gyr later after the ISM has been enriched by a factor of $\simeq$4, perhaps triggered by AGN activity or a merger event. A further examination of the ages and metallicities of the general stellar population and the

Table 2.1: NGC 3115 Basic Parameters

Parameter	Value	Source
Right Ascension (J2000)	$10^h05^m13.98^s$	*a*
Declination (J2000)	-07°43′06.″9	*a*
Morphological Type	$S0^-$	*a*
Major-Axis Diameter	7.2 arcmin	*a*
Minor-Axis Diameter	2.5 arcmin	*a*
Heliocentric Radial Velocity	663 ±4 kms^{-1}	*b*
Asymptotic Radial Velocity	263 ±5 kms^{-1}	*b*
Central Velocity Dispersion	314 ±4 kms^{-1}	*b*
Inclination of disc	86°	*c*

[a] NED. http://nedwww.ipac.caltech.edu/.

[b] This study.

[c] Capaccioli et al. (1993).

GC population in this galaxy using updated Simple Stellar Population (SSP) models can test the plausibility of these scenarios.

2.3. Observations and Data Reduction

The observations were carried out on the 18/19th of December 2001 with the GMOS instrument (Hook et al., 2004) on the Gemini North telescope (Program ID GN-2001B-Q-44). The B600 grism with 600 lines/mm was used with a longslit 1 arcsec wide by 335 arcsec long. The data were binned by 4 in the spatial dimension and 2 in the spectral dimension producing a spectral resolution of ~4.4 Å FWHM (110 kms^{-1}) sampled at 0.9 Å/pixel. The seeing throughout the observations was generally $\leq$ 0.8 arcsecs and the binned pixel scale was 0.3 arcsec/pixel. The wavelength range is ~3800-6400 Å. Two sets of integrations were completed, one each for the major and minor axis of the galaxy, with a total integration time for each axis of 7200s. The centre of the major axis longslit was offset from the galaxy centre along the major axis by 120 arcsecs as can be seen in Figure 2.1, to extend the radial coverage and reduce the galaxy light in the sky background region. For the minor axis the sky region was defined at either end of the longslit. As can

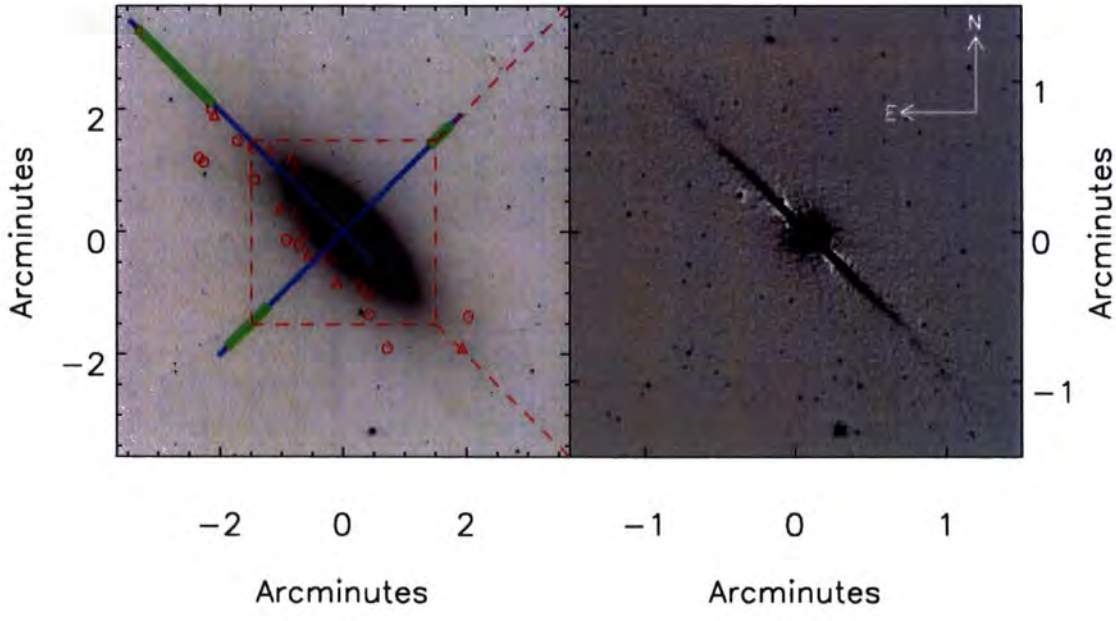

Figure 2.1: Left Panel: Positions of the major and minor axis longslits (blue solid lines), slit widths are exaggerated by a factor of ~5, green regions indicate the sky estimation regions. Red circles denote positions of GC's examined by Kuntschner et al. (2002) with line index measurements, red triangles have only kinematical data from Kuntschner et al. (2002) available. Right Panel: The inner region of the left panel after the subtraction of a smooth median image, to remove the galaxy halo. The edge-on disc of NGC 3115 is clearly visible. Both images were produced using Hawk-I J-band imaging.

be seen from Figure 2.1 the sky subtraction regions are located at large radii where the galaxy flux is only 5 - 6% of the sky level, hence over-subtraction of galaxy light should not be a major problem. This is discussed in more detail in Section 2.3.2. Two velocity standards HD97907, HD73665 and a photometric standard Feige 34 were also observed using the same experimental set up.

The standard Gemini **IRAF** routines were used to carry out bias subtraction, flat-fielding, and cosmic ray subtraction.

2.3.1 Scattered Light Correction

After the standard reduction procedures utilised for the reduction of longslit spectroscopy a further step was required to correct for the effect of light scattering within the GMOS instrument, at present it is believed that the light originates from the classically ruled diffraction gratings. During the execution of this study it was noted that light scattering within the instrument seriously compromised the measurement of line indices at large galactocentric radii. From subsequent experience with the GMOS instrument in longslit mode it appears that this is an unavoidable feature of this and presumably many other spectrographs when they are used to study bright spatially extended objects such as nearby galaxies.

The scattered light has the effect of decreasing measured line indices by applying a DC offset to the spectra; this can be understood to be due to the fact that line strength indices are measured as equivalent widths and are therefore extremely sensitive to the continuum level (see Section 2.3.4 for more details). In practice the weakening of line strengths has two important consequences, the first is that when line strength indices are compared to SSP models, spuriously low metallicities are arrived at. The left hand panel of Figure 2.2 demonstrates this fact by the comparison of the measured line strength indices (in this case from the major axis of NGC 3585) to the SSP models of Thomas et al. (2003, 2004). As can be seen, the uncorrected line strengths are weaker in general than the corrected ones, an examination of Figure 2.3 shows that this effect is negligible for the bright inner regions of galaxies, but grows increasingly important with galactocentric radii. This apparent decrease in metallicity is particularly disturbing, as at first observation this appears entirely possible, only a closer examination of the extremely high implied metallicity gradients would alert an observer to the fact that a problem had occurred. The right hand panel of Figure 2.2 demonstrates the second effect of the

decreasing line strengths, namely that the implied age of the stellar population rapidly becomes unfeasibly large at larger radii, this effect is much more noticeably unphysical and therefore can act as a useful warning of the existence of scattered light within the data.

Fortunately the standard GMOS longslit set-up utilised in this investigation provided the opportunity to remove this scattered light. This was possible because the 2-D spectrum produced contained 3 unexposed regions created by the bottom of the slit and two slit spacers located at 1/3 and 2/3 of the distance along the spatial dimension of the image (see for example Figure 2.4). After bias subtraction these regions should contain no flux, however light scattered within the spectrograph meant that this was not the case. To correct for this effect it was possible to interpolate the scattered light level between the 3 unexposed regions and to subtract this from the image. See Figure 2.5 for an example of this procedure carried out on data described in Chapter 3 from observations of the minor axis of NGC 7332 made with an essentially identical set-up to those used in the study of NGC 3115. In total scattered light accounted for a ~few% of the total incident light. This however was sufficient to account for ~50% of the counts at the largest radii. After correction residual scattered light should be of a negligible level.

The data was then wavelength calibrated with the wavelength calibration being accurate to ≤ 0.2 Å. The 2-D spectrum was then extracted into a series of 1-D spectra which were sky subtracted and binned in the spatial dimension until the target S/N (measured in a region near to the Hβ line) of 20 or 60 was reached. After binning to S/N = 60 a total of 108 (major axis) and 44 (minor axis) spectra were produced, it is from these spectra that all of the kinematics and line indices were measured, though in later figures these have been rebinned in groups of 4 (radially) to allow clearer presentation. The binned 1-D spectra were then flux calibrated using the photometric standard and a reddening correction of E(B - V) = 0.146 (Schlegel et al., 1998) applied using the standard **IRAF** routines.

2.3.2 Sky Subtraction

Clearly an accurate sky subtraction is a necessity when attempting to measure accurate kinematics and line indices at large galactocentric radii. If the sky spectrum is strongly contaminated by diffuse stellar light it can introduce large errors in measured indices and kinematic quantities such as σ, h_3 and h_4. To investigate the magnitude of this effect sev-

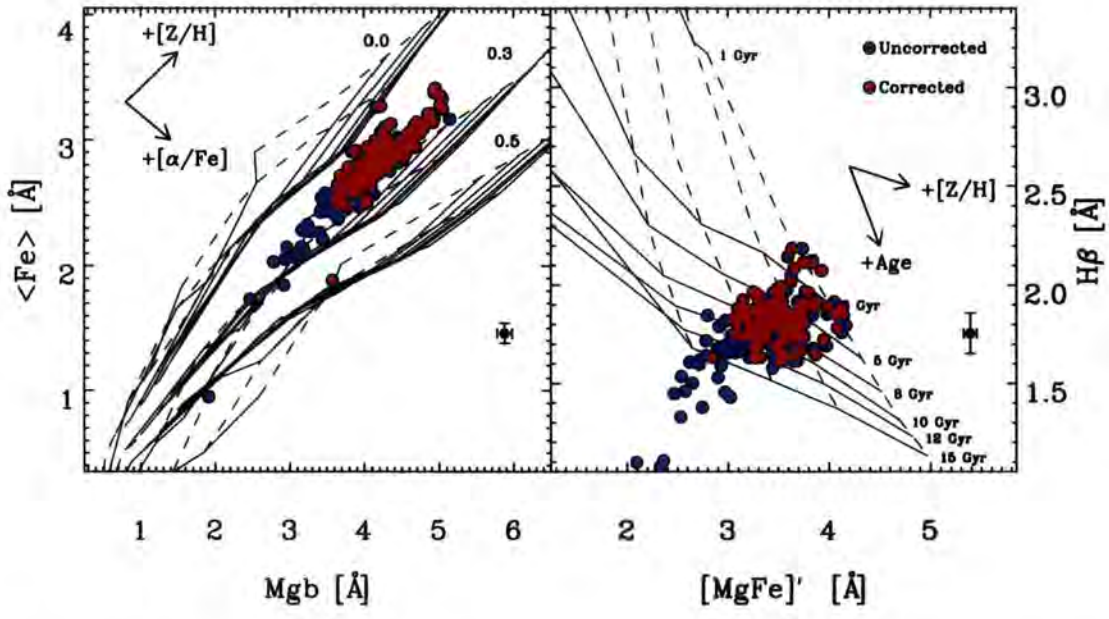

Figure 2.2: The effects of scattered light on measured stellar population parameters for the major axis of NGC 3585. Left Panel: The weakening of line strengths due to scattered light has the effect of making the measured metallicity appear lower, whilst the apparent [α/Fe] remains constant. Right Panel: The weakening of the age sensitive indices such as the Hβ index has the effect of making the apparent age of the stellar population increase at larger radii. Overplotted for comparison are the SSP models by Thomas et al. (2003, 2004) with abundance ratios [α/Fe] = 0.0, 0.3, 0.5, the models have ages 1-15 Gyr and metallicity [Z/H] = -2.25, -1.35, -0.33, 0.0 and +0.35. In both panels average error bars are displayed towards the bottom right of each panel, as well as the various stellar population parameter vectors. The metallicity gradient of this galaxy means that central galaxy data points are located towards the right (highest [Z/H]) and radius increases towards the left (lower [Z/H]).

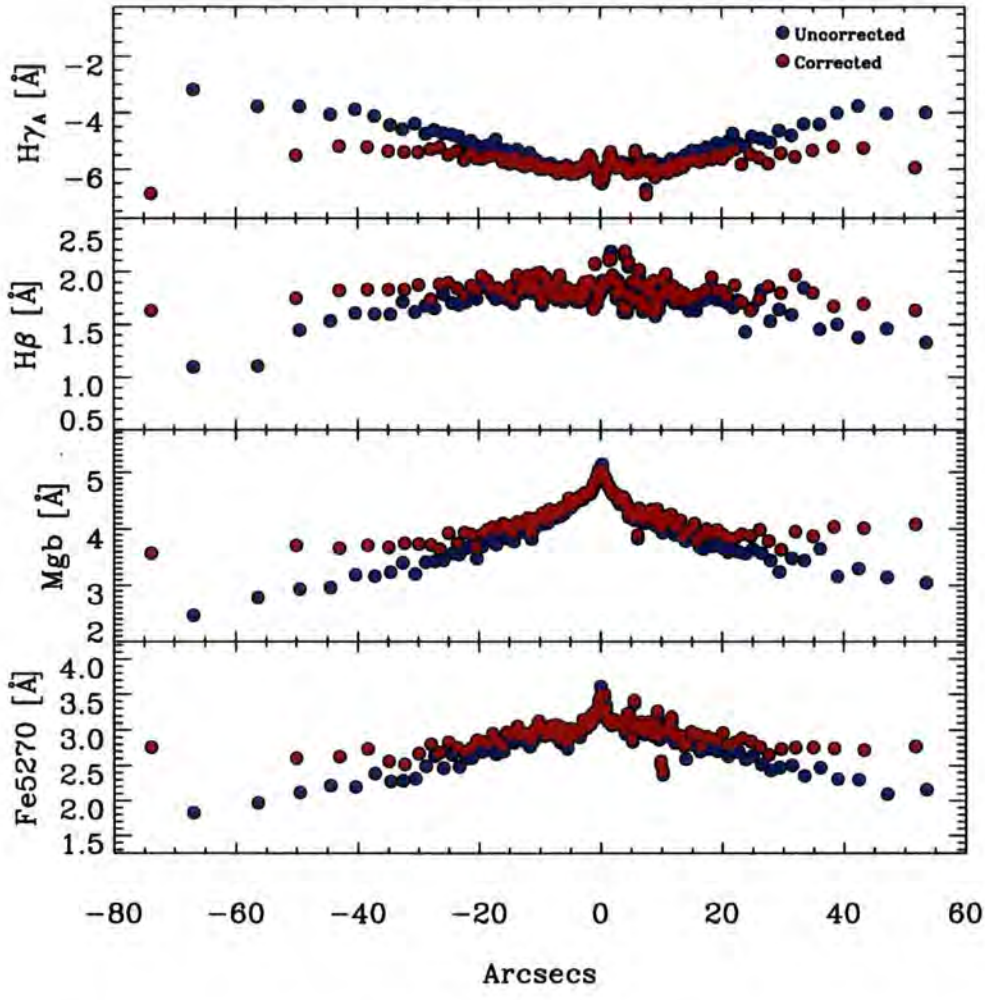

Figure 2.3: Demonstration of the effect of scattered light on measured line indices. Measured selected Lick/IDS line strength indices for the major axis of NGC 3585. Indices were measured using identical methods to those used for NGC 3115 both from spectra without applying the scattered light correction described (blue circles) and with the correction applied (red circles). In all cases the measured line strength is weaker at larger radii (where scattered light begins to dominate the total flux) if the scattered light correction described previously has not been carried out.

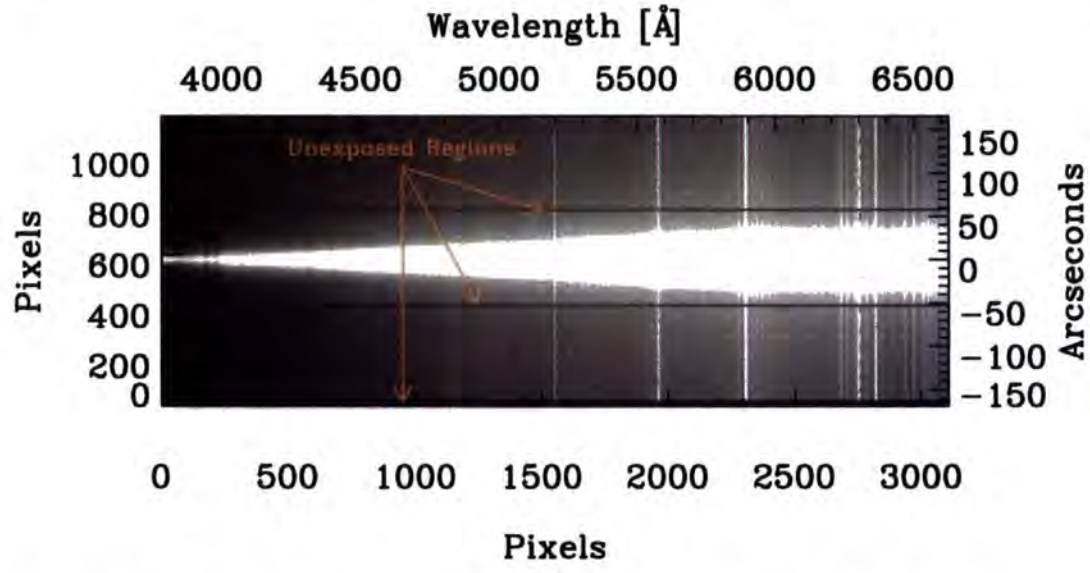

Figure 2.4: Example of bias subtracted, flat fielded and wavelength calibrated 2-D spectrum, in this case from the minor axis of NGC 3115. The unexposed regions of the spectrum are evident as the horizontal regions of lower (though non-zero) counts located at the bottom, 1/3 and 2/3 along the spatial dimension of the detector.

eral methods were used, the simplest of which was to re-reduce our data using the minor axis sky to sky subtract the major axis and vice versa. The line indices were remeasured and compared to those measured previously, for all indices considered here the changes in measured index were < 0.1 Å except for the Mg b line which showed quite considerable variation. This change in the Mg b line can be understood as being due to changes in the strength of the 5200 Å sky emission feature between the major and minor axis exposures. Later work has since shown that this problem can be largely ameliorated using interpolation techniques similar to those described in Chapter 3 to remove the influence of emission lines from ionised gas within the target galaxy.

The second test carried out was to reduce the data assuming $\pm$ 20% errors (chosen to reflect the variation from exposure to exposure) in the sky spectra, again any changes in the measured indices were < 0.1 Å for all cases except for the very last (and largest) radial bin. Therefore errors introduced by the sky subtraction should be entirely negligible for all but the very largest (and most binned) radial bins.

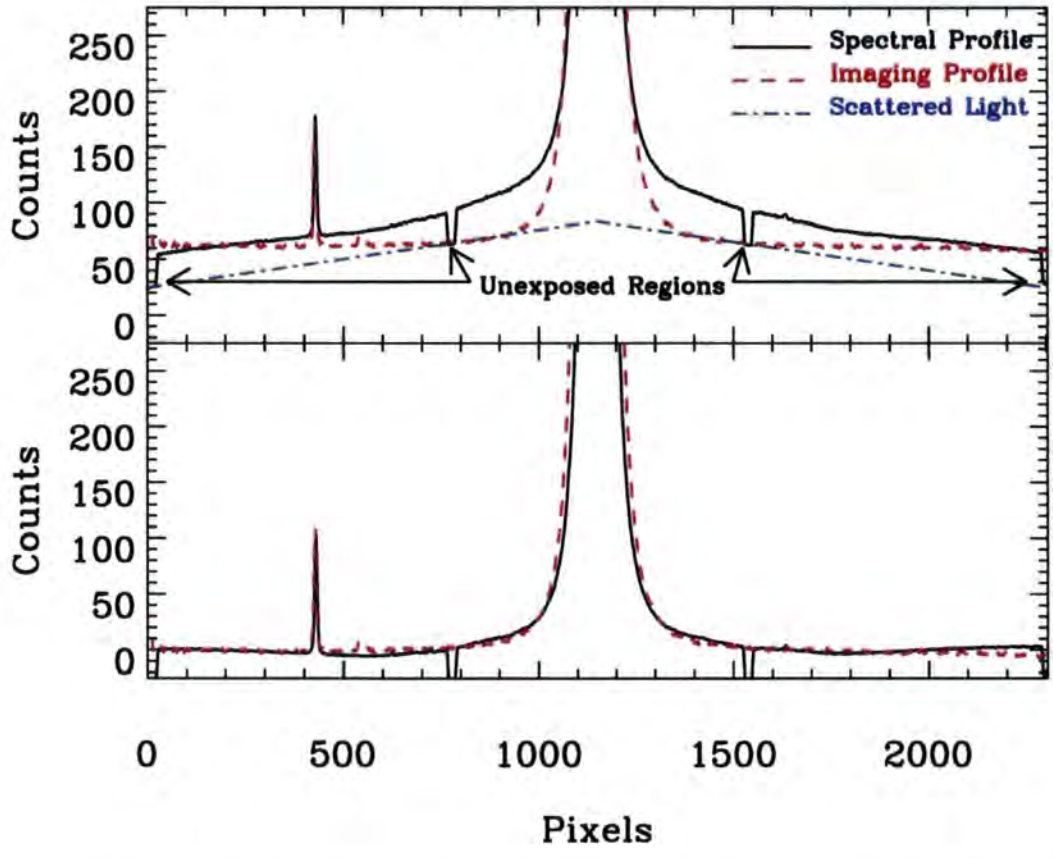

Figure 2.5: Upper Panel: Spectral and imaging profiles of the minor axis of NGC 7332. As can clearly be noted the spectral profile (black solid line) displays significant wings relative to the imaging profile (red dashed line) due to light scattering within the instrument. By interpolation between the unexposed chip regions indicated (created by slit spacers) a scattered light profile (blue dot-dash line) can be calculated. Lower Panel: The result of subtracting the scattered light profile from the spectral profile and sky subtracting both the imaging and spectra. As can be seen the considerable extra flux seen in the spectral profile between 500 and 1800 pixels has now been entirely removed.

2.3.3 Kinematics

The first step in analysing the spectra was to measure the line of sight velocity distribution (LOSVD) for each of the binned spectra. This kinematic information, as well as being of interest in and of itself is essential for the accurate measurement of line strength indices. The publicly available **IDL** implementation of the pPXF method (Cappellari & Emsellem, 2004) was employed to determine the recessional velocity, velocity dispersion, and the Gauss-Hermite moments h_3 and h_4 for the individual spectra. The pPXF method is an optimal template fitting method where input stellar population templates (or stellar spectra) are fit with the kinematics to the input spectrum in a way which minimises template mismatch errors, the actual fitting is achieved using a maximum penalised likelihood method. Further details of this method and the various subtleties of its implementation are provided in Chapter 3. In this case the NGC 3115 spectra were fit in pixel space over the wavelength range 4900 - 5450 Å using both the stellar velocity templates observed during the run and additional stellar templates from the library of Vazdekis (1999) (see Figure 2.6 for an example fit). Errors were estimated by remeasuring 100 Monte-Carlo simulations of the spectra with added photon noise. Additionally, as a check of accuracy, the redshift and velocity dispersion were measured by Fourier cross-correlating the spectra against the velocity standards using the fxcor implementation in **IRAF**. As the two methods produce consistent results, the more comprehensive pPXF implementation was used for the remaining analysis.

2.3.4 Line Strength Indices

The Lick/IDS Line Strength System

The system of line strength indices most commonly used for optical studies is the Lick/IDS system (Worthey & Ottaviani, 1997; Trager et al., 1998). The Lick/IDS system grew out of a programme started in 1972 by S. Faber and collaborators to study the stellar populations of early type galaxies. During the period 1972 to 1984 the group collected a large sample of galaxy, globular cluster and Milky Way stellar spectra. Due to the great consistency achieved through collection with a single instrument, the Image Dissector Scanner (IDS), this library is still one of the most reliable as well as extensive currently published. This library was used as a basis for defining the Lick/IDS line strength system, originally a system of 11 indices (Burstein et al., 1984; Faber et al., 1985), which has in subsequent

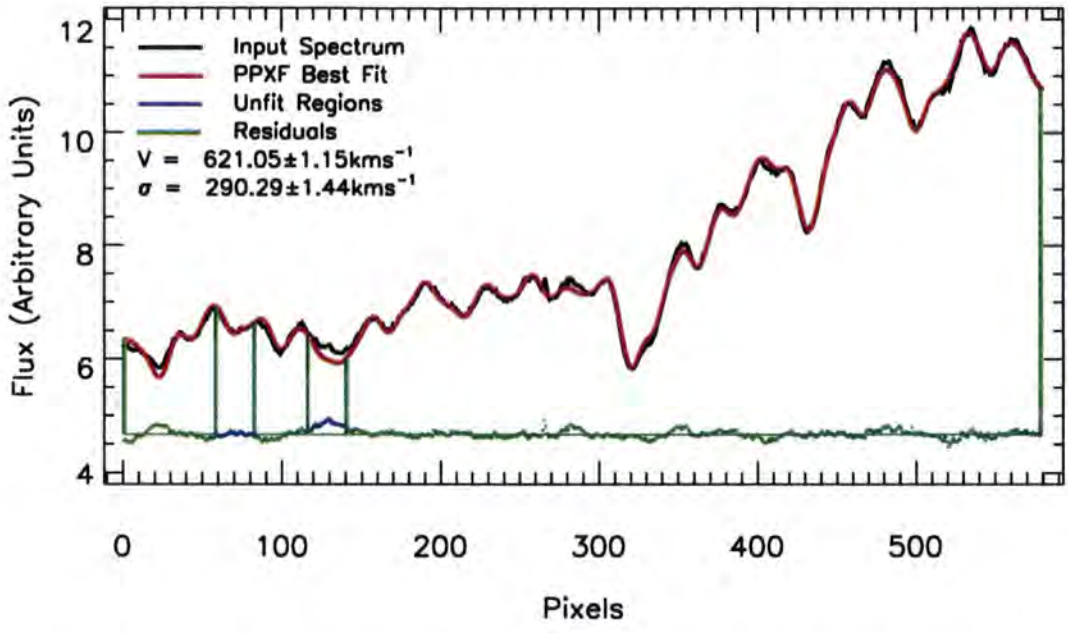

Figure 2.6: Example best fit model produced by pPXF (red line) for input NGC 3115 central spectrum (black line). Also displayed are regions not included in the derivation of the best fit model, due to the potential influence of emission lines from [OIII] (blue lines), and the residuals between the input and best fit models (green points).

years been extended to 25 plus additional related indices. The most significant revisions to the system with regard to the measurement of the stellar population parameters of integrated stellar populations was the addition of ten new indices by Worthey (1994) and the inclusion of additional age sensitive indices in the form of the Hδ and Hγ Balmer lines by Worthey & Ottaviani (1997). These additional age sensitive indices add more leverage to attempts to disentangle the formation of composite stellar populations (see e.g. Serra & Trager (2007)).

The great consistency of the Lick system, married to the large number of defined indices and the relatively wide range of stellar types contained within the library has made this system particularly useful in the construction of theoretical simple stellar population (SSP) models. Originally these models predicted the measured line strengths for a given IMF, single age, single metallicity stellar population (Worthey, 1994; Worthey & Ottaviani, 1997), an additional later extension was the inclusion of the effect of variable α-element enhancements on the predicted line strengths (e.g. Thomas et al. (2003, 2004)).

In order to compare the results of this investigation to those of other studies of early type stellar populations and to SSP models it is necessary to place the line strengths mea-

sured here onto the Lick/IDS system. The first step in achieving this is to match the spectral resolution of these observations to that of the Lick/IDS system. The spectra described here are relatively stable and display a constant spectral resolution of ~4.4 Å FWHM, however the IDS spectrograph has an instrumental resolution which varies with wavelength between ~9-11 Å FWHM. Fortunately the level of this variation has been determined by Worthey & Ottaviani (1997) and it is therefore possible to convolve the spectra of the current work with a wavelength dependent Gaussian kernel to reproduce the varying Lick/IDS resolution before the line indices are measured.

Measuring Line Strengths

The next step in fixing the present observations to the Lick/IDS system is to measure the line strengths using the Lick definitions (displayed in Table 2.2). The Lick/IDS system defines three passbands for each line index, one of which covers the line index region itself and two pseudo-continua located blue-ward and red-ward of the main feature. These pseudo continua are defined such that they should be free from any strong or variable lines. They can therefore be used to provide an estimate of the true continuum at that wavelength. To measure a line strength the mean height of the pseudo-continua are measured and then a straight line drawn between them, the strength of the index is then simply the difference in flux between the line and the actual amount of flux measured in the index band (see Figure 2.7 for an illustration). For reasons of tradition the units of the measured quantities vary depending on the type of feature being measured, with atomic features measured as equivalent widths (EWs) and molecular features such as the CN bands measured in logarithmic units (magnitudes).

Using the definitions provided in Table 2.2 the line strength indices for each index were then measured using a custom IDL program which included the effects of fractional pixels on the measured line strength.

Correcting Line Strengths For The Effect of LOSVD

The next step required to firmly place the observations onto the Lick/IDS system is to correct the measured indices for the effects of the line of sight velocity distribution. The absorption features observed in galaxy spectra are a convolution of the luminosity weighted integrated spectrum of the stellar populations present with the instrumental broadening and the Line of Sight Velocity Distribution (LOSVD) of the stellar populations. Hence

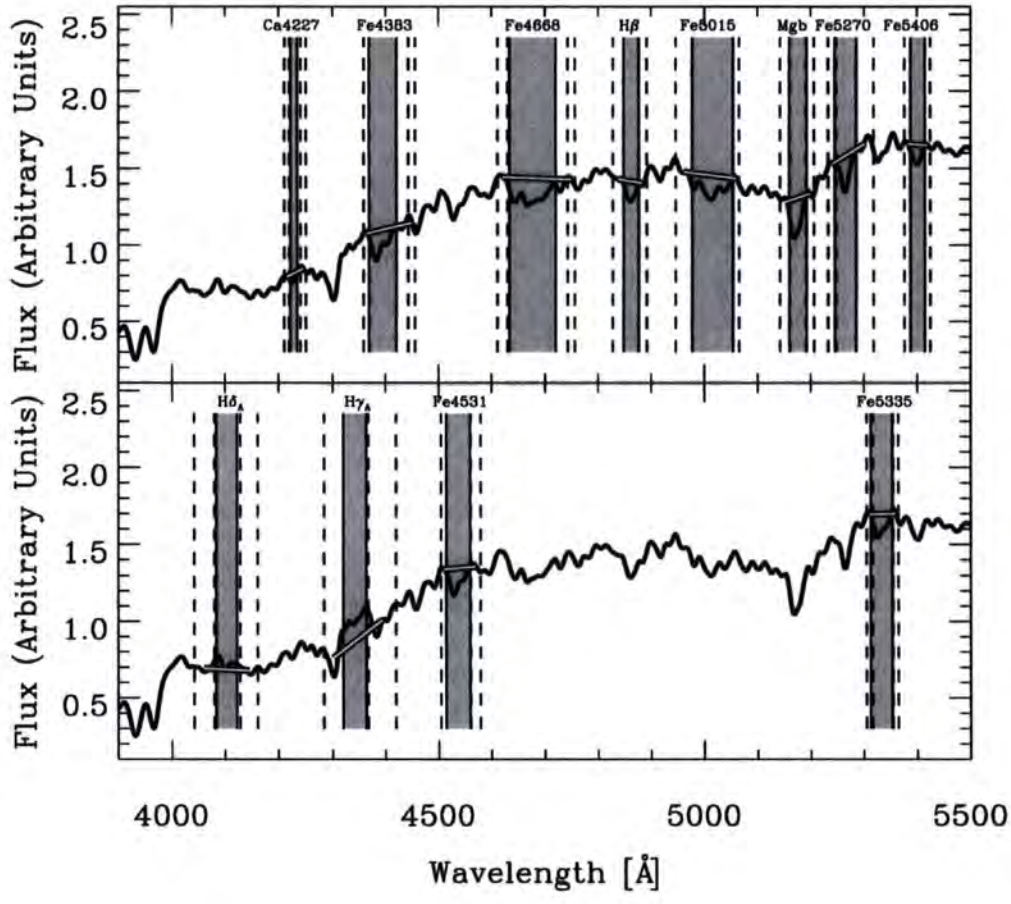

Figure 2.7: NGC 3115 central spectrum with selected Lick/IDS system central bandpasses (grey shaded regions), blue and red sidebands (dashed lines) and pseudo continua (black and white lines connecting blue and red sidebands).

Table 2.2: Lick/IDS line strength definitions

#	Index Bandpass	Blue Continuum	Red Continuum	Units	Name
01	4142.125 - 4177.125	4080.125 - 4117.625	4244.125 - 4284.125	Mag	CN_1
02	4142.125 - 4177.125	4083.875 - 4096.375	4244.125 - 4284.125	Mag	CN_2
03	4222.250 - 4234.750	4211.000 - 4219.750	4241.000 - 4251.000	Å	Ca4227
04	4281.375 - 4316.375	4266.375 - 4282.625	4318.875 - 4335.125	Å	G4300
05	4369.125 - 4420.375	4359.125 - 4370.375	4442.875 - 4455.375	Å	Fe4383
06	4452.125 - 4474.625	4445.875 - 4454.625	4477.125 - 4492.125	Å	Ca4455
07	4514.250 - 4559.250	4504.250 - 4514.250	4560.500 - 4579.250	Å	Fe4531
08	4634.000 - 4720.250	4611.500 - 4630.250	4742.750 - 4756.500	Å	Fe4668
09	4847.875 - 4876.625	4827.875 - 4847.875	4876.625 - 4891.625	Å	H_β
10	4977.750 - 5054.000	4946.500 - 4977.750	5054.000 - 5065.250	Å	Fe5015
11	5069.125 - 5134.125	4895.125 - 4957.625	5301.125 - 5366.125	Mag	Mg_1
12	5154.125 - 5196.625	4895.125 - 4957.625	5301.125 - 5366.125	Mag	Mg_2
13	5160.125 - 5192.625	5142.625 - 5161.375	5191.375 - 5206.375	Å	Mgb
14	5245.650 - 5285.650	5233.150 - 5248.150	5285.650 - 5318.150	Å	Fe5270
15	5312.125 - 5352.125	5304.625 - 5315.875	5353.375 - 5363.375	Å	Fe5335
16	5387.500 - 5415.000	5376.250 - 5387.500	5415.000 - 5425.000	Å	Fe5406
17	5696.625 - 5720.375	5672.875 - 5696.625	5722.875 - 5736.625	Å	Fe5709
18	5776.625 - 5796.625	5765.375 - 5775.375	5797.875 - 5811.625	Å	Fe5782
19	5876.875 - 5909.375	5860.625 - 5875.625	5922.125 - 5948.125	Å	Na_D
20	5936.625 - 5994.125	5816.625 - 5849.125	6038.625 - 6103.625	Mag	TiO_1
21	6189.625 - 6272.125	6066.625 - 6141.625	6372.625 - 6415.125	Mag	TiO_2
22	4083.500 - 4122.250	4041.600 - 4079.750	4128.500 - 4161.000	Å	$H\delta_A$
23	4319.750 - 4363.500	4283.500 - 4319.750	4367.250 - 4419.750	Å	$H\gamma_A$
24	4091.000 - 4112.250	4057.250 - 4088.500	4114.750 - 4137.250	Å	$H\delta_F$
25	4331.250 - 4352.250	4283.500 - 4319.750	4354.750 - 4384.750	Å	$H\gamma_F$

Notes: Standard Lick/IDS line strength definitions reproduced from http://astro.wsu.edu/worthey/html/index.table.html.

to some extent the measured line strengths depend on the LOSVD of the spectrum, in particular on the velocity dispersion of the stellar population which can have the effect of smearing the absorption feature out of the Lick/IDS index band and into the side bands, hence depressing the measured index.

Clearly since an aim of this study is to examine the radial changes in stellar populations in NGC 3115 it is unacceptable to have a situation where the measured line strength indices, and hence the implied stellar populations parameters of age, metallicity and [α/Fe] are dependent on the kinematics of the populations and not in fact the actual chemical make up and age of the stars.

In order to correct for this problem the measured line strength indices are corrected to the strength they would display if they were at zero velocity dispersion; this was done following the procedure of Kuntschner (2004). This procedure corrects the line index measurements not only for the effects of velocity dispersion but also the non-gaussian h_3 and h_4 terms. Kuntschner (2004) finds that for changes of ± 0.1 in h_4 with constant $\sigma = 250$ kms^{-1} the LOSVD correction changes by $\pm 5\%$ with corresponding errors in the age and metallicity estimations of 15 - 20%. Clearly for a galaxy such as NGC 3115, with central velocity dispersion of around 300 kms^{-1}, the effect of these corrections on the spectra from the central few arcsecs could be non negligible. Therefore only indices for which Kuntschner (2004) has provided corrections for these effects (17 indices) are measured, though in practice only the Hδ_A, Hγ_A, Hβ, Fe5015, Mg b, Fe5270, and Fe5335 indices are utilised in the following analysis. Errors in the line indices were calculated by 500 Monte - Carlo simulations of the input spectra.

Lick Offsets

The final step in placing observations firmly onto the Lick system is usually to observe a number of Lick library standard stars which were also measured by the original Lick set-up. By measuring the line strengths of these standard stars made with the same set up as those used for the actual science observations it is possible to determine a set of offsets between the Lick system and the observational system currently in use (see e.g., Kuntschner, 2000). This offset system aids the removal of the final small systematic differences introduced by the fundamental differences in equipment used.

Unfortunately in this study an insufficient number of standard stars were observed to allow the accurate calculation of the Lick offsets directly. However, making use of the

stellar library observed by Jones (1997) it was possible to determine the offsets for indices measured on flux calibrated spectra to the original Lick/IDS system (which was not flux calibrated) assuming that the Jones library is well flux calibrated. The spectra were first broadened to the Lick/IDS resolution with a wavelength dependent Gaussian assuming a spectral resolution of the Jones library of 1.8 Å (FWHM). Then the offsets were determined for the index measurements in common with the Lick stellar library (Worthey, 1994) for up to 128 stars. The offsets and associated errors (see Table 2.3) were derived with a biweight estimator. The offsets are generally small (< 0.1 Å) but individual indices can show larger offsets (e.g., $H\gamma_A$, Fe5015). Here, only a single offset per index is considered and possible trends with line strength are ignored. Several indices (e.g., $H\delta_A$, CN_2, G4300) show weak evidence for such trends which are, however, difficult to quantify (see also Vazdekis, 1999). This determination of Lick offsets derived from Jones stars is in excellent agreement with an earlier investigation carried out by Worthey & Ottaviani (1997, Their Table 9). For the present study the offsets listed in Table 2.3 are applied under the assumption that the flux calibration of the present data is consistent with that applied by Jones (1997).

2.4. Galaxy Kinematics

Figure 2.8 shows the result of the kinematic measurements. The velocity measurements are based on spectra binned to have S/N = 20, the other parameters were derived from spectra binned to have S/N = 60. As a check that changes in S/N do not affect the measured quantities, the data was re-binned to S/N of 30, 40 and 50; the kinematics were then remeasured with no significant trends in measured quantities being observed.

Each of the parameters measured here shall be discussed in turn but in general the measured kinematic data is in very good agreement with published data from several authors including Kormendy & Richstone (1992), Capaccioli et al. (1993), Bender et al. (1994) and Fisher (1997) in almost all respects except for the inferred h_4 value and the rotational velocity at large radii. A possible explanation for the observed discrepancy in h_4 is discussed in Section 3.3.3.

The inner rotation curve of the major axis measured here is in good agreement with all the prior data sets examined including Illingworth & Schechter (1982), Kormendy & Richstone (1992), Capaccioli et al. (1993), Bender et al. (1994), Fisher (1997) and Emsellem

Table 2.3: Offsets to the Lick/IDS system derived from Jones (1997) library

Index	Offset	Number of stars
$H\delta_A$	-0.36 ± 0.05 Å	108
$H\delta_F$	-0.16 ± 0.03 Å	110
CN_1	0.003 ± 0.002 mag	117
CN_2	0.006 ± 0.002 mag	115
Ca4227	0.00 ± 0.02 Å	126
G4300	-0.28 ± 0.04 Å	128
$H\gamma_A$	0.38 ± 0.04 Å	126
$H\gamma_F$	0.09 ± 0.02 Å	126
Fe4383	0.28 ± 0.05 Å	126
$H\beta$	-0.12 ± 0.02 Å	128
Fe5015	0.23 ± 0.04 Å	126
Mg b	-0.08 ± 0.02 Å	128
Fe5270	-0.07 ± 0.02 Å	128
Fe5335	-0.04 ± 0.03 Å	128
Fe5406	-0.06 ± 0.02 Å	126

Notes: Column (1) gives the index name, while column (2) gives the mean offset (Lick - Jones) to the Lick/IDS system evaluated from the Jones (1997) stars in common with Lick. Column (3) shows the number of stars used in the comparison.

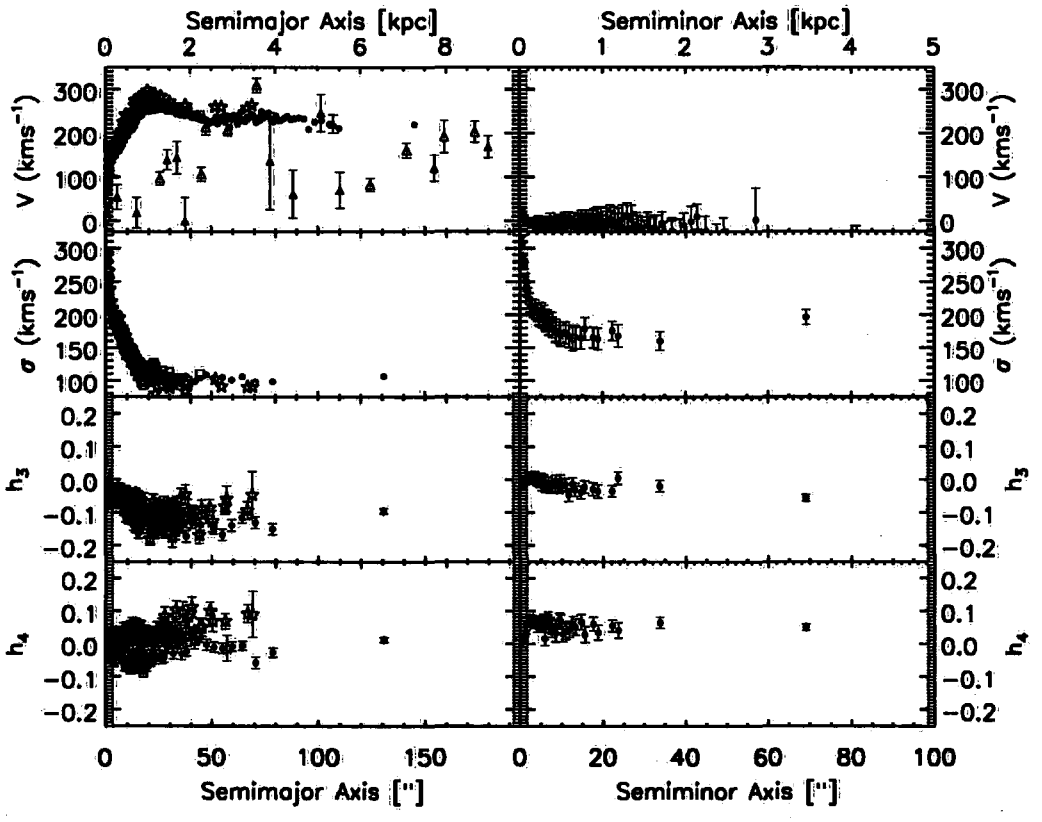

Figure 2.8: Comparison of measured LOSVD parameters with literature values. Filled circles are from this study, asterisks from Bender et al. (1994), and squares from Fisher (1997). Triangles show GC data from Kuntschner et al. (2002) de-projected to the major axis; filled triangles are the blue sub-population and unfilled the red sub-population. Several GC points are omitted because they exhibit counter rotation or have implied rotation velocities of greater than 400 kms^{-1}. Boot-strapped 1σ error bars are over-plotted for values determined in this study, except for major axis velocity and velocity dispersion data where they are omitted in the interests of clarity. Typical errors in V and σ are $\leq$ 12 kms^{-1}. The major axis data has been mirrored about the minor axis and about the central recessional velocity, the minor axis has similarly been mirrored about the major axis.

et al. (1999). At larger radii however other authors including Capaccioli et al. (1993) have measured an essentially flat rotation curve with rotational velocity around 260 kms^{-1}. However the observations presented here provide some evidence for some drop off in rotation velocity beyond 70 arcsec. As observed by several authors, there is no evidence for minor axis rotation. Statistics are insufficient at present to determine if either of the GC sub-populations can be better associated with structures such as discs or spheroids within NGC 3115. It is however clear that the bulk of the clusters examined rotate in a manner consistent with that of the bulk of the stellar content even at larger radii. In fact of the 26 clusters with kinematics examined here 21 rotate in a prograde manner, but with apparently lower velocities than that displayed by the integrated light of NGC 3115.

The velocity dispersion of NGC 3115 is also in good agreement with other measured results from the authors cited previously. However the data we present here extends to significantly larger radii than previous studies. One obvious feature of the data presented in Figure 2.8 is that the minor axis velocity dispersion is considerably higher than that of the major axis at equivalent radii (i.e. at equal R_e). The fact that the minor axis data displays a higher velocity dispersion than the major axis is not entirely unexpected, as data presented by Kormendy & Richstone (1992) hints at this being the case. The 2-D spectroscopy presented in Emsellem et al. (1999) also displays evidence for lines of constant velocity dispersion being elongated in the minor axis direction (at least within the inner 5 arcsec). A difference in measured velocity dispersion for the major and minor axes can be explained if the galaxy consists of a fast rotating, kinematically cool disc component and a slower rotating, kinematically hot spheroidal component. This possibility is re-examined later in the light of line index measurements.

The values of h_3 determined here are entirely consistent with values determined previously by Bender et al. (1994).

The h_4 values measured here are generally consistent with those measured previously except at larger radii, where we observe a value h_4 of 0.0, whilst Bender et al. (1994) find a value of around 0.1. This discrepancy could be due to several factors including differing experimental set-up and method of measuring h3 and h4. In fact as is described in further detail in Chapter 3 offsets of just such a magnitude are possible due to various subtle biases in the pPXF method. Another potential cause of the disagreement in measured h_4 include any intrinsic deviations from gaussianity in the line spread function of either of the spectrographs used, this non gaussianity would be interpreted as being due to the

Table 2.4: Major Axis Kinematics

Radius ["]	Velocity [km/s]	σ [km/s]	h_3	h_4
-130.71	229.33	106.66	-0.098	0.013
±	4.15	5.49	0.008	0.007
-78.66	245.07	98.98	-0.158	-0.028
±	7.9	8.98	0.017	0.014
-70.52	244.13	98.48	-0.140	-0.062
±	8.04	10.53	0.018	0.017
-64.41	242.45	106.53	-0.122	-0.008
±	8.29	9.1	0.017	0.013
-59.47	242.97	101.13	-0.147	-0.012
±	8.68	8.88	0.019	0.013
-55.11	242.83	104.85	-0.175	-0.018
±	7.97	9.24	0.017	0.014

Notes: More extensive table available in electronic format. Tables providing minor axis kinematics, major and minor axis line strengths, ages, [α/Fe] and [Z/H] are also available. All data provided is binned to S/N = 60.

presence of higher order components in the LOSVD because it would not also be present in the input stellar population templates. However such an effect is certainly not evident in the data presented here and would appear unlikely.

2.5. Line Indices

2.5.1 Abundance Ratios

Figure 2.9 presents Mg*b* vs. <Fe> where <Fe> = ((Fe5270 + Fe5335) / 2) (González, 1993), for the major and minor axes of NGC 3115. The GC data points are separated into red and blue sub-populations by (V - I) colour (see Kuntschner et al. (2002) and Figure 2.10). Model predictions from Thomas et al. (2004) are overplotted for [α/Fe] of 0.0, 0.3 and 0.5 with ages = 3 (left-most line in each group), 5, 8 and 12 (right-most line in each group) Gyr and have [Z/H] which range from -2.25 (bottom left) to +0.35 (top right). The effects of age and metallicity are essentially degenerate in this diagram, with sensitivity to abundance ratios maximised. As described in Kuntschner et al. (2002), abundance ratios are most accurately determined for larger ages/metallicities.

The measurements for the centre of NGC 3115 from the major axis data are in reasonable agreement with those from Fisher et al. (1996) and also from Trager et al. (1998). The implied α - element over-abundance of [α/Fe] $\approx$ 0.17 was determined by χ^2 minimization of the data and the models of Mg*b* vs. <Fe> from Thomas et al. (2004). This χ^2 procedure, which is similar to the one introduced by Proctor et al. (2004) fits the set of indices used here (Hβ, Fe5015, Mg b, Fe5270 and Fe5335) to the models of Thomas et al. (2004), allowing variable ages, [α/Fe] and [Z/H]. A possible break in the value of [α/Fe] is visible for Mg*b* < 4 with an increase in [α/Fe] to around 0.25. In comparison, the minor axis data starts off at values consistent with the central portion of the major axis, and then begins to trend off towards [α/Fe] = 0.3 much more rapidly.

A break in the major axis data and differences between the two axes can be interpreted as evidence for the existence of at least two distinct populations, with typical values of [α/Fe] $\sim$ 0.17 and 0.3. Since a move towards lower Mg*b* and <Fe> corresponds to a move to increasing radius it raises the possibility of observing radial trends in the strengths of other line indices, which will be examined in more detail in the next section.

The data presented extends to sufficiently large radii that the mean metallicity of the

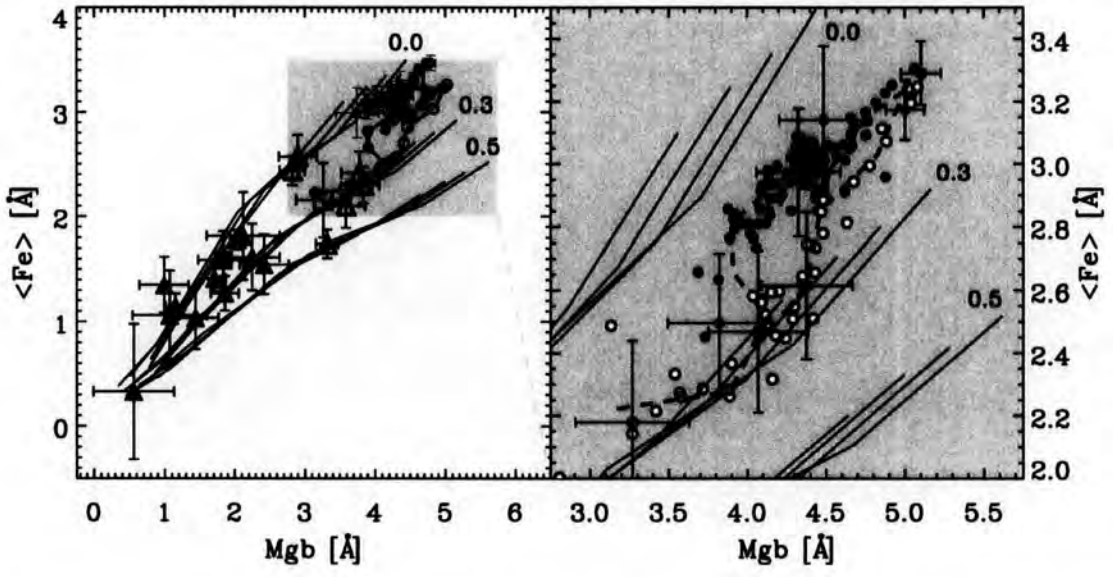

Figure 2.9: Comparison of the [α/Fe] ratios of the galaxy data and GC population through the use of an Mgb vs. <Fe> diagram. In the left panel filled and open black circles are binned major and minor axis galaxy data from this paper, filled grey circles show results from Fisher et al. (1996), the filled diamond is the central galaxy result from Trager et al. (1998). Filled black triangles are the blue globular cluster sample and unfilled triangles are the red globular cluster sample, both from Kuntschner et al. (2002). The filled black square is the error weighted mean of the blue cluster subpopulation and the black square the error weighted mean of the red cluster subpopulation. Overplotted are models by Thomas et al. (2003, 2004) with abundance ratios [α/Fe] = 0.0, 0.3, 0.5, the models have ages 3-12 Gyr and metallicity [Z/H] = -2.25, -1.35, -0.33, 0.0 and +0.35. The right panel shows the unbinned galaxy data presented here, dashed lines denote the positions of the binned data. Representative error bars are plotted for spectra located at small, intermediate and large radii, errors are a combination of bootstrapped 1σ errors and those introduced by a $\pm$5% error in the sky subtraction.

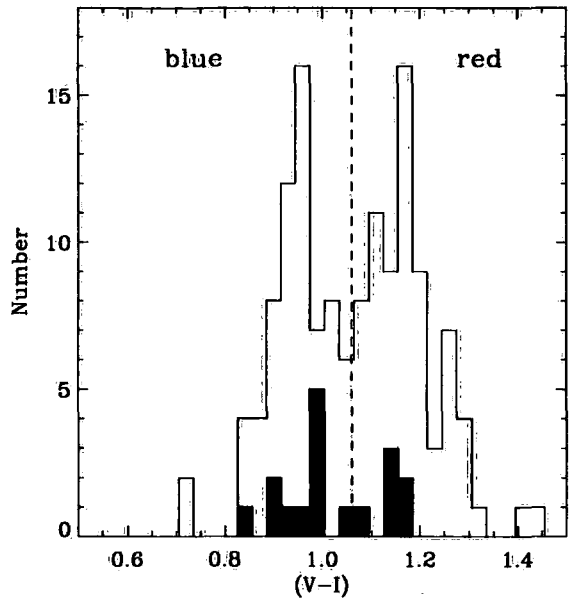

Figure 2.10: Figure 5 from Kuntschner et al. (2002). Histogram of the V-I colours of potential NGC 3115 GCs from Kundu & Whitmore (1998). Overplotted are the 17 GCs with high S/N spectra from Kuntschner et al. (2002), the vertical dashed lines indicates the dividing line between red and blue populations at V-I = 1.06.

stellar population is similar to that of the most *metal rich* GCs. Figure 2.9 shows that on both the major and minor axis the mean abundance ratios at the largest radii are also consistent with those of the cluster population although the spread in abundance ratios appears to be smaller. No significant population of GCs are found with properties similar to the stellar population at intermediate radii on the major axis.

2.5.2 Radial Profiles of Indices

Figure 2.11 displays the radial profiles of the measured Lick indices, [α/Fe] and [Z/H]. The values of effective radius (henceforth R_e) used here are those listed in Capaccioli et al. (1993) for the spheroidal component of the galaxy.

The differences in [α/Fe] between major and minor axes is more clearly demonstrated here, as it is evident that at larger radii the major axis data again becomes consistent with that of the minor axis. This type of behaviour could be understood in terms of changes in the relative contributions of disc and spheroidal components, with both major and minor axes being dominated at small radii by a nuclear component. At intermediate radii the major axis would be affected by the influence of the disc component, whereas the minor

axis would simply be tracing the stellar content of the spheroidal component. The change in the behaviour of the major axis at large radii could then be understood as evidence for truncation of the disc component contribution at around 80 arcsecs on the major axis, and the return to dominance of the spheroidal component.

The other metallicity tracing indices (Mgb, Fe5270 and Fe5335) display similar trends, with slight evidence for breaks in the major axis data at around the same radius as the one seen in [α/Fe]. This has previously been observed by Fisher et al. (1996) in their edge-on sample of S0 galaxies (unfortunately they did not examine the minor axis of NGC 3115), who found that the Mg_2 index is stronger with a lower gradient at larger radii on the major axis than on the minor axis. As can be seen from Figure 2.11 the values for Mgb, Fe5270 and Fe5335 determined here for the major axis are in good agreement with those determined by Fisher et al. (1996). Differences between the two datasets (in particular for Hβ) can be attributed to variations in the experimental set-up, errors in flux calibration, the different methods employed to correct for the broadening effect of the LOSVD, corrections for emission and the uncertainty on the corrections to the Lick system. In the case of Hβ where the largest offset is observed it should be noted that the central value provided by Trager et al. (1998) is in fact closer to the data presented here.

2.5.3 Age Determinations

Figure 2.12 examines the behaviour of age-sensitive indices along the major and minor axes of NGC 3115. Model grids are interpolated between the [α/Fe] = 0.0 and 0.3 models from Thomas et al. (2003, 2004) with [α/Fe] determined as described previously. Note that whilst the [α/Fe] ratios used to produce the major axis grids are appropriate for the longslit data described here, they are generally not appropriate for the GCs which tend to have mean [α/Fe] $\sim$ 0.3. However the minor axis grids provide a good approximation to the mean [α/Fe] of the GC's and hence the best age determinations for the clusters.

The Hβ, Hγ_A and Hδ_A indices are plotted against [MgFe]'[1]. This index was found by Thomas et al. (2003) to be independent of [α/Fe] and a good tracer of total metallicity.

There appears to be a difference in age between the two axes with the major axis having a mean age of around 5 - 8 Gyr and the minor axis an age of around 12 Gyr. This would suggest a small amount of star formation may have continued in the disc

[1][MgFe]' = $\sqrt{\text{Mgb} \times (0.72 \times \text{Fe5270} + 0.28 \times \text{Fe5335})}$ (Thomas et al., 2003)

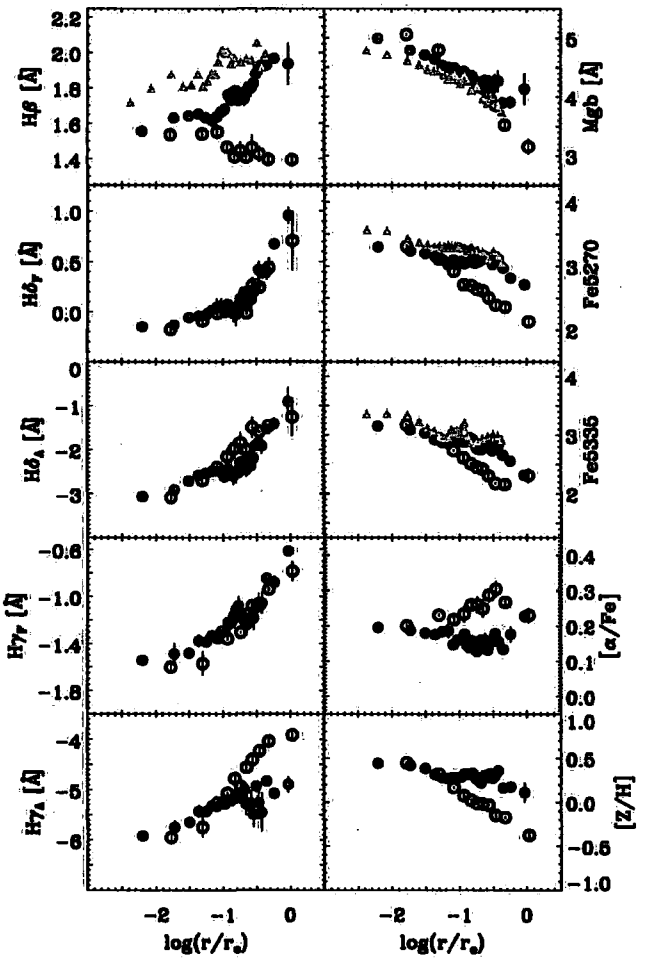

Figure 2.11: Radial profiles of Lick indices, [Z/H] and [α/Fe]. [Z/H] and [α/Fe] determined by χ^2 minimisation as described in Section 2.5.1. Filled black circles show major axis data, open circles show minor axis data and light grey triangles show data from Fisher et al. (1996). Error bars are 1-σ errors in each bin. Note that r_e = 93 and 35 arcsec for the major and minor axes respectively (Capaccioli et al., 1993).

component for several Gyr after the formation of the spheroid.

The age determinations from the Hβ index appear to change at lower [Z/H] but in the opposite sense for each axis, with the major axis appearing to become younger and the minor axis older. As Hβ is relatively unaffected by changes in [α/Fe] this cannot be explained as being due to changes in [α/Fe] along either axis, but could be explained for the major axis by more recent star formation in the outer parts of the disc (in spiral arms perhaps). Another possibility would be that some undetected Hβ emission in the inner regions of the disc weakens the observed Hβ index in the inner regions. This final possibility however seems unlikely since we find negligible signs of [OIII] emission. For the minor axis data it would seem plausible that the populations at larger radii could be older and would in fact represent the older generation of stars also being traced by the GC populations. This possibility would seem to gain credence from the fact that at larger radii the minor axis data displays [α/Fe], ages and [Z/H] values that are entirely consistent with those determined from the red GC sub-population.

The remaining age estimators Hγ_A and Hδ_A also show an age offset between the minor and major axis in the same sense as Hβ, but there is little or no evidence for an age gradient.

Figure 2.13 shows the radial profiles of ages determined by the χ^2 minimisation described previously. As should be expected the trends previously described are obvious with the major axis appearing to have an age of 5 - 8 Gyr and the minor axis having an age of between 12 - 14 Gyr.

A further comment is that despite the use of different age sensitive indices the age determinations for the GC's made here are entirely consistent with those of Kuntschner et al. (2002) with both GC populations having a mean age of around 12 Gyr. In fact the agreement is now improved as the mean ages of the sub-groups determined by Kuntschner et al. (2002) varied from $\sim$ 6 Gyr to 12 Gyr, depending on the Balmer line being examined. This spread can now be understood as being due to the [α/Fe] sensitivity of the Hγ_F and Hδ_F lines used in the Kuntschner analysis, which can now be corrected using the newer SSP models provided by Thomas et al. (2004).

2.6. A Simple Two Component Model

To test the hypothesis that radial trends in [α/Fe] could be explained by intrinsic

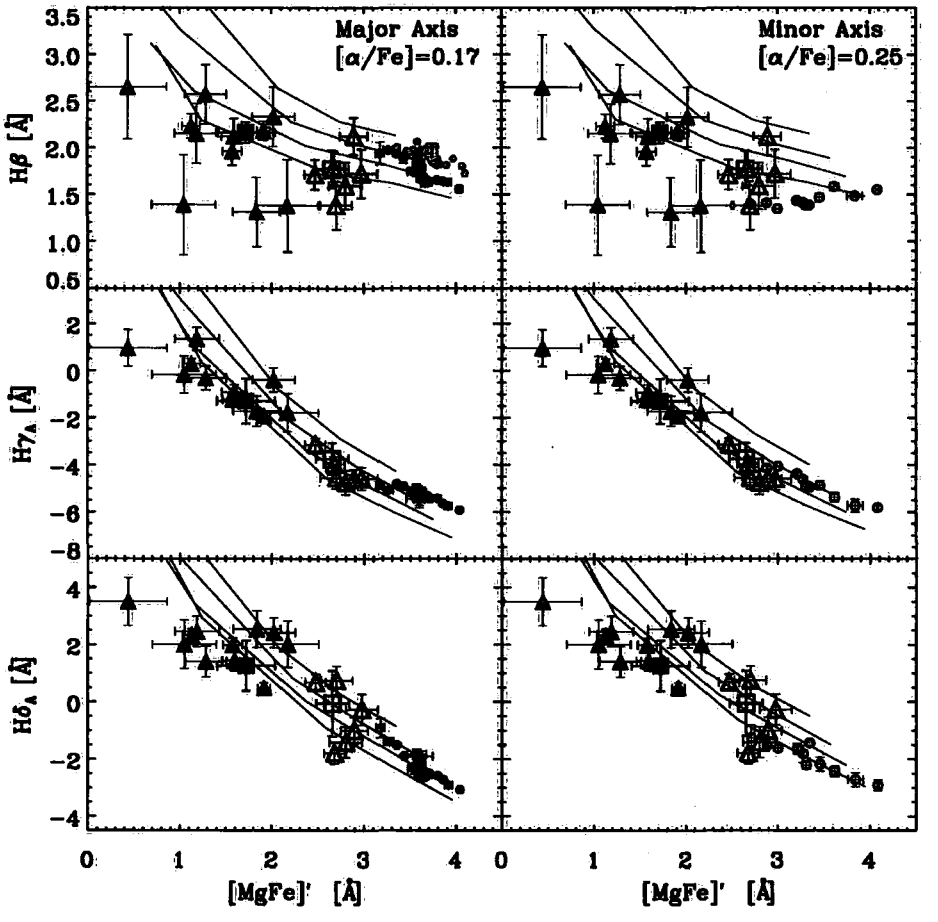

Figure 2.12: Age-metallicity diagnostic plots for major and minor axis data. Symbols are as in Figure 2.9. Overplotted are models by Thomas et al. (2003, 2004) with abundance ratios [α/Fe] indicated in the top right corner of each column, a value of [α/Fe] = 0.25 was chosen for the minor axis as an average of the values determined at small and large radii. These [α/Fe] ratios are interpolated from the 0.0 and 0.3 values listed in Thomas et al. (2004), the models have metallicity [Z/H] = -2.25 to +0.35, lines indicate ages from top to bottom of 3, 5, 8 and 12 Gyr respectively. Error bars for galaxy data are the 1-σ errors on each of the radial bins.

differences in the disc and spheroid components a simple model was constructed.

The relative contributions of the disc and spheroid components were determined from archived GMOS images of NGC 3115 obtained in 2004 (Program ID GS-2004A-Q-9, PI R. M. Sharples) in the g, i and r bands. The program GALFIT (Peng et al., 2002) was used to carry out a simple bulge to disc decomposition. Because only the relative contribution of the two components is required for a simple first order model, a full isophotal decomposition was unnecessary and a simple de Vaucouleurs model of the spheroid with r_e = 93 arcsec (Capaccioli et al., 1993) was subtracted from the original image to isolate the disc light contribution. As a test of this approach, GALFIT was allowed to attempt to fit the images with a Sersic function with variable r_e and n, both with and without masking of the disc region and with varying starting parameters. The results in terms of r_e and n varied considerably but the distribution of flux in the residual image remained fairly constant, with the disc tending to provide a peak of around 30 - 40% of the flux on the major axis.

The results of this bulge subtraction can be seen in Figure 2.14. As previously noted by Capaccioli et al. (1988) the disc shows considerable flaring in the outer regions, which these authors attributed to the disc ceasing to be self gravitating in this region. This behaviour may also be attributable to the existence of a thick disc component in NGC 3115. There is also evidence for structure within the disc (spiral arms?), which could be taken as evidence for some residual star formation events. Note that the inner region is not well fit by this model. A more realistic model would require several components, but is beyond what is required for the present analysis.

A model can be used to predict [α/Fe] at any point, if it is assumed that the residual light traces an enriched disc and nuclear component with [α/Fe] $\sim$ 0.0 and that the fitted spheroid traces a lower metallicity (Fe) - enriched population of [α/Fe] $\sim$ 0.3. By weighting the [α/Fe] value by the relative fractions of the two components it is possible to estimate the observed [α/Fe] at any point. Figure 2.15 shows the result of this procedure for both axes. This simple model reproduces the general trends observed with [α/Fe] quickly rising on the minor axis and a much more Fe-enriched major axis which trends back towards the asymptotic values of the minor axis at large radii. The remaining differences between the model and observed values can be explained by a number of factors including incorrect values for the intrinsic [α/Fe] of the two components and the effect of other components unaccounted for. Other factors such as intrinsic gradi-

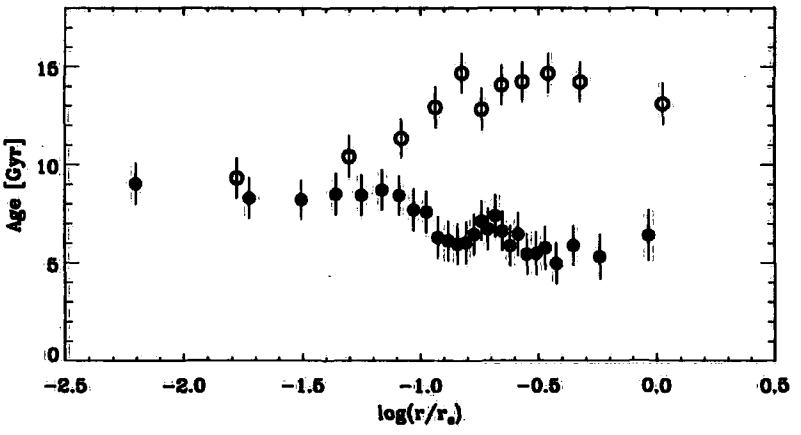

Figure 2.13: Radial profiles of measured age for major and minor axes. Ages determined by χ^2 minimisation as described in Section 2.5.1. Symbols as previously defined.

ents in [α/Fe] could also play a part. However to first order we believe that differences in [α/Fe] profiles between the two axes of NGC 3115 can be explained as being due to the existence of at least two distinct stellar populations within the galaxy, with different spatial distributions and enrichment histories.

2.7. Discussion

In general all of the kinematical measurements determined here are in good agreement with previous studies, the most interesting finding being that the disc of the galaxy is particularly cold ($v_{\rm disc}$ / $\sigma_{\rm disc}$ > 2) and hence rotationally supported. An interesting extension to this work would be to improve the statistics of the kinematics beyond 100 arcsecs, which would probe the region where substantial flaring of the disc has been observed. The fact that the rotation velocity on the major axis remains high even at large radii where the integrated light is dominated by the underlying spheroid implies that in NGC 3115 the halo is also rotating significantly (v / $\sigma \sim 1.5$) in the same sense as the disc.

These observations have confirmed that the GC population shows clear evidence for rotation, in the same sense as that of the disc. Statistics on the GC kinematics at present are not sufficient to associate particular cluster populations to any specific structural feature. However if increased numbers of GC kinematics are determined it may prove possible to demonstrate that the red GC subpopulation has kinematics consistent with a thick disk or bulge component, as is found in the case of the MW system.

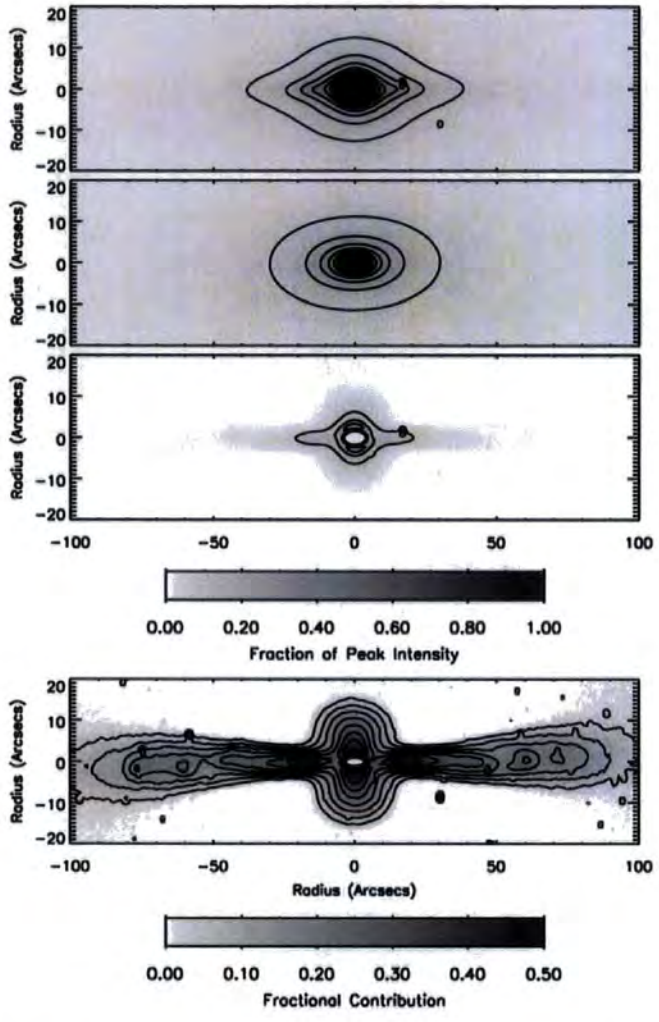

Figure 2.14: Top image shows original GMOS i band image. The 2nd image shows the simple de Vaucouleurs model for the spheroidal component. The 3rd image shows the residual image after the 2nd is subtracted from the 1st. These 3 images are all scaled to the peak intensity of the original image for clarity. Contours show the 0.1, 0.2, 0.3, 0.4, 0.5, 0.6, 0.7, 0.8, 0.9 fractions. The lower image shows the fraction of the total emission provided by the residual components. Considerable flaring of the disc is visible, as is substructure consistent with spiral arm structures. Contours show the 0.1, 0.2, 0.3, 0.4 and 0.5 fractions.

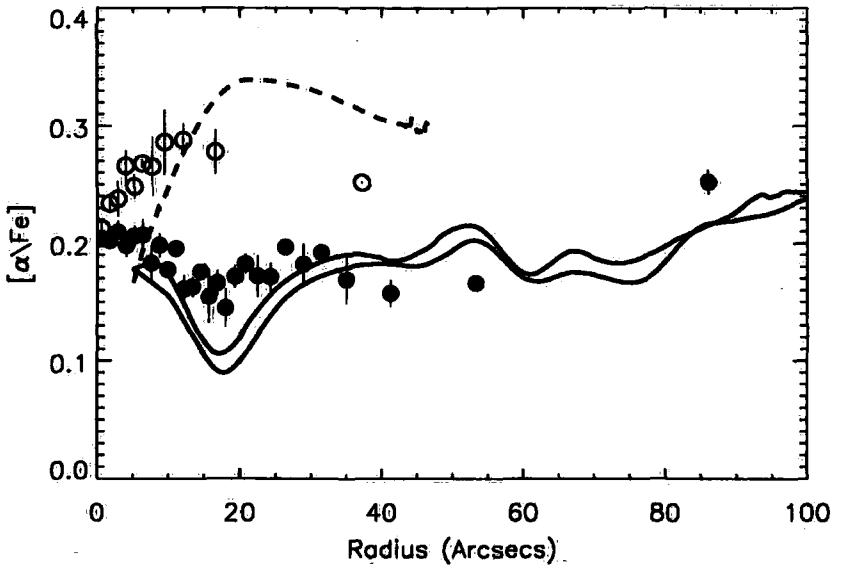

Figure 2.15: Model predictions for variation of [α/Fe] for major and minor axes. The solid line shows the model prediction for the major axis, the dashed line displays the model prediction for the minor axis, both made assuming [α/Fe] = 0.0 for the disc and 0.3 for the spheroid. The circles show radially binned [α/Fe] measurements shown previously in Figure 2.11 for the respective axes. Slight differences between both sides of the major axis are visible in the model predictions, which have been folded about the centre. However the magnitude of these differences are within the uncertainties of around $\pm$0.05.

The investigation of the Lick absorption line indices presented has shown that the stellar disc component is considerably different from the spheroidal component in almost all measured parameters. Most informative in terms of constraints on formation theories is the implication that the disc of NGC 3115 is several Gyr younger, and significantly enriched in metals, compared to the spheroid of the galaxy. This has been hinted at previously by studies of the optical colours of NGC 3115, for example Silva et al. (1989), who noted that in B - i the disc was 0.5 mag bluer than the spheroid. This colour difference however could be attributed either to a younger stellar population in the disc or to the disc having a lower metal abundance compared to the spheroid. This study has convincingly demonstrated that a lower metal abundance cannot explain this colour difference since the major axis displays a *higher metal abundance* than that of the minor axis. The difference in colour can therefore clearly be attributed to an age difference of 5 - 7 Gyr for the two components and is also consistent with the observation that [α/Fe] ratios are lower in the inner region of the major axis.

The red GC sub-population is most consistent with the larger radii minor axis data in its measured parameters. This suggests that both the spheroid and the red GC population may have formed from the same material at around the same time. An interesting extension would be to probe to larger radii to see if the observed trends in metallicity and [α/Fe] shown in Figure 2.11 continue, and eventually lead to the minor axis spheroid data tracing stellar populations similar to those that make up the lower metallicity blue GC population. This blue population of GC's could then possibly be attributed to an initial burst of star formation during the halo formation of the galaxy, the kinematics of this component may prove essential in determining if this is in fact the case, as the kinematics of the blue population would then be expected to be more random and halo-like. One unanswered question is whether or not there exists a GC population associated with the substantial younger disc component of this galaxy. At present the number of GC's for which spectroscopy exists is too small to exclude this possibility, although the fact that none of the GC's examined to date have line-strength indices comparable to those measured for the disc component seems to indicate that such a population must be small if it exists. If no such population exists, this in itself would prove interesting as it would imply that GC's are not necessarily formed whenever a sizeable amount of star formation occurs.

2.8. Conclusions

This chapter has presented kinematical data and absorption line strength measurements for the major and minor axes of the S0 galaxy NGC 3115, and has compared these measurements to similar data for the GC system of NGC 3115. The main conclusions are:

- NGC 3115 has a significant stellar disc component, which is both kinematically and chemically distinct from the surrounding spheroidal component.

- The spheroidal component of NGC 3115 is consistent with having a uniformly old ~ 10 - 12 Gyr age and [α/Fe] of 0.2 - 0.3. At large radii the minor axis (which should trace the spheroidal component exclusively beyond the central few arcsec) is consistent in age, [α/Fe] and metallicity with the red GC sub-population, hinting at a common origin for the two.

- The major axis data displays clear evidence for contamination by a younger (5 - 8 Gyr old) more chemically enriched stellar disc. The observation that the disc of NGC 3115 is bluer than the spheroid is primarily an age difference, not a metallicity difference effect.

- Previously observed discrepancies in age determination between the Hβ and higher order Balmer lines for the GC sample can largely be explained by changes in the higher order Balmer lines due to varying [α/Fe].

- The GC system displays clear evidence for prograde rotation in the same sense as the disc and spheroidal components.

Chapter 3

The Formation of S0 Galaxies

3.1. Abstract

This Chapter presents preliminary results from a large survey intended to elucidate the formation and evolution processes of S0 galaxies. Through deep Gemini/GMOS longslit observations of 18 edge-on S0 galaxies the kinematics and stellar populations of this class of galaxy have been examined in detail. The observations presented here demonstrate that the Tully-Fisher relation for S0 galaxies is systematically offset from that of the local spiral relation by an amount between ΔM_B = -1.50 ± 0.16 and ΔM_B = -1.92 ± 0.15, depending on the choice of spiral TF slope used. In line with the conclusions of other authors it is found that the scatter in the S0 TF relation is dominated by intrinsic sources and not by measurement error. Taken together these two results lead to the conclusion that S0 galaxies are in general most likely to be the result of the truncation of star formation in normal spiral galaxies, with the large intrinsic scatter of the S0 TF relation being mostly due to the individual galaxies undergoing the transformation from spiral to S0 at different epochs. Furthermore a simple model is presented which demonstrates that the offset for each sample galaxy is consistent with the amount of fading predicted for objects where disc ages have been determined using a study of the Lick/IDS line strengths of the galaxy discs.

3.2. Introduction

From the study of NGC 3115 presented in Chapter 2 it can be seen that the undoubtedly complex formation histories of galaxies such as NGC 3115 can be reduced to a manageable level of complexity by making the simplifying assumption that NGC 3115 is composed of just two components, a bulge (or spheroid) and a disc. Other structural components such as bars or larger scale halos could then be thought of as perturbations on top of this simple model. One obvious question which arises from Chapter 2 is how common is the behaviour found in NGC 3115? Do all S0 galaxies consist of these same components? Do they always have older spheroids and younger discs? Are the measured ages of these components consistent with other indicators of galaxy formation and evolution such as offsets from the Tully-Fisher relation?

In order to answer these questions, and through them to shed light upon the formation of S0 galaxies, a large survey of the kinematics and stellar populations of S0 galaxies was designed. This survey builds on our study of NGC 3115, extending the sample of S0 galaxies which have extremely deep longslit spectroscopy of both axes to around 20 galaxies in total. In one sense this sample represents an extension of the groundbreaking work of Fisher et al. (1996), who studied a similarly sized sample of S0s with lower S/N data. The Fisher et al. (1996) sample suffered somewhat from a lack of homogeneity, with a different (somewhat limited) number of line strengths available for different galaxies and some galaxies which had minor axis spectra and some which did not. Despite these problems Fisher et al. (1996) found that several of their sample behaved in a broadly similar manner to that observed in NGC 3115 (i.e. major and minor axes which display very different line strength gradients), others however displayed line strengths which did not appear to vary strongly between axes. Due to the lower S/N data however, it is difficult to determine if the minor axis data simply did not extend to large enough radii to observe significant differences between the axes in some cases. Nevertheless Fisher et al. (1996) did find that the bulges of their S0s displayed significant metallicity gradients, steeper on average than those of Elliptical galaxies, with the discs displaying much shallower metallicity gradients. The interpretation of this finding was that the bulges of S0 galaxies were formed via the dissipative collapse at early times. This picture is somewhat at odds with more recent imaging surveys of the bulges of S0 galaxies which find that the majority of types S0-S0/a actually host pseudo-bulges (Laurikainen et al., 2007). Pseudo-bulges are

central light concentrations found in galaxies which are thought to be formed by slower secular processes that occur after the initial burst of galaxy formation believed to create classical bulges (those formed from dissipative collapse or mergers at early times). The processes which form pseudo-bulges are generally thought to involve the influence of bars, with the bar leading to the redistribution of disc stars and gas to the central regions of the galaxy. The data-set provided by the study presented here will provide the perfect opportunity to attempt to reconcile these two sets of observations.

One aspect of the data which can be used to shed light on the formation of S0 galaxies is through the examination of the Tully-Fisher relation (Tully & Fisher, 1977) for S0 galaxies. The Tully-Fisher relation (TFR) relates the distance independent quantity of the maximum rotation velocity of a spiral galaxy with the absolute magnitude of the galaxy. The general interpretation of such a correspondence (and the measured value of the slope) is that there exists a relatively constant value of the mass-to-light ratio for spiral galaxies. Many studies have examined the spiral TF relation using many different wavelength bands, generally finding small values of the scatter of around 0.3-0.6 mag from the B to I bands (Sakai et al., 2000; Tully & Pierce, 2000; Kannappan et al., 2002). The search for an analogous relation for S0 galaxies has proved difficult due to the lack of measurable gas kinematics in most S0 galaxies requiring the more demanding task of measuring rotation curves to large radii from stellar absorption line spectroscopy. Nevertheless in recent years several authors have attempted to measure the S0 TFR. Neistein et al. (1999) searched for evidence of an S0 TFR using absorption line spectroscopy of 18 galaxies, finding that despite large scatter of around 0.7 mag the S0 TFR was offset from that of the spiral by 0.5 mag in the I band. Similar results were found by Hinz et al. (2001, 2003) for a sample of S0s found in the Coma and Virgo clusters. Conflicting results have however been presented by Mathieu et al. (2002) for a small sample of 6 carefully modelled S0s, which they found to have a small scatter of 0.3 mag, but very large offset of 1.8 mag in the I band. A result which bridged the gap in some respects between these two conclusions was found by Bedregal et al. (2006a), who found using their own sample of 7 Fornax cluster S0s, when combined with a large meta sample including each of the previously described samples, that the B band TFR for S0s was offset from the spiral relation by between 1.3 and 1.7 magnitudes, and displayed a large scatter of around 0.9 mag. They found that for their Fornax Cluster S0s a simple disc fading model was adequate to explain the observed TFR offsets.

The implications for the formation of S0 galaxies of the existence of either a small or large TFR offset are extremely important. If the conclusion of a large spiral-to-S0 offset is correct, then S0s can simply be the result of faded spirals which ceased forming stars several Gyr ago. In this case the large scatter in the S0 TFR would most simply be explained as being due to each galaxy ceasing its star formation at different times, something which can be constrained by the colours or spectra of the galaxy discs. If there is a small offset between spiral and S0 TFRs, then the formation of S0 galaxies may well be achieved by multiple different formation routes. The large scatter would then simply be an outcome of the different processes presumably acting with a range of influence. For example galaxies produced in mergers would most likely have properties which varied depending on parameters such as the mass ratio of the merging objects and how much gas was available for the subsequent star formation required to rebuild a galaxy disc. It would seem that such a formation scenario is unlikely to be responsible for the majority of S0s given the ubiquity of significant galaxy discs in S0 galaxies, however a merger scenario may be important for some of the transition E7/S0 class where larger spheroidal components are observed (see e.g. NGC 3115 and NGC 3585 later in this Chapter).

The survey presented here can go a long way to determining which picture is correct. This is principally because it does not suffer some of the drawbacks of the earlier works. This sample was, as described below, composed entirely of nearly edge-on galaxies, where the influence of the disc and spheroidal components are more easily separated. Being composed exclusively of a sample of almost edge-on galaxies reduces the uncertainties on some of the corrections required to determine the maximum rotation velocity, having such high S/N data allows the measurement of rotation curves to much greater radii than has been achieved in the earlier works, again increasing the accuracy of the determination of V_{max}. The large sample size (currently 18 and around 20 objects when complete) covering a range in mass, bulge-to-total ratio, and environment also allows an examination of trends of TFR offset with these parameters. Other improvements include having minor axis data as well. This helps to more accurately determine the star formation histories of the sample galaxies. In this way it becomes possible to check if the star formation histories implied from the spectra are compatible with the measured TFR offset.

3.2.1 Target Selection

For any such study of galaxy formation the selection of the sample to be investigated is crucial. In this case an attempt was made to select as representative a sample of S0 galaxies as was possible within the inevitable observational constraints. The main limiting factor in this study was simply the very large allocations of 8m telescope time required per galaxy (6 hours in total to complete imaging and spectroscopy of both axes to allow measurement of line indices to $2R_e$), a consequence of the need to measure high S/N absorption line spectra to large galactocentric radii. Even accepting the fact that such a project does not make particularly rigorous demands of observing conditions (Gemini Band 3 is acceptable), practical limits meant that a sample size much larger than 20 was impossible. Therefore the sample as originally designed was limited to 21 galaxies, which would be split between 3 environments, as defined by the local Tully density (Tully & Fisher, 1988), comprising field, group and cluster environments. The Tully density is simply the number of galaxies per cubic Mpc around a particular galaxy as determined from the projected position of the galaxy on the sky and its recessional velocity.

The initial sample was selected by searching the Hyperleda catalogue[1] with the following constraints and by examining DSS images of the returned images:

1. The galaxy should be observable from either Gemini-North or South, in either semester. This in itself does not provide strong limitations as the allowed range of declination is -90° to +80°, although objects close (±15°) to the limits are in practice difficult to observe.

2. Hyperleda morphological type code equal to or less than 0, ensuring S0 or E classification.

3. The galaxy should contain a close to edge-on disc: Hyperleda inclination of 70° or greater. The individual estimates of inclination from Hyperleda are not particularly accurate but all galaxies selected using this criteria did in fact prove to have inclinations in the acceptable range.

4. Recessional velocity less than 4000kms^{-1}, ensuring an identical set-up could be used in all cases, without for example the Hα feature redshifting out of the wavelength coverage.

[1] http://leda.univ-lyon1.fr/

5. Galaxy $\log D_{25}$ from Hyperleda greater than 1, ensuring that the galaxy would be large enough that sufficient data points would be available to measure a reliable rotation curve.

An additional complicating factor was the fact that the project was to be observed in service mode over several semesters, at both Gemini-North and South, this meant that top priority objects would not always be observed and the final list of galaxies observed was somewhat at the whim of the weather or the telescope operators. To explain further, the original selection of targets consisted of 44 galaxies which met the criteria to be defined above. Each semester 6-12 of these galaxies would then be submitted for observation, of which 3-6 would generally be observed, with attempts at increasing prioritisation when necessary to ensure sufficient numbers of galaxies per environment bin were observed.

The result of this process is that to date from the original sample of 44 galaxies, 18 (including the NGC 3115 data described in Chapter 2) have completed both i-band imaging and major axis spectroscopy, with 15 of those 18 galaxies having both major and minor axis spectroscopy completed. Thumbnail images showing the galaxies within the approximate GMOS field of view are displayed in Figure 3.1, with galaxy properties provided in Table 3.1.

Table 3.1: Sample galaxies RA, DEC, and recessional velocities from NED, B_T from RC3 catalogue (de Vaucouleurs et al., 1991), M_B determined B_T using distance modulus (sources listed below) and extinction from Schlegel et al. (1998) provided by NED. Inclination is from the Hyperleda catalogue. Hubble type and Tully Density Parameter from Tully & Fisher (1988), Group name, Number of galaxies within the group, virial radius of the group and group mass from Ramella et al. (2002).

Galaxy	RA (J2000)	DEC (J2000)	B_T (Mag)	M_B (Mag)	Incl (°)	$\log D_{25}$ $\log(0.1')$	Velocity (kms^{-1})	T	(m -M) (mag)	Group	N	Radius (Mpc)	Log(M) ($M_\odot$)	TD (Mpc^{-3})
NGC 148	00 34 15.5	-31 47 10	13.13	-18.50	90	1.30	1516	-2	31.56 ± 0.15[4]	S017	7	1.12	13.33	0.28
NGC 1023	02 40 24.0	39 03 48	10.35	-20.20	76.7	1.87	637	-2	30.29 ± 0.16[2]	U139	4	0.60	12.93	0.57
NGC 1380	03 36 27.2	-34 58 33	10.87	-20.44	90	1.66	1877	-2	31.23 ± 0.18[2]	S129	74	1.46	14.08	1.54
ESO 358 G006	03 27 18.0	-34 31 35	13.92	-17.47	90	1.16	1279	-	31.35 ± 0.32[2]	S129	74	1.46	14.02	1.50[1]
NGC 1527	04 08 24.1	-47 53 49	11.74	-19.59	90	1.66	1174	-2	31.28 ± 0.22[2]	-	-	-	-	0.54
NGC 1596	04 27 38.1	-55 01 40	12.10	-18.86	90	1.59	1510	-2	30.92 ± 0.16[2]	-	-	-	-	0.92
NGC 3098	10 02 16.0	24 42 40	12.89	-19.18	90	1.38	1387	-2	31.91 ± 0.15[4]	-	-	-	-	0.32
NGC 3115	10 05 14.0	-07 43 07	9.87	-20.27	81.6	1.92	663	-2	29.93 ± 0.09[2]	S146	3	0.49	11.86	0.08
NGC 3301	10 36 56.0	21 52 56	12.31	-19.68	90	1.56	1321	0	31.89 ± 0.15[4]	U313	3	0.86	12.41	0.53
NGC 3585	11 13 17.1	-26 45 18	10.88	-20.91	90	1.82	1399	-5	31.51 ± 0.18[2]	-	-	-	-	0.12
NGC 4179	12 12 52.1	01 17 59	11.91	-20.26	90	1.65	1256	-2	32.03 ± 0.15[4]	-	-	-	-	0.37
NGC 4281	12 20 21.5	05 23 11	12.25	-19.78	75.8	1.46	2711	-2	31.94 ± 0.28[2]	U490	401	2.64	14.88	0.81
NGC 4762	12 52 56.0	11 13 51	11.12	-19.14	90	1.92	984	-2	30.17[3]	U490	401	2.64	14.88	2.65
NGC 5854	15 07 47.7	02 34 07	12.71	-19.88	90	1.48	1737	-2	32.36 ± 0.15[4]	U677	17	0.88	13.67	0.74
NGC 5864	15 09 33.5	03 03 10	12.77	-19.94	90	1.40	1885	-2	32.51 ± 0.15[4]	U677	17	0.88	13.67	0.74
NGC 6725	19 01 56.6	-53 51 47	12.19	-21.72	90	1.42	3602	-	33.62 ± 0.15[4]	-	-	-	-	0.39[1]
NGC 7041	21 16 32.4	-48 21 49	12.09	-20.11	90	1.55	1946	-2	32.05 ± 0.31[2]	-	-	-	-	0.12
NGC 7332	22 37 24.5	23 47 54	12.02	-19.95	90	1.47	1172	-2	31.81 ± 0.20[2]	-	-	-	-	0.12

Notes: [1] No Tully density parameter available, value is assumed to be the same as a near neighbour within the same group. [2] Distance Moduli from the SBF method, presented in Tonry et al. (2001). [3] Distance Modulus from the Fundamental Plane, presented in Gavazzi et al. (1999). [4] Distance Moduli based on Virgo + Great Attractor model, given in NED based on the local velocity field model of Mould et al. (2000).

Table 3.2: Observing Log: Some galaxies are listed more than once if they were observed over several semesters. For the purposes of this Thesis 18 galaxies are of interest, those which are highlighted in bold, these galaxies have completed both imaging and major axis spectroscopy.

Semester	Gemini-North	Status	Gemini-South	Status
06B				
	NGC 3098	Complete	**NGC 148**	Complete
	NGC 4762	Complete	**NGC 6725**	Complete
	NGC 7332	Complete	**NGC 7041**	Complete
07A			**NGC 5854**	Complete
			NGC 5864	Imaging, Maj
			NGC 4958	Imaging
			NGC 4179	Imaging
			NGC 3957	Imaging
			NGC 3585	Imaging
07B	**NGC 1023**	Complete	**ESO 358-G006**	Complete
	NGC 3301	Complete	**NGC 1380**	Complete
	NGC 4251	Imaging	**NGC 1596**	Complete
	NGC 4425	Imaging	**NGC 1527**	Imaging, Maj
	NGC 4570	Imaging	NGC 1380A	Imaging
			NGC 1401	Imaging
08A			**NGC 3585**	Maj & Min, complete
			NGC 4179	Complete
			NGC 4281	Imaging, Maj
			NGC 4550	Imaging

Notes: Maj and Min denote completed major or minor axis spectroscopic observations respectively. Complete indicates the completion of imaging and major and minor axis spectroscopy.

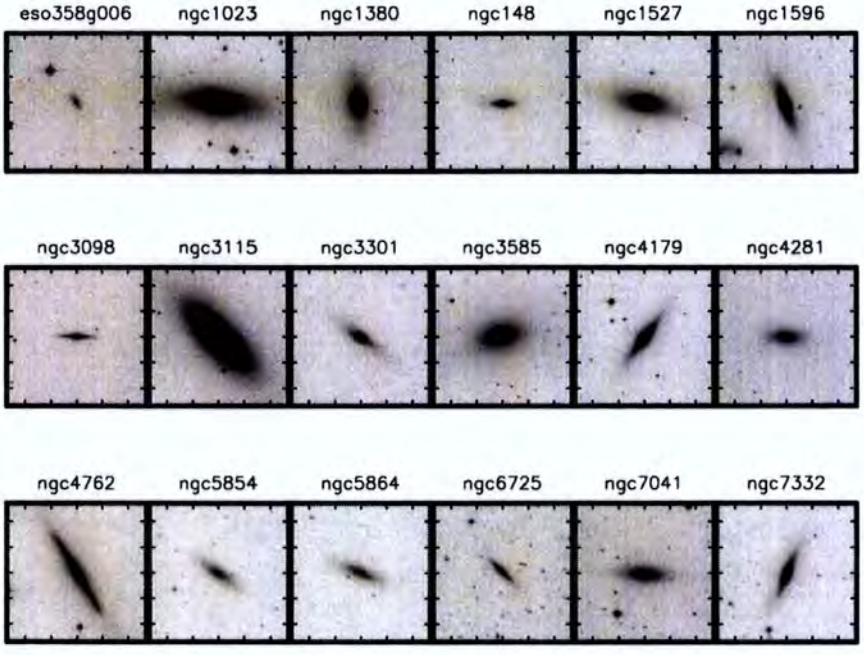

Figure 3.1: Thumbnail DSS images of all 18 nearly edge-on S0 galaxies for which we have spectroscopic data. Thumbnails are 5.5×5.5 arcmin in size, approximately the same field of view as the GMOS instrument. All images are orientated North through East.

3.3. Observations and Data Reduction

All observations were undertaken in service mode using the GMOS instruments on the Gemini North and South Telescopes during semesters 06B to 08A. The full observing log can be seen in Table 3.2. Each target galaxy was imaged using an i band filter for 800s (as 4×200s exposures, in some cases with an additional 10s exposure to allow investigation of regions saturated in the longer exposures), the imaging data was binned 2×2 and therefore has a pixel scale of 0.146×0.146 arcsecs^2 and a field of view of approximately 5.5×5.5 arcminutes^2.

All spectroscopic observations utilised the B600 grism with 600 lines/mm in combination with a 1 arcsec wide longslit, the data were binned by either 4 or 2 in the spectral dimension leading to a spectral resolution of ~4.8 Å FWHM (σ=118kms^{-1} at 5100 Å) sampled at either 0.9 Å/pixel or 1.8 Å/pixel. As in the case of NGC 3115 (Chapter 2) for most target galaxies two sets of integrations were completed, in this case generally totalling 8400s per axis. Usually the centre of the galaxy is located in the centre of the longslit, though occasionally it was necessary to offset along the longslit, either to allow

for an adequate sky subtraction region or to allow the selection of an adequately bright guide star. The wavelength range covered by the spectra is ~3900-6700 Å, and as such covers all of the most important optical absorption lines, as well as the Hα emission line as a useful extra probe of ongoing star formation. This project was designed as a poor seeing (Band 3) candidate and hence the seeing was generally >1 arcsec during the observations.

Additional flux standard stars were observed using the same set up once per semester at each telescope.

The reduction of the *i* band imaging was achieved using the Gemini **IRAF** package. In brief the required procedure was to bias subtract and flatfield the data, followed by subtraction of a scaled fringe frame, before mosaicing each of the three GMOS CCDs together into a single image. Individual exposures could then be combined into a master image, scaled to a one second exposure time.

The reduction of the spectroscopic data was similar to that used in the study of NGC 3115, with the initial steps of bias subtraction, flat fielding, cosmic ray removal, wavelength calibration and rectification of the 2D images being undertaken using the standard Gemini **IRAF** routines. These procedures produce 2D spectra with wavelength calibrations accurate to ≤ 0.2 Å over the entire 3800-6700 Å wavelength range, the individual spectra must then be combined to produce the final master 2D spectrum. In one slight difference between this larger S0 study and the NGC 3115 study each 2D spectrum was rebinned onto a uniform wavelength scale, with integer pixel values (1 Å per pixel for spectra binned by 2 and 2 Å per pixel for those binned by 4) before the combination of individual frames.

A further difference was the decision to correct the 2D spectra for the effects of instrumental distortion, in practice even after wavelength calibration and rectification some curvature of the spectra may remain. If this curvature is not corrected the 1D spectra extracted from a single spatial column of the 2D spectrum will vary in galactocentric radius with wavelength, with the most severe problems typically occurring blueward of 4200Å. To ameliorate this problem a low-order polynomial was fit to the peak of the light distribution of the 2D spectrum (in every case this was the centre of the galaxy), this polynomial was then used to correct the 2D spectrum, the curved regions on the 2D spectrum were shuffled up to bring them into spatial alignment, in effect "straightening" out the curvature. The presence of stars in most slitlets also provided a useful check that

the correction applied was indeed applicable over the entire 2D spectrum. In practice the amount of correction was small, generally less than 5 pixels for the very bluest portion of the spectra, and less than one pixel for the regions between 4800-5800Å.

The individual images were then corrected for the influence of scattered light using the technique described in Section 2.3.1 before being combined using **imcombine** in **IRAF**.

3.3.1 Sky Subtraction

After the scattered light removal process one or more sky estimation regions were defined for the 2D spectra, these regions were defined by manual examination of the profiles of the galaxy spectra along their spatial dimension, and were chosen to cover the regions where no clear gradients in the profiles were visible. See for example Figure 3.2 for a demonstration of the location of sky estimation regions. The median sky spectrum for one pixel in the spatial dimension was then determined and combined with the scattered light profile subtracted earlier to produce a 2D sky+scattered light image for use in the later extraction.

As is the case with any study of galaxy spectra, an accurate sky subtraction is essential if galaxy line strengths and kinematics are to be measured with confidence. One particular concern when studying large resolved objects such as nearby galaxies is that the sky subtraction regions of the 2D spectra cannot be located at large enough radii to completely avoid additional flux from the galaxy still being present. To help mitigate this problem the major axis longslits were often offset along the slit direction to allow the sky subtraction regions to be located at larger galactocentric radii. For the majority of galaxies studied here the optical imaging demonstrates that the chosen sky subtraction regions were indeed located at large enough radii to make the contribution of galaxy integrated light negligible (see for example Figure 3.2 for a demonstration of the large regions available for sky estimation on either side of the minor axis of NGC 7332). However in one particular case, that of the major axis of NGC 4762 the galaxy is simply too large to allow the 330 arcsec long GMOS longslit to extend from the centre of the galaxy to the distance ideally required to produce an entirely pure sky spectrum. In this case no special corrections are made but instead it is cautioned that any conclusions (at larger radii in particular) may be influenced by an oversubtraction of galaxy flux. Oversubtraction can in particulat have the effect of changing the derived stellar population parameter gradi-

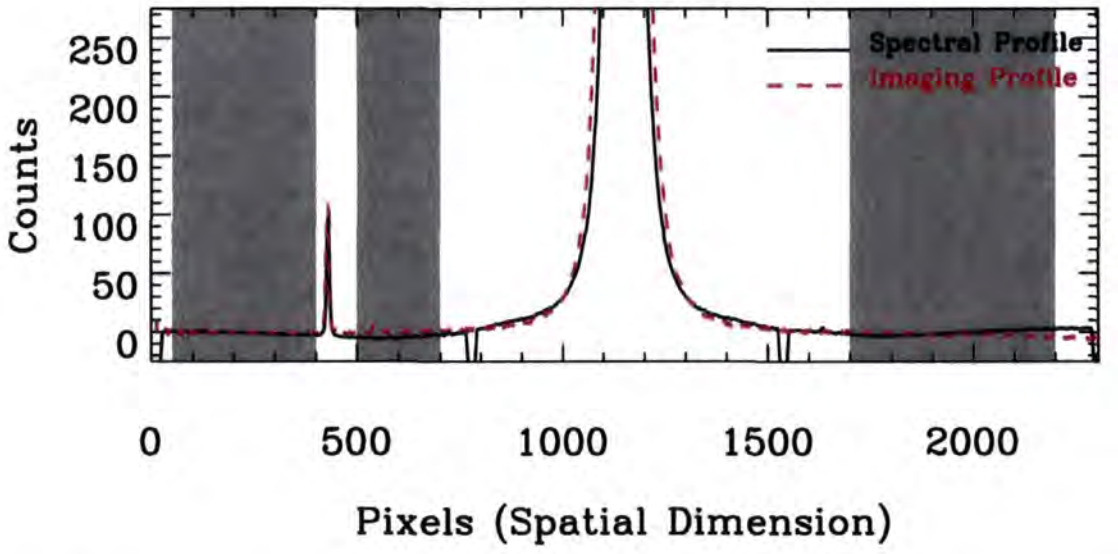

Figure 3.2: Demonstration of the placement of sky estimation regions for the minor axis of NGC 7332. The black line is the profile of the 2D spectrum along the spatial dimension, the red dashed line shows the imaging profile along the same axis. The filled grey regions denote the regions (50-400, 500-700 and 1700-2200 pixels) where the background sky was be determined.

ents, therefore in future analyses of this data-set various methods will be used to estimate and correct for this effect.

3.3.2 Spectral Extraction

After sky subtraction the 2D spectra were extracted into a series of 1D spectra binned spatially to reach a pre-determined S/N ratio. In this case it was decided to use a S/N ratio of 100 per Å measured between 5000 and 5100Å. This high S/N ratio was chosen for two main reasons; this S/N ratio allows the accurate measurement of higher order LOSVD kinematics given the choice of instrumental set up (as discussed in Section 3.3.3), and a S/N ratio of 100 at 5100Å ensures that even the bluer line strength indices such as Hγ and Hδ are significant and can be used in the following analysis. Having such a large S/N would make possible a more complicated analysis of the stellar populations, including the ability to attempt to fit more complicated star formation histories than the simple single stellar populations usually used.

The actual binning of the spectra was accomplished using the "CCD Equation" in the form:

$$\frac{S}{N} = \sqrt{\frac{N_{\rm obj}}{N_{\rm obj} + n_{\rm pix}(N_{\rm sky} + N_{\rm read}^2)}} \tag{3.1}$$

where N_{obj} is the number of counts from the object under study, N_{sky} the counts from the sky (and in this case also the scattered light which was removed), n_{pix} the number of pixels in the spatial dimension being binned, and finally N_{read} is the number of counts per pixel contributed by the instrumental read noise. Where a radius is provided (as in the kinematic figures) the quoted radius for each spectrum is the radius at which half the galaxy light in the bin was reached.

The individual 1D spectra were then flux calibrated with the **IRAF** program **calibrate** using response functions determined from the appropriate spectrophotometric standard star for the given semester and telescope.

3.3.3 Kinematics

From the outset the main aim of this study has been to examine the stellar populations of the target S0 galaxies. As such the experimental set-up was optimised towards measuring the maximum number of line strength indices as accurately as possible. However it is necessary to know the kinematic properties of the stellar populations under study so that corrections can be applied for the effects of the kinematics on the measured line strength indices (See Section 2.3.4). Additionally the kinematics of galaxies can themselves provide important clues to the formation and evolution processes that led to the object as currently observed. Therefore the measurement of the kinematics of our objects is an important secondary goal, within the bounds set by the fact that the observations were not optimised to measure high precision kinematics.

As in the study of NGC 3115 the Penalised Pixel Fitting Method (pPXF) of Cappellari & Emsellem (2004) is used to measure galaxy kinematics. This method especially lends itself to the current work due to the ability to directly mask regions with suspected emission, a procedure not possible with other methods for measuring kinematics such as the Fourier Correlation Quotient (Bender, 1990). As many of the sample galaxies are expected to display significant emission the ability of pPXF to ignore regions where emission is likely to cause problems fitting emission free templates to the data is a great bonus.

One departure from the procedure used in the study of NGC 3115 (Chapter 2) is that in this instance the preliminary stellar population models from Vazdekis et al. (in

preparation) are used as stellar population templates[2]. These models are built from the Medium-resolution Isaac Newton Telescope Library of Empirical Spectra (MILES) spectral library (Sánchez-Blázquez et al., 2006), one of the most comprehensive stellar libraries to date. The stellar population models cover the range of metallicity ([M/H]=-1.68 to +0.2) and age (0.1 to 17.78 Gyr) likely to be encountered in this study. The rather high value of the upper age limit in the template library is relatively unimportant as the models have some inherent uncertainty to their age scale and change relatively little at ages larger than 13 Gyr. This broad range of stellar population templates helps to further reduce the effects of template mismatch, a problem already minimised by the pPXF method.

The most constraining choice of experimental set-up was the decision to select a grism and wavelength range which gave an intermediate spectral resolution of around 4.8Å but a wide wavelength range covering all of the Lick/IDS line strength indices. One drawback of such a choice is that the intermediate spectral resolution makes accurate measurement of higher order LOSVD terms difficult at lower velocity dispersions. To test the limits to which these parameters can be measured it is therefore necessary to carry out a series of simulations of the data to determine the useful range of application. This set of simulations can also be used to examine the appropriate choice of the pPXF bias term. This is an optional input which is chosen to better help pPXF recover the true LOSVD, it is in fact the threshold below which a deviation in the LOSVD is determined to be due to noise and above which it is determined to be due to a real higher order component. As the appropriate value depends sensitively on the input data parameters, such as wavelength range, spectral resolution and sampling it is necessary to carry out simulations to determine the correct choice of bias.

Monte-Carlo Simulations of pPXF

To test the limits of pPXF to recover accurate kinematics using the input experimental set-up a set of Monte-Carlo simulations of the data was carried out. In these simulations the input stellar population templates were converted to the spectral resolution, sampling and wavelength range appropriate for the actual data. They were then convolved with a range of LOSVDs before pPXF was used to attempt to recover the input kinematics. In

[2]Available from: http://www.ucm.es/info/Astrof/users/pat/models/download/download.html

these simulations the bias parameter and S/N ratio of the input spectra were also varied; for each permutation of σ (7 values), h_3 (7 values), h_4 (7 values), bias (9 values) and S/N (5 values), 30 Monte Carlo simulations with added noise were completed. This leads to a total number of simulations of over 463,000, with σ values of 0, 50, 100, 150, 200, 250 and 300 kms^{-1} (covering the range of σ encountered in this survey), h_3 and h_4 values of -0.3, -0.2, -0.1, 0.0, 0.1, 0.2 and 0.3, S/N from 20 to 100 in steps of 20, and bias values ranging from 0.1 to 0.9 in 0.1 steps.

The first task is to determine the optimum choice of bias parameter to use. The bias parameter is the "penalty" used in the pPXF fit and as suggested by the pPXF manual it is chosen such that, "when sigma > 3*velscale, the mean difference between the output [h3,h4] and the input [h3,h4] is well within the scatter of the simulated values". For the particular dataset available here the velscale is $50kms^{-1}$ (as it is simply the spectral pixel scale in velocity units i.e 2Å in kms^{-1}) for data binned by two in the spectral dimension and $100kms^{-1}$ for the data binned by 4 in the spectral dimension. The optimum choice of bias was around 0.7 in both cases, although in practice the results were not strongly affected by the chosen value.

The second task is to determine over what range of parameters it is possible to recover accurate kinematics. For example it is significantly easier to recover the higher order h_3 and h_4 terms at larger σ. Figures 3.3 and 3.4 demonstrate this fact for the example of input S/N=100, Bias=0.7, and extreme values of h_3=0.3 and h_4=-0.3 for both the velocity scale = $50kms^{-1}$ and $100kms^{-1}$ respectively. As is to be expected, as the input velocity dispersion falls below the instrumental resolution ($\sim 120kms^{-1}$) it becomes more difficult to recover the higher order LOSVD terms. This inability to recover h_3 and h_4 leads to significant errors in the recovered values of velocity and σ. This behaviour can be understood as being due to the pPXF program compensating for its inability to determine the higher order terms by adjusting the implied velocity and σ to compensate. Figures 3.5 and 3.6 conclusively demonstrate the fact that velocity and h_3 are anti-correlated, as is the pair σ - h_4. Also obvious is the observation that the magnitude of the error introduced by not correctly recovering h_3 and h_4 is dependent on the S/N ratio of the input data.

In the most extreme of cases displayed in Figures 3.3 and 3.4 it can be seen that the covariance between velocity and h_3, and between σ and h_4, can lead to systematic errors in the recovered velocity of up to $\sim 20kms^{-1}$ and σ of $\sim 30kms^{-1}$ for velocity dispersions below $\sim 100kms^{-1}$. For the more plausible values of h_3=0.1 and h_4=-0.1, the correspond-

ing systematic errors are $\sim$5kms^{-1} and σ of $\sim$10kms^{-1}. In either case these uncertainties are of no major concern, as the main aim of this study is to recover accurate line strength indices and the measured kinematics are needed only to correct line strength indices for the effects of the LOSVD. These corrections are entirely negligible below $\sigma\sim$100kms^{-1}.

Figure 3.7 investigates the ability of pPXF to accurately recover the velocity and σ in the simplest case of zero h_3 and h_4, in this instance for two input choices of S/N, 20 and 100. As can be seen, velocity is recovered accurately in all cases. However σ can only be recovered accurately to around half the instrumental resolution (around 50kms^{-1} for our data). When combined with the results of the previous section this means that for all but the smallest target galaxy (ESO 358-G006) it is possible to measure the velocity dispersion accurately to $\sim$50kms^{-1} in the case of zero h_3 and h_4. However as h_3, h_4 cannot be measured below $\sim$100kms^{-1} the recovered velocity dispersions between 50 and 100 kms^{-1} can be systematically offset by up to 30kms^{-1}. Nevertheless as previously discussed this does not impact the accuracy of the measured line strengths in any significant way.

In conclusion with the appropriate choice of bias parameter pPXF is able to accurately recover velocity, σ, h_3 and h_4 for the data presented here when σ is greater than 100kms^{-1}. Below this limit potentially significant ($\sim$30kms^{-1}) systematic offsets in velocity and σ are possible due to the inability to recover h_3 and h_4. These issues do not cause any significant problems for the later measurement of line strength indices.

Measurement of Kinematics

After the limits of application were determined each spectrum could be measured using pPXF. In the present work, the best fit was determined over the (observed) wavelength range 4900-5450Å with regions likely to be affected by emission masked. One additional step was included over the procedure used in the study of NGC 3115, to account for the inability to measure the higher order LOSVD terms below a velocity dispersion of 100kms^{-1}. pPXF was run first in a mode that measured only velocity and velocity dispersion. If the velocity dispersion exceeded 100kms^{-1} then pPXF was run again with the freedom to include h_3 and h_4 if they improved the fit. This procedure ensures that values for h_3 and h_4 are only derived in the region of parameter space where they are actually measurable and hence helps to reduce spurious kinematic fits at low σ. This procedure was unnecessary in the study of NGC 3115 as over the range of radii studied the velocity dispersion never fell below the σ=100kms^{-1} limit for the recovery of h_3 and h_4.

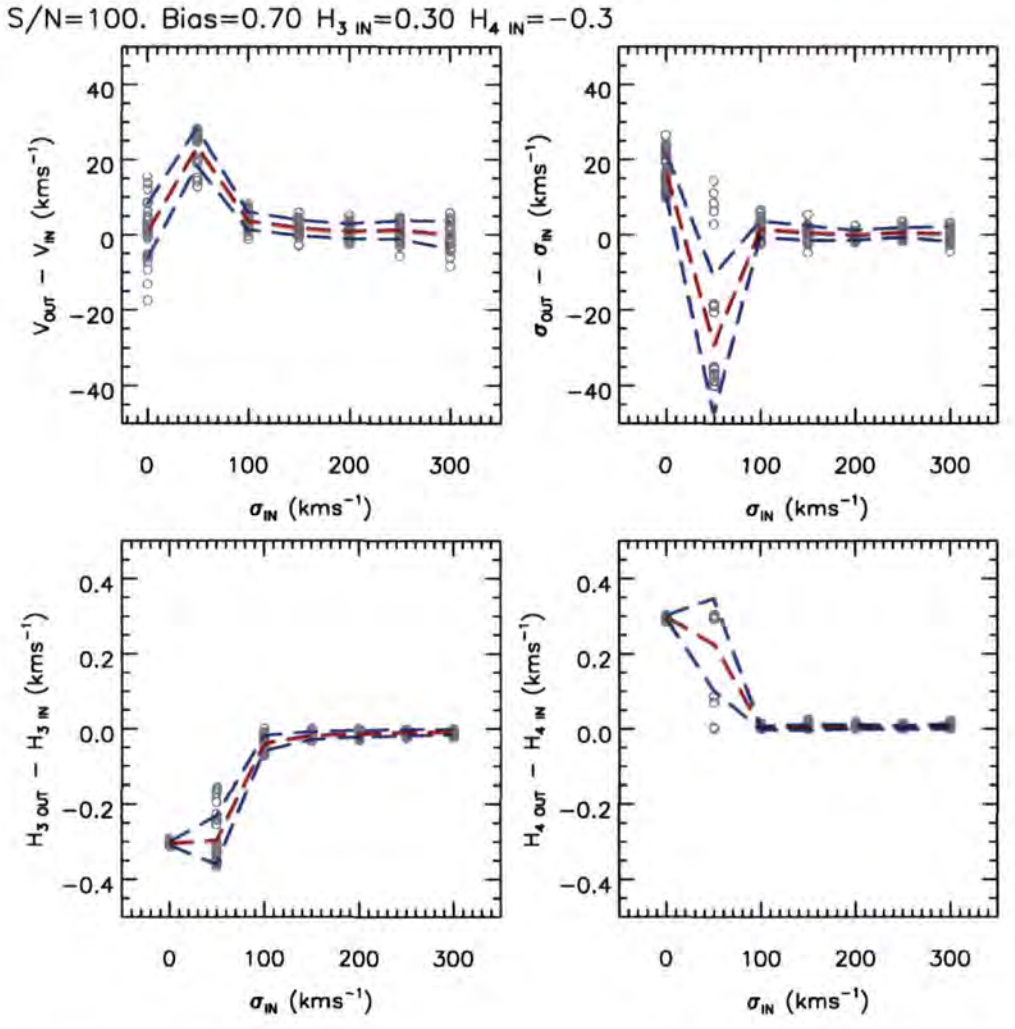

Figure 3.3: Example simulation undertaken to determine the practical measurement limits for our data using the pPXF method. Unfilled circles are Monte Carlo re-simulations of the input template spectra after convolution with the desired input values of σ, h_3 and h_4. There are 30 resimulations with added poissonian noise for each choice of velocity dispersion, the red line is the mean of these resimulations, the blue lines are the 1-σ errors associated with these resimulations. As can be seen clearly, it proves impossible to measure the higher order h_3 and h_4 below the instrumental resolution of our set up of around 100 kms^{-1}. This simulation was conducted with a set-up matched to the majority of our data which has a velocity scale (velscale) of 50kms^{-1}.

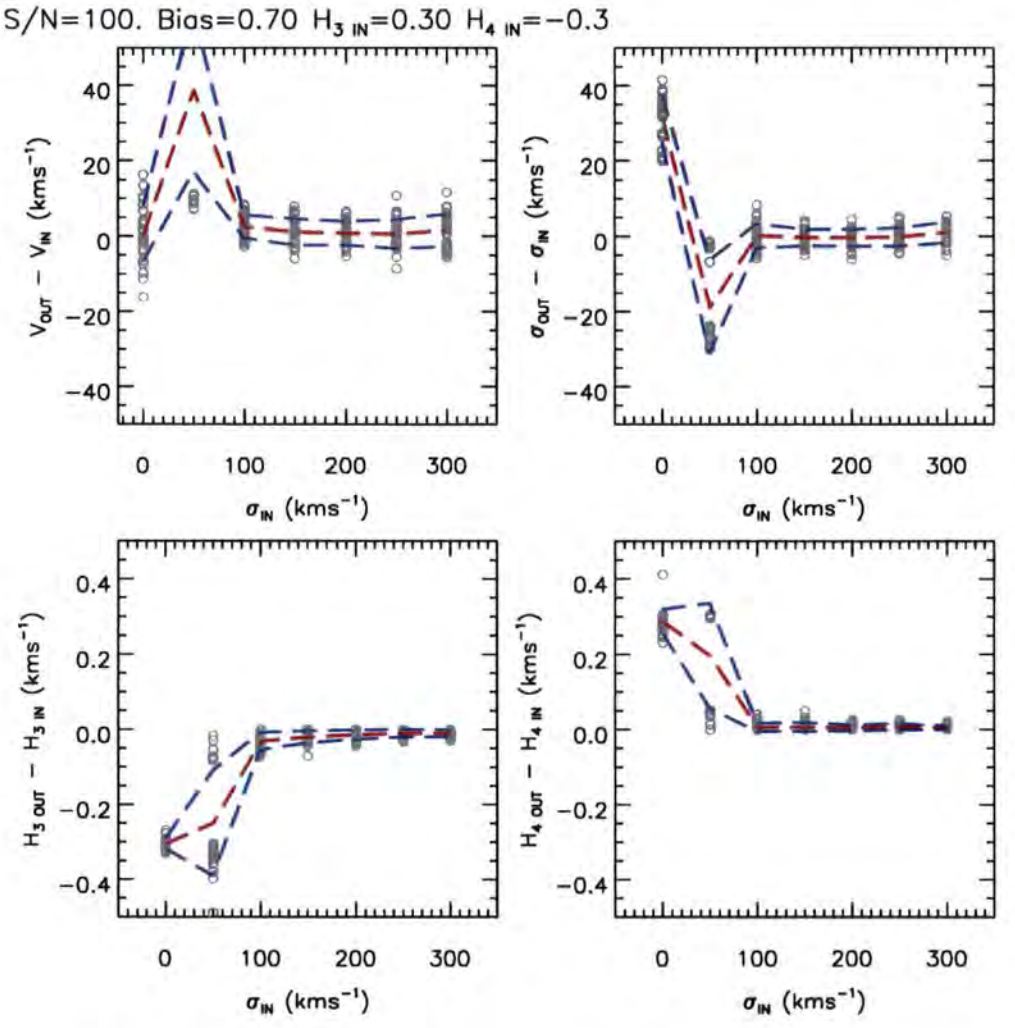

Figure 3.4: As in Figure 3.3, except that in this simulation the velscale parameter has been changed to 100kms^{-1}, in this case matching our earlier epoch data which was binned by 4 in the spectral dimension.

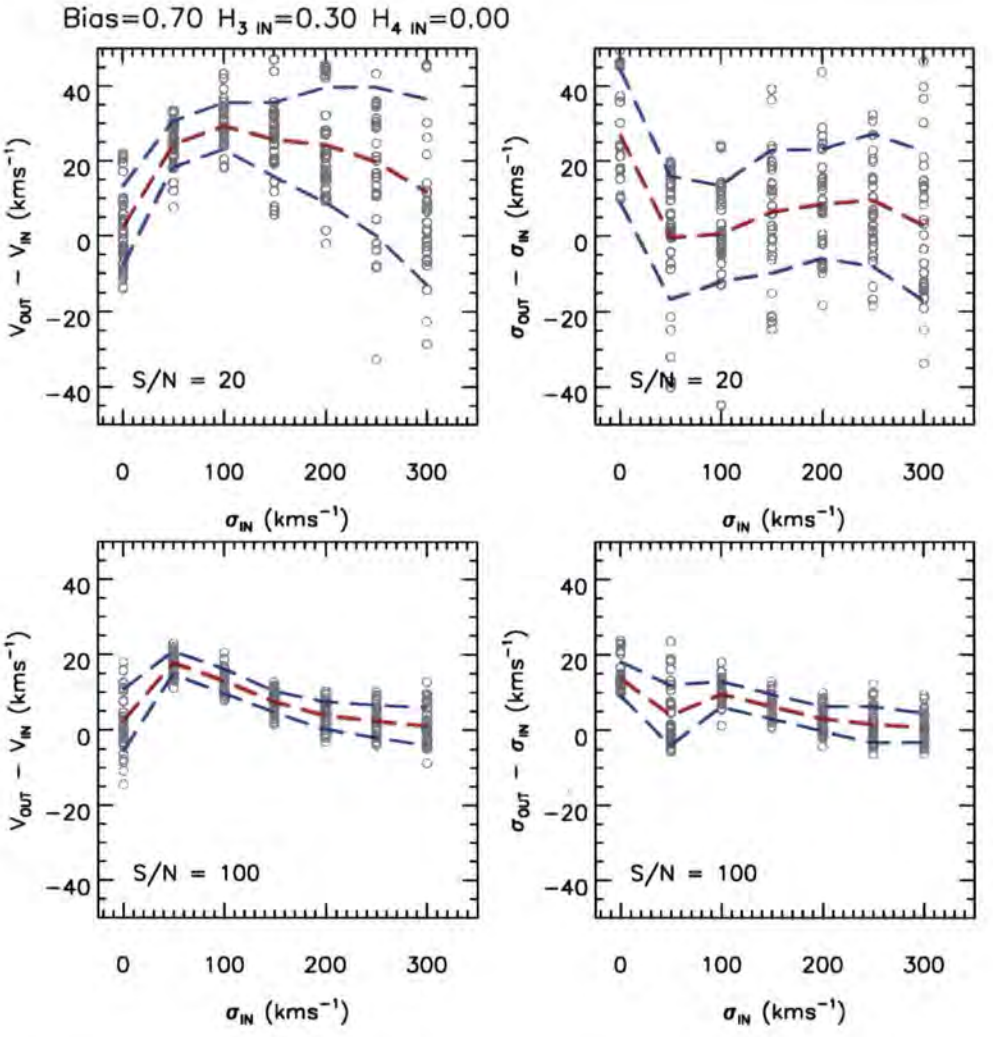

Figure 3.5: In this figure the ability of pPXF to recover the input velocity and σ at two choices of S/N, 20 (top panels) and 100 (bottom panels) given an extreme value of h_3 of 0.3 has been applied to the data is examined. In this case the recovered velocity is over-estimated for velocity dispersions below the instrumental resolution. This is simply an effect of the fact that at these low velocity dispersions h_3 is unmeasureable. The velocity is therefore altered in the pPXF fit to compensate. In comparison the measurement of the velocity dispersion is relatively unaffected by the addition of the h_3 component.

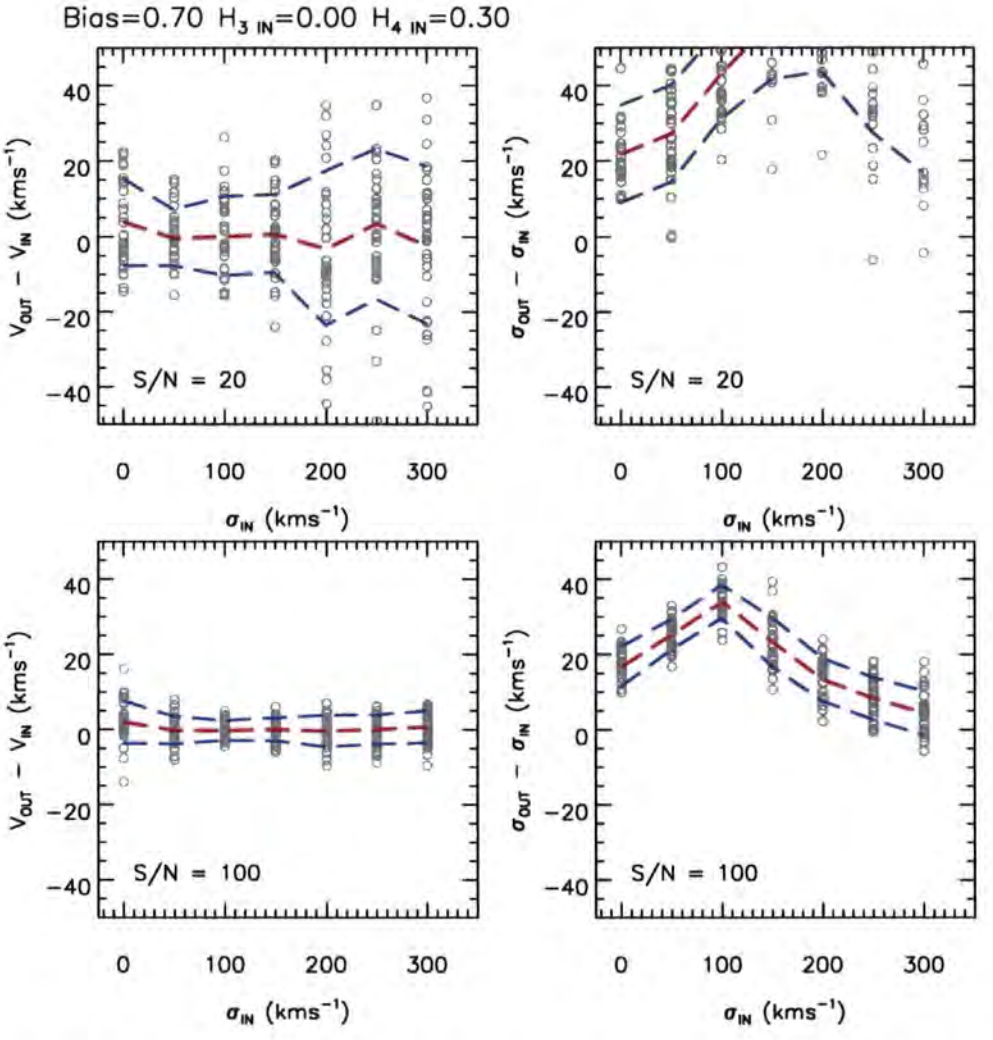

Figure 3.6: As in Figure 3.5 except that in this case an additional large h_4 component has been applied to the data. In contrast to Figure 3.5 it is now the velocity dispersion which displays a systematic overestimation in the fit, for essentially the same reason as previously. As it becomes harder to measure the h_4 component the pPXF code compensates by varying the measured velocity dispersion.

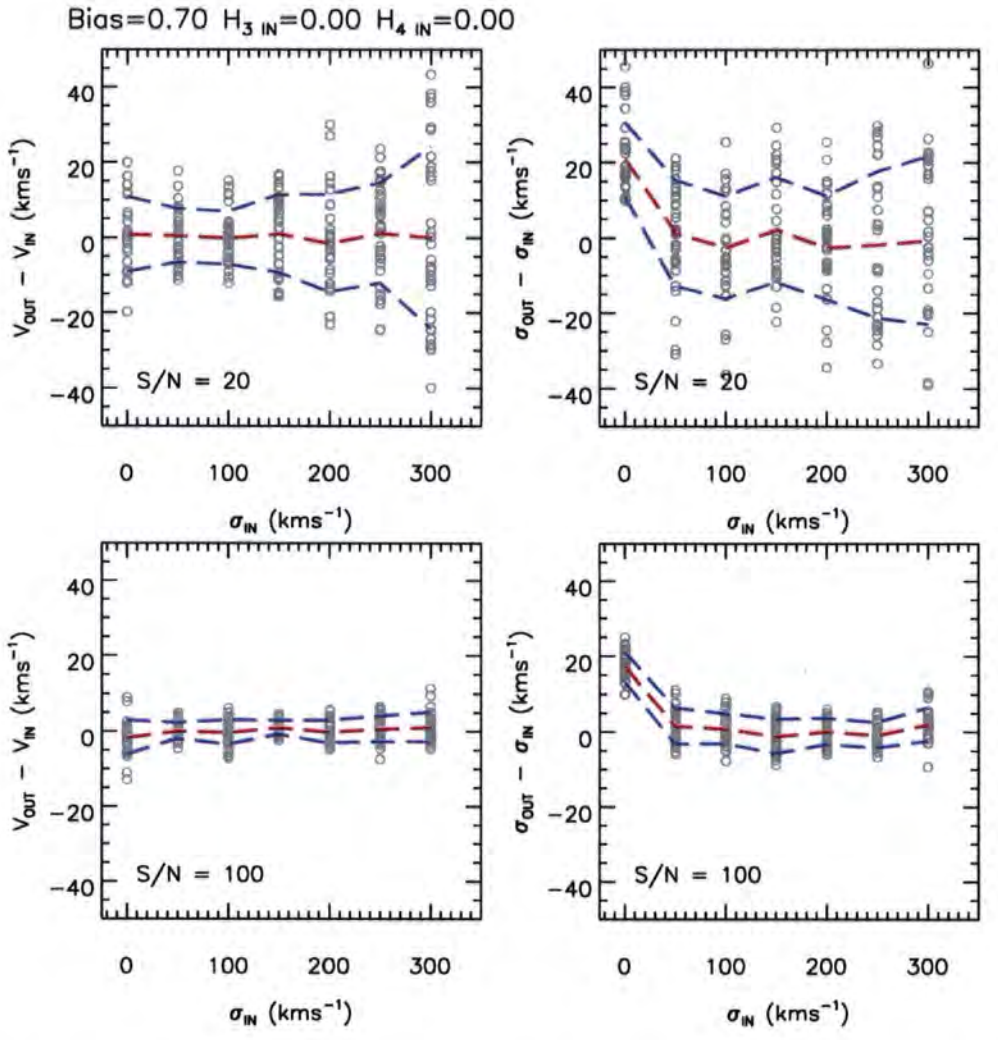

Figure 3.7: In this figure pPXF's ability to recover the input velocity and σ at two choices of S/N, 20 (top panels) and 100 (bottom panels) is examined. As can be seen the velocity can be accurately recovered at all input velocity dispersions for both choices of S/N, the velocity dispersion however can only be recovered accurately above around $\sigma \sim 50 \mathrm{kms}^{-1}$.

3.3.4 Emission Line Correction

Recent work has contradicted the long held belief that early type galaxies are devoid of significant dust or nebular emission. For example the SAURON project (Sarzi et al., 2006) has demonstrated that approximately 75% of their sample of 48 early type and lenticular galaxies display a detectable level of emission, rising to 83% when only lenticulars are considered. This discovery is problematic for the study of the stellar populations of galaxies as the SSP models utilised in the study of stellar populations do not include the effects of emission, hence variations in the intensity of emission can be incorrectly interpreted as variations in the stellar populations of the galaxy. Of particular concern are the Fe5015 absorption feature which can be affected by $[OIII]_{\lambda 5007}$ emission in its central bandpass and $[OIII]_{\lambda 4959}$ in its blue pseudocontinuum, and Mgb which can be affected by $[NI]_{\lambda 5200}$ emission in its red pseudocontinuum. These indices, if contaminated by emission and left uncorrected, would lead primarily to incorrectly determined metallicities and α-element abundances. Age estimates could also potentially be biased by emission, as much of the power to determine the ages of stellar populations comes from the hydrogen based indices Hγ, Hδ and Hβ, all of which can of course be affected by emission. Clearly if the standard SSP model approach is to be used to correctly interpret the data then the measured absorption lines must be unaffected by the presence of emission lines.

As well as creating a problem, the existence of nebular emission within the target galaxies can also prove to be interesting in its own right, as a study of the properties of the emission can lead to a better understanding of the processes which create it. The existence of nebular emission can be explained in two ways: as the product of material lost by stars during their lives or through the presence of material of external origin, presumably accreted gas rich satellites. It has been demonstrated that the amount of mass lost by the stellar component of a galaxy is sufficient to explain the mass of ionised material of $\sim 10^3$-$10^4 M_\odot$ (Goudfrooij et al., 1994) generally found in early type galaxies (Faber & Gallagher, 1976). However the kinematics and orientation of the emission and associated dust is often found to indicate that the emitting material is decoupled from the stars of the host galaxy, strongly implicating an external origin for the material. In the SAURON sample around 50% of galaxies with observed emission displayed misalignments indicative of an external origin for the material. In a few cases the emitting material can be conclusively tied to an external origin. In the case of NGC 1596 the counter-rotating ionised gas observed in its central regions can be tied to the existence of a large-scale tidal stream

of HI from the companion dwarf irregular galaxy NGC 1602 (Chung et al., 2006). There are also a host of other interesting side questions that the study of the properties of the ionised gas can also illuminate: What is the eventual fate of the gas? will it cool to form a new generation of stars, or be heated to join the X-ray emitting halos of galaxies. What powers the nebular emission? Is it either young or exotic older stellar types? AGN? Or shocks? At present no definitive answer exists to these questions, but clearly the study of nebular emission in early type galaxies can do much to constrain many other areas of astrophysics.

Therefore there exists a similar predicament as was the case in the study of the absorption line kinematics, the wish to optimise the ability to examine the stellar populations of the integrated light of the galaxy whilst still recovering what information is possible about the nebular emission from the data.

GANDALF Emission Line Removal

To achieve the twin goals of recovering emission free absorption line indices from the spectra and measuring the kinematics and magnitude of any emission present a modified version of the GANDALF (Gas AND Absorption Line Fitting) code of Marc Sarzi was used. A more complete description of this code can be found in Sarzi et al. (2006) and references therein but in brief the code makes use of a similar method to the pPXF program described previously:

- The regions likely to be affected by emission are masked, pPXF is used to determine the best fit absorption line kinematics and optimal template. This determination of the LOSVD is carried out over the full wavelength range to be studied, in this current case ~3900-5500Å (excluding chip gap regions which have lower S/N), this procedure takes around a minute per spectrum on a normal desktop computer. Any extension to cover the full wavelength range of the spectra leads to unacceptable increases in computation time, of the order of 5-10 minutes per spectrum.

- The templates in the library (which is the same library as used in the measurement of the kinematics) are convolved with the measured LOSVD to produce the optimal template.

- The best fit values of amplitude, mean velocity, and intrinsic velocity dispersion of the [OIII] line are determined assuming gaussianity. This is achieved by compari-

son of the convolved best fit templates (which were determined outside the masked regions) and the observed spectrum in the masked (emission affected) regions.

- The mask is removed and the best fit amplitudes for the other lines to be fit is determined, under the condition that they have the same kinematics as [OIII].
- If the amplitude-to-noise ratio (how significant the line is relative to the noise in the input spectrum) of the line is greater than 3 the best fit emission line model is subtracted from the input spectrum. This produces the final emission corrected spectrum.

Slight modifications to the GANDALF code were required to allow the measurement of emission lines other than those originally determined by the code. In partcular the code was originally designed to work with SAURON data, which has a very limited wavelength range of ~4800-5300Å. The code was therefore adapted to also correct for emission in the Hδ and Hγ features. Its method for doing this is exactly the same for all other emission lines.

Figure 3.8 displays the result of carrying out the above procedure on one of the most extreme cases of emission line contamination seen in the sample. In this example from the minor axis of NGC 1596, strong [OIII] lines are already visible in the input spectrum (black line). The best fit emission line model is displayed as the blue line (the best fit template is excluded for clarity) and the resulting emission corrected spectrum is displayed as the red line. As can be seen, the effect of emission on the strength of the Hβ feature is significant and could lead to severe problems in the estimation of stellar population parameters if left uncorrected.

In one final step the GANDALF output is utilised to help correct the input spectrum for one further effect. It is an unfortunate consequence of the choice of wavelength range that the blue continuum of the Hβ feature is affected by the presence of a chip gap. This chip gap leads to a lower S/N and increased incidence of cosmic ray residuals in the Hβ blue continuum resulting in spurious Hβ line strengths. To help mitigate this we make use of the GANDALF best fit model to replace the affected region which occurs between ~4780-4840Å. No other regions required for line strength measurements are affected by this problem.

After correction by GANDALF the final emission-line-corrected spectra covering the range 3900-5500Å are produced, from which line-strength indices can be measured.

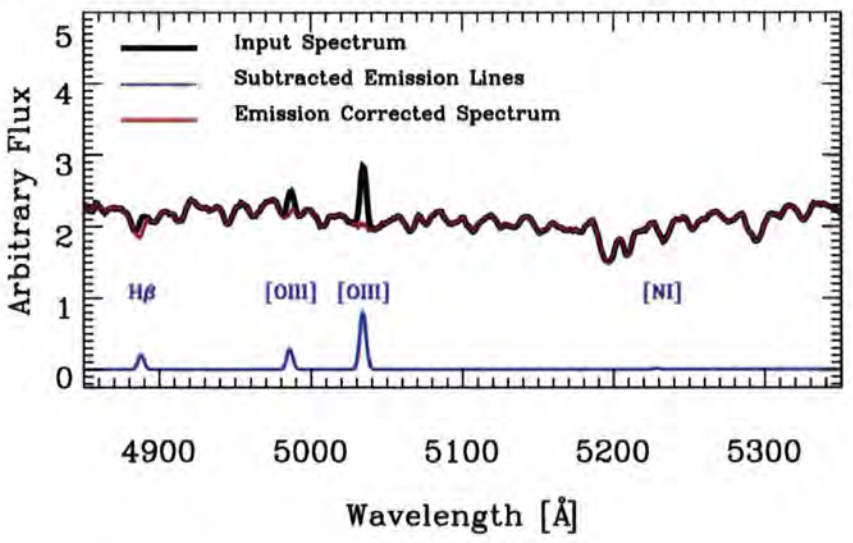

Figure 3.8: Example GANDALF fit. The black spectrum shows an input minor-axis spectrum of NGC 1596, one the galaxies within the sample with the most significant emission-line contamination. The blue spectrum is the best fit emission line model produced by GANDALF. The red spectrum is the emission corrected input spectrum, later used to measure the absorption-line indices. The species responsible for the emission lines are labelled.

3.3.5 Line Strength Indices

After the emission line subtraction the LICK/IDS line strength indices were measured from the corrected spectra, the procedure used was exactly the same method as described in Section 2.3.4. As explained previously the measured line strengths must be corrected for the effects of the LOSVD on their observed strength. In this current study this correction is carried out in a novel way. The correction procedure makes use of the fact that during the measurement of the kinematics of the stellar population an optimal template is produced. This template is constructed from stellar population models which have no intrinsic LOSVD. They must be convolved with the difference in instrumental resolution and the LOSVD within pPXF to match the observations. By measuring the absorption-line strengths of the optimal template, before it has been convolved to match the observations (but after smoothing to the Lick/IDS resolution) and after the convolution with the LOSVD (including the higher-order terms and smoothing to the Lick/IDS instrumental resolution) it is possible to estimate by how much the line strengths on the measured spectra must also be affected by the LOSVD. In this way it is possible to deter-

mine the additive and multiplicative corrections to be applied to the measured indices to remove the effect of the LOSVD on the measured line strength. The errors on the LOSVD correction are calculated as the 1-σ scatter in the correction determined from 30 Monte Carlo resimulations of the optimal template with added Poissonian noise. The computed error in the correction is combined in quadrature with the other sources of error in the measurement of the line indices to produce the final error estimate.

The left panel of Figure 3.9 demonstrates the effect of a simple σ -only LOSVD on the measured strength of the Mg*b* index, in this case calculated for the optimal template determined for the spectra displayed in Figure 3.8. The right panel compares the resulting velocity dispersion correction for Mg*b* with that determined by Kuntschner (2004) for old (age > 3 Gyr) populations, the maximum difference in applied correction is less than 2% at all values of velocity dispersion. In common with the findings of Kuntschner (2004) it is found that for old stellar populations the determined LOSVD correction is relatively unaffected by the age or metallicity of the stellar population present. However for younger stellar populations changes of age and metallicity can lead to more significant deviations in the corrections. This is not of major concern to the current study for two reasons, the first is simply that the majority of stellar populations under study here are in fact older than 3 Gyr, the second that this technique of utilizing optimal templates to derive the LOSVD corrections ensures the measured LOSVD correction is appropriate to the stellar population under study.

After correction for the effects of the LOSVD the final step required to place the measured line strength indices onto the Lick/IDS system is to calculate zero-point offsets between Lick/IDS library standard stars observed with the same observational set-up as used here. Lick standard stars were not directly observed during this project, due to the additional burden in observing time, however it is possible to determine Lick offsets for GMOS-S using observations collected as part of GS-2003B-Q-63 which were made available by Bryan Miller. Using a set of 28 stars from this sample, taken with an almost identical set-up to that used here (identical grism, with in this case a 0.5 arcsec longslit) it was possible to derive offsets for GMOS-S to the Lick system. As GMOS-N and GMOS-S are identical instruments it is assumed that the offsets are suitable for use with both our North and South data, an assumption that is supported by the fact that the measured offsets are all comparable to those described in Section 2.3.4. All line indices used in this study are corrected using these offsets.

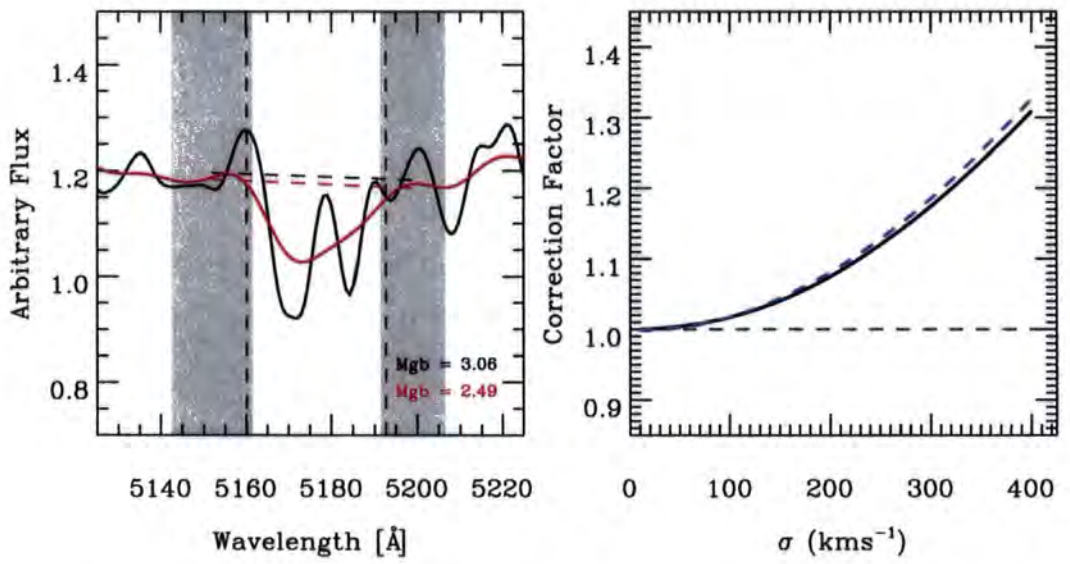

Figure 3.9: **Left Panel** : The effect of velocity broadening on the Mg*b* feature, in this case for the optimal template fit to the NGC 1596 spectrum displayed in Figure 3.8. The black line represents the optimal template after convolution with a velocity dispersion of 50kms^{-1} and the red line after convolution to 300kms^{-1}, values which approximately cover the range of σ encountered in this study. The corresponding measured index strength is given in the bottom right corner. The grey regions denote the blue and red continua, the horizontal lines are the resulting pseudocontinua and the dashed vertical lines the central bandpass of the Mg*b* feature. **Right Panel** : The behaviour of the velocity dispersion correction for Mg*b* determined for the optimal template with a purely Gaussian LOSVD (black line) and the correction determined by Kuntschner (2004) for old stellar populations (blue dashed line).

3.4. Results

3.4.1 Absorption Line Kinematics

As the final derived line indices depend somewhat on the measured kinematics of the stellar population (through the LOSVD correction) it is necessary to be confident that the kinematics derived here are accurate. Only by comparison with previously published data for the same galaxies is it possible to begin to estimate the potential systematic uncertainties inherent in the observation set-up used.

The galaxies NGC 1023 and NGC 7332 are of particular interest due to the fact that these objects have been studied several times, and have had their higher-order LOSVD terms measured for both axes from high (S/N = 60) quality 2D SAURON data. Figures 3.10 and 3.11 compare the kinematics derived here with those measured previously by Emsellem et al. (2004), Simien & Prugniel (1997b) and in the case of NGC 1023, Debattista et al. (2002). Also displayed are the i band images taken as part of this study, both before and after unsharp masking. This procedure helps to highlight structures within the galaxies. Of obvious note in these images are the disc of NGC 7332 and structures within the disc of NGC 1023 which may be due to residual spiral structure. In the case of NGC 1023 the measured velocity and σ of all 4 independent measurements are remarkably consistent for both major and minor axes, slightly troubling however is the observation that the measurements of h_3 and h_4 presented here disagree with those of Emsellem et al. (2004) at a small but systematic level. This mismatch is of the order of ± 0.05, which whilst significant is not large enough to have any noticeable impact on the measured line strengths, it is also significantly smaller than some of the disagreements between the Emsellem et al. (2004) and Debattista et al. (2002) kinematics.

In the case of NGC 7332 all three data sets display excellent agreement for all but the minor axis velocity dispersion in the inner regions, where the data presented here underestimates the velocity dispersion compared to the other observations by around $30 \mathrm{kms}^{-1}$. While in this case the different observations are within the corresponding 1-σ error bars, this is still a troubling level of disagreement, even though as in the case of the h_3 and h_4 offsets seen in NGC 1023 this difference in velocity dispersion has an essentially negligible effect on the measured line strength.

Similar figures to those described above detailing the kinematic properties of the re-

maining sample galaxies are presented in Appendix A along with brief notes on the observed kinematics of each galaxy. It is clear from an examination of these figures that the kinematics presented here are in excellent agreement with previously published data in almost all cases, and in those cases where statistically significant differences are evident, that they occur in regions of LOSVD space which have little influence on the measured line indices (i.e at low σ).

3.4.2 The S0 Tully-Fisher Relation

In order to study the Tully-Fisher relation for the galaxies studied here it is first necessary to convert the measured kinematics into a more astrophysically meaningful quantity, in this case the circular rotation velocity (V_{max}). The corrections which must be applied to the observed rotation curve (V_{obs}) of a galaxy to determine V_{max} are complicated and therefore deserve a comprehensive explanation. The particular procedure to convert V_{obs} to V_{max} used here makes use of the approach of Neistein et al. (1999) with some modifications to include procedures used by Bedregal et al. (2006a).

Simple Bulge + Disc Models

As a first step the correction requires structural parameters which describe the orientation and scale of the disc of the galaxy under study, these structural parameters are the inclination i and disc exponential scale length R_{exp}. In common with the study of Bedregal et al. (2006a) these parameters have been measured from 2MASS imaging (Jarrett et al., 2003) by a full two-dimensional bulge+disc model fit to the imaging. Because near infrared observations are used no correction for extinction either within the MW or internal to the target galaxies is required. Unlike the Bedregal et al. (2006a) study however the measurement of the structural parameters was made from the deeper J band 2MASS images rather than the K_s band imaging. The 2MASS imaging was preferred for this portion of the study over the i band imaging carried out here due to practical limitations in fitting the extremely high S/N i band data. In short substructure visible in the i band data made fitting a simple bulge + disc model impossible in most cases, as this simple approach is all that is required for the correction procedure utilised here the smoother lower significance 2MASS data was therefore preferred, although as shall be discussed later some substructure is still visible in the 2MASS imaging.

A further difference between the approach used by Bedregal et al. (2006a) and that

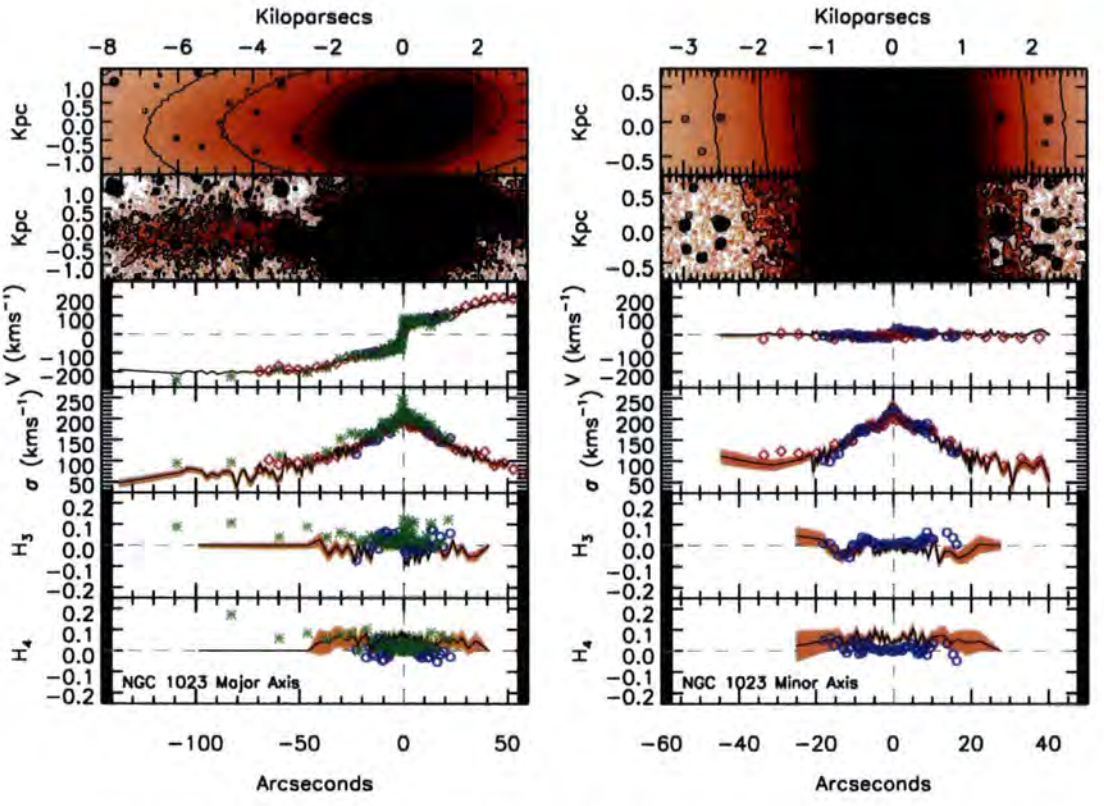

Figure 3.10: **Left Panel** : NGC 1023 Major Axis Kinematics. Upper frame GMOS i band image, 2^{nd} panel is a median subtracted version of the upper image obvious residuals emanating from the central regions may be the hallmark of residual spiral structure. In the kinematic panels the solid black line is the measured quantity, with the orange region defining the $\pm$ 1σ errors. Blue unfilled circles are the results from the SAURON survey (Emsellem et al., 2004), red unfilled diamonds are the measurements of Simien & Prugniel (1997b), green crosses come from Debattista et al. (2002). The velocity and velocity dispersion were measured from data binned to S/N=30, the h_3 and h_4 values were derived from our S/N=100 spectra. **Right Panel** : As in left panel but now for the minor axis of NGC 1023. Physical distances provided on the upper panel are determined using the measured distance provided in Table 3.1.

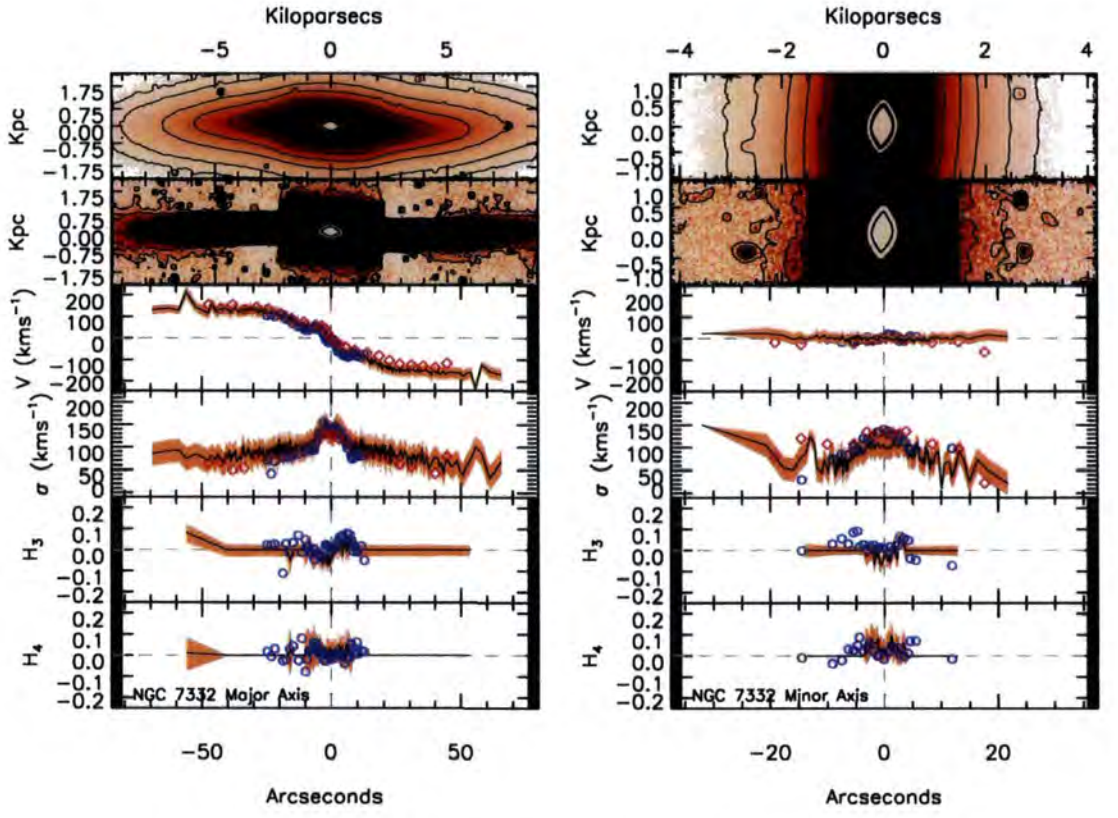

Figure 3.11: As in Figure 3.10 but for NGC 7332.

used here was in the choice of software to carry out the model fits to the 2MASS imaging. In Bedregal et al. (2006a) the GIM2D code (Simard et al., 2002) was used, whereas in this study the GALFIT code (Peng et al., 2002) was utilised.

The following procedure was used to determine the best fit Sérsic + Exponential disc model for each target galaxy. In all but 2 cases (NGC 3115 and NGC 3585), this simple model provided an acceptable fit. In the case of NGC 3115 and NGC 3585, an extra Sérsic component was required to allow GALFIT to converge to an acceptable fit, implying that these galaxies contain an extra large scale halo component.

1. SExtractor (Bertin & Arnouts, 1996) was run on the input image to find stars and other contaminating sources. A mask was produced to allow GALFIT to disregard these objects in the fitting procedure.

2. A bright (but unsaturated) star from the input image was extracted for use in the GALFIT software to determine the point spread function of the image.

3. A constraints file was produced which helped minimise the parameter space involved in the fitting procedure. These constraints included requiring the Sérsic function to have an n value of between 0.7 and 5, and the Sérsic and exponential disc components to have central positions which varied by less than one pixel, and position angles which varied by less than 1°. The latter constraint was relaxed in the case of NGC 1023, where the obvious bar structure led to an apparent misalignment between disc and bulge. The choice of Sérsic n values is motivated by the fact that the majority of galaxies have profiles which lie within this range, with n=2 defining a perfect exponential profile and n=4 the standard de Vaucoleurs $r^{\frac{1}{4}}$ profile.

4. GALFIT was allowed to run on the input image with first guesses at values such as disc and bulge magnitudes, PAs and scale lengths.

5. If the resulting fit displayed an acceptable χ^2 (anything between 0.1 and 2 in this case) and little evidence for systematic problems in the residual image (i.e. no obvious disc misalignments) the fit was accepted.

6. In the case of problem cases, where for example discs were misaligned the constraint file could be altered to force the fit toward a more accurate solution. This step was generally required when GALFIT would converge on a disk component fit at 90° to the actual disc, this was usually due to the presence of extra small scale

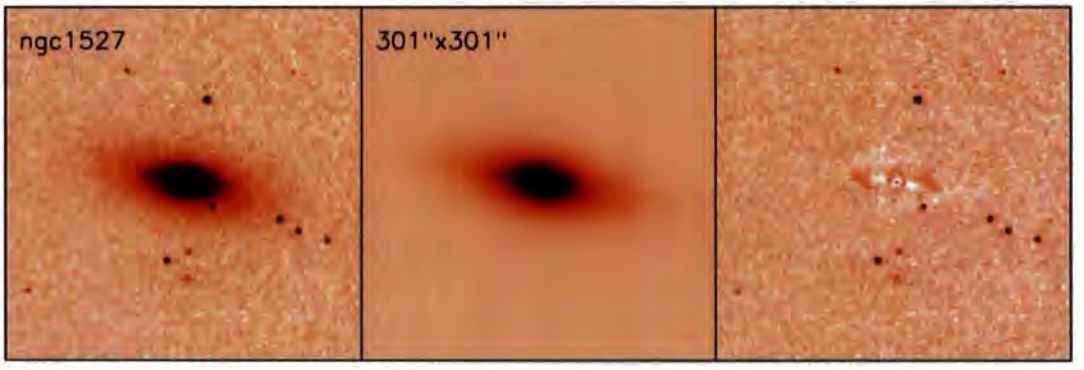

Figure 3.12: **Left Panel** : 2MASS J band image of NGC 1527. **Central Panel** : Best fit GALFIT Sérsic + Exponential disc model. Field of view of the fitting region is indicated. **Right Panel** : Residuals remaining after subtracting the model from the input image.

components in the inner region of the galaxies confusing the fit. By forcing the PA of the exponential to be close to that observed by eye for the disc a more reasonable fit was reached.

7. In two cases (NGC 3115 and NGC 3585) a further spheroidal component proved necessary to allow a stable fit. This larger scale component is necessary to describe the large halos of these galaxies.

An example GALFIT fit is shown in Figure 3.12 for the case of NGC 1527, similar figures for the remaining sample galaxies are displayed in Appendix 7.2. In most cases the fits produced by GALFIT are extremely good, only in cases where problems would be expected are there significant issues with the fits. For example in the case of NGC 4762 fitting of the disc proved difficult due to the disc displaying clear truncation, with evidence for other components such as thick disc and disc warps adding to the complexity of the fit. Most residual images display some evidence for unfit extra components present in the galaxy images, the most common being evidence of spiral structures (e.g. NGC 3301, NGC 5864, NGC 6725), boxy or peanut bulges (e.g. NGC 3098) or bars (e.g. NGC 1023).

As a comparison is to be made between the sample of Bedregal et al. (2006a) and that presented here it is necessary to ensure that the measured disc parameters using either method are consistent. To determine if this is indeed the case the 9 Fornax S0s of the Bedregal et al. (2006a) sample were re-examined using GALFIT and 2MASS J-band images. The conclusion of this investigation was that the disc exponential scale length and inclination is relatively insensitive to the choice of 2MASS band and software used

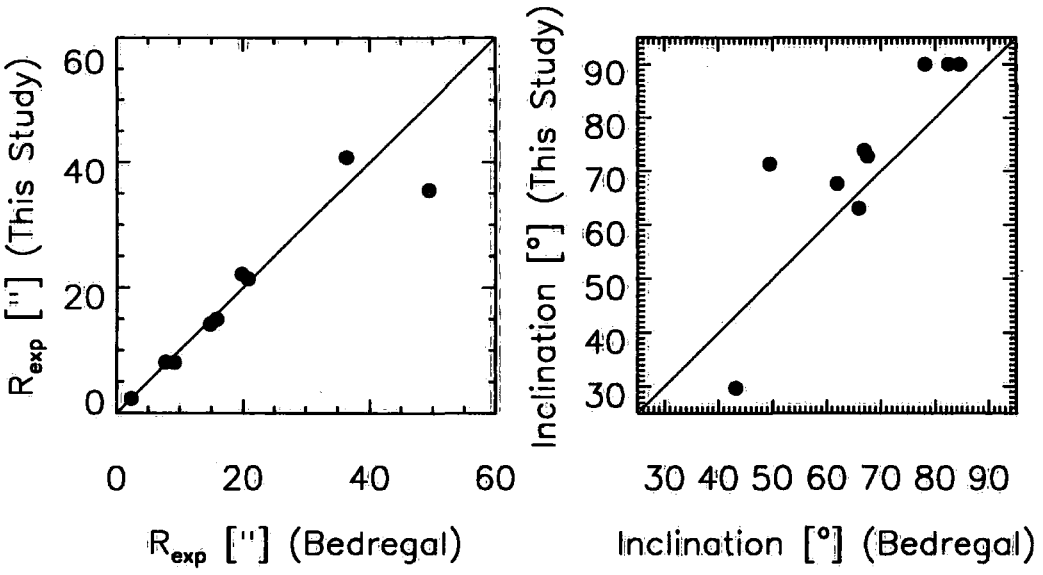

Figure 3.13: **Left Panel** : Exponential disc scale lengths measured by Bedregal et al. (2006a) using GIM2D on 2MASS K_s band images and this study using GALFIT on 2MASS J band images, for the sample of Fornax cluster galaxies from Bedregal et al. (2006a). The solid line is the one-to-one relation. **Right Panel** : Measured inclinations for the Bedregal et al. (2006a) galaxies. The solid line is one-to-one relation.

in the fitting. As Figure 3.13 demonstrates, the agreement in measured exponential scale length is extremely good, with the correspondence in implied inclination being less good. The parameters of the best fit Sérsic models are however found in most cases to be in stark disagreement, with the results from GALFIT often appearing to trade the measured Sérsic index and the scale length in such a manner that although the bulge parameters varied the overall bulge-to-total ratio remained fairly similar to that found by Bedregal et al. (2006a). Nevertheless the two parameters of particular importance to the determination of the maximum rotation velocity appear to be relatively well constrained by the fitting procedure utilised here. The one drawback of making use of GALFIT is that the errors in the measured parameters are generally severely underestimated, especially in cases such as this where some use of a constraints file is required. In this case therefore errors of 20% are assumed for all measured disc parameters, as this number appears to approximate the scatter between the values determined here and those measured for the same galaxies in previous studies which attempted bulge + disc model fitting on the galaxies (Baggett et al., 1998; Bedregal et al., 2006a).

Derivation of Circular Velocity

The derivation of the true circular velocity of a galaxy depends sensitively on the choice of model employed. In this case the model and correction procedure of Neistein et al. (1999) is used, as the Neistein et al. (1999) data set is comparable to that presented here and fortuitously their sample of 18 nearby S0 galaxies includes 3 which overlap with the sample presented here, NGC 1023, NGC 3115 and NGC 7332. By comparing the circular velocity determined here for these 3 galaxies and for the 2 galaxies which overlap with the Bedregal et al. (2006a) sample it is possible to gain an understanding of the various systematic errors associated with the correction procedure, input kinematics and input disc parameters. The circular velocity determination proceeded as follows:

In the case of ESO358-G006 the rotation curve was deprojected to an edge-on aspect. This was done assuming that an edge on disc has an intrinsic axis ratio q_0=0.22, which leads to the following relation:

$$V_\phi(R) = \frac{V_{\rm obs}(R)}{\sin i} = V_{\rm obs}\sqrt{\frac{1-q_0^2}{2e-e^2}} \tag{3.2}$$

Where V_{obs} is the observed rotation velocity at any given point. For all remaining sample galaxies the measured inclination was greater than 67° and the correction essentially negligible and hence not applied.

As described in Neistein et al. (1999) in the case of highly inclined galaxies the observed mean velocity relative to the actual velocity V_ϕ at the tangent point is reduced due to the line-of-sight integration through the galaxy disc. To determine the magnitude of this effect Neistein et al. (1999) constructed a simple model of an exponential disc which had a scale height (h_z) of $0.2R_{exp}$, using this model they determined that the corrections for this line-of-sight integration effect are of the form:

$$V_\phi(R) = \frac{V_{\rm obs}(R)}{f(R/R_{\rm exp})} \tag{3.3}$$

and

$$\sigma_\phi^2 = \sigma_{\rm obs}^2 - \frac{1}{2}(V_\phi - V_{\rm obs})^2 \tag{3.4}$$

where

$$f(x) = \frac{\exp(-x)}{-0.5772 - \ln x + x - \frac{1}{2}x^2/2! + \frac{1}{3}x^3/3! - ...} - x \tag{3.5}$$

These corrections were applied in all cases. At this point ESO358-G006 caused an additional problem in that the velocity dispersion was unmeasureable using the set up utilised here. Therefore the measured velocity dispersion from Bedregal et al. (2006a) was used to determine V_ϕ in this case.

The final correction which must be applied is the correction for the "asymmetric drift". This corrects for the fact that some component of the motion of the stars is non circular (due to their velocity dispersion). Neistein et al. (1999) show that for the case of a flat rotation curve where $V_\phi/\sigma_\phi > 2.5$, the correction takes the form:

$$V_c^2 = V_\phi^2 + \sigma_\phi^2(2\frac{R}{R_{exp}} - 1) \tag{3.6}$$

In all but two cases (ESO358-G006 and NGC 3585) these two conditions are met in the larger radii bins and the equation above is applied to the velocity and velocity dispersion determined using Equations 3.3 and 3.4. In the cases of ESO358-G006 and NGC 3585 the requirement that $V_\phi/\sigma_\phi > 2.5$ is relaxed to $V_\phi/\sigma_\phi > 1.5$, and the values of V_{max} determined for these two galaxies should therefore be considered as upper limits.

The quoted V_{max} for each galaxy is the mean circular velocity found in the regions that satisfy the above conditions, that the rotation curve be flat, and that $V_\phi/\sigma_\phi > 2.5$ (or 1.5). See Figure 3.14 for an example of the result of applying the described procedure in the case of NGC 3115. Table 3.3 presents the measured maximum circular velocity determined for each of the sample galaxies.

Determination of the S0 Tully-Fisher Relation

The final remaining quantities required to determine the TFR for S0 galaxies are the absolute magnitudes of the target galaxies. In this case the B-band magnitudes from the RC3 catalog (de Vaucouleurs et al., 1991) have been chosen, as any offsets in zeropoint between the TFR for spirals and S0s which are due to variations in age are likely to be maximised for bluer wavebands, which are dominated by the light of younger stars. Therefore the B_T magnitudes from the RC3 catalog for each sample galaxy have been corrected for galactic extinction using the extinction maps of Schlegel et al. (1998), then

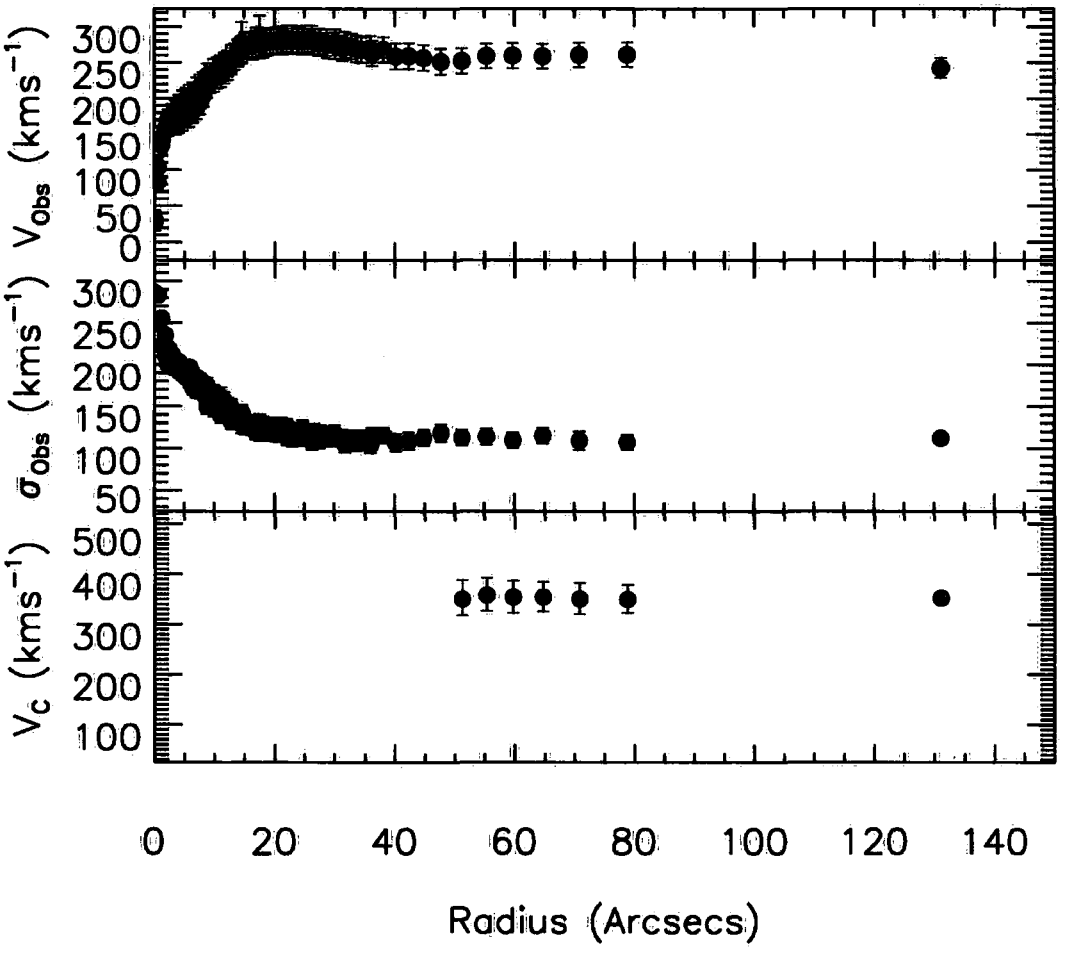

Figure 3.14: **Top Panel** : Observed rotation curve (V_{obs}) for NGC 3115. **Middle Panel** : Velocity Dispersion Curve for NGC 3115. **Bottom Panel** : Circular velocity (V_c) determined after carrying out the procedure outlined previously to correct for integration along the line of sight and asymmetric drift. The determined maximum circular velocity is the mean of the 7 points displayed, each of which satisfy the conditions of being located in a region which is on the flat part of the rotation curve and where $V_\phi/\sigma_\phi > 2.5$.

Table 3.3: Tully Fisher Parameters of Sample Galaxies

Galaxy	B_T (Mag)	A_B Extinction (Mag)	m-M (Mag)	V_{max} kms^{-1}
NGC148	13.13±0.13	0.07	31.56±0.15	227.5±16.0
NGC1023	10.35±0.06	0.26	30.29±0.16	279.8±25.0
NGC1380	10.87±0.10	0.08	31.23±0.18	305.7±23.2
ESO358G006	13.92±0.14	0.04	31.35±0.32	125.6±48.0
NGC1527	11.74±0.13	0.05	31.28±0.22	255.3±23.1
NGC1596	12.10±0.13	0.04	30.92±0.16	235.2±17.8
NGC3098	12.89±0.17	0.16	31.91±0.15	201.1±25.0
NGC3115	9.87±0.04	0.20	29.93±0.09	353.1±29.6
NGC3301	12.31±0.13	0.10	31.89±0.15	191.4±28.5
NGC3585	10.88±0.13	0.28	31.51±0.18	366.5±13.4
NGC4179	11.91±0.13	0.14	32.03±0.15	255.5±22.6
NGC4281	12.25±0.09	0.09	31.94±0.28	339.5±29.0
NGC4762	11.12±0.07	0.09	30.17±0.30	219.8±18.1
NGC5854	12.71±0.15	0.23	32.36±0.15	184.4±15.2
NGC5864	12.77±0.12	0.20	32.51±0.15	194.1±28.7
NGC6725	12.19±0.14	0.29	33.62±0.15	297.8±20.1
NGC7041	12.09±0.13	0.17	32.03±0.15	334.5±28.5
NGC7332	12.02±0.13	0.16	31.81±0.20	214.4±7.9

Notes: B_T from RC3 catalog (de Vaucouleurs et al., 1991). Extinction from NED, calculated from the work of Schlegel et al. (1998). Distance moduli from various sources listed in Table 3.1. Maximum rotation velocties determined from the kinematics presented in Section 3.4.1 using the procedure outlined in Section 3.4.2.

converted into absolute magnitude using the distance moduli provided in Table 3.1. No correction is made for the extinction due to dust internal to the sample galaxies, as the amount of dust found in S0 galaxies is generally thought to be small. Figure 3.15 displays the resulting S0 TFR for the sample galaxies, as well as other S0 galaxies examined by Bedregal et al. (2006a), Neistein et al. (1999), Mathieu et al. (2002) and Hinz et al. (2001, 2003).

To the sample of 18 edge-on S0s presented here an additional 5 galaxies from the sample of Bedregal et al. (2006a) are added. These galaxies help to constrain the faint end of the TFR. These 5 galaxies from Bedregal et al. (2006a) are NGC 1375, NGC 1380A, NGC 1381, IC 1963 and ES0358-G059. In the case of the two galaxies which overlap with the sample presented here (NGC1380 and ES0358-G006), the measurements made here are preferred. In any case the differences between the values of V_{max} determined here for NGC 1380 and ES0358-G006 and those determined by Bedregal et al. (2006a) are in excellent agreement (see Figure 3.15). Other data sets used in the study by Bedregal et al. (2006a) are omitted from the TFR determination made here due to the uncertainty in the homogeneity of the samples and methods of V_{max} determination. They are however displayed in Figure 3.15 for illustrative purposes.

With a combined sample of 23 galaxies, each of which displays considerable uncertainty in the measured V_{max} it is impractical to attempt to constrain both the slope and intercept of the TFR. Therefore following the approach of Bedregal et al. (2006a) the slope of the S0 TFR is fixed to match that found for local spiral galaxies by Tully & Pierce (2000) and Sakai et al. (2000). As the slope is fixed the usual debate inherent in studies of the TFR (see for example Willick (1994)), that between fitting in the forward direction (rotation velocity is a predictor of absolute magnitude) or inverse (absolute magnitude is a predictor of rotation velocity) is moot, as all that is being fit is a single zero point offset. Nevertheless in this case the inverse method outlined by Bedregal et al. (2006a) is used as this allows a direct comparison between the two studies and additionally allows an estimate of the intrinsic scatter in the S0 TFR. To this end the following inverse TFR was fit:

$$\log(V_{max}) = a + bM_B \tag{3.7}$$

where b is set to be equal to the inverse of the spiral galaxy TFR slope quoted in Tully & Pierce (2000) (1/-7.27) or Sakai et al. (2000) (1/-7.97). The constant a is then varied to

determine the least squares fit between the data and Equation 3.7, with each data point weighted by the following function:

$$w_i = \frac{1}{\sigma_i^2} \tag{3.8}$$

where

$$\sigma_i^2 = \sigma^2_{\log(V_{max}),i} + b^2\sigma^2_{M_B,i} + \sigma^2_{int} \tag{3.9}$$

The term σ^2_{int} allows the quantification of the intrinsic level of scatter found in the S0 TFR, that is any source of scatter not directly attributable to measurement error. The simplest method to determine σ^2_{int} is simply to iterate Equation 3.7 for varying values of σ^2_{int} until the reduced χ^2 of the fit approaches 1, which is the approach used here.

The result of this procedure is that the B-band S0 TFR for the 23 galaxies included here is found to display an offset from the spiral TFR of :

$$\Delta M_B = -1.92 \pm 0.15 \tag{3.10}$$

for the Tully & Pierce (2000) slope, and an offset of:

$$\Delta M_B = -1.50 \pm 0.16 \tag{3.11}$$

for the Sakai et al. (2000) slope (in neither case is the uncertainty in the spiral zeropoint included in the offset error) .

These values are very similar (but slightly larger) than the values found by Bedregal et al. (2006a) for their larger, but less homogeneous sample (it included a total of 60 galaxies from 6 different studies), where they determined offsets of -1.7±0.4 and -1.3±0.1 for the Tully & Pierce (2000) and Sakai et al. (2000) slopes, respectively. This slight difference can be understood through an examination of Figure 3.15, where it becomes clear that in the enlarged sample used in Bedregal et al. (2006a) there are several galaxies which lie much closer to the spiral TFR than any galaxies found in the current sample. It is difficult to tell at present if these galaxies are outliers in the S0 TFR or merely misidentified spiral galaxies, although of the 9 galaxies closest to the spiral relation, 3 are classed as Sa or later

by the HyperLeda catalog and would therefore not have been accepted by the selection criteria for the S0 sample presented in the present work. Several others galaxies which appear close to the spiral TFR display evidence for complicated morphologies, such as dust lanes misaligned with either axis or disturbed outer halos, perhaps indicating that they are not the fully relaxed disc systems they are believed to be.

The investigation of the magnitude of the intrinsic scatter of the S0 TFR also produced a result consistent with that found by Bedregal et al. (2006a), with the total scatter found to be 0.86±0.13 mag of which 0.70±0.13 mag is the result of intrinsic scatter within the relation, for the case of the Tully & Pierce (2000) slope. This is to be compared with values of 0.88±0.06 mag and 0.78±0.06 mag found by Bedregal et al. (2006a) for the same fixed slope. In the case of the Sakai et al. (2000) slope the total scatter was found to be 0.75±0.15 mag with an intrinsic component of 0.70±0.15 mag. In either case the overwhelming component of the observed scatter in the S0 TFR is found to be intrinsic to the sample. The implications of this finding shall be discussed in more detail in Section 3.5.

3.4.3 Emission Line Kinematics

As discussed in Section 3.3.4, the GANDALF code was used to measure emission line kinematics for the target galaxy spectra. The results of this procedure are that 13 of the 18 target galaxies are found to have some level of emission in the O[III] feature. In this case a galaxy was determined to display O[III] emission if more than 5 of the individual S/N=100 spectra were found by GANDALF to display O[III] emission with amplitude over noise of greater than 3. This fraction of S0s with measurable emission lines (72%) is slightly less than the 83% found by the SAURON team for their sample of 24 S0s (Sarzi et al., 2006), or the 85% found by Macchetto et al. (1996) for their optical imaging survey. The reasons for this difference in measured fraction of S0s displaying emission are likely to include the differences in sensitivity and set-up and potentially more interesting, differences in the samples observed.

Of the 13 galaxies with measurable gas kinematics, 4 are observed to display complex or counter-rotating kinematics (NGC 1596, NGC 3301, NGC 5854 and NGC 7332), several others display evidence for misalignments between the stellar rotation axis and that of the gas. The remaining galaxies appear to display gas kinematics which broadly match those of the stellar component of the galaxies or which have too few measured points to draw firm conclusions. Figure 3.16 demonstrates the correspondence between the O[III]

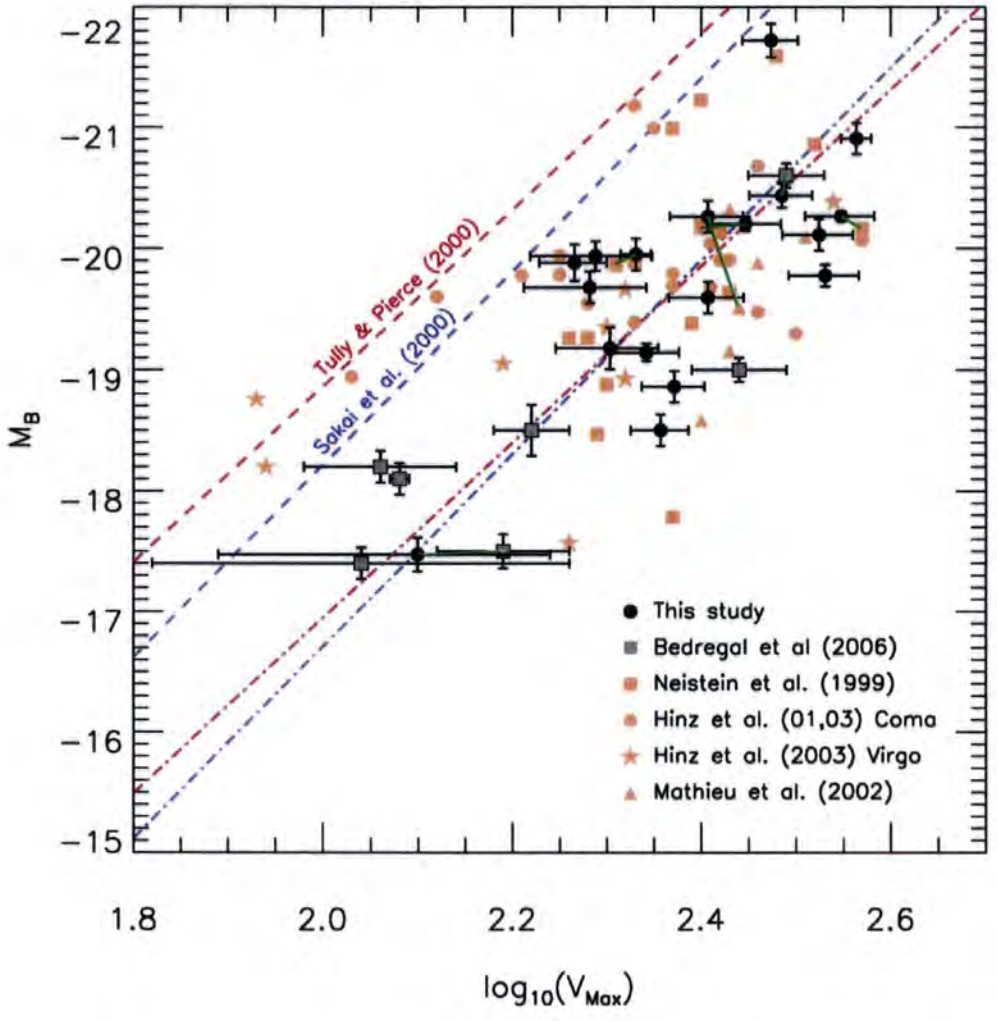

Figure 3.15: The B-band Tully Fisher relation for S0 galaxies. Galaxies investigated in this study appear as filled black circles, grey squares denote objects from the Virgo cluster sample of Bedregal et al. (2006a), objects from other studies are plotted as orange symbols for illustrative purposes. The indicated red and blue dashed lines are the Tully Fisher relations found for spiral galaxies by Tully & Pierce (2000) and Sakai et al. (2000) respectively. The red and blue dot-dash lines demonstrate the position of the best fit Tully-Fisher relation for the combined sample of galaxies examined here plus those of Bedregal et al. (2006a), assuming that the gradient is the same as that found by Tully & Pierce (2000) or Sakai et al. (2000) for the spiral TFR. Green lines join two different determinations of the properties for the same galaxy.

kinematics measured here (red line) and those determined by Falcón-Barroso et al. (2004) (blue circles). As can be seen the agreement between the gas kinematics measured here and by Falcón-Barroso et al. (2004) is excellent, with the complex counter rotating nature of the gas kinematics clearly evident.

It is tempting to ascribe the more complex and counter rotating gas kinematics to be due to gas which has recently been accreted. In the case of NGC 1596, this in fact is strongly indicated to be the case by Chung et al. (2006), with gas from the companion galaxy NGC 1602 currently being seen to be spread into two tidal tails, one of which crosses NGC 1596. NGC 7332 may present a similar case with gas being stripped from its gas rich companion NGC 7339, though at present the evidence for this is less convincing than in the case of NGC 1596, as a cloud of HI has been detected between the two galaxies (Morganti et al., 2006), but not a complete bridge as in the case of the NGC 1596-NGC 1602 pair.

Those galaxies which appear to show regular gas rotation are typified by galaxies such as NGC 1380. In this case gas rotates in the same direction as the stellar component and with similar mean velocity but as expected reaches the circular velocity more rapidly (see Figure 3.17) as it does not suffer the effects of asymmetric drift. In the case of NGC 1380 it appears likely that this observed emission-line gas is associated with the dust lane visible along the galaxies major axis, as dust in early types is usually associated with gas emission (e.g. Tran et al. (2001)).

3.4.4 Absorption-Line Strengths

The study of the line strength indices, and through them the age, metallicity and α-element enhancement of the stellar populations of S0 galaxies has been the major aim of this study from its inception. A thorough description of the results of this investigation is a subject for a Thesis in itself and at this point only a broad overview of the preliminary results can be given, in part because the complex spectral bulge-to-disc decompositions necessary to fully comprehend these systems have not yet been completed. Therefore what follows is best appreciated as a first-order approximation of the behaviour of the different components of S0 galaxies, with the implicit understanding that the stellar populations derived are often the combination of two (or more) very different populations (generally bulge and disc). An in-depth description of the effect on measured line strengths and implied stellar population parameters of combining different stellar popu-

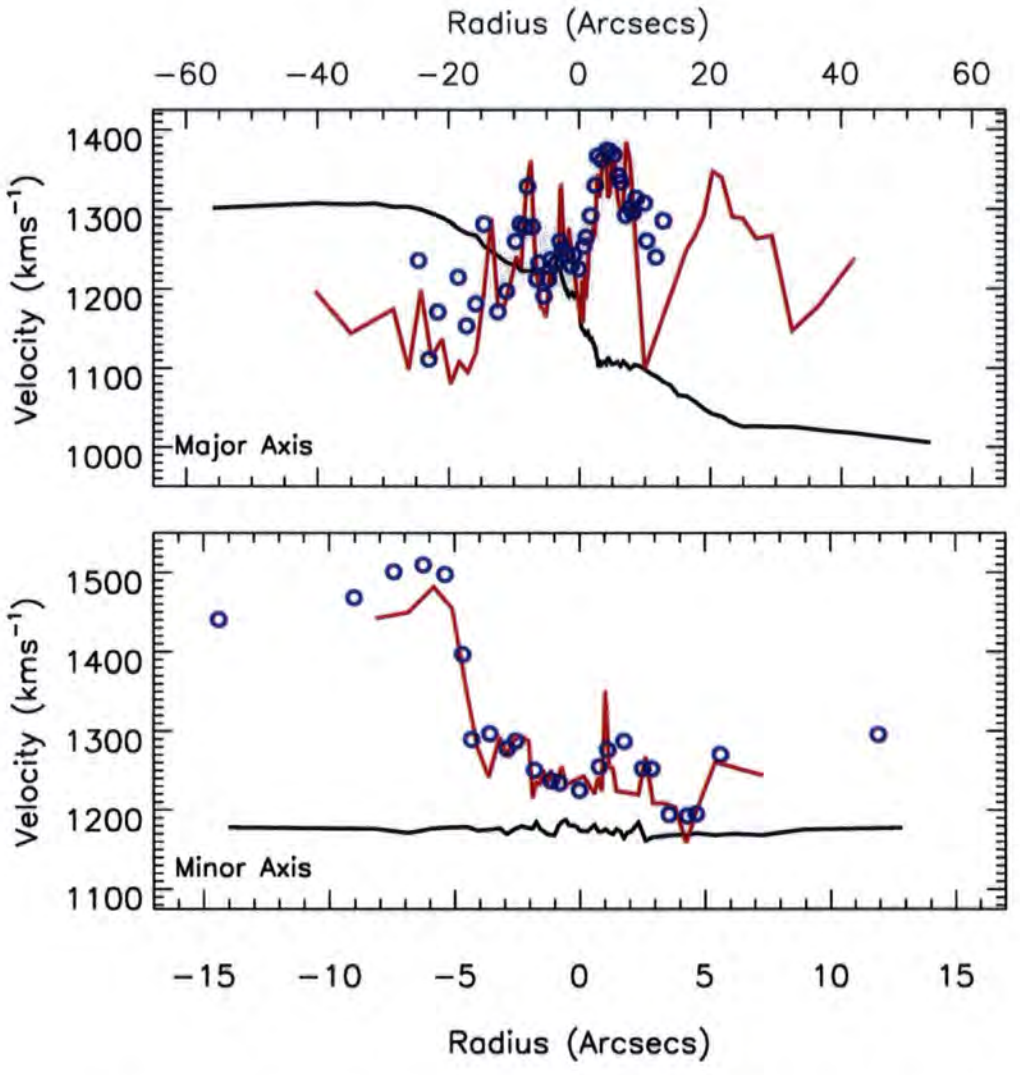

Figure 3.16: Emission-line kinematics for the major (top) and minor (bottom) axes of NGC 7332. The black line shows the stellar rotation curve for this galaxy. The red line is the O[III] emission line rotation curve measured here. The blue circles are the O[III] rotation curve from the SAURON project (Falcón-Barroso et al., 2004).

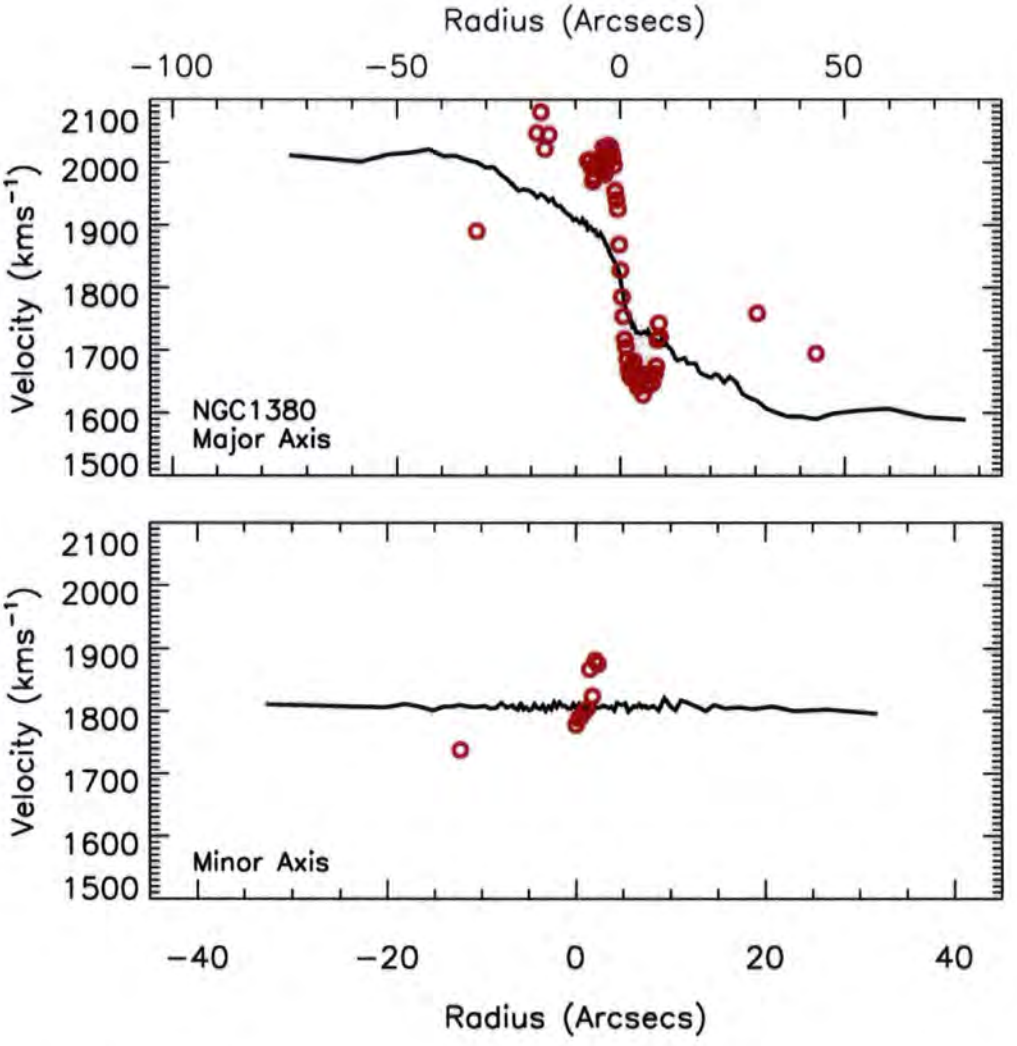

Figure 3.17: Emission line kinematics for the major (top) and minor (bottom) axes of NGC 1380. The black line shows the stellar rotation curve for this galaxy. The red circles are the O[III] emission line rotation curve measured here.

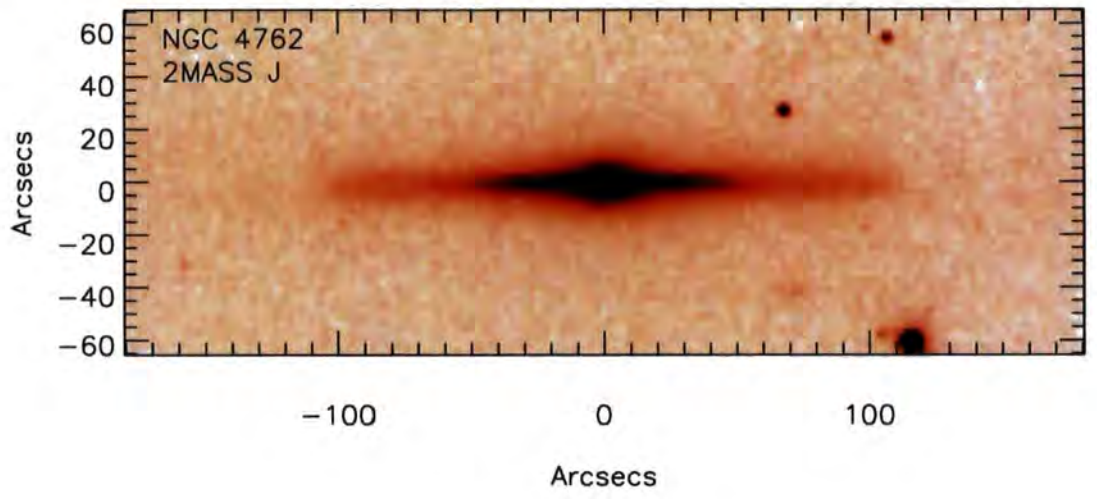

Figure 3.18: 2MASS J-Band Image of NGC 4762.

lations can be found in Serra & Trager (2007).

Therefore to simplify matters it is useful to consider in detail a subset of the sample galaxies which illuminate properties of the larger sample, and to study these galaxies carefully in those regions where one component strongly dominates over the other. By considering the sample galaxies in this way the behaviour of the line-strength indices of the galaxies can be seen to fall into two clear groups. The first group of galaxies can immediately be seen to display gradients in line-strength indices which differ significantly from major to minor axis, in the sense that the major axes at larger radii (where the light contributed by the bulge component is negligible) is significantly more metal rich, generally younger, and often displays lower [α/Fe] than the minor axis. The second class of galaxies display line-strength indices which appear to be very similar on both major and minor axes.

Type 1 - NGC 4762

The archetype of the first group of galaxies is NGC 4762. As Figure 3.18 demonstrates this galaxy is extremely disc dominated, especially at larger radii on the major axis. Ignoring for the present the fact that the disc component is potentially composed of both thick and thin components it is possible to make significant headway towards understanding the formation of this galaxy by studying the major (disc) and minor axis (bulge) line strength indices.

As the right-hand panels of Figure 3.19 demonstrate, the behaviour of the major and

minor axis line strengths are quite different. Initially, within the first 4-5 arcseconds the major and minor-axes present very similar iron, magnesium and hydrogen-sensitive line strengths. This can be understood as being due to the bulge component dominating the light within this region. Beyond around 4-5 arcseconds however, the major axis iron and magnesium-sensitive indices tend to remain fairly constant whilst the minor axis indices drop off in a manner similar to that seen typically in Elliptical galaxies. There is also a region on the major axis between 5 and 10 arcseconds where the line strengths drop slightly before increasing again. This region can be understood as being the region where the bulge contributes a minor but non-negligible fraction of the light (the bulge R_e is around 11 arcseconds). Beyond around 10 arcseconds the major axis light is totally dominated by the luminosity of the disc. Similarly beyond 2-3 arcseconds the minor axis appears to be clear of the influence of any disc material. The left hand panels of Figure 3.19 are similar to those presented for NGC 3115 in Figure 2.9 and in this case similar inferences can be drawn. Firstly, the top-left figure demonstrates as was the case in NGC 3115, that the major axis displays an α-enhancement closer to solar than the minor axis. Secondly the lower-left figure demonstrates that the major axis at larger radii appears to be younger than the minor axis, though in this case care must be taken due to the fact that the model grids plotted are for the case of [α/Fe]=0.3 and are therefore most applicable to the minor axis data. The model grids will move significantly if a value of [α/Fe] is chosen to match that of the major axis.

In order to learn more about this galaxy it is possible to carry out χ^2 minimisation of the measured line strengths with model SSPs like that used in Section 2.5.1 for the study of NGC 3115. In this example a reduced set of 8 indices (Hγ_A, Hδ_A, Fe4383, Fe5015, Mgb, Fe5270, Fe5335 and Fe5406) has been used. This selection of Lick/IDS indices avoids indices which have problems such as regions affected by CCD problems (Hβ) or mismatches with the data and the SSP models (typically C or N-sensitive indices). As in Chapter 2 the SSP models of Thomas et al. (2003, 2004) are utilised in the χ^2 minimisation procedure. Figure 3.20 displays the radial behaviour of the measured stellar population parameters. One warning is that within around 2 arcseconds the data becomes unreliable due to the effects of the seeing becoming important, and in particular the possible variation in seeing between different exposures.

As can be seen in Figure 3.20 the broad outlines drawn from the behaviour of the individual line strengths has been confirmed, with the disc of NGC 4762 being considerably

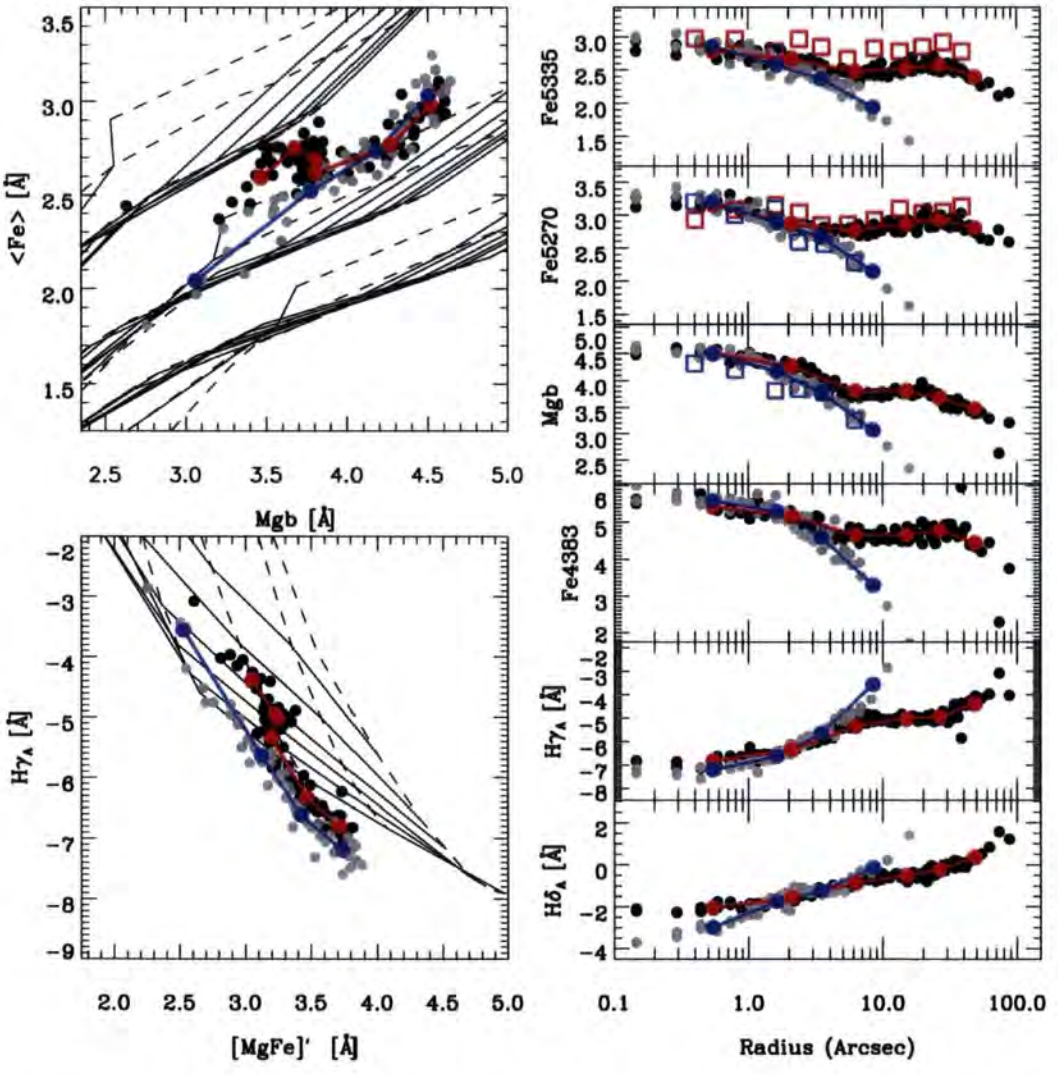

Figure 3.19: **Top Left** : Mg*b* vs. <Fe> diagnostic plot for the major (black circles) and minor (grey circles) of NGC 4762, the red and blue circles are the binned data points for the major and minor axes respectively. This figure is analogous to that discussed in Section 2.5.1 for the case of NGC 3115. **Bottom Left** : Age-metallicity diagnostic plots for major and minor axis data, in this case the model grid is for Thomas et al. (2003, 2004) models with α/Fe = 0.3, a value only strictly applicable for the largest radii minor axis data points. Symbols are as previously defined. **Right** : Radial index gradients for the major and minor axis of NGC 4762, unfilled squares are data from Fisher et al. (1996), overplotted for comparison.

younger (3-4 Gyr) when compared to the bulge of the galaxy (~9-11Gyr). The major axis also displays evidence of a gradient in age, in the sense that the larger radii data is considerably younger than the inner regions. This again is probably best understood as due to the fact that within the inner 10 arcseconds the bulge still provides a non-negligible fraction of the light and hence skews the measured age towards the 9-11 Gyr seen in the bulge. Although it should be noted that in their Lick line strength study of edge-on disk galaxies Yoachim & Dalcanton (2008) found that the dominant thin disk components displayed strong radial age gradients, with the outer regions younger than 1 Gyr. To be certain whether the gradient seen in age along the major axis is due to superposition of the two components (disc and bluge), or due to some intrinsic gradient in the disc population, or even some combination of the two, requires more complex bulge-to-disc decomposition than is possible in this current work.

Outside of the inner 2 arcseconds the minor axis of NGC 4762 displays a metallicity gradient of $\Delta\log([Z/H])/\Delta\log(r) = -0.55$, which is consistent with the steepest metallicity gradients found by Sánchez-Blázquez et al. (2007) for their sample of 11 early-type galaxies. In contrast, the major axis displays a positive metallicity gradient initially, which as explained can be understood as being due to the decreasing influence of the bulge component. After this point the metallicity remains fairly constant with radius, until the very largest radii where some evidence of a decrease in metallicity is visible. The formal metallicity gradient for the major axis, ignoring the slight variations if extremely close to zero, $\Delta\log([Z/H])/\Delta\log(r) = 0.01$. Little evidence for gradients in $[\alpha/Fe]$ is seen, with the possible caveat that the major axis at larger radii, may display $[\alpha/Fe]$ marginally closer to solar, than that displayed by the minor axis.

NGC 4762 is therefore an example of a galaxy which neatly fits the expected behaviour of a spiral galaxy which has been transformed into an S0 by the truncation of star formation. The cause of the transformation is difficult to determine. However the fact that the two components appear so regular, with little evidence of significant mixing (in particular for the minor axis which displays a very steep metallicity gradient) strongly points to the fact that whatever the process was it cannot have been very traumatic. In particular a recent significant merger event could not produce the galaxy as currently observed, as major mergers lead to significant mixing of components which would tend to weaken the metallicity gradient of the bulge, and also to reduce the measured age of the bulge component, through the addition of other most likely younger more metal rich

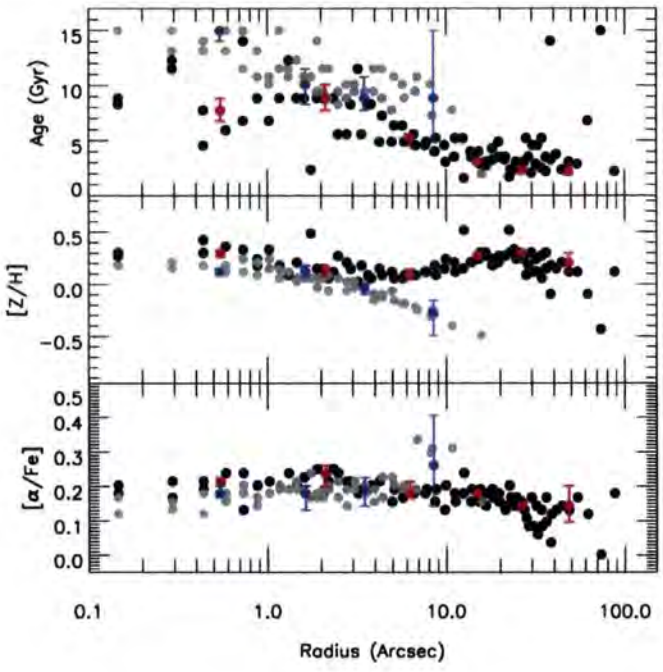

Figure 3.20: Radial profiles of age, metallicity and α-element enhancement determined for NGC 4762 major and minor axes using the χ^2 fitting procedure outlined in Sections 2.5.1 and 3.4.4.

disc material. It would seem that the conversion of NGC 4762 from a sprial to an S0 is most likely to have been accomplished by ram-pressure stripping during the infall of NGC 4762 into the higher-density environment of the Virgo cluster.

Type 1 - NGC 3585

NGC 3585 provides another example of a galaxy displaying similar behaviour to that seen in NGC 4762, this is despite the fact that NGC 3585 contains at least 3 components. As Figure 3.21 shows the best fit model of NGC 3585 comprises three components, a large Sérsic halo, an inner Sérsic bulge and an exponential disc. In this sense NGC 3585 is similar to NGC 3115, with its disc being embedded within a larger spheroidal halo, the main difference in the two cases being the relative influence of the disc component, with the disc of NGC 3585 providing a significantly smaller fraction of the total luminosity than the disc of NGC 3115.

Despite the added complexity due to the addition of an extra component the behaviour of the line strength indices of this galaxy is fairly similar to that of NGC 4762. As Figures 3.22 and 3.23 demonstrate the iron and magnesium-sensitive indices are again

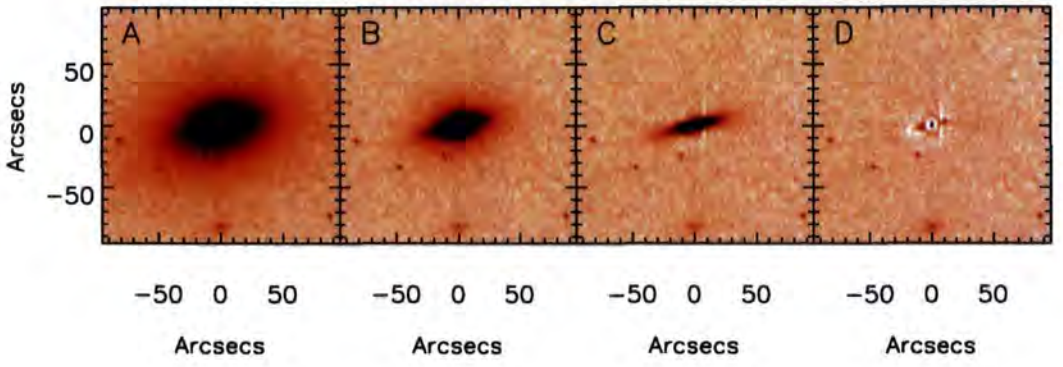

Figure 3.21: **Panel A** : 2MASS J band image of NGC 3585. **Panel B** : Image A after subtraction of best fit large spheroidal halo component. **Panel C** : Image A after subtraction of best fit large spheroidal halo component and inner Sérsic bulge. **Panel D** : Image A after subtraction of best fit large spheroidal halo component, inner Sérsic bulge and exponential disc model.

found to be stronger on the major axis. The magnitude of the metallicity offset is smaller than that seen in NGC 4762, most likely because of the large halo component which reduces the measured disc metallicity from the true value. Despite this effect the gradient in metallicity on the minor axis of $\Delta\log([Z/H])/\Delta\log(r)$=-0.44 is still considerably steeper than that seen on the major axis of $\Delta\log([Z/H])/\Delta\log(r)$=-0.28. Only a complete bulge-to-disc decomposition can determine the true disc metallicity in this case. The offsets in age and $[\alpha/Fe]$ are similarly smaller than those seen in NGC 4762, also presumably due to the existence of the extra stellar component present to large radii in this case.

In the case of this galaxy it is difficult to draw firm conclusions about the processes involved in its formation before the stellar populations of the 3 components are fully separated. However one potential explanation for the formation of this galaxy would be in a major merger event which produced the large scale spheroidal population, with the smaller embedded disc and central bulge forming later from gas settling onto a plane.

Type 2 - NGC 3098

The second common type of behaviour seen in the stellar populations of the sample galaxies is typified by NGC 3098. This is a disc dominated galaxy with a clearly boxy bulge, as seen in Figure 3.24. In this case the gradients in line strengths appear to be consistent for both the major and minor axes (See Figure 3.25). This agreement is also seen in

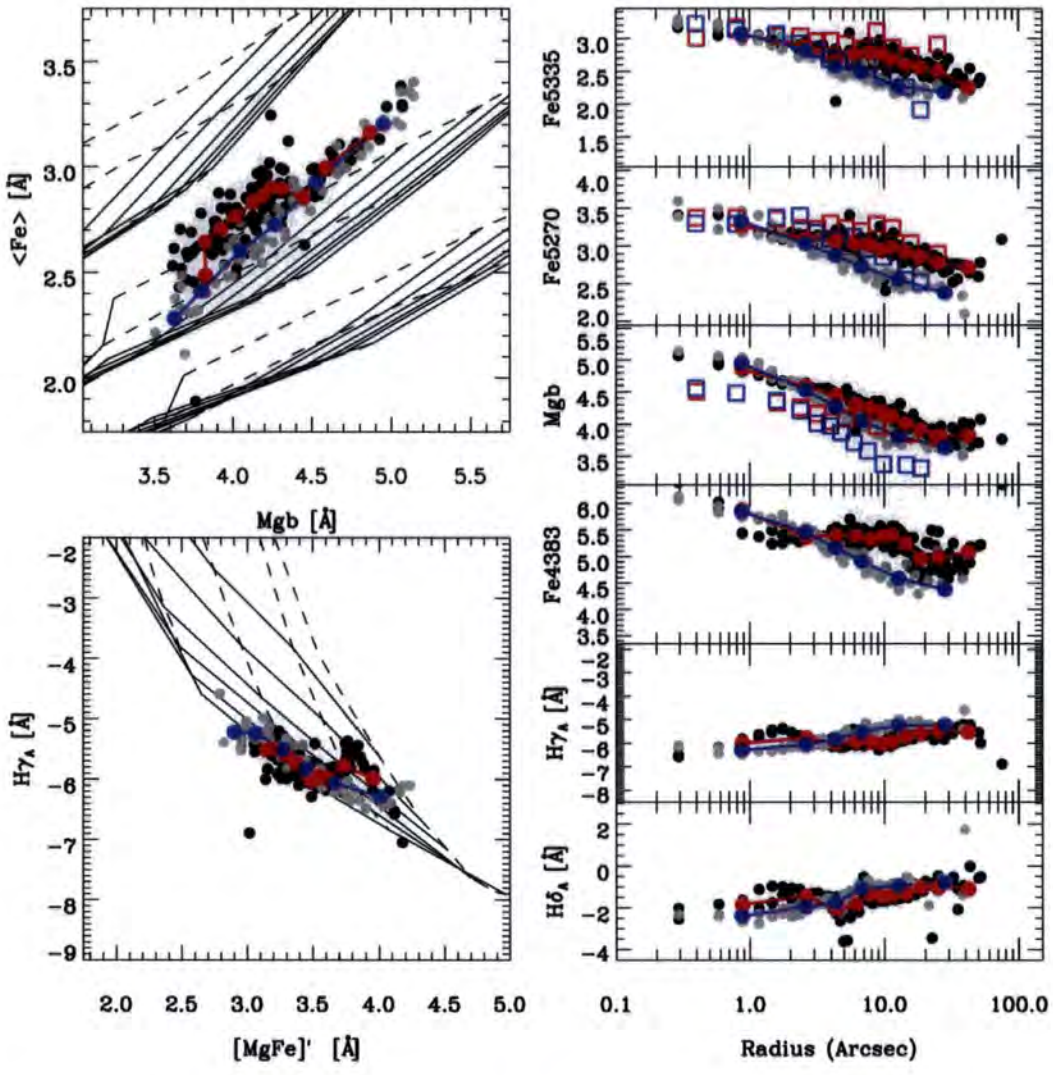

Figure 3.22: **Top Left** : Mg*b* vs. <Fe> diagnostic plot for the major (black circles) and minor (grey circles) of NGC 3585, the red and blue circles are the binned data points for the major and minor axes respectively. **Bottom Left** : Age-metallicity diagnostic plots for major and minor axis data, in this case the model grid is for Thomas et al. (2003, 2004) models with α/Fe = 0.3, a value only strictly applicable for the largest radii minor axis data points. Symbols are as previously defined. **Right** : Radial index gradients for the major and minor axis of NGC 3585, unfilled squares are data from Fisher et al. (1996), overplotted for comparison. The relatively large differences between the Fisher et al. (1996) data and those presented here can mostly be attributed to the large LOSVD corrections necessary for this galaxy, corrections which were not available for the earlier Fisher et al. (1996) work.

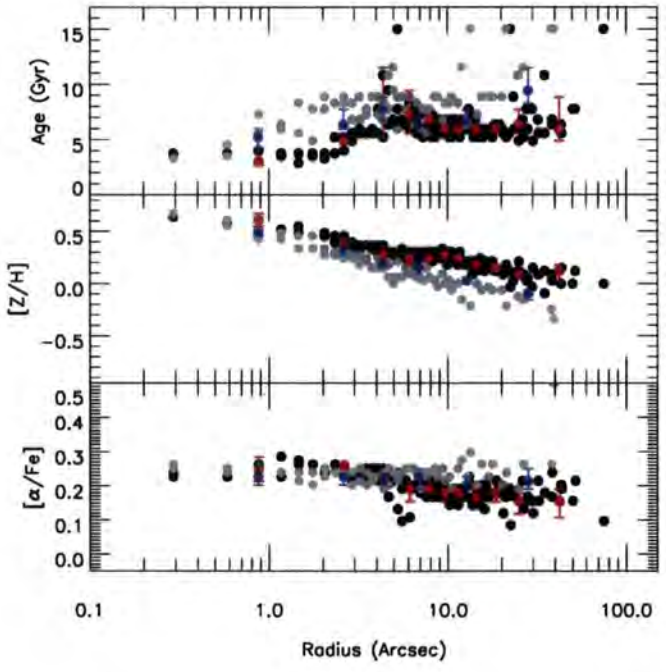

Figure 3.23: Radial profiles of age, metallicity and α-element enhancement determined for NGC 3585 major and minor axes using the χ^2 fitting procedure outlined in Sections 2.5.1 and 3.4.4.

the stellar population parameters derived using the χ^2 minimisation procedure (Figure 3.26), where in age (with large scatter), metallicity and α-element enhancement the major and minor axes agree remarkably well. There appear to be two plausible explanations for this behaviour, either the minor axis data does not extend to sufficiently large radii to begin to see the region where differences begin to be significant, given the low surface brightness these observations probe to however this seems unlikely. More interesting is the possibility that in this case the major and minor axes are simply populated by the same stellar populations. In the latter explanation the bulge of this galaxy would be a pseudo-bulge, produced by secular evolution of a bar component, and composed of stars from the disc of the galaxy. If this interpretation is correct, the conversion of this galaxy from a spiral to an S0 could possibly be ascribed to the same process which produces the prominent pseudo-bulge, bar instability leading to star formation and the evacuation or conversion of all of the gas of the galaxy. As this galaxy is not located in a high density region, ram pressure stripping is not a plausible mechanism for removing the cold gas reservoir, leaving a mechanism intrinsic to the galaxy itself the most likely explanation, in this case that the galaxy has simply depleted its supply of gas.

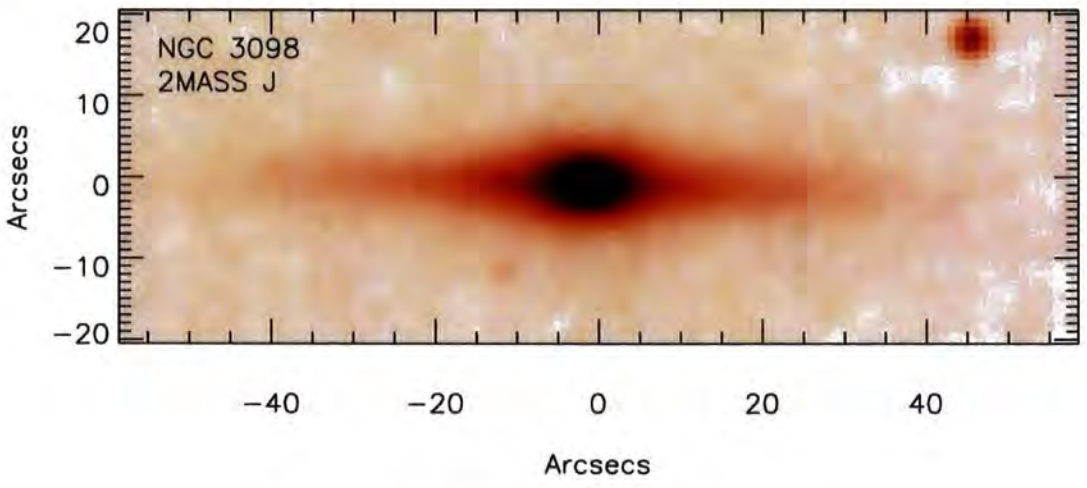

Figure 3.24: 2MASS J-Band Image of NGC 3098.

Of the 15 sample galaxies which have both major-and-minor axis spectroscopy, 8 can be classed as having type-1 behaviour (major and minor axes display significantly different stellar populations at the largest radii examined), 5 galaxies are seen to display type 2 behaviour (major and minor axis appear to have similar stellar populations), and two are difficult to classify at present due to the small spatial extent of the data. Only with the completion of the full bulge-to-disc decompositions will it be possible to determine complete formation histories for all of the sample galaxies.

3.5. Discussion

This chapter has presented preliminary results from a large spectroscopic and imaging survey of nearby S0 galaxies. 18 galaxies have been observed spectroscopically to date, 15 of which have deep spectroscopy of both major and minor axes. Taken together this sample comprises the largest deep survey of the stellar populations and kinematics of S0 galaxies to date.

An examination of the kinematics of the major axes of this sample of galaxies reveals that all 18 display regular disc-like rotation, which in all cases is probed to sufficiently large radii to reach the flat part of the rotation curve. A more detailed examination of the kinematics of these galaxies reveals that a significant fraction display some evidence for kinematic substructure within their inner regions, whether due to inner discs or bars. All galaxies (except ESO358-G006 where σ cannot be measured) contain bulge-like structures

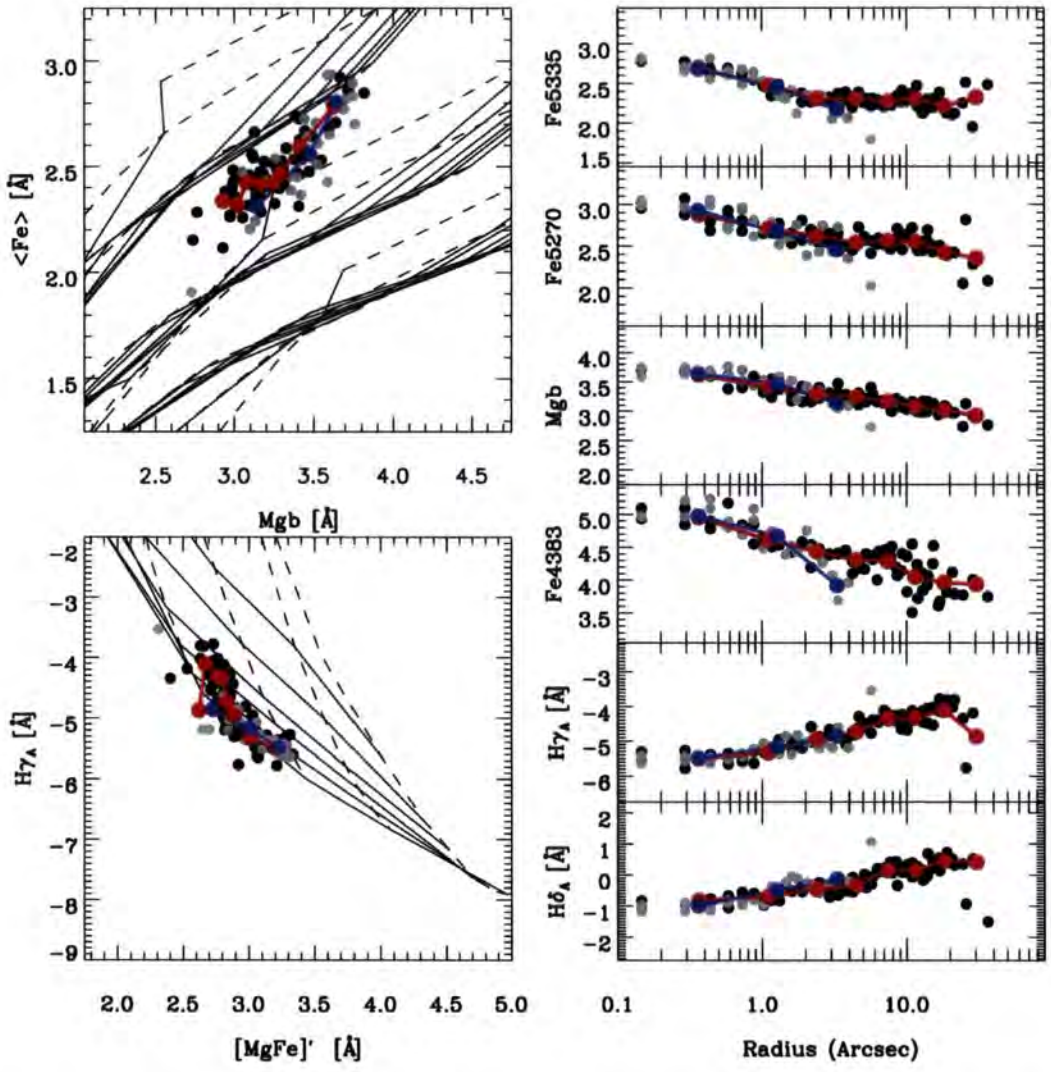

Figure 3.25: **Top Left** : Mg*b* vs. <Fe> diagnostic plot for the major (black circles) and minor (grey circles) of NGC 3098, the red and blue circles are the binned data points for the major and minor axes respectively. **Bottom Left** : Age-metallicity diagnostic plots for major and minor axis data, in this case the model grid is for Thomas et al. (2003, 2004) models with α/Fe = 0.3, a value only strictly applicable for the largest radii minor axis data points. Symbols are as previously defined. **Right** : Radial index gradients for the major and minor axis of NGC 3098.

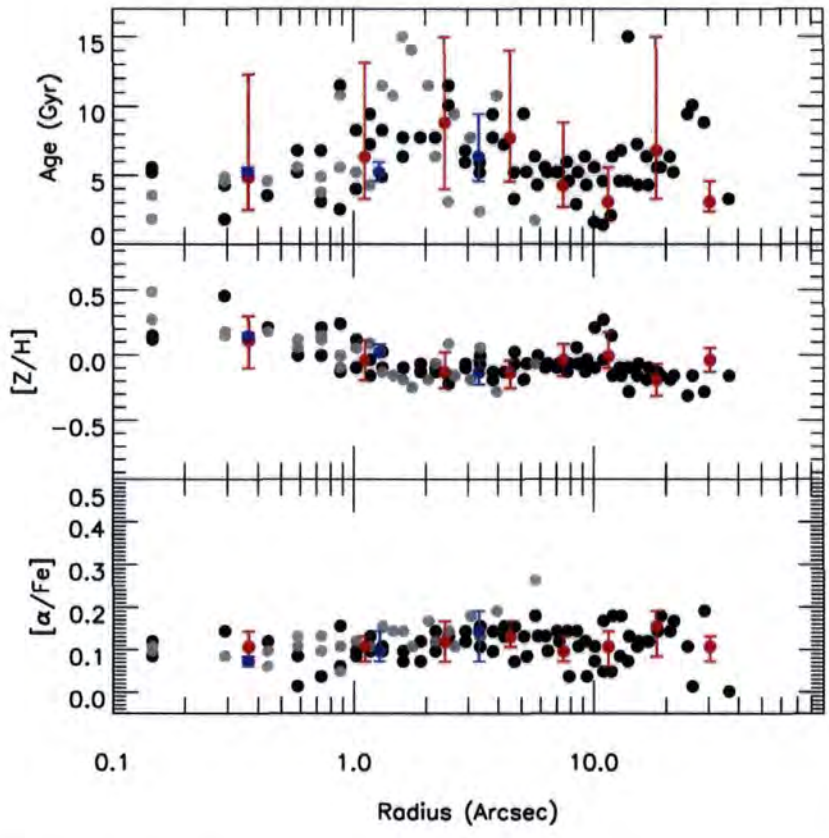

Figure 3.26: Radial profiles of age, metallicity and α-element enhancement determined for NGC 3098's major and minor axes using the χ^2 fitting procedure outlined in Sections 2.5.1 and 3.4.4.

which exhibit enhanced velocity dispersions relative to the regions around them, hence none of these galaxies provide analogues to the population of almost bulgeless spirals seen in the nearby Universe. Whether this means that such bulgeless spirals do not become S0's, or that in the process of converting to S0's they gain a bulge is difficult to tell at present, another possibility is simply that the selection of the sample is biased against such objects which even if they had ceased forming stars may not be classified as S0s. The deep i band imaging of the target galaxies reveals that all 18 galaxies are close to edge-on. However 6 are sufficiently inclined that spiral structure is unambiguously observed in unsharp mask images of the galaxies (ESO358-G006, NGC 1527, NGC 3301, NGC 5854, NGC 5864, NGC 6725). Other galaxies exhibit different structures commonly found in S0s such as lenses, or rings. Work to be carried out in the future will utilise the i band imaging to carry out a systematic examination of the different components found in these S0 galaxies; for the present work however lower S/N 2MASS J-band imaging has been used to determine coarse bulge and disc parameters. These disc parameters have been used in combination with the kinematic data to determine rotation curves corrected for inclination, integration along the line of sight and asymmetric drift. These rotation curves have then been utilised to determine the offset of the Tully-Fisher relation for S0 galaxies (for this sample + 5 additional galaxies from the study of Bedregal et al. (2006a)) from that of the TFR of spiral galaxies, assuming that the slope of the S0 TFR is the same as that for the spiral relation. The result of this procedure is the offset between the TFR for S0s and spirals is found to be ΔM_B = -1.92±0.15 assuming the spiral TF slope of Tully & Pierce (2000), this value is entirely consistent with that found by Bedregal et al. (2006a) (ΔM_B = -1.7±0.4) using a larger (60 galaxies) but much less homogeneous (combined from 6 different studies) sample of S0s. Similarly the scatter in the S0 TF relation determined here is found to be consistent with that found by Bedregal et al. (2006a). Most interestingly, the magnitude of the scatter is dominated by factors not directly attributable to measurement errors, with 0.7±0.13 mag of the total 0.86±0.13 mag scatter being attributed to intrinsic scatter.

The commonly accepted explanation for the observed offset between spiral and S0 TF relations is simply that S0s are spirals in which star formation has ceased, leaving the galaxy disc to fade with time as the younger more luminous stars die. At present it is unclear whether the usual objection to this picture, that S0s are bulge dominated is in fact correct (see the earlier discussion in Section 3.2), but even if it indeed proves to be

the case, it is possible that during the transformation event a significant amount of star formation could occur in the inner regions leading to a build up of bulge luminosity. In this picture the scatter in the S0 TF can simply be understood as being due to the fact that different galaxies will undergo the transformation process at different times, and hence will have faded by differing amounts by the present. Additional scatter can be introduced by the behaviour of the bulges of the galaxies, with some galaxies displaying classical old bulges at the time of transformation, and others younger pseudo-bulges, in either case the addition of a final gasp (or later burst caused by infalling material) of star formation in the form of a central starburst can also complicate the analysis.

In order to determine whether such a picture has merit, it is possible to search for correlations between parameters such as the age of the S0 discs and bulges and the corresponding offset from the spiral TF relation. In order to do this average stellar populations for the bulge and disc components must be determined. The bulge stellar population was calculated using the χ^2 method described previously, the input Lick indices were the error-weighted average of the measured major axis indices within $R_e/8$ (where R_e is the effective radius determined for the bulge component in the exponential disc + Sérsic bulge models described previously). This restricted choice of radii ensures that the disc component does not contribute significantly to the determined bulge stellar population. Similarly the disc stellar populations were determined using the χ^2 method on the weighted average of the major axis line strengths measured outside of $1R_e$, ensuring that the disc component dominates the luminosity in the region used to determine disc stellar populations. This method of course neglects many complicating factors, for example gradients in the stellar population parameters of the individual components (especially the disc), but to first order it provides a reasonable approximation of the average behaviour of the two components.

Figure 3.27 demonstrates the result of plotting the measured SSP age of the S0s discs and bulges against the measured offset from the spiral TFR. As can be seen, a correlation between disc age and the offset from the Spiral TFR is readily apparent. Following Bedregal et al. (2006a) it is found that the Spearman Rank Correlation test shows that this correlation is significant at the 99.6% level. This significance is significantly larger than the 85 to 90% found by Bedregal et al. (2006a) for their sample of 9 galaxies (the range depends on which combination of indices were used to determine the stellar population ages). The reasons for such a difference are not immediately apparent but may in part

be due to the larger sample size and higher-S/N data available in this sample relative to that available to Bedregal et al. (2006a). The correlation between bulge age and TFR offset is somewhat less significant at 95.5%, a number which agrees well with the range found by Bedregal et al. (2006a) of between 90% and 97.5%. However the strength of the correlation can be strongly affected by one or two objects, as an example if NGC 4281 is removed from the analysis (the upper left point in the right panel of Figure 3.27) the bulge age-offset correlation increases to above 99% significance, clearly then further work remains to be done before this correlation can be trusted. The strongly significant correlation between disc (and to some extent bulge age) and observed offset from the spiral TFR is even more remarkable when the many sources of possible error are considered. For example the derivation of the ages of stellar populations using line strength indices generally leads to uncertainties of the 1-2 Gyr level, which is highly significant for younger populations. The derivation of the measured TFR offset itself is also of course beset with problems due to difficulties such as measuring accurately the maximal rotation velocity of galaxies without significant gas emission. Hence the strength and sense of the observed correlation is compelling evidence that the overall picture of S0 galaxies being the descendants of normal star-forming galaxies is correct.

In order to confirm that disc (and some degree of bulge) fading can explain most of the observed offset in the S0 TFR a simple model was produced. This model differs somewhat from those which are generally used in such a study, for example in the case of Bedregal et al. (2006a) who produce a model of a spiral galaxy which displays a constant star formation rate of 1 $M_{\odot}yr^{-1}$ for 5 Gyr then ceases star formation. The observed decrease in luminosity can then be matched to the observed offset in the TF relations to determine the epoch at which the galaxy ceased forming stars. Additional components such as bulges, with or without starbursts at various epochs, can then be added to help match the observed offsets. In this study a method which acts in the reverse direction is utilised to produce a very simple model of the evolution of S0 galaxies. In this case the data on the actual present-day S0s is evolved backwards to see if they become consistent with the spiral TF relation at some point in the past. Instead of fading, the galaxies are brightened. To build these simple models several assumptions must be made: first that the SSPs describing the stellar populations of the bulge and disc at the present time are representative of an average population in those two components and will not be strongly affected by a small number of unusual stellar types, and secondly that the same

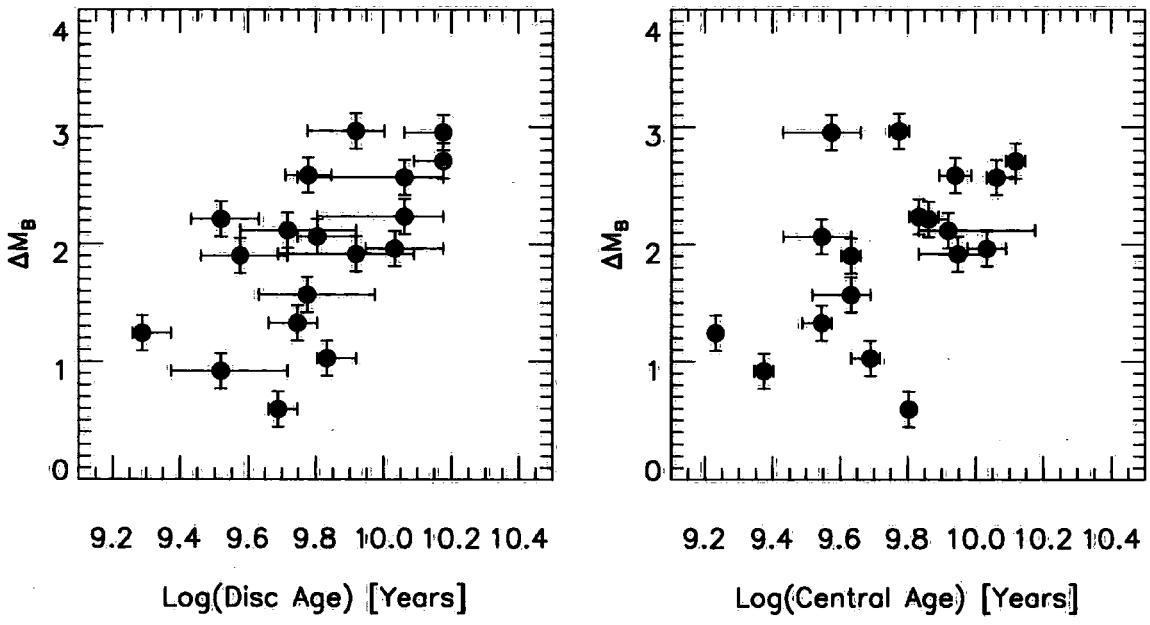

Figure 3.27: **Left Panel** : The Tully Fisher offset, ΔM_B versus the age of the disc. **Right Panel** : The Tully Fisher offset, ΔM_B versus the age of the centre (bulges) of the galaxies ($R_e/8$).

case applies to a theoretical spiral galaxy SSP. The method utilised to build the models is straightforward:

1. The SSP ages and metallicities determined for each component are used to determine the appropriate integrated magnitude per unit stellar mass for that component as seen today using the models of Maraston (1998, 2005). These models are essentially the integrated magnitude version of the Lick index models (Thomas et al., 2003, 2004) utilised to determine the ages and metallicities of the disc and bulges. Hence using them keeps the choice of model SSPs consistent.

2. The luminosity of each component is then weighted by the bulge to disc ratio determined in the simple exponential disc + Sérsic bulge model determination. When combined a total luminosity per unit mass for the model galaxy as observed now is determined.

3. The disc is regressed in age until it is 1 Gyr old. This number is the number assumed to represent the mean SSP age of a star-forming spiral which is likely to be located on the spiral TF relation and is similar to that observed for the thin discs of edge-on disc galaxies by Yoachim & Dalcanton (2008). The appropriate M/L ratio (absolute

magnitude per unit stellar mass) for the disc of this age, with the same metallicity as seen currently is then determined, again from the models of Maraston (1998, 2005).

4. The bulge is regressed by the same duration and the absolute magnitude per unit stellar mass of bulge material of that age and metallicity determined from the models. The luminosity of the bulge and disc are again weighted by the bulge-to-disc ratio before being added to produce the total magnitude of the object as it would appear with a disc of 1 Gyr in age and the equivalent younger bulge. In cases where the bulge is younger than the disc, the bulge is fixed at 1 Gyr old.

5. The change is magnitude between the galaxy as observed and the galaxy as it would appear when its disc had a mean age of 1 Gyr can then be computed.

6. The procedure was repeated for assumed spiral SSP ages of 0.5 Gyr and 2 Gyr.

In Figure 3.28 the results of this simple model are presented, in terms of a Tully-Fisher relation for the model galaxies as they would appear when their discs had SSP ages of 1 Gyr (filled black squares). The grey squares with the error bars denote the galaxies as currently observed. The grey filled and unfilled circles demonstrate the positions of the galaxies if they were observed when their discs were 0.5 and 2 Gyr old respectively. As the figure demonstrates, despite the no doubt simplistic nature of this model and the sources of error involved it is entirely plausible that the S0 galaxies observed in this study are the ancestors of normal spiral galaxies which ceased star formation several Gyr ago.

Further preliminary work has indicated that the J, H and K_S S0 TFR also display significant offsets from the local spiral relations of the order of 1 mag. It is however more difficult to produce similar models utilising these NIR bands. This is principally because the integrated magnitude in the B-band is highly dominated by the youngest stellar populations, whereas in the case of the NIR bands the integrated effect of older stellar populations are non-negligible. Therefore models which attempt to explain the NIR S0 TFR would require more sophisticated star formation histories.

3.5.1 Future Work

The rich (and currently incomplete) data-set presented here presents many opportunities for further work. Of particular interest is a more comprehensive study of the stellar populations of the sample galaxies. An important goal will be to make use of the high-S/N i-band imaging to attempt to tie structural components and deviations from the

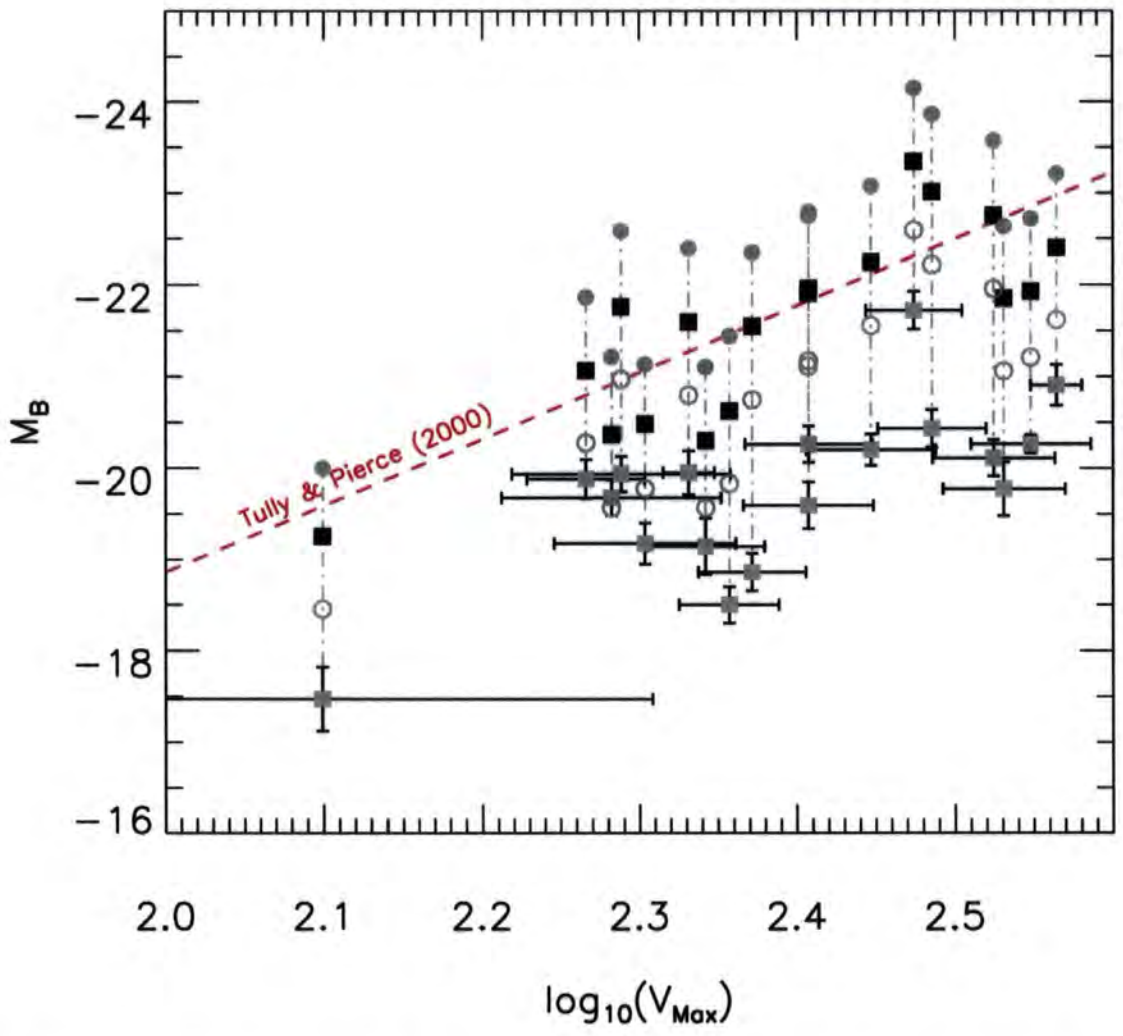

Figure 3.28: Results of the simple disc fading model. Grey squares show the 18 S0 galaxies examined here as currently observed. Filled black squares show the galaxies as they would appear assuming the discs of the galaxies had an SSP age of 1 Gyr, unfilled grey circles show the same but for SSP age of 2 Gyr, and the filled grey circles have SSP age 0.5 Gyr. The dashed red line represents the local spiral Tully Fisher relation found by Tully & Pierce (2000).

simple bulge + disc models to the observed kinematic and stellar population substructures (c.f. the observations of NGC 3115 in Chapter 2). Studying such peculiarities in the stellar populations and kinematics can do much to constrain the importance of events such as mergers or gas accretion on the formation histories of S0 galaxies. An interesting question that may be answered by such an investigation includes whether or not the kinematic substructure seen in the inner regions of many of the S0 galaxies in this sample was produced at the same time as the process which converted the galaxy from a spiral to an S0. More in-depth bulge-to-disc decompositions and potentially more complicated stellar population models can also be applied to the data to allow the determination of more detailed star-formation histories.

The extension of the simple model of disc fading presented here to include more realistic star-formation histories and galaxy behaviour could potentially be very useful. With a more realistic model and a better understanding of the uncertainties involved, together with a larger sample of S0 galaxies, it would be possible to search for evidence of evolution in the slope or zero-point of the spiral S0 relation with time, something which is extremely difficult through simply measuring the TF relation to higher z due to observational difficulties. This analysis would be predicated on the assumption that galaxies seen as S0s today were representative of the spiral population when they evolved off the spiral TF relation, and also that on average no significant perturbing effects (such as minor mergers or gas accretion) have occurred to one population and not the other since that point

Another interesting area of research that can be aided by the present data-set is the study of the environmental dependence of S0 properties. In the most common explanation for the truncation of star formation in S0 galaxies, the star formation ceases because gas is stripped from the galaxy by ram-pressure stripping as the galaxy passes through a hot intracluster medium (Gunn & Gott, 1972; Abadi et al., 1999; Bekki et al., 2002; McCarthy et al., 2008). This explanation works well for cluster or group galaxies but cannot explain the formation of field S0s, since in this case there is no hot gas with which to strip the cold gas of the galaxy. It may therefore be that field S0s form through a different process to group or cluster S0s, a difference that may lead to observable differences in physical properties of the galaxies. Through the examination of the larger complete sample it may be possible to determine if such trends with environment exist.

3.6. Conclusions

This Chapter has presented the main preliminary results from a large survey investigating the kinematics and stellar populations of nearby edge-on S0 galaxies. The main conclusions are:

1. All 18 galaxies display regular disc-like kinematics. Some display kinematic substructure indicative of minor accretion events.

2. 72% of the sample galaxies display some level of ionised gas emission.

3. The behaviour of the stellar populations of the sample S0s in all but two cases can be described in simplistic terms as consisting of two components, a bulge and disc. The bulge may be of old classical type or a younger pseudobulge. In the former case the gradients in age and metallicity of the major and minor (disc and bulge) axes varies greatly, with the disc component displaying constant or slowly decreasing metallicity, occasionally with a decreasing age at larger radii. The bulge components in this case display gradients in metallicity similar to those seen in elliptical galaxies. In the latter case both disc and bulge display shallower metallicity gradients which are consistent within a particular galaxy.

4. The offset of the S0 TFR from that of spiral galaxies is found to be ΔM_B = -1.92±0.15 mag when assuming the spiral TF slope of Tully & Pierce (2000), with a scatter of 0.86±0.13 mag, most of this scatter (0.7 mag) is found to be intrinsic and not due to observational error. These findings are in good agreement with those of Bedregal et al. (2006a).

5. The simplest interpretation of these observations is that S0 galaxies comprise a class of objects which are generally (some galaxies display peculiarities which require further study, such as massive stellar halos) the result of the truncation of star formation in ordinary spiral galaxies. This truncation process cannot be particularly traumatic as the resultant S0 galaxies still retain much of the kinematics and structure of their parent galaxies, including regular disc kinematics and in at least some cases spiral structure. The large intrinsic scatter in the S0 TF relation can be understood as being due to the different times at which these galaxies ceased to form stars.

6. Future work with this data set will include more sophisticated analysis of the star formation histories of the individual galaxy components, more comprehensive modelling of the transformation of spirals to S0s and an analysis of the dependence of galaxy parameters on environment.

Chapter 4

Gemini/GMOS Spectroscopy of the Spheroid and Globular Cluster System of NGC 3923

4.1. Abstract

In this chapter a technique to extract ultra-deep diffuse-light spectra from the standard multi-object spectroscopic observations used to investigate extragalactic globular cluster (GC) systems is presented. This technique allows a clean extraction of the spectrum of the host galaxy diffuse light from the same slitlets as the GC targets. The utility of the method for investigating the kinematics and stellar populations of galaxies at radii much greater than usually probed in longslit studies, at no additional expense in terms of telescope time, is demonstrated. To demonstrate this technique Gemini/GMOS spectroscopy of 29 GCs associated with the elliptical galaxy NGC 3923 is examined. The measured stellar population parameters of the GC system and those of the spheroid of NGC 3923 at the same projected radii are compared. The GCs are found to have old ages $>$ 10 Gyr, [α/Fe]$\sim$0.3 and a range of metallicities running from [Z/H] = -1.8 to +0.35. The diffuse light of the galaxy is found to have ages, metallicities and [α/Fe] abundance ratios indistinguishable from those of the redder GCs.

4.2. Introduction

In recent years great strides have been made in the spectroscopic study of globular clusters (GCs), with large samples of spectroscopically determined ages, metallicities and α-element abundances being accumulated with the aim of using these data to infer star-formation histories for their host galaxies (Kissler-Patig et al., 1998; Kuntschner et al., 2002; Puzia et al., 2004, 2005; Strader et al., 2005; Pierce et al., 2006a,b; Cenarro et al., 2007; Strader et al., 2007). GCs are particularly suitable for this analysis because they can be assumed to be simple stellar populations (SSP) where all of their stars formed at one epoch from a single cloud of gas with an almost uniform metallicity. This makes them much simpler to model than the integrated stellar populations of the diffuse light of galaxies, where many star-formation events at different epochs greatly complicate analysis of the spectra.

The great promise of this approach to simplify the examination of the star-formation history of galaxies is however dependent on one critical assumption: that the stellar populations of GCs are somehow representative of the field stars that form the bulk of a galaxy's stellar population. This would occur naturally if GCs form with some fixed proportion to those stars that form (or eventually end up) in unbound star forming regions during a star-formation event and with similar element abundances. There are several observations that appear to bear out this assumption, including observations by Larsen & Richtler (2000) that show that the number of Young Massive Clusters (YMCs) correlates with the star-formation rate per unit area in the galaxies that host them. These YMCs are believed to be the low-redshift analogues to the star clusters that survived for a Hubble time to form the mostly old GC populations seen in galaxies today. The almost constant value observed for the number of GCs normalized to the total baryonic mass of a galaxy (McLaughlin, 1999) also provides strong support for the idea that GCs closely trace the major star-formation events of a galaxy.

A more direct way to approach this issue is to examine the ensemble parameters of large numbers of GCs and compare them with those measured for the host galaxies' diffuse stellar light. If the GCs do indeed act as a faithful tracer of the different star formation events in a galaxy's history, then the average GC stellar population should closely resemble that of the overall galaxy.

To date little work has been done in comparing the stellar population parameters

measured from line-index analyses for GCs with those determined for the host galaxy diffuse stellar component. Principally this is because at the galactocentric radii where the GCs selected for spectroscopic analysis are found, the surface brightness of the underlying galaxy halo light is very faint. In Chapter 2 the stellar populations along the major and minor axes of the isolated S0 galaxy NGC 3115 were compared to the stellar populations of the GC population of NGC 3115 taken from Kuntschner et al. (2002). For this galaxy it was found that the stellar population along the minor axis at $\sim 2R_e$, was indistinguishable from that of the more metal rich GCs in terms of age ($\sim$12 Gyr), [Z/H] ($\sim$-0.5 dex) and [α/Fe] ($\sim$0.3 dex). Furthermore, at larger radii along the minor axis the stellar population became more metal-poor, implying that if it were possible to observe the halo stellar population at even larger radii it may begin to resemble the more metal poor GCs. The existence of such a halo population with similar metallicities in both integrated light and GCs is interesting, as this is not what is observed in the MW, potentially indicating differences in formation routes for these galaxies. Nevertheless these results hint at a strong connection between the formation of the spheroid of NGC 3115 and its GC system.

Ideally this type of analysis would be repeated for many galaxies to see how universal this behaviour is. However the large additional burden of telescope time required for the longslit measurements on top of the long exposure times required for the Multi-Object Spectroscopy (MOS) GC investigations makes this approach impractical. In this chapter a new technique is presented which allows us to combine both parts of this type of study into one set of observations with no extra cost in terms of telescope time. As an additional benefit, this technique can also be used to extract kinematic parameters for the host galaxy at radii well beyond those commonly achieved for standard longslit studies.

To demonstrate this method the galaxy NGC 3923 is examined (see Table 4.1 for details), NGC 3923 is a large nearby (D $\sim$ 17.9 Mpc) elliptical galaxy with a prominent shell structure (Malin & Carter, 1983). NGC 3923 is the brightest galaxy of an average sized group with a low early-type fraction, perhaps suggesting that the group is dynamically young (Brough et al., 2006).

An HST ACS study of the GC system of NGC 3923 by Sikkema et al. (2006) confirmed previous observations (Zepf et al., 1994, 1995) that the GC system has a bimodal colour distribution and an unsually high specific frequency (S_N>5) for an early-type galaxy in a lower-density environment. Sikkema et al. (2006) searched for evidence of a GC sub-

population formed during the merger event thought to be responsible for the creation of the shell structures. They concluded that their photometric data did not support the presence of any younger GC population with ages similar to that of the shell structures, which they believe to have formed 0.8-1.2 Gyr ago. They did however find that the bimodal V-I colour distribution and radial density profiles of the blue and red GCs were typical for old GC systems in ellipticals. Sikkema et al. (2007) used the same HST ACS data to study the shell structures of NGC 3923 finding them to be similar in colour or slightly redder than the galaxy diffuse stellar light.

Other studies have examined the stellar population and kinematics of the central regions of NGC 3923. Thomas et al. (2005a) found the nuclear regions to have an age of 3.3 Gyr, [Z/H] = +0.62 and [α/Fe] = 0.31, while Denicoló et al. (2005) using a similar method found values of 2.6 Gyr, [Z/H] >0.67 and [α/Fe] = 0.14 respectively.

4.3. Observations and Data Reduction

Whilst a specific example using data obtained from the Gemini Multi Object Spectrograph (GMOS) instrument is presented here, the approach described should be equally applicable to similar MOS intruments such as FORS1/2 on the VLT or LRIS/DEIMOS on Keck. All observations were taken with the Gemini South-GMOS (Hook et al., 2004) as part of Gemini program GS-2004A-Q-9.

Pre-imaging of NGC 3923 for object selection was undertaken on 2004 January 19 and consisted of 4×200 seconds exposures in Sloan g′ and 4×100 seconds in r′ and i′ for each of 3 fields (one central, one SW and one NE of the galaxy centre). For a thorough discussion of the procedure used to reduce the pre-imaging and select GC candidates see Forbes et al. (2004) and Bridges et al. (2006). A full examination of the photometric properties of the GC system of NGC 3923 and other galaxies investigated in this project will be presented in a forthcoming paper by Faifer et al. (in prep).

GMOS Nod-and-Shuffle masks were produced for each of the three fields in addition to one MOS mask for the central pointing (see Figure 4.1). Since it is the MOS mask that provides the data described presently, any further discussion of the Nod-and-Shuffle masks and the kinematic investigation of NGC 3923 derived from them is left to Chapter 5.

The MOS mask consisted of 37 slitlets of width 1 arcsec by a minimum length of 4 arc-

Table 4.1: NGC 3923 Basic Parameters

Parameter	Value
Right Ascension (J2000)	$11^h51^m01.8^s$
Declination (J2000)	-28°48′22"
l	287.28°
b	32.22°
Morphological Type	E4
Magnitude	10.8 B mag
Major-Axis Diameter	5.9 arcmin
Minor-Axis Diameter	3.9 arcmin
Heliocentric Radial Velocity	1739 ± 9 kms^{-1}
J Half-Light Radius	43.8" †

Table data from NED:

http://nedwww.ipac.caltech.edu/

Except:

† 2 Micron All Sky Survey

www.ipac.caltech.edu/2mass/

sec. The mask was exposed using the B600_G5303 grism for 8×1800 seconds at a central wavelength of 500 nm and 8×1800 seconds at a central wavelength of 505 nm (to cover the CCD chip gaps), yielding 8 hours of on-source integration. The seeing ranged from 0.6 - 0.9 arcsec during the observations. Bias frames, flat fields and copper-argon (CuAr) arc spectra were observed throughout the observations as part of the Gemini baseline calibrations. The MOS spectra produced typically cover the wavelength range 3900-5500 Å although because the wavelength range depends on slit position, some spectra start at ~3500 Å while others end at ~7200 Å.

Data reduction of the MOS spectra through to the point of producing rectified and wavelength calibrated 2D spectra was accomplished utilising the Gemini/GMOS packages in IRAF as described in Bridges et al. (2006). From the CuAr arcs, wavelength calibrations with residuals ~0.1 Å were achieved. The extraction of the target GC spectra from each 2D spectrum was undertaken using the APALL task in the APEXTRACT package using an optimal (variance-weighted) extraction. Flux calibration was achieved using GMOS longslit observations of the flux standard star LTT3864 made during the same semester with identical observational set-up. The extraction of the NGC 3923 diffuse light spectra from the MOS slitlets was undertaken using a custom IDL script implementing the algorithm described below.

4.4. Method

Modern multi-object spectroscopic instruments such as GMOS are capable of taking spectra of around 40 objects simultaneously over fields of view of around 6×6 arcmin^2. Each MOS slitlet is typically around 1 arcsec wide by a few (4-10) arcsec long. Generally the GCs are unresolved from the ground, producing spectra smeared over ~1 arcsec (in the spatial direction) for typical seeing values. The rest of the slitlet collects background (sky + galaxy) photons used to background subtract the GC spectrum.

For the typical field of view of the current generation of MOS instruments and the distance and size of the target galaxies being investigated by these studies, it can be seen that significant amounts of target galaxy flux are contained in the MOS slitlets being used to study the GCs (See Figure 4.1). The flux incident on each slitlet can then be thought of as a sum of contributions from the target GC, the actual sky background (both atmospheric and extra-galactic) and a contribution from the diffuse light of the target

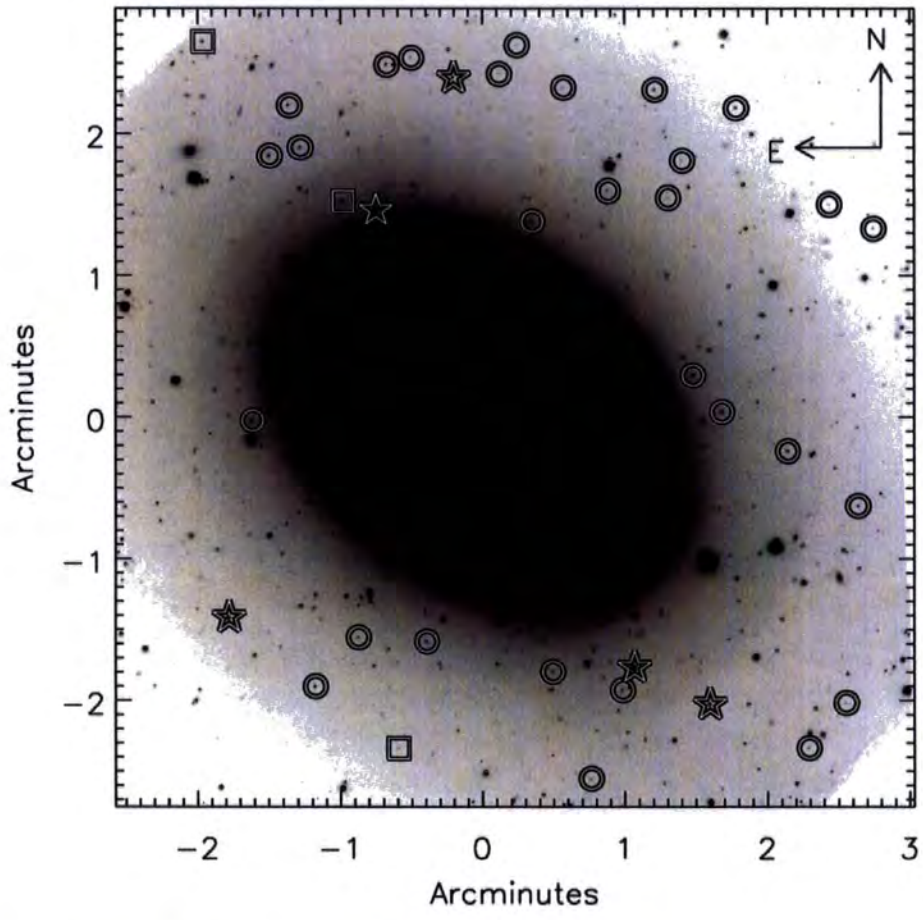

Figure 4.1: NGC 3923 GMOS i′ band image. Circles show the position of photometrically chosen targets later confirmed by spectrocopy to be GCs, asterisks show targets found to be Milky Way stars and squares are targets found to be background galaxies/QSOs. The problem of placing a slitlet at large enough galactocentric radii to produce an uncontaminated sky spectrum when using modern MOS instruments with fields of view around 6×6 arcmin^2 is apparent. Also visible are the shell structures of NGC 3923 on the major axis.

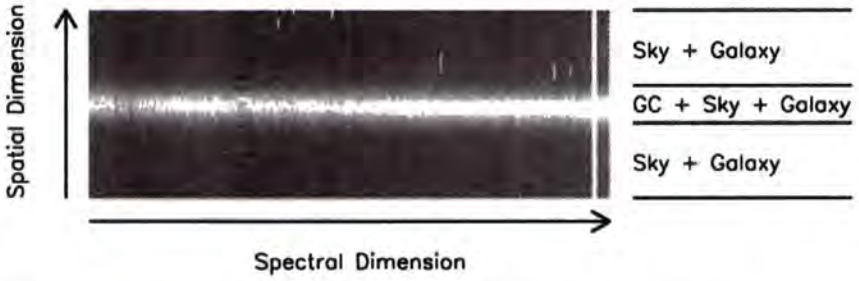

Figure 4.2: Example of a typical 2D MOS spectrum, showing target spectrum (in this case a GC spectrum) and sky regions typically used to sky subtract the target spectrum. For typical MOS GC studies these sky regions can contain useful amounts of host galaxy diffuse light.

galaxy. Figure 4.2 shows an example of a typical 2D MOS spectrum, showing the regions containing the different contributions to the flux. If the instrument has a sufficiently large field of view, it is possible to place a slitlet at large galactocentric radii where the spectrum measured would be essentially a pure sky spectrum, uncontaminated by galaxy flux. This sky spectrum could then be subtracted from the background regions of each of the GC slitlets to produce a sky-subtracted galaxy diffuse-light spectrum for each of the individual slitlets. This simplistic approach has successfully been applied in a study similar to this one involving the GC system of NGC 524, with experience showing that slitlets located beyond $5R_e$ provide an adequate sky spectrum.

In practice the field of view of the current generation of MOS instruments is often too small to allow a slitlet to be located at large enough galactocentric radii to produce a "pure" sky spectrum of the accuracy required (at least for stellar population studies). In cases such as the study of NGC 3923 the following algorithm can be applied to allow the calculation of the sky spectrum even in cases with small FOV, by combining the spectroscopic dataset with wider-field imaging data.

4.4.1 Algorithm

1. The spectra are reduced as normal to the point where the individual spectra are cut out, rectified and wavelength calibrated. See Bridges et al. (2006) for more details, but in brief the 2D spectra from GMOS are bias subtracted, flatfielded, the 3 CCDs mosaiced together and finally wavelength calibrated using the Gemini/GMOS **IRAF** package.

2. A sky + galaxy spectrum is produced for each slitlet. The spectra are produced using the usual method for calculating a sky spectrum from a 2D slitlet (i.e., the spectrum used to sky subtract a 2D frame). Figure 4.3 displays three such sky + galaxy spectra for a range of galactocentric radii; as is expected those spectra taken from slits which lie closer to the galaxy centre contain more flux.

3. Each spectrum is rebinned onto a uniform wavelength scale.

4. The wider-field pre-imaging is combined to produce a master wide-field image of the target galaxy. (In this case making use of the g′ band imaging as this best matches the wavelength coverage of the spectra, though it should be noted that if the i′ band imaging is used instead, the measured line indices differ by less than 0.1 Å. However care should be taken to ensure that the observed optical light profile being used should match that of the spectral region being examined, i.e., the use of an IR image to set the scaling for optical spectra is probably unwise because of the different photometric profiles displayed by galaxies in the different wavelength regimes.)

5. Using the master image of the field, the local background in an annulus around each of the target GCs is calculated.

6. The actual sky background number of counts in the image is measured for a region located at large galactocentric radii. Experience with the data for NGC 3923 showed that this value was always very similar to the local background measured for the GC with the largest galactocentric distance.

7. For each wavelength pixel of the rebinned spectra the number of counts is plotted against the local background around the corresponding object determined from the wide field image. (See Figure 4.3 for the pixels corresponding to 5100 Å). As can be seen in the lower panel of Figure 4.3 the correlation of local background with number of counts in the spectra is reasonably good. This correlation can then be fit with a simple straight line and extrapolated to the value calculated for the sky background at large radius from the wide field image. In the example in Figure 4.3 the value of the sky brightness measured at large radii to represent the uncontaminated sky value was around 1000 counts in the g′ band, leading to an estimate of the "pure" sky spectrum having around 32 counts in the pixel located at 5100 Å.

8. When repeated for each wavelength pixel, this procedure results in a spectrum that is a good approximation of a "pure" sky spectrum. Note that the produced sky spectrum is only accurate in the regions where a significant number of the spectra overlap in wavelength coverage. In the case of the example GMOS data this restricts the analysis of the galaxy spectra to the wavelength range 4400 - 5500 Å where the majority of the 37 input spectra have coverage.

9. Each of the 37 rebinned sky + galaxy spectra are then sky subtracted using the "pure" sky spectrum, leaving 37 spectra that are essentially pure galaxy spectra. The spectra measured from individual exposures can then be combined in the usual manner; examples of 3 of the spectra produced by combining 16 individual exposures can be seen in Figure 4.4.

In cases where wider-field imaging is not available it is possible to obtain similar results using an iterative procedure. In this case an initial guess for the sky brightness assumed to represent pure night sky is made (by extrapolating the observed galaxy profile for instance) and the entire procedure from steps 6 to 8 can then be iterated with the assumed night sky brightness being varied until sky line residuals in the final diffuse-light spectra are minimised.

4.4.2 Kinematics

GC radial velocities were measured using the FXCOR task in the RV package of IRAF. Radial velocity standard stars were not observed as part of this investigation due to the extra overhead in observing time this requires. Spectra from the simple stellar population library of Vazdekis (1999) are therefore used as templates. These templates span a range of age of 1-18 Gyr and a metallicity range from [Fe/H] = +0.2 to -0.7. To this sample an additional 6 stellar spectra from the Jones (1997) library were added to extend the metallicitiy range covered by the templates to [Fe/H] < -1.5. This wide range of age and metallicity helps to minimise the effects of template mismatch on the measured velocities. A 3-σ clipped mean of the velocities derived from these templates is used as the final velocity for each GC. The errors are estimated from the mean of the errors measured by FXCOR for those velocities not removed by the clipping procedure.

Objects with velocities in the range 1200-2400kms^{-1} are assumed to be associated

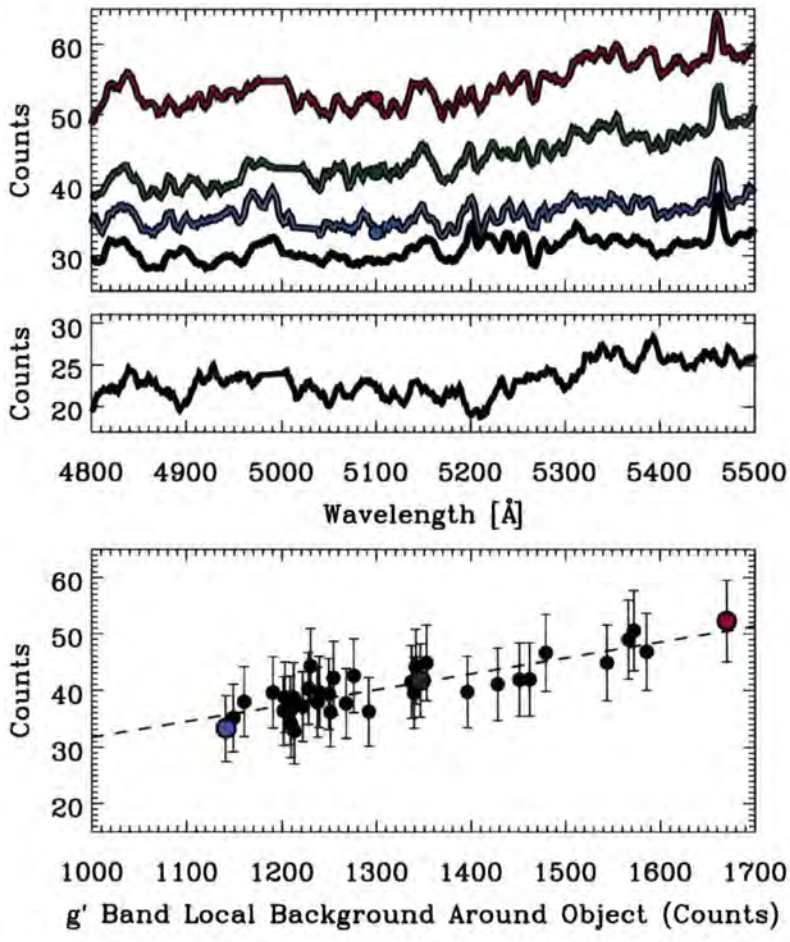

Figure 4.3: **Upper Panel** : Upper three spectra are the "sky + galaxy" spectra extracted from slits covering the range of galactocentric radii covered in this study. The fourth spectrum (black line) shows the extrapolated "pure" sky spectrum using the algorithm described in the text. **Mid Panel** : This spectrum is the result of subtracting the extrapolated sky spectrum from the uppermost "sky + galaxy" spectrum. Redshifted (z=0.006) absorption lines due to Hβ, Mgb, Fe5270 and Fe5335 are clearly visible. **Lower Panel** : A typical result of the extrapolation process used to determine the actual pure sky spectrum in this case for the pixel located at 5100 Å. The position of the 3 points from panel A is also displayed here for instructive purposes, as are the measured number of counts and statistical error at this pixel for the other 34 slitlets (black circles) in this mask.

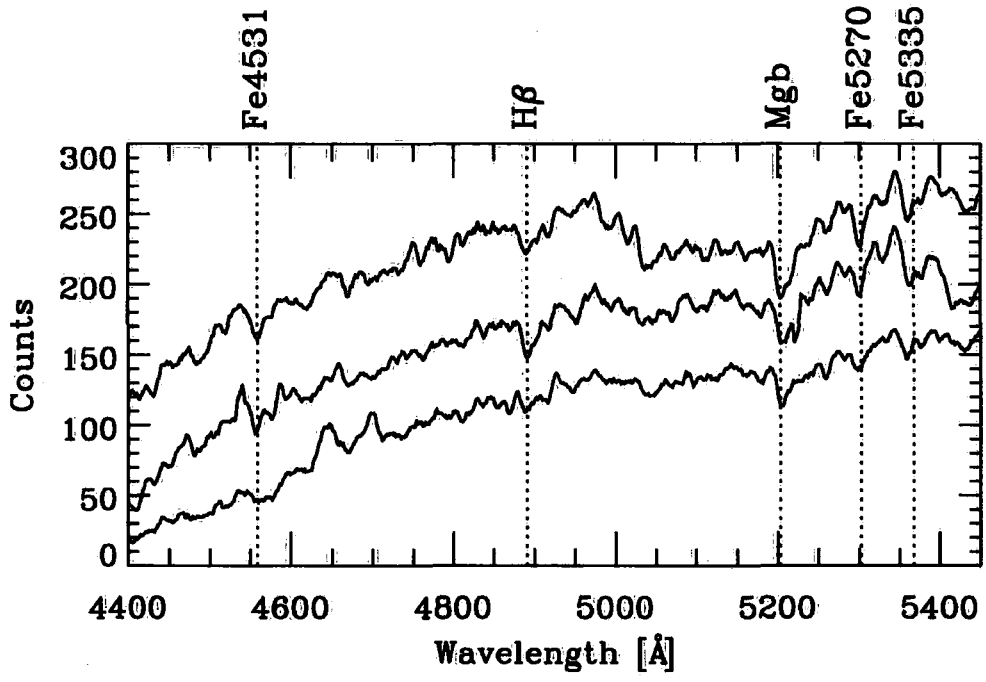

Figure 4.4: Representative diffuse-light spectra for NGC 3923 measured using our new technique from three different MOS slitlets, and hence different galactocentric radii. These spectra are the results of coadding 16 individual exposures, they have been smoothed to the Lick/IDS resolution. Redshifted (z=0.006) absorption lines due to several species are present.

with NGC 3923 and were classified as GCs. 29 out of 37 (78%) objects observed with the MOS mask have velocities within this range. Of the remaining objects, 2 were z~0.3 galaxies, one was a z~1.3 quasar and 5 were Milky Way stars.

The recessional velocities of the NGC 3923 diffuse-light spectra were measured using the publicly available IDL implementation of the pPXF method (Cappellari & Emsellem, 2004). This method was chosen as it allows a simultaneous measurement of the radial velocity and velocity dispersion from the spectrum, both of which are important in studies of the diffuse light of galaxies. In this instance the spectra were fit in pixel space over the wavelength range 4800-5400 Å using the same templates as the GCs. The final velocity and velocity dispersion for each slitlet is taken to be the mean of the velocities/velocity dispersions determined from 100 Monte-Carlo re-simulations of the input spectra with added photon noise. The error in the measured velocity is taken to be the dispersion in the 100 best fit velocities. As a check of consistency the recessional velocity of the diffuse light spectra was remeasured using the FXCOR task in IRAF and no significant differences between the two methods were observed.

4.4.3 Line Indices

By binning all 37 diffuse light spectra together a single spectrum of sufficient signal-to-noise (S/N > 60 per Å) to measure accurate absorption-line indices was produced. Since NGC 3923 shows evidence of slight rotation (Figure 4.5) it is necessary to remove the effects of rotation on the spectra by correcting the spectra to some common velocity before coadding them. In this instance the velocity of each of the 37 spectra was measured as described previously, then using the DOPCOR task in IRAF each of the spectra was de-redshifted to zero redshift before combining.

For ease of comparison with other studies the stellar populations are examined using the Lick/IDS system. As described in Chapters 2 & 3 there are several steps that must be taken to ensure that measured indices are securely on the Lick/IDS system (Worthey & Ottaviani, 1997; Trager et al., 1998). The first is to convolve the spectra with a wavelength-dependent Gaussian kernel to reproduce the variable Lick/IDS resolution of 9-11 Å. Then the Lick/IDS indices are measured from the flux-calibrated spectra using the wavelength definitions from Worthey & Ottaviani (1997), Trager et al. (1998) and the

INDEXF index measuring code of N Cardiel[1]. Uncertainties on the measured indices are a combination of errors introduced by photon (both target and sky) noise and errors in the measured redshift of the spectra (essentially negligible in all cases).

The line indices for the spheroid spectra must also be corrected for the smearing effects of the line-of-sight velocity distribution (LOSVD). This effect is entirely negligible for GC spectra with velocity dispersions of the order a few kms^{-1}, but cannot be ignored for galaxies with velocity dispersions over $\sim$100 kms^{-1}. As the measured diffuse-light spectrum has a velocity dispersion of around 200 kms^{-1} this step is important. As in Chapter 2 this effect is corrected for using the procedure of Kuntschner (2004), which can also be used to correct line indices for the additional influences of the higher-order LOSVD terms h_3 and h_4. Kuntschner (2004) provides a new parameterisation for the LOSVD line strength corrections derived by determining the difference in measured Lick/IDS line strengths measured from template spectra before and after convolving with various choices of σ, h_3 and h_4. For NGC 3923 the correction for h_3 and h_4 is not implemented due to the effect of the correction given the measured values of σ, h_3 and h_4 being minimal relative to the other errors.

The final step required to firmly fix measurements to the Lick/IDS system is to measure standard stars from the Lick library using our observational set-up and compute offsets between the two. In common with the studies described in Chapters 2 & 3, no Lick standard stars were observed as part of this project. Hence the same observations of Lick standard stars made by Bryan Miller as part of GS-2003B-Q-63 and described in Chapter 3 were used to determine the appropriate Lick offsets for GMOS-S. These offsets were applied to all measured line indices presented in Table 7.1. It should be noted that while useful for comparison between observations taken using different instruments, or for comparing measured indices to models based on the Lick/IDS system e.g. Thomas et al. (2003, 2004), this step is not essential for a simplest first order differential comparison between two sets of observations made with the same instrument, such as that described here.

Using the procedure outlined (neglecting the higher-order LOSVD corrections) Lick line-strength indices were measured for all 29 confirmed GCs, as well as the single coadded spheroid diffuse light spectrum. This single diffuse-light spectrum is located at a

[1]Available at: http://www.ucm.es/info/Astrof/software/indexf/indexf.html

luminosity weighted distance of 3 R_e (throughout it is assumed R_e=43.8 arcsec measured in the J-band (Jarrett et al., 2003), though V, R and I band estimates from Bender et al. (1988) are essentially identical). The S/N of the GC spectra ranges from $\sim$ 11-56 per Å measured in the region 5100-5150 Å, giving errors in the Hβ index of 0.12-0.72 Å.

4.5. Results

Table 7.1 presents velocities and Lick/IDS line-strength indices for all 29 of our confirmed GCs, as well as the single coadded diffuse light spectrum, and a series of GC composite indices binned by g'-i' colour. In addition to examining the GC spectra the 37 diffuse light spectra from the MOS exposure have been extracted (see Figure 4.4 and Table 7.5) with S/N ratio ranging from 5 to 12, which is sufficient to measure velocities in all cases and velocity dispersions in most cases.

4.5.1 Kinematics

A more detailed discussion of the kinematics of NGC 3923 and its GC system will be presented in Chapter 5, where the GC velocities from additional masks at larger radii obtained using the Nod-and-Shuffle method (Cuillandre et al., 1994) will be added.

In this section the spheroid of NGC 3923 is examined for rotation and in Section 4.5.2 the velocities of the spheroid are compared to the velocities measured for the GCs examined in the same slits.

Here the results of a search for evidence of rotation in the diffuse stellar halo of NGC 3923 are presented (see Figure 4.5), this was achieved by carrying out a non-linear least squares fit to the equation:

$$V(\theta) = V_{rot}\sin(\theta - \theta_0) + V_0$$

where $V(\theta)$ is the velocity measured for the diffuse light in each slitlet, V_{rot} is the amplitude of the projected rotation velocity, V_0 the systematic velocity of NGC 3923, θ the azimuthal angle of each slitlet relative to the galaxy major axis and θ_0 is the position angle of the line of nodes. This approach determines the best-fitting simple flat rotation curve (see Zepf et al. (2000) for details).

The conclusion of this procedure is that there is evidence for slight rotation along the

major axis of NGC 3923, with the best fitting amplitude being 31 ± 13 kms^{-1} along a position angle of 290 ± 19° where the major axis is approximately at PA = 315°. This result is in good agreement with that of Koprolin & Zeilinger (2000) who found a small (53 ± 13 kms^{-1}) but non negligible major axis rotation for NGC 3923. It is however different to the results of Carter et al. (1998) who found that the inner 25 arcsec of NGC 3923 showed no rotation on its major axis but had minor axis rotation of amplitude ~ 20 kms^{-1}. The difference in conclusions between the different studies may be attributed to the different radial ranges over which they are sensitive; the method utilised here to extract the spectra provides a measurement of the rotation of the galaxy at a radius at least a factor of two greater than the largest radial point available to either Carter et al. (1998) or Koprolin & Zeilinger (2000).

These measurements of the kinematics of NGC 3923 cover a range in effective radii of between 2 and 4 R_e, demonstrating the great power this approach has for illuminating the kinematics of the outer regions of galaxies.

4.5.2 Reliability of Velocities

One concern with the procedure for extracting diffuse host galaxy spheroid light from the same slitlets as the target GC spectra is that the spheroid spectra could be contaminated by flux from the target GCs. In general this should not be of major concern due to the careful selection of the sky regions of the 2D spectrum. As a test of this assumption Figure 4.6 displays the measured diffuse light velocity against the target velocity (GC, Milky Way star, background galaxy or QSO) from the same slitlet. In Figure 4.6 the filled circles are target objects classified by their velocities as GCs, filled stars are objects classified as Milky Way stars, the three background objects (two z~0.3 galaxies and a z~1.3 QSO) are omitted from the plot for clarity, although they are included in the fit which produces the dashed best fit trend line (which has slope equal to zero within the errors). As can be seen clearly, there is no correlation between the velocities measured for the target spectra and those measured for the diffuse light; in particular even for the brightest target objects (generally the MW stars) the measured velocity for the spheroid of NGC 3923 is still consistent with the recessional velocity of NGC 3923. This indicates that contamination of the diffuse light spectra by the target object spectra is negligible.

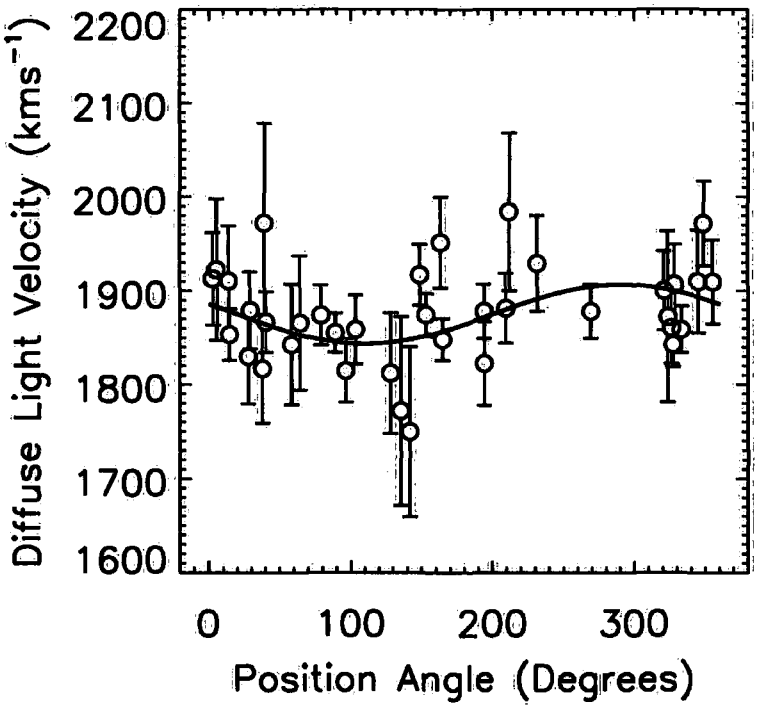

Figure 4.5: Velocity vs. Azimuthal angle for NGC 3923 spectra extracted from MOS slitlets (circles). The solid line is the best fit flat rotation curve indicating rotation amplitude of 31 kms^{-1} $\pm$ 13 with position angle 290° $\pm$ 19° (north through east).

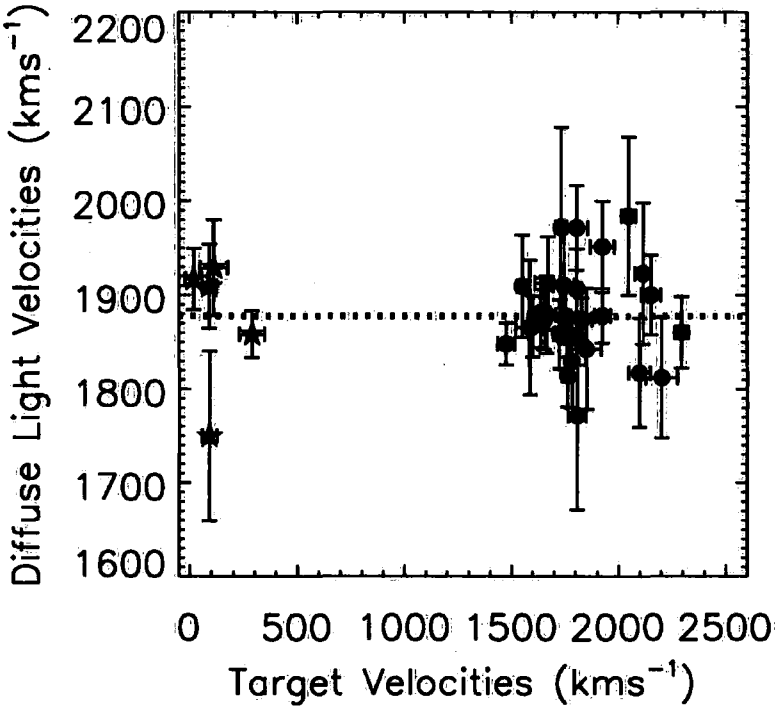

Figure 4.6: Measured velocities from NGC 3923 diffuse light spectra vs. the measured velocities of the targets observed in the same slits. Stars indicate targets classified as Milky Way stars, filled circles those targets classified as GCs belonging to the NGC 3923 system. Two z~0.3 galaxies and a z~1.3 quasar are excluded for clarity. The dotted line shows a linear fit to the data, indicating no correlation between the velocities measured for the targets and the galaxy diffuse light.

4.5.3 Stellar Populations

In this section the stellar populations of the GCs and the diffuse light of NGC 3923 are examined. To begin some of the qualitative properties of the stellar populations will be examined through examination of age-metallicity diagnostic plots. Following this the data is analysed in a more quantitative manner by χ^2 fitting of the data to stellar population models to determine ages, metallicities and α-element abundances.

Index-Index Plots

The left panel of Figure 4.7 presents an Mg*b* vs. <Fe> plot[2] for the 29 GCs as well as the NGC 3923 diffuse light spectrum measured in this Chapter. Model predictions from Thomas et al. (2003, 2004) are overplotted for [α/Fe] = 0.0, 0.3 and 0.5, ages 1-12 Gyr and metallicity running from -2.25 (bottom left) to +0.67 (top right). This choice of indices produces a figure which is insensitive to age but can be used to constrain the metallicity and α-element abundance ratios (Kuntschner et al., 2002). As can be seen the GCs (light grey circles) have metallicities ranging from -1.7 to +0.5 and appear to have a wide range of α-element abundance ratios. When the GC data is binned by colour (coloured circles) the behaviour of the binned data becomes more systematic, with the points showing a clear preference for a constant α element abundance ratio of ~0.3, even as the metallicity of the binned data decreases from around 0.0 to -1.5. These bins cover the range of colour displayed by the majority of extragalactic GCs, and have mean g' - i' colour of 0.82, 0.99, 1.09 and 1.19 (See Table 7.1). The position of the mean colour of each bin relative to the peaks of the blue and red GC distributions can be seen in Figure 4.8. In particular the mean colour of the third bin can be seen to correspond closely to that of the peak of the red GC distribution. If all GC data are combined to produce a composite GC data point (white triangle); the combined GC spectrum has a metallicity of ~ -0.8 and an abundance ratio consistent with 0.3 within the (significant) errors. It is interesting that both the central regions of NGC 3923 measured by Trager et al. (1998) and Beuing et al. (2002) (grey triangle and square) and the NGC 3923 diffuse light spectrum measured in this study (white star) also lie along the same [α/Fe] = 0.3 track. However the fact that the data point from Denicoló et al. (2005) (black triangle) for the central $R_e/8$ of NGC 3923 is offset relative to the other two observations illustrates the magnitude of

[2] <Fe> = (Fe5270 + Fe5335)/2. (González, 1993)

possible systematic errors in this type of study. The difference in metallicity between the inner nuclear data and our large radii diffuse stellar data point can be understood in terms of a radial metallicity gradient in the galaxy. A further point of note is the close agreement between the mean of the GC spectrum and the NGC 3923 diffuse light spectrum which was measured at the same projected radii.

The right panel of Figure 4.7 presents an [MgFe]′ vs Hβ age-metallicity plot[3] with symbols as previously defined. Here it is necessary to choose a fixed value of [α/Fe] for the grids and in this case 0.3 has been chosen as this value is close to that found for each of the populations described in the previous section. It can be seen that three GCs appear to lie along grid lines consistent with young or intermediate ages. These objects are however generally among the lowest-S/N objects in the sample. When other age-metallicity diagnostic plots (Hγ and Hδ vs. [MgFe]′) are considered as well as the fact that similar numbers of objects lie below the grid it appears that these objects may just be statistical outliers in a distribution centred on uniformly older ages. This point shall be rexamined when the results of the χ^2 fitting procedure are studied. The binned GC data again behaves in a systematic manner, in which all the data points lie along a constant age line of around 12 Gyr, with metallicities consistent with those seen in the previous plot. The mean of the GC system as a whole and the NGC 3923 diffuse light point can also be seen to be very consistent in terms of age and metallicity.

The close agreement in apparent age, metallicity and [α/Fe] between the NGC 3923 diffuse light spectrum measured at 3 R_e and the GC system (especially the red GCs) at the same projected radii is tantalising. Such close agreement hints at a deep connection between the two populations exactly as would be expected if the two populations formed coevally from the same material. This interpretation is however dependent on the assumption that the GCs examined here are representative of the full GC population. The sample presented here appears to be a fair match to that present in NGC 3923 over the range of projected radii studied, though only observation of a significantly larger sample of GCs carefully chosen to match the full sample in terms of colour and luminosity would allow this to be determined with certainty.

[3] [MgFe]′ = $\sqrt{\text{Mgb} \times (0.72 \times \text{Fe5270} + 0.28 \times \text{Fe5335}}$ (Thomas et al., 2003)

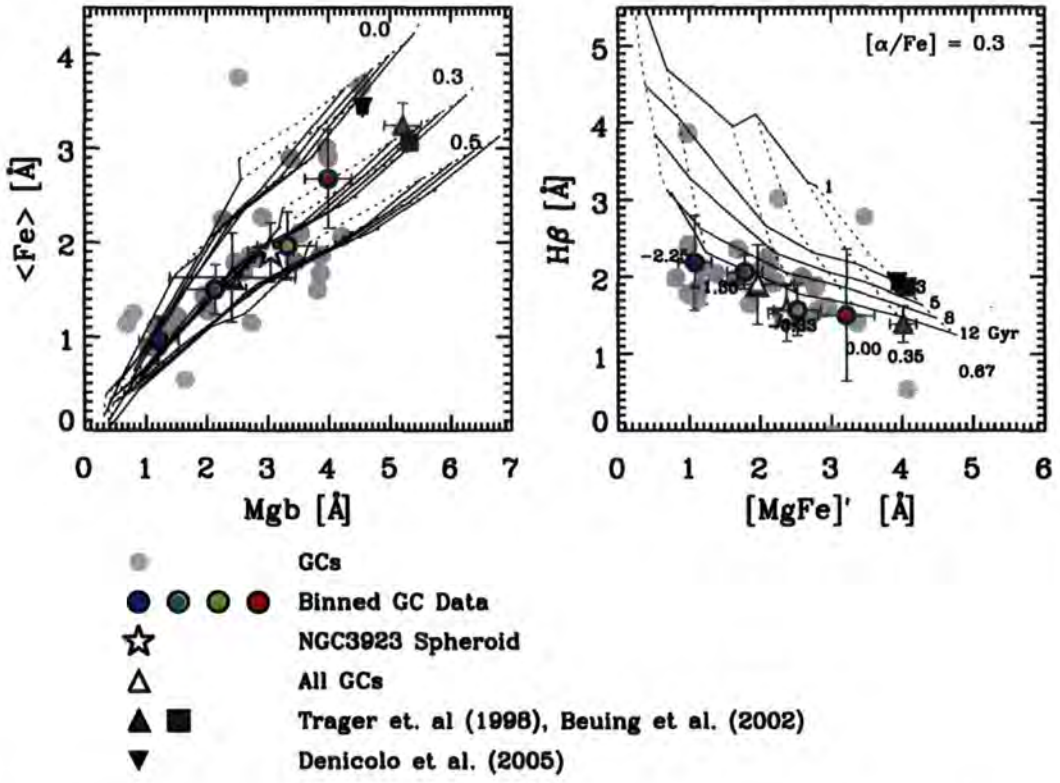

Figure 4.7: Left Panel. Comparison of the [α/Fe] ratios of the diffuse light and GC population of NGC 3923 through the use of an *Mgb* vs. <Fe> diagram. Light grey circles are the 29 GCs measured here (error bars omitted for clarity). The coloured circles are the result of binning the 29 GC data points into 4 bins of 7/8 GCs per bin by g'-i' colour, the error bars show the 1σ scatter in each bin. The white triangle is the result of binning all 29 GC spectra into one bin. Again the error bar represents the 1σ scatter in the bin. The grey triangle, square and black triangle are the central NGC 3923 values from Trager et al. (1998), Beuing et al. (2002) and Denicoló et al. (2005) respectively. The white star shows the values measured from the single high-S/N coadded spectrum of the diffuse light of NGC 3923. Overplotted are models by Thomas et al. (2003, 2004) with abundance ratios [α/Fe] = 0.0, 0.3, 0.5, the models have ages 3-12 Gyr and metallicity [Z/H] = -2.25, -1.35, -0.33, 0.0, +0.35 and +0.67. Right Panel. Age-Metallicity diagnostic plot. Symbols as in left panel. Models are overplotted for a fixed value of [α/Fe] = 0.3

Derived Stellar Population Parameters

Using the multi-index fitting method of Proctor & Sansom (2002) and Proctor et al. (2004) the ages, metallicities and α-element abundances for the stellar populations being studied here are derived. This technique compares the measured Lick indices with SSP models, in this case the SSP models of Thomas et al. (2003, 2004) (TMK04) which to date remain the only SSP models in which the effects of α-element abundance ratios on Balmer line indices at low metallicity are included. For a more thorough description of the different treatments of α-element abundance ratios in modern SSP models see Mendel et al. (2007).

The procedure used to determine the best fitting SSP model is as follows. The total set of measured Lick/IDS indices is compared to the TMK04 SSPs and a minimum χ^2 fit obtained; simultaneously a set of χ^2 minimization fits are determined with each of the indices omitted. The lowest total χ^2 fit from this set is then chosen, the necessary index removed and the process repeated until a stable fit is arrived at where no highly aberrant (3σ) indices remain. In this instance all GCs displayed some indices which were sufficiently aberrant to be excluded from the fit, most often due to problems with the spectra in those regions due to chip problems or cosmic rays. Although all fits utilised a minimum of 9 indices, most GCs are fit with at least 13 indices. Errors in the derived parameters are determined via Monte-Carlo simulations of the input index measurements with their measured errors. The results of this procedure are displayed in Table 7.4.

In common with previous studies it is found that the molecular bands Mg_1 and Mg_2 appear depressed, an observation generally explained as being due to problems with flux calibration. This explanation has been tested by examining the effect of using the flux calibration curves found from repeat observations of the same standard star (in this case LTT4364) observed for a different programme using the same observational set-up as used here. It is found that even when using curves derived from the same standard star the measured Mg_1 and Mg_2 indices of the GCs after flux calibration could vary systematically by as much as 0.01 mag, which is of the same order as the deviations observed in the fitting procedure. Other indices were much less affected by the change in flux calibration, presumably due to the much narrower wavelength coverage of these indices. Accordingly Mg_1 and Mg_2, as well as Ca4227 which was similarly depressed, were therefore removed from the fitting procedure. The CN indices tended to be enhanced relative to the models, in agreement with previous findings (Beasley et al., 2004a; Pierce et al., 2006a) for GCs. The Ca4668 index also tended to be unreliable and was therefore ex-

cluded from the fits.

The quantitative χ^2 fitting procedure produces results in good agreement with the more qualitative discussion in the previous section. It is found that the GCs examined have ages consistent at the one sigma level with old ages (>10 Gyr) in all but one case. The GCs exhibit a spread of metallicities from [Z/H] = -1.8 to +0.35 and α-element enhancement ratios generally consistent with ~0.3 dex, although several objects display [α/Fe] of below zero or greater than 0.5, at the limits of the models. From the sample of 29 GCs studied here only one object (ID: 197) displays an age which is inconsistent with a mean age greater than 10 Gyr, however this result is not significant being only a 1.5σ deviation. A more thorough analysis of the distribution of stellar population parameters is somewhat limited by the small sample size. However to first order the distribution of ages is consistent with a single value of around 12 Gyr plus measurement errors. The distribution of metallicity however is inconsistent at the greater than 99.9% significance with having a single value plus measurement errors. The distribution of metallicity measured is consistent with a mean of -0.65 dex and an intrinsic scatter of 0.5 dex plus measurement errors, assuming a Gaussian distribution of metallicities. Similarly the distribution of [α/Fe] is also inconsistent with a single value plus measurement errors at the greater than 99.8% significance level, in this case it is estimated that an intrinsic scatter of 0.12 dex plus measurement errors around a mean of 0.31 dex is required to explain the observations.

This analysis has been repeated for the binned GC data and for the line indices measured for the diffuse light halo of NGC 3923. The binned GC data are again found to behave in a manner consistent with the more qualitative examination of the index-index plots. All bins have ages consistent with being older than 10 Gyr, all four bins display a smoothly increasing metallicity with colour, ranging from [Z/H] = -1.375 to -0.125, and all display [α/Fe] consistent with 0.3. The considerably larger errors present in the measured parameters for the reddest colour bin, are a result of this bin being composed almost entirely of lower luminosity and hence lower-S/N objects. Apparently through chance selection this bin contains GCs of considerably lower luminosity than the average for GCs examined spectroscopically here (see Figure 4.8). This results in a mean g′ magnitude fully half a magnitude below any of the other bins; together with the effect of error weighting the indices when combining them this explains why this bin is of significantly lower S/N than the others.

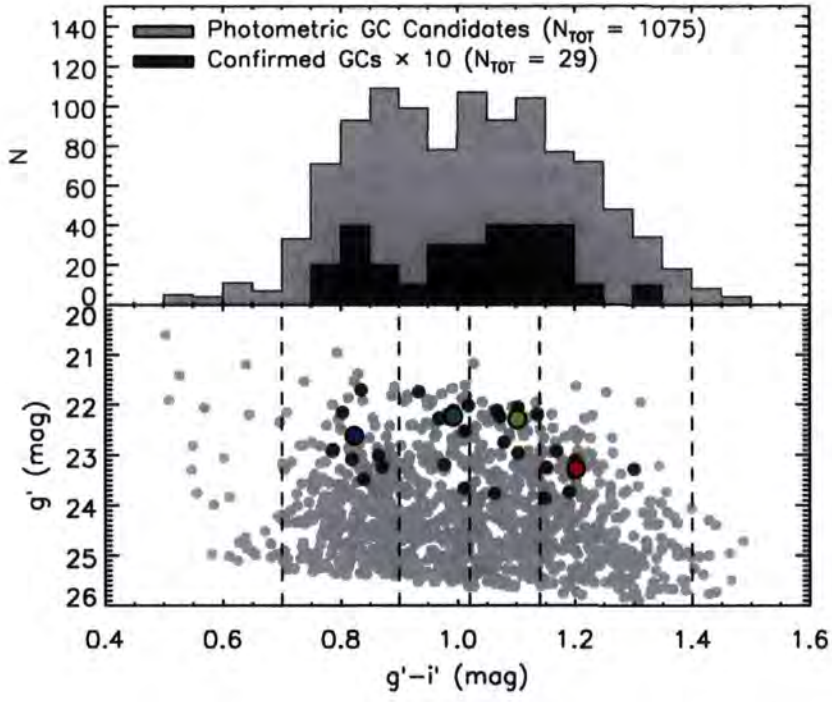

Figure 4.8: **Top Panel** : The light grey histogram shows the distribution of g′-i′ colours for photometrically selected candidate GCs around NGC 3923 from our GMOS pre-imaging. The dark histogram (multiplied by a factor of 10 for clarity) shows the distribution of g′-i′ colours for our 29 spectroscopically confirmed GCs. **Bottom Panel** : g′-i′ vs g′ colour-magnitude diagram for our photometric (light grey circles) and spectroscopically (dark grey circles) confirmed GCs. The coloured circles indicate the error weighted mean values for each bin, the dashed lines indicate the arbitrary choice of bin ranges.

The "Super GC" bin, containing the error-weighted indices of all 29 GCs unsurprisingly predicts ages, metallicities and α-element abundances in good agreement with those of the colour-binned GCs. The fit gives an old age for the GC population as a whole, a metallicity [Z/H] = -0.8 and an α-element abundance ratio consistent with 0.3.

Turning attention to the measured parameters for the diffuse light of NGC 3923 at $\sim 3R_e$ it is found to display old ages, metallicity [Z/H] of -0.325 and [α/Fe] of 0.34. These results are entirely consistent with that found for the red bin of GCs (see Figure 4.9), those GCs displaying g′-i′ colours in the range 1.02 to 1.14.

Stellar Population Parameter Correllations

Figure 4.9 can be used to search for correlations between the ages, metallicities and alpha-element enhancements measured for the various stellar populations using the χ^2 fitting procedure outlined previously.

One interesting observation is that there is no evidence for the observed trend of decreasing [α/Fe] with increasing metallicity seen in the GC systems of some galaxies (e.g. NGC 3379 (Pierce et al., 2006a), NGC 4649 (Pierce et al., 2006b)), but not in others (NGC 1407 (Cenarro et al., 2007), VCC1087 (Beasley et al., 2006)).

Another interesting feature visible in the higher S/N data (filled circles) is that the Thomas et al. (2003, 2004) models tend to introduce a slight trend of increasing age with increasing metallicity. This trend, which has been previously observed in the NGC 1407 system (Cenarro et al., 2007) and the MW GC system (Cenarro et al., 2007; Mendel et al., 2007) appears to be a peculiarity of the Thomas et al. (2003, 2004) models; Mendel et al. (2007) found that the Lee & Worthey (Lee & Worthey, 2005) and Vazdekis (Vazdekis, 2007) SSP models do not display this trend. However as the age determinations at the lowest metallicities are already highly uncertain due to the possible effects of horizontal branch morphology, this effect is not significant and does not affect any conclusions made so far.

4.6. Discussion

In summary, spectra have been obtained for 29 GCs associated with NGC 3923, as well as 37 spectra of the diffuse light at radii of 2-4 R_e. By combining these 37 diffuse-light spectra a single spectrum has been produced with a luminosity-weighted distance of 3 R_e of sufficient S/N to determine an age, metallicity and α-element abundance ratio by comparison with Lick line strength indices for Simple Stellar Population models.

There is evidence in the data for slight rotation of amplitude 31 ± 13 kms^{-1} in the spheroid of NGC 3923 between approximately 2 and 4 R_e along the major axis of the galaxy.

All 29 GCs examined in this chapter are consistent with being old (>10 Gyr) and none display any persuasive evidence for being young enough to be associated with the shell-forming event. These results therefore support the conclusions of Sikkema et al. (2006) who, using HST ACS photometry for the GC system of NGC 3923, found no evidence of a young GC subpopulation.

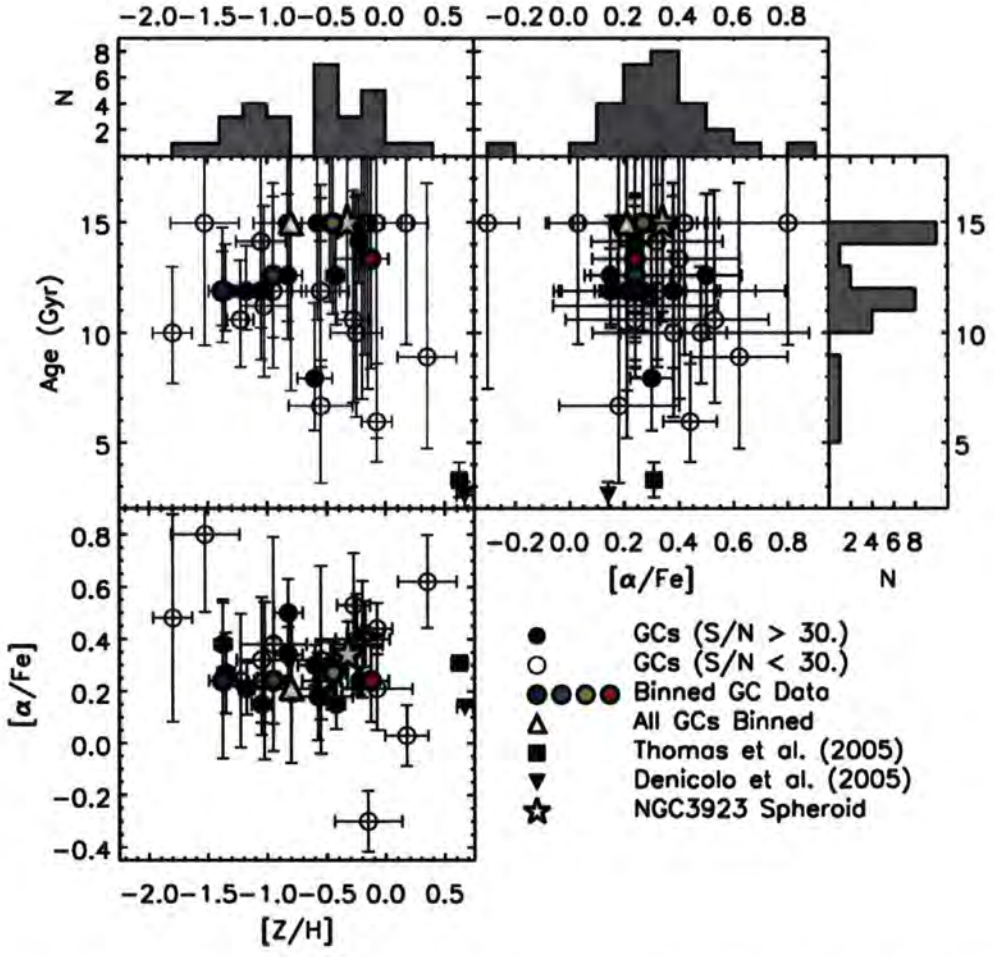

Figure 4.9: Ages, metallicities and [α/Fe] ratios measured for the NGC 3923 GCs (filled circles have S/N per Å> 30, unfilled have S/N < 30 per Å), GC data binned by colour (coloured circles), NGC 3923 central regions from Thomas et al. (2005a) (filled square), Denicoló et al. (2005) (filled triangle) and NGC 3923 spheroid (unfilled star).

The GCs examined display a wide range of metallicity from [Z/H] = -1.8 to +0.35. In contrast to other studies (Puzia et al., 2005; Pierce et al., 2006a,b) this data displays no evidence for a significant subpopulation of GCs with extremely high ([α/Fe]>0.5) α-element abundance ratios. This data also does not show any clear tendency for α-element abundance to increase with decreasing metallicity as had been found in these studies. It must be noted however that α-element abundance ratios are not well constrained at low metallicity and that the results of these previous studies may be consistent within the errors with a universal value of [α/Fe] = 0.3. In agreement with both these studies and with measurements of the Milky Way GC population it is found that the majority of the GCs examined here with accurate abundance ratios have [α/Fe] consistent with 0.3.

The stellar population of the diffuse light of NGC 3923 between ~ 2 and $4R_e$ is entirely consistent in age, metallicity and α-element abundance ratio with the red GC population. It also agrees within the respective errors with the mean of the GC population examined spectroscopically; however, there is a slight difference in metallicity for the mean of the total GC population and the stellar population of the diffuse light of the galaxy. With the current sample size, it is impossible to determine if this offset is real or merely the result of a statistical fluctuation.

This similarity between the stellar populations of the spheroid of NGC 3923 at large radii and the redder GCs is in good agreement with previous findings, both spectroscopic (in NGC 3115; Norris et al. (2006)) and photometric (in NGC 4649; Forbes et al. (2004)), and supports the view that the two populations formed coevally.

The fact that the stellar populations of the GCs studied here do not match those of the inner regions of NGC 3923 is most likely due to the fact that GC systems are observed to display variation in the mix of red and blue populations with radii. Therefore the GC populations which make up the region between 2-4R_e are not likely to be the same as those that inhabit the inner regions of the galaxy. Additionally GCs are thought to be vulnerable to disruption by tidal effects within the inner regions of galaxies meaning that projection effects become a more serious issue at smaller galactic radii, with GCs at large radii projected onto the inner regions of the galaxy becoming more important.

By comparing the stellar population parameters determined here for the spheroid of NGC 3923 at large galactocentric radii with those of the inner regions of NGC 3923 measured by Thomas et al. (2005a) (using the index measurements of the inner $R_e/10$ by Beuing et al. (2002)) and Denicoló et al. (2005) (using index measurements of the inner

$R_e/8$), evidence is found for metallicity and age gradients in the spheroid of NGC 3923 but no evidence of an [α/Fe] abundance ratio gradient. Specifically Thomas et al. (2005a) find a luminosity weighted age for the central region of the galaxy of 3.3 Gyr, a metallicity of [Z/H] = 0.62 and [α/Fe] = 0.31. This is in good agreement with the conclusions of Denicoló et al. (2005) who find an age of 2.6 Gyr, a metallicity of [Z/H] > 0.67 and a slightly lower value of [α/Fe] of around 0.14. This close agreement is to be expected as both studies make use of the same TMK04 models to derive their stellar population parameters. Therefore it appears that the outer regions of NGC 3923 are considerably older, less enriched in metals, but have a similar α-element abundance ratio as the inner regions of the galaxy. The first two points are not unexpected considering that the values for Thomas et al. (2005a) and Denicoló et al. (2005) are provided for apertures of $\leq R_e/8$, and the spectroscopy described here of the spheroid of NGC 3923 has a luminosity-weighted effective radius of $3R_e$.

Such a situation is very similar to that found for the isolated elliptical NGC 821 by Proctor et al. (2005) using longslit spectroscopy. In this case Proctor et al. (2005) found that NGC 821 displayed a strong gradient in both metallicity and age, in the sense that metallicity decreases with radius and age increases with radius. As in NGC 3923 the galaxy displays a constant value of [α/Fe] close to 0.3. NGC 3923 and NGC 821 display similar metallicity gradients of $\sim$-0.7 dex/ΔlogR but the normalisation for NGC 3923 is shifted to higher metallicities than in NGC 821. As discussed in the case of NGC 821 (Proctor et al., 2005), this high value of the metallicity gradient tends to rule out merger models for the formation of NGC 3923, as merger models predict lower values for the metallicity gradient due to the violent mixing that takes place during mergers tending to wash out gradients (Kobayashi, 2004).

Another scenario considered by Proctor et al. (2005) to explain the formation of NGC 821 is where a minor merger event funnels gas to the inner region of the galaxy producing a minor star-formation event and adding a layer of "frosting" to the majority older population already present. This star-formation event presumably did not produce a significant number of star clusters stable enough or at large enough galactocentric radii for them to survive and be detectable at the present time. This scenario for the formation of NGC 821, can also be applied to the formation of NGC 3923, where it can naturally explain the formation of the shell structures. However the same problem that caused Proctor et al. (2005) to reject this explanation in the case of NGC 821 still applies in the

case of NGC 3923, namely that the gas forming the new stars would presumably be of different metallicity and α-element abundance than the galaxy at these radii it would then have to form stars over the correct timescale, with the appropriate enrichment such that they appeared to fall exactly on the trends of metallicity and α-element abundance that the rest of the galaxy exhibits. This appears to require an unlikely amount of fine tuning. However recent work by Serra & Trager (2007) shows that when examining a composite stellar population using SSP models, it is the young component which dominates the age determined for the composite. They further find that the chemical composition (metallicity and [α/Fe]) of the best-fit SSP model closely follows that of the older population which dominates the mass. This explanation would also not rule out the young age of around 1 Gyr determined by Sikkema et al. (2006) for the shell features of NGC 3923, as any 1 Gyr stellar population present in the inner regions could, with the correct choice of mass fraction, appear to be around 3 Gyr, when combined with a majority older stellar population.

A final possible formation scenario considered by Proctor et al. (2005) to explain the formation of NGC 821 is that the gas for the recent starburst is fuelled by gas from the galaxy itself, perhaps through gas cooling smoothly onto an inner disc. High spatial resolution IFU observations of the inner regions of NGC 3923 would help to search for the signatures of such a structure. Serra & Trager (2007) note that if high enough S/N spectroscopy is available it is possible to disentangle the different stellar populations present through examination of the discrepancy between the SSP parameters determined using different Balmer-line indices. This result therefore provides a possible route to determining the relevance of these models for the formation of NGC 3923.

4.7. Conclusions

Low-resolution spectra have been obtained for 37 GC candidates around the shell elliptical NGC 3923 using GMOS on Gemini-South. By examination of the radial velocities of the targets it is found that 29 are GCs associated with the target galaxy. Making use of a new technique of extracting integrated spectra at extremely low surface brightness levels kinematic properties have been determined for the diffuse light of NGC 3923 out to around 200 arcsec on both major and minor axes, corresponding to half-light radii in the range 2-4R_e. Some evidence is found for low amplitude rotation along the major axis

of around 30kms^{-1}. The detailed kinematic properties of NGC 3923 (including its observed velocity dispersion in this range) and its GC system will be studied in more detail in Chapter 5.

The ages, metallicities and [α/Fe] ratios of the 29 GCs have been measured and compared to those found for the diffuse light of NGC 3923 at the same projected radii. All of the GCs examined are found to have old ages ($\geq$10 Gyr), with metallicities running from [Z/H] = -1.8 to +0.35 and α-element abundance ratios generally consistent with a constant value of [α/Fe] = 0.3. The data does not provide any support for the existence of a younger population of GCs associated with the $\sim$1 Gyr old merger event proposed to have produced the shell system of NGC 3923. The diffuse light of NGC 3923 is observed to have properties indistinguishable from those of the more metal rich (and redder) GCs.

Taken together these results provide support to the theory that the spheroids and GC systems of galaxies are produced during the same star-formation events, and that the study of the stellar populations of GC systems can provide important insights into the stellar populations of galaxies at galactocentric radii which at present are difficult to study using direct measurements of their integrated light.

Chapter 5

The Globular Cluster Kinematics and Galaxy Dark Matter content of NGC 3923

5.1. Abstract

This Chapter presents additional spectroscopic observations of the GC system of NGC 3923 to explore its kinematic properties. By combining 45 additional GC velocities with the 29 GC velocities reported in Chapter 4 a total sample of 74 GC velocities is produced, which extend to over 6 arcminutes (~6 R_e) from the centre of NGC 3923. An examination of the velocities demonstrates that the GC system of NGC 3923 displays no appreciable rotation. The projected velocity dispersion of the GC system is consistent within the errors with being constant with radius. The application of non-parametric isotropic models to the velocity dispersion profile demonstrates that a significant increase in the mass-to-light ratio at large radii is required to explain this observation. The observed M/L profile is seen to match that determined by previous X-ray observations. Thus, additional support is provided for the presence of a significant dark matter halo associated with NGC 3923.

5.2. Introduction

The study of the mass distributions and dark matter content of galaxies is an area of significant interest to those interested in the formation and evolution of galaxies. The current cold dark matter (CDM) paradigm posits that dark matter is the dominant matter component found in the Universe, and hence drives the formation of structure throughout the history of the Universe. However making measurements of the actual distribution of DM with which to confront theory can prove to be difficult, in particular measuring the DM distribution on the scales of galaxies can prove to be extremely trying for any galaxies other than extremely large early-types (where significant X-ray emission is present) or spiral galaxies (where gas emission can be traced to large radii to trace flat rotation curves, e.g. Persic et al. (1996)). Intermediate to low mass early-types are of notable concern, since these galaxies usually lack significant X-ray or ionised gas emission and lack readily observable tracers of the stellar kinematics at large radii (such as absorption line kinematics, see Chapter 3 for examples), due to the inherent faintness of the stellar populations at radii where the DM is expected to dominate (beyond $2R_e$). For these galaxy types in particular then (but all others as well), the use of dynamical probes such as GCs and planetary nebulae (PNe) are of particular importance.

Globular clusters are well suited to this type of study for several reasons including their ubiquity around any relatively massive galaxy (e.g. see Peng et al. (2006) for Virgo Cluster galaxies), their extended distribution which ensures significant numbers can be found at the radii where the DM component becomes significant and the fact that they are bright enough to be observed to large distances. The study of the kinematics of large samples of GCs around galaxies also provides other useful clues to the formation histories of galaxies in addition to the relative amounts of dark and baryonic matter. For example in some galaxies the GC system or a sub-population of it is found to rotate with the galaxy (e.g. NGC 3115, Chapter 2, Kuntschner et al. (2002)), perhaps indicative of a common formation history for the stellar component and the GC system. If sufficient GCs are studied it becomes possible to search for differences in the behaviour of sub-populations, such as the clusters associated with the red and blue (metal rich and metal poor) GC sub-populations. Such differences can be instructive when combined with information provided by the ages and metallicities of the GC populations. For example in the Milky Way it is seen that the older more metal poor GCs form a velocity disper-

sion supported spherical halo, whereas the metal rich GCs rotate much more rapidly and are associated with the thick disc of the MW (Armandroff (1989) and Ashman & Zepf (1998) for a more thorough description). Observations such as these can clearly do much to constrain theories of galaxy formation, with for example any theories which lead to substantial mixing of the GC populations in the time since their formation clearly ruled out.

At first glance PNe would appear to be very similar to GCs, having essentially the same benefits of extended spatial distributions, ubiquity and ease of identification due to their strong emission lines of [OIII]. However work by Romanowsky et al. (2003) found that the PNe velocity dispersion profiles for three intermediate-luminosity ellipticals (NGC 821, NGC 3379 and NGC 4494) decline with radius in such a manner that little or no DM is required to explain the observations. This conclusion, which is in clear contradiction with the conventional cosmological model, prompted both theoretical and observational investigation of the causes of this observation. On the theoretical side, work by Dekel et al. (2005) on numerical simulations of spiral galaxy mergers has shown that halo stars at large radii can have highly radial orbits, leading to a decreasing projected velocity even in the presence of a massive DM halo. Some observational support of this idea is provided by observations of the GC kinematics of NGC 3379 (Bergond et al., 2006; Pierce et al., 2006a) which shows GC kinematics which are consistent with the presence of a significant DM component not seen in the Romanowsky et al. (2003) analysis. Presumably the older GCs are less affected by the hypothetical merger event and continue to trace the potential of DM more faithfully. Other evidence comes from a PNe study of NGC 4697 by Sambhus et al. (2006) who found strong evidence of distinct PNe subpopulations, one of which is found to be dynamically unusual, out of dynamical equilibrium with the galaxy potential and possibly associated with a younger population formed in a merger event.

The examination of dynamical tracers such as GCs and PNe is therefore an extremely promising area of research, with much to be learned about the processes that lead to the formation of galaxies as currently observed. In recent years a growing number of studies have made use of 8m class telescopes to build large samples of GC velocities around samples of early-type galaxies. In general these have been of larger cluster galaxies which are known to harbour large GC populations. The project of which this study is a part intends to widen the host galaxy mass and environment range so far studied. To date NGC

3379 (Pierce et al., 2006a) and NGC 4649 (Bridges et al., 2006) have been studied. Both galaxies displayed GC velocity dispersion profiles which were constant with radius, a finding indicative of the presence of DM. To these studies can be added investigations of the GC systems of NGC 4636 (Schuberth et al., 2006; Chakrabarty & Raychaudhury, 2008), M49 (Sharples et al., 1998; Côté et al., 2003), NGC 1399 (Richtler et al., 2008) and NGC 5128 (Woodley et al., 2007), all of which have found similarly constant GC velocity dispersion profiles, providing strong evidence for the existence of significant amounts of DM in these galaxies. The examination of the GC systems of these galaxies for signs of the rotation seen in the MW metal-rich GC population has been less conclusive. Rotation has been observed in some galaxies (NGC 3115, NGC 5128, M87) but not in others (NGC 1399, NGC 3379, NGC 4472 and NGC 4649), with the picture becoming even more complicated when the GCs are split into red and blue sub-populations. Generally it can be stated that the blue sub-population displays a higher velocity dispersion than the red population, but beyond this the picture is confused with considerable variation from galaxy to galaxy. The study of the orbits of the GCs has generally been stymied by the need for extremely large samples of GC velocities (several hundred in order to solve for both the mass distribution and orbital anisotropy simultaneously). Where fewer velocities are available other input such as an X-ray profile can be used to constrain the potential, allowing the observed dispersion profile to be used to determine the GC orbits. In NGC 1399, NGC 4472 and M87 the GCs display orbital characteristics consistent with isotropy, but in NGC 4649 there is some evidence of a trend towards increasingly tangentially biased orbits with radius (Bridges et al., 2006).

This Chapter continues the study described in Chapter 4, adding an additional 45 GC velocities to produce a total sample of 74 GC velocities. For a more thorough description of this galaxy and its properties see Chapter 4. The only previous study which has studied the DM content of NGC 3923 is the X-ray study of Fukazawa et al. (2006), which found that the M/L in the B-band increased from 3.5 in the inner regions to around 15 at 18kpc, a trend strongly supporting the presence of a DM halo associated with this galaxy.

5.3. Observations and Data Reduction

This Chapter continues and expands the study first presented in Chapter 4. To the 29 GC velocities determined from MOS spectroscopy are added an additional 45 GC ve-

locities measured using the Nod-and-Shuffle (N&S) method. As described in Chapter 4 pre-imaging for object selection was undertaken for 3 fields (central, SW and NE) on 2004 January 19, comprising 4×200 seconds in Sloan g', and 4×100 seconds in r' and i'. A more complete description of the procedure used to reduce and select GC candidates is presented in Forbes et al. (2004) and Bridges et al. (2006). A full description of the reduction and analysis of the MOS spectroscopy is provided in Chapter 4, so in the current section the focus shall be on the reduction of the N&S spectroscopy.

GMOS N&S masks were produced for each of the 3 fields for which pre-imaging was carried out. The central field containing the largest number of targets was examined twice, once with MOS spectroscopy (described in Chapter 4) and once with N&S. The masks contained a total of 44 (central field), 46 (SW field) and 48 (NE field) slitlets, each of which was 1 arcsecond wide by at least 2.25 arcseconds long. The majority of the slitlets per mask (30-35) were placed on GC candidates, with the remaining slitlets placed on other objects of interest to fill up the mask. Each N&S mask was exposed using the B600_G5303 grism for 4×1800 seconds at a central wavelength of 505 nm and 4×1800 seconds at a central wavelength of 510 nm, yielding 4 hours of on-source integration per mask. Additionally the spectra were exposed through the g_G0325 and GG455_G0329 filters which restricted the wavelength coverage to a well-defined bandpass of ~4600-5550Å. This restriction in wavelength coverage allowed more freedom in the positioning of slitlets and hence in choice of targets, as spectra could now be aligned in the spatial dimension without overlapping. The wavelength coverage of each spectrum was still sufficient to cover most of the strong absorption lines found in optical spectra and includes the most important lines for such studies, Hβ, Mgb, Fe5270 and Fe5335. Bias frames, flat fields and copper-argon (CuAr) arc spectra were observed throughout the observations as part of the standard Gemini baseline calibrations.

The reduction of the N&S spectra was accomplished using the standard Gemini/GMOS packages in IRAF, a brief description of which shall be given here to help illustrate the benefits and problems associated with using this technique for GC studies. In N&S spectroscopy the target is placed at one end of the slit, it is exposed as normal for a period of time, the telescope is then nodded to a sky position whilst shuffling the charge on the CCD between science and un-illuminated storage regions. The image that results contains two spectra - one of the object and one of the sky, both of which importantly were obtained on exactly the same pixels after traversing identical optical paths. Therefore

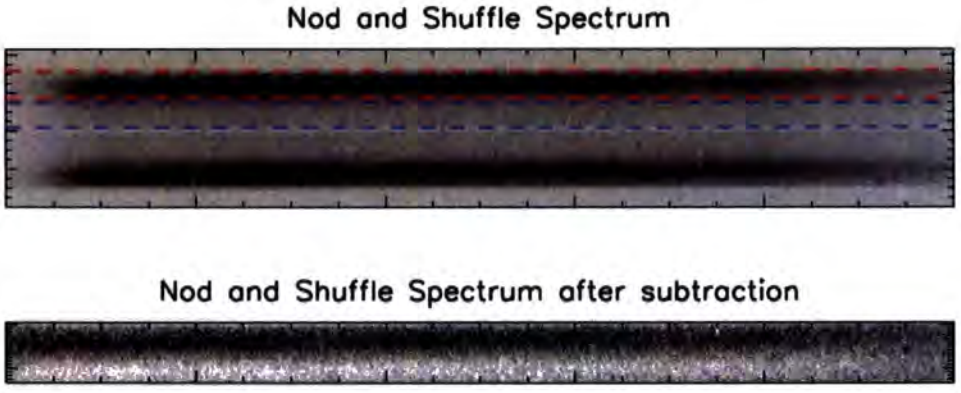

Figure 5.1: **Top Panel** : Example 2D GMOS Nod and Shuffle spectra. The red dashed lines indicate the region containing target flux, for the upper spectra, the blue dashed regions indicate the sky region for the upper spectrum. The second spectrum below appears almost as a mirror image of the first. **Bottom Panel** : The result of shifting the upper spectrum down and subtracting from the lower spectrum to remove the sky, two object spectra remain, one negative the other positive.

when subtracting the sky spectrum from the object spectrum effects such as flat-fielding errors, fringing, and variation in the sky all cancel out. In the case of the data here, only a small offset was applied in the nodding procedure such that the object appears in both the science and the sky spectra, only at different ends of the slit. Figure 5.1 presents an example 2D N&S spectrum, where the target spectra can be seen at the top and bottom of the respective 2.5 arcsecond-long slits, in between lies the sky spectrum. To produce these spectra the standard reductions for Gemini/GMOS IRAF N&S tasks were used to provide bias subtraction, flat fielding, extraction of each spectra pair into separate extensions and then wavelength calibration. At this point it is possible to shift one spectrum up to overlap with the other, such that the sky region of one spectrum is over the target spectrum of the other. Subtracting one spectrum from the other then produces a sky subtracted target spectrum pair, as seen in the bottom panel of Figure 5.1, where one spectrum is negative and the other positive. It is then a simple matter to trace and extract each spectrum as normal and combine each exposure together (remembering to flip the negative spectra to positive ones) to produce the final 1D spectrum. An example 1D spectrum for one of the NGC 3923 GCs studied using this technique is shown in Figure 5.2.

In theory the use of the N&S method should have one major advantage over standard

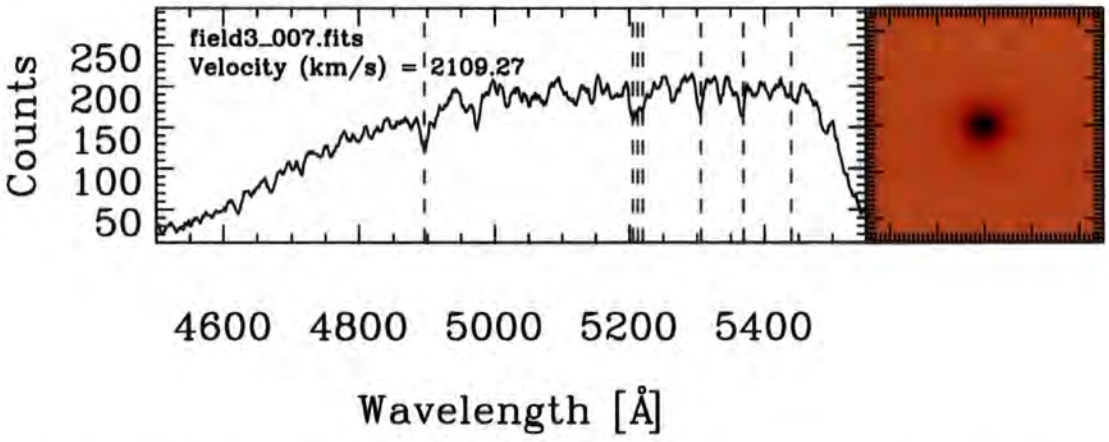

Figure 5.2: Example 1D GC spectrum with g′ = 21.7 mag measured using the N&S method. The effect of using the filter combination to reduce the wavelength coverage can be seen by the sharp drop off beyond 5450Å. The determined velocity of this GC is displayed, as well as the positions of various absorption lines after redshifting by this velocity. To the right is a 5×5 arcsecond g′ image of the GC.

MOS observations: the ability to pack more objects onto each mask. This is because the improved sky-subtraction accuracy means that shorter slitlets are required to determine equally good sky spectra, allowing more spectra to be packed onto each mask. In practice however an added complication of the N&S method meant that no real benefit was gained from using it. The problem arises because of the very nature of the N&S method where charge is moved around the CCD, allowing both sky and target light to fall on the same regions (at different times) before being moved out of the way. In practice the shuffling procedure can have significant problems. In the case of the GMOS CCDs small regions exist which do not allow the charge to move through them efficiently. These "charge traps" cause trails of charge deficit as can be seen in Figure 5.3. The net effect of these charge traps is that they lead to artifacts which in the final extracted 1D spectra are indistinguishable from absorption features. Several methods have been developed to deal with these traps (see for example Abraham et al. (2004)). However none is straightforwardly applicable to the data available here as generally they require additional steps during the data observations, such as additional exposures which have been spatially dithered to avoid the same regions of the spectrum falling onto the same charge traps. Hence these charge traps make some regions of the GMOS CCD unusable in the present case, leading to the unfortunate loss of several spectra per mask. It is because of this

Figure 5.3: Examples of GMOS charge traps (white vertical streaks).

problem and the additional complexity of N&S reduction that MOS observations for this type of study are to be preferred, at least for observations in the optical region.

5.3.1 GC Velocity Determination

The velocities of the GCs were determined using the same methods used to measure the velocities of the GCs studied using the MOS observations (Chapter 4). In short the FXCOR task in the RV package of IRAF was used. No radial velocity standard stars were observed, so therefore template spectra from the simple stellar population library of Vazdekis (1999) were used as templates. As described in Section 4.4.2 a further 6 stellar spectra from the Jones (1997) library were added to ensure adequate coverage of the low-metallicity region. Hence the template spectra spanned a range in metallicity from [Fe/H] < -1.5 to +0.2 and in age from 1-18 Gyr. The quoted velocity for each object is the 3-σ clipped mean of the velocities derived from the FXCOR fits to each template; the errors are estimated from the mean of the errors measured by FXCOR for those velocities not clipped.

Objects with velocities in the range 1100-2500kms^{-1} (V_{gal}±700 kms^{-1}) are assumed to be associated with NGC 3923. This is marginally different to that quoted in Chapter 4, where 1200-2400 kms^{-1} was used. However it makes essentially no difference as no new objects from the MOS observations would fall into this range. In total 61 N&S objects fall within this range. However there is considerable overlap between the MOS and N&S observations and of these 61 objects 45 prove to be new GCs. A total of 25 objects were examined with both MOS and N&S (occasionally twice with N&S) allowing an examination of the robustness of the measured velocities and their errors. Figure 5.4 displays the velocity measured using the N&S observations versus the velocity measured using the MOS observations for 20 objects which were observed twice and which were of sufficient S/N to recover velocities from the lower-S/N N&S data. As can be seen, the agreement between the two measurements is exceptionally good, with no sign

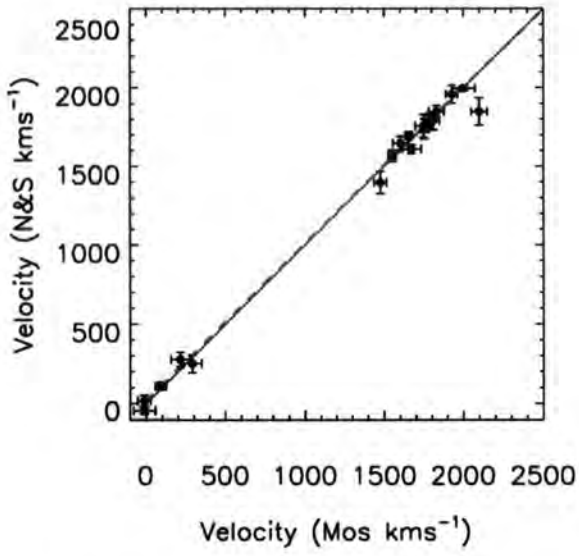

Figure 5.4: Comparison of the velocities of 20 objects common to the MOS and Nod-and-Shuffle fields. Five of the objects in common were not of sufficient S/N to measure velocities in the shallower N&S observations. The solid black line is the one-to-one relationship and the dashed blue line the error weighted linear least squares fit to the data.

of any systematic variation between the two methods. This good agreement allows the simple weighted averaging of velocities measured using both techniques in the case of overlaps. In the few cases where N&S targets were observed on two separate N&S masks but no velocity was recovered, the spectra were coadded and then velocity measurement reattempted. However in no case were any additional velocities recovered. In total after combination of repeat observations 74 secure velocities were arrived at. The spatial distribution of these 74 GCs can be seen in Figure 5.5. Table 7.6 provides the positions, photometry (measured from the g, r and i band pre-imaging) and velocities for the 74 objects confirmed as NGC 3923 GCs.

5.4. Results

5.4.1 Kinematic Analysis

Figure 5.6 shows a histogram of the velocities of all 74 confirmed GCs, and for the red (42 GCs) and blue (32 GCs) sub-populations separately. The split between red and blue GCs was determined to be at g-i = 1.0 mag, which is the approximate location of the dip in

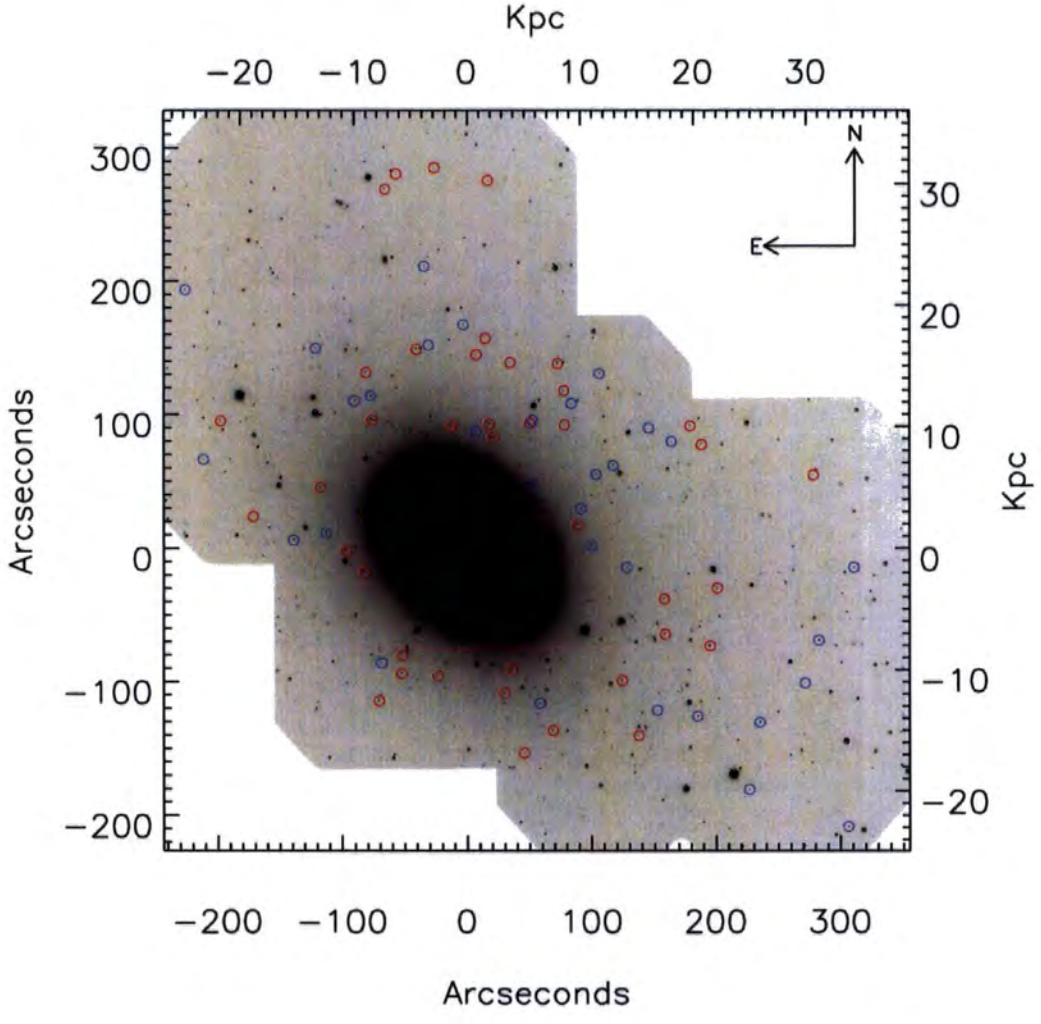

Figure 5.5: The position of kinematically confirmed GCs associated with NGC 3923. Red and blue circles indicate red and blue GC subpopulation members respectively. Red GCs have g-i > 1.0, and blue GCs have g-i < 1.0 mag.

the full g-i colour histogram shown in Figure 4.8. As can be seen from the figure, unlike in the studies of NGC 4649 (Bridges et al., 2006) or NGC 3379 (Pierce et al., 2006a), the recessional velocity of NGC 3923 (~1800 kms^{-1}) is sufficiently high that contamination from Milky Way stars can be ignored. In fact an examination of the velocities determined for all objects shows that no objects lie within 300 kms^{-1} of the lower cut off of 1100 kms^{-1} required for GC classification. An examination of the environment around NGC 3923 also demonstrates that contamination of the sample by GCs associated with nearby neighbour galaxies is likely to be negligible. Therefore it is assumed that all 74 objects with velocities between 1100 and 2500 kms^{-1} are GCs associated with NGC 3923.

Figure 5.7 displays histograms which highlight the distribution of azimuthal angle and galactocentric radius displayed by the 74 GCs. As would be expected the alignment of the positions of the masks along the major axis of NGC 3923 (See Figure 5.5) leads to a relative dearth of GCs located along the minor axis of NGC 3923, especially towards the SE of the galaxy centre (located at around 210° on the Figure 5.7). The histogram of galactocentric distance demonstrates that velocities have been measured for GCs located at large galactocentric radii, up to around 5-7 R_e. In the following analysis NGC 3923 is assumed to have an effective radius of 53.4 arcseconds as reported by Fukazawa et al. (2006) and originally determined by Faber et al. (1989). The use of this value which differs slightly from the value of 43.8 arcseconds quoted in Chapter 4 allows consistency between the present study and the X-ray one of Fukazawa et al. (2006). The measurement of GC kinematics at such large radii is important as at such distances the mass of the stellar component should be negligible, making the detection of any dark matter component much simpler than attempts made in the inner regions of galaxies where the baryonic component dominates.

5.4.2 Rotation of the GC system of NGC 3923

Using the same approach as outlined in Section 4.5.1 the rotation of the GC system of NGC 3923 has been examined. As in Section 4.5.1 a non-linear least squares fit to the equation:

$$V(\theta) = V_{rot}\sin(\theta - \theta_0) + V_0$$

was carried out, in this case for each of the three GC samples, total, red sub-population

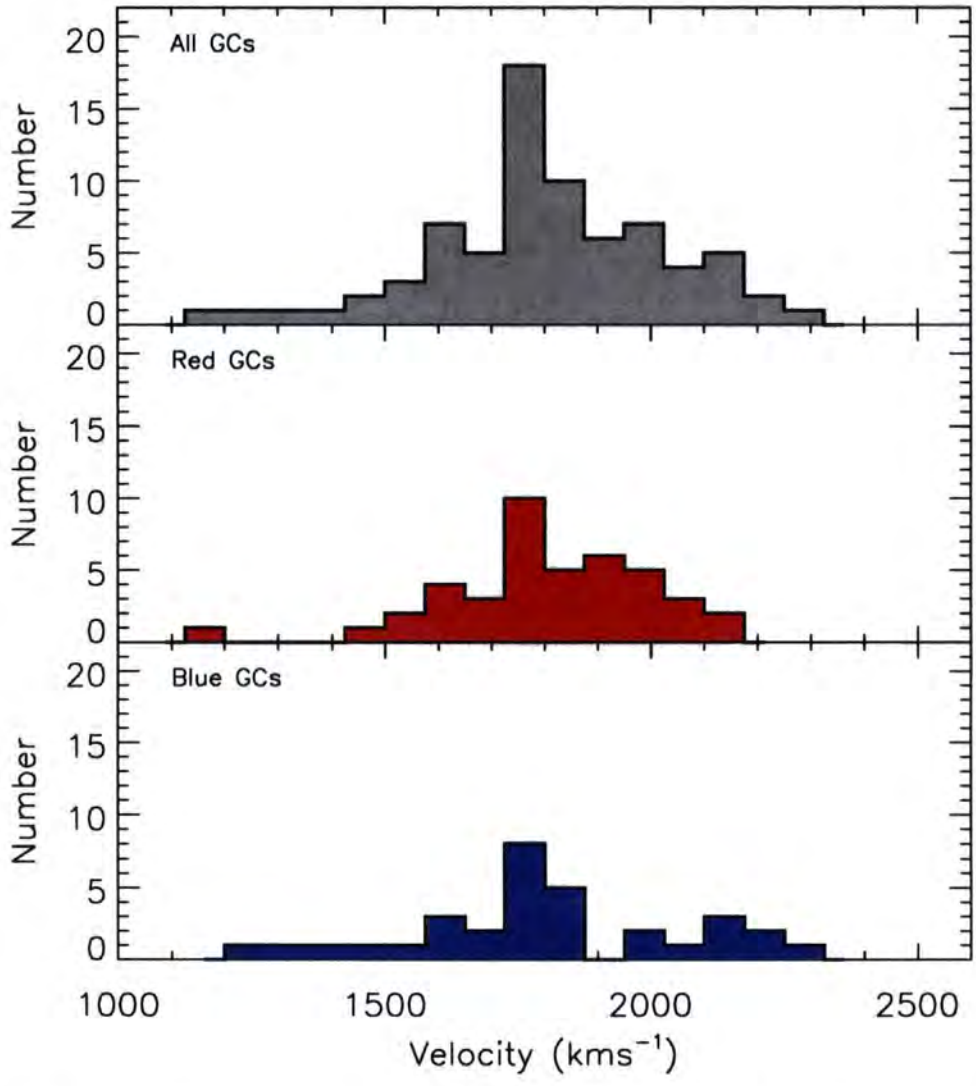

Figure 5.6: Histogram of GC velocities, upper panel shows all 74 GCs studied here, middle panel shows the 42 velocities of the red GCs, the lower panel is for the 32 blue GCs.

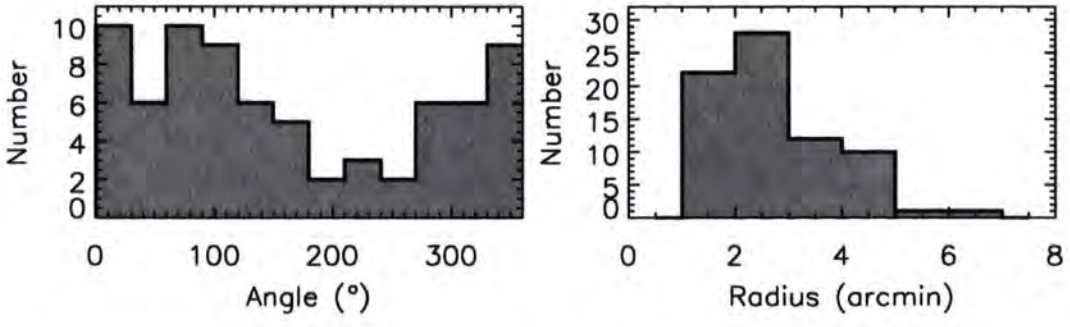

Figure 5.7: Histograms of azimuthal angle and galactocentric radius for the 74 NGC 3923 GCs.

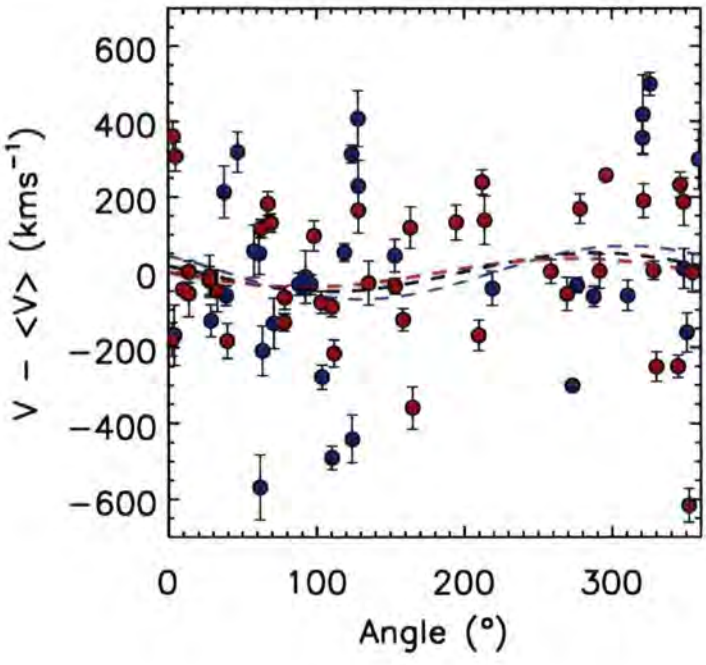

Figure 5.8: Velocity versus azimuthal angle for all 74 NGC 3923 GCs. Blue circles are blue GCs, Red circles are red GCs. The black dashed line represents the best-fitting rotation curve for the full sample, the blue and red dashed lines are the best-fitting rotation curves for the red and blue sub-populations. The implied rotation amplitudes of 37.6±45.6 kms^{-1} (red), 70.5±65.4 kms^{-1} (blue) and 51.2±36.7 kms^{-1}(total) all of which are not statistically significant.

and blue sub-population. In practice the value of V_0 was allowed to vary between samples. However the overall effect of this was small, as the mean velocities of the three groups varied by less than 10 kms^{-1}. The GC mean velocity and systemic velocity of NGC 3923 differ by approximately 70 kms^{-1}. This means that using the GC mean velocity instead of the systemic velocity could be masking some rotation. To assess whether or not this effect is significant, the rotation of the total sample was re-estimated using the mean GC velocity ±70 kms^{-1}, in neither case was the result significantly changed. Figure 5.8 shows the best fit rotation curves derived using this procedure, in all three cases no significant detection of rotation is made.

The lack of rotation observed in the GC system is consistent with the similarly small amount of rotation found for the integrated light of NGC 3923, either found using velocities determined from the observations in Section 4.5.1, or in longslit studies by Carter et al. (1998) and Koprolin & Zeilinger (2000).

5.4.3 Velocity Dispersion

Figure 5.9 presents the radial behaviour of the velocity dispersion of the GC system for the total (top), red subpopulation (middle) and blue subpopulation samples respectively. In each case the velocity dispersion was estimated using the lowess estimator (Gebhardt et al., 1994; Gebhardt & Fischer, 1995), which estimates the velocity variance at each point by fitting a least squares linear fit to the individual points in some kernel around the point in question. The relative importance of each point in the fit is weighted by the inverse square of the distance between the point being fitted and the others within the kernel. The velocity dispersion is simply estimated as the square root of the variance measured by the lowess method. As a check of consistency this method was compared with the velocity dispersion estimations produced by the maximum likelihood method; for any reasonable bin size (minimum number of GCs per bin > 15) the maximum likelihood method recovered velocity dispersions which did not differ significantly from those found using the lowess method.

Figure 5.9 demonstrates that within the errors the velocity dispersion profile of each sample is constant. Also of interest is the fact that velocity dispersions measured for the integrated light of the galaxy (blue squares) using the method outlined in Section 4 are also consistent with the same constant value. The implications of these two results are best understood through an examination of simple dynamical models of the NGC 3923 system.

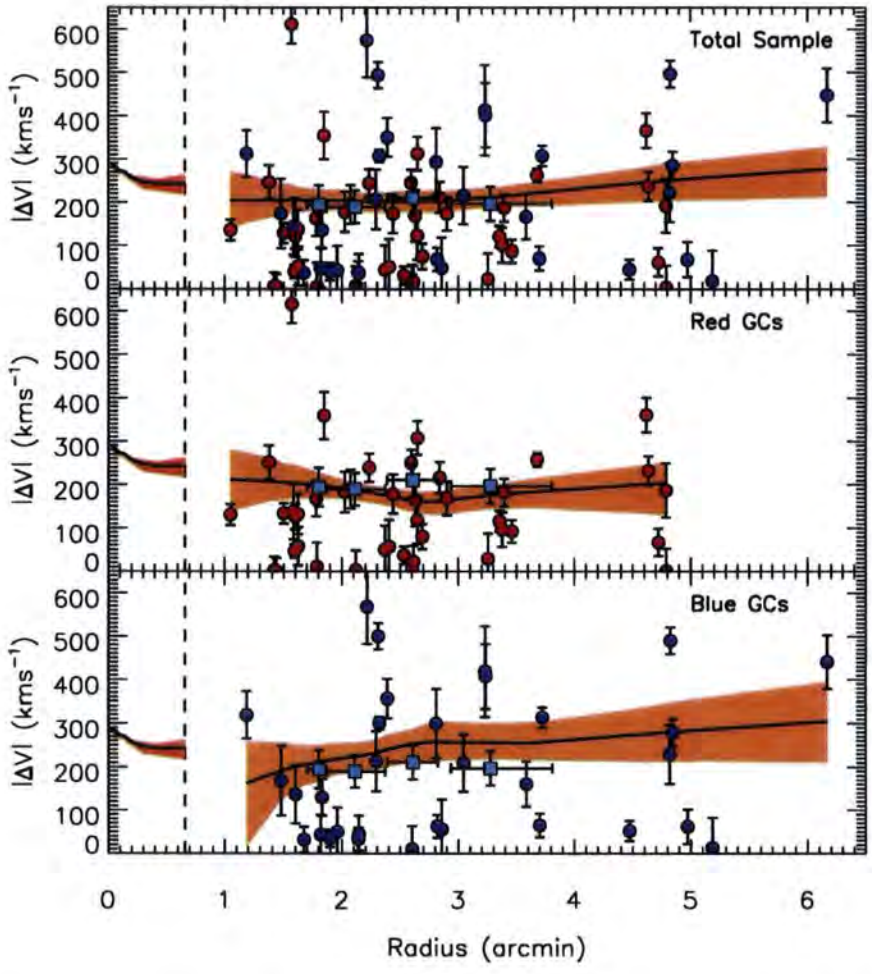

Figure 5.9: Velocity dispersion versus radius for NGC 3923 GCs. **Top Panel** : The circles are the GC velocities, the solid black line is the lowess estimator fit to the GC data, with the orange shaded region defining the 68% confidence bands of the fit. The orange region interior to (to the left of) the dashed black vertical line is the velocity dispersion for the inner regions of NGC 3923 as measured by Carter et al. (1998). The blue squares represent the velocity dispersion measurements of the spheroid of NGC 3923 made using the method presented in Chapter 4. **Middle and Bottom Panels** : As in top panel, but for the red and blue GC subsamples respectively.

5.4.4 Dynamical Models

There are two approaches generally in use to measure the M/L profiles of galaxies using dynamical tracers such as globular clusters. The present state of the art is to use orbit-based models (e.g. Gebhardt et al. (2003); Thomas et al. (2005b)). However at present the small number of clusters and the lack of an accurate cluster number density profile make this approach impractical. Therefore the simpler isotropic modelling approach shall be used to provide a first estimate of the variation of M/L with radius in NGC 3923.

The model applied here is identical to that implemented in Pierce et al. (2006a) for the NGC 3379 system. The model is non-parametric and assumes isotropy as outlined in Gebhardt & Fischer (1995). Additionally the model assumes that the potential is spherical, an approximation that should hold reasonably true due to the relatively low ellipticity of NGC 3923 and especially its GC system which is also seen to be close to circularly distributed (F. Faifer private communication). The kinematic data used is a combination of stellar kinematic data for the inner 40 arcsec from Carter et al. (1998) and the GC velocity dispersion estimates provided by the lowess smoothing described in Section 5.4.3. The other required input is an estimate of the distribution of the particles acting as dynamical tracers. Ideally this consists of the surface brightness profile (for the regions with stellar kinematics) and the GC number density profile (for the regions with kinematics determined from the GCs). In the case of NGC 3923 accurate GC number density profiles do not yet exist and as such the stellar surface brightness profile must be used at all radii for both components. In practice, although not ideal, this approximation should not prove to be of major concern as in most galaxies studied so far the distribution of the GCs (especially the red GCs) matches the surface brightness profile of the galaxy extremely well, see for example Forbes et al. (2004) for the example of NGC 4649 or Tamura et al. (2006) for the case of M87 and NGC 4552. It should however be noted that should the distribution of GCs prove to be significantly shallower than that of the surface brightness of the galaxy the implied M/L ratio will be changed. The surface brightness profile used here is a V band profile which was kindly provided by David B. Fisher; as a check the R band profile of Jedrzejewski (1987) was transformed into the V band by matching in the overlap region, with no significant differences between the profiles observed.

The actual procedure used to determine the model is relatively straightforward; the observed surface brightness profile and velocity dispersion profiles must first be deprojected using an Abel deprojection of the form:

$$l(r) = -\frac{1}{\pi}\int_r^{R_{\max}} \frac{\mathrm{dI(R)}}{\mathrm{dR}} \frac{\mathrm{dR}}{\sqrt{R^2 - r^2}} \tag{5.1}$$

$$l(r)v_r^2(r) = -\frac{1}{\pi}\int_r^{R_{\max}} \frac{\mathrm{d[I(R)}\sigma_{\mathrm{p}}^2\mathrm{(R)]}}{\mathrm{dR}} \frac{\mathrm{dR}}{\sqrt{R^2 - r^2}} \tag{5.2}$$

where $l(r)$, I(R), σ_p^2(R) and $v_r(r)$ are the luminosity density, surface brightness profile, projected velocity dispersion profile and finally the deprojected surface brightness profile. The deprojected profiles for surface brightness and velocity dispersion can then be used with the isotropic nonrotating Jeans equation to determine the total mass profile $\mathscr{M}(r)$ and total mass density $\rho(r)$. The required Jeans equation has the form:

$$\mathscr{M}(r) = -\frac{rv_r^2}{G}\left(\frac{\mathrm{d\,ln}l}{\mathrm{d\,ln}r} + \frac{\mathrm{d\,ln}v_r^2}{\mathrm{d\,ln}r}\right) \tag{5.3}$$

$$\rho(r) = \frac{1}{4\pi r^2}\frac{\mathrm{d}\mathscr{M}}{\mathrm{d}r} \tag{5.4}$$

There are several issues regarding the smoothing required for these functions, which are discussed more fully in Gebhardt & Fischer (1995). With the output of Equation 5.4 it is a simple matter to determine the M/L profile by dividing the total mass density by the luminosity density calculated previously.

In the upper panel of Figure 5.10 the solid black line displays the velocity dispersion profile produced by combining the stellar data within the inner 40 arcsec with the GC data outside of 40 arcsec. The orange shaded regions represent the 1-σ confidence bands in the measured velocity dispersion estimated by 100 Monte-Carlo resimulations of the data. The red and blue lines represent the measured velocity dispersions of the red and blue GC subpopulations respectively, the black dashed line is the expected isotropic velocity dispersion profile predicted for a constant M/L$_V$ of 6.5 given the input surface brightness profile. This choice of M/L$_V$ was made so that the expected isotropic velocity dispersion profile would match the observed one inside of 1R$_e$ where galaxies are thought to be dominated by baryons as the effect of any DM halo should be negligible. The blue squares again represent the measured velocity dispersion of the galaxy as derived in Chapter 4 using the MOS extraction method. It is important to note that these points are not involved in the model fit in any way, they are merely illustrative of the fact

that the GCs and stellar components appear to have similar velocity dispersions. This figure demonstrates that at larger radii the GC velocity dispersion profile becomes increasingly more inconsistent with the simple isotropic constant-M/L model. The choice of subsample is also relatively inconsequential with all three subsamples inconsistent with the model at their outermost points.

The middle panel of Figure 5.10 uses the information from the upper panel to produce the projected M/L_V profile, the horizontal dashed line represents the constant M/L_V=6.5 model which fits the inner regions of NGC 3923 reasonably well. Again the choice of sample does not affect the conclusion that beyond 2-3R_e the M/L ratio of NGC 3923 begins to rise, a result seen in several previous studies of the GC systems of early-type galaxies (Pierce et al., 2006a; Bridges et al., 2006). As was found in the study of NGC 4649 (Bridges et al., 2006) the M/L profile predicted by the GCs and the X-ray profile (black dot-dash line) are in good agreement, especially at larger radii. In this case the X-ray mass profile of Fukazawa et al. (2006) was divided by the V-band light profile used here in order to determine the X-ray M/L_V profile.

The two sets of asterisks on the plot present SSP predictions for the M/L_V ratio given the known SSP ages and metallicities of the stellar population of the integrated light at these two radii (from the data presented in Chapter 4 for the larger radii points, and from Thomas et al. (2005a) for the inner measurements). The SSP models utilised were from Maraston (2005) for Salpeter IMF (blue asterisks) and Kroupa IMF (green asterisks). The small disagreement between these SSP predictions and the value of M/L_V observed, especially in the inner regions is interesting. In part the disagreement in the inner regions is due to the fact that the SSP age fits are luminosity weighted, and hence tend to reflect the youngest age component present. Therefore while the majority of the stellar population present may in fact have an age and metallicity (and hence M/L) more similar to that seen at large radii, the value measured in the inner region is biased by the presence of a younger component towards lower M/L. It is nevertheless interesting that the M/L_V implied by both the SSP models and the X-ray profile agree and are considerably lower than that required to fit the stellar kinematics in the inner region. Perhaps this indicates that the dynamics of stars within the inner regions are somewhat complicated, and/or that the X-ray gas within the inner regions is not currently in equilibrium. The fact that the stellar population at larger radii is predicted to have M/L ratios in better agreement with the constant M/L required to fit the inner regions kinematics also lends

some support that the correct choice of constant M/L was chosen. Because the change in predicted M/L from the inner regions to $3R_e$ is only a factor of 2, this also demonstrates the impossibility of explaining the observed increasing M/L ratio determined from the GC kinematics as being due to changes in stellar population alone. One further way in which the agreement between the SSP models and the kinematical estimate of M/L can be improved is to change the assumed distance of NGC 3923. At present a distance of 17.9 Mpc for NGC 3923 is adopted. This distance is the one used in the Fukazawa et al. (2006) X-ray analysis and hence simplifies comparison between the two studies. However if a distance of 22.9 Mpc is used instead (this is the value found by Tonry et al. (2001) using the SBF method), the required mass-to-light ratio to fit the inner kinematics drops to a value of 5 in the V band, much more consistent with the SSP estimates at large radii. Overall this change of distance does not affect the conclusion that dark matter must be present, it merely changes the assumed constant M/L value displayed by the stellar population of NGC 3923.

5.5. Discussion

An examination of the GC radial velocities has not detected any rotation in the NGC 3923 GC system, a finding which is in agreement with studies of the kinematics of the integrated light of NGC 3923 which also find little or no rotation (e.g. Carter et al. (1998); Koprolin & Zeilinger (2000), Chapter 4 of this thesis). This lack of rotation in the GC systems of early-type galaxies is not uncommon, with little or no rotation having been observed in the GC systems of NGC 4649 (Bridges et al., 2006), NGC 1399 (Richtler et al., 2004), NGC 3379 (Bergond et al., 2006) and NGC 4472 (Côté et al., 2003). Some GC systems however do display significant rotation, for example NGC 5128 (Woodley et al., 2007) and M87 (Côté et al., 2001). The cause of this variation maybe partly due to projection effects. Nevertheless the current observations do not fit comfortably with theoretical simulations of galaxy formation. These simulations tend to predict that significant amounts of angular momentum should be found in the outer regions of galaxies, especially in cases where the galaxies formed in major merger events in the more recent past (i.e. $z < 3$) (Vitvitska et al., 2002). To explain this disagreement it may be possible to call on angular momentum transport to move the angular momentum beyond the radii to which current GC studies are presently sensitive; only an extension of these studies to

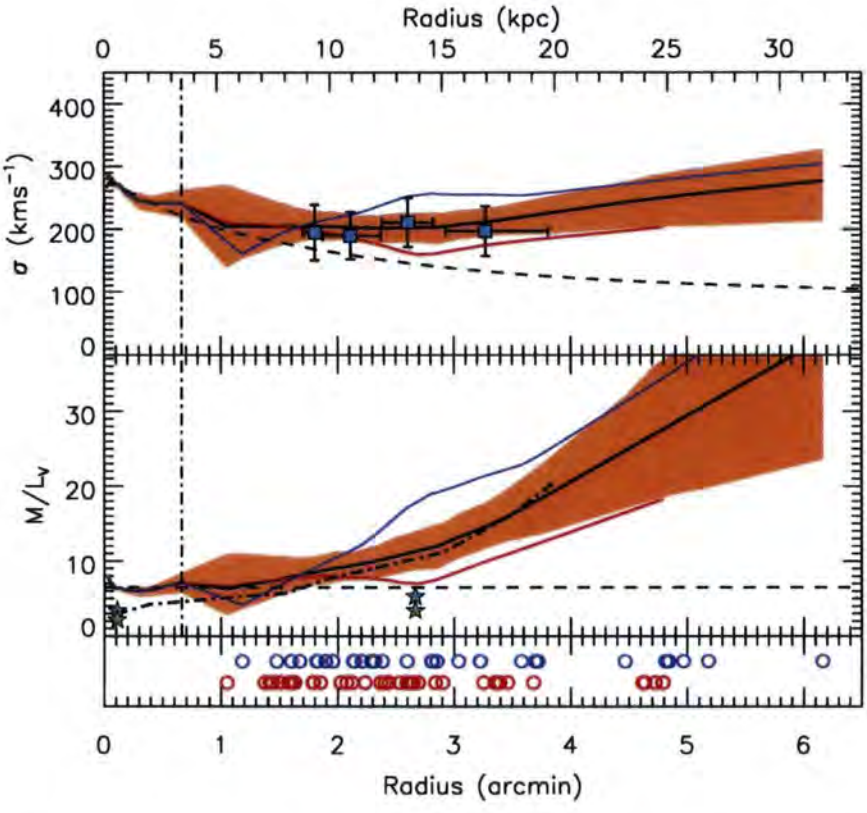

Figure 5.10: **Upper Panel** : Velocity dispersion versus projected radius for NGC 3923 GCs and (to the left of the vertical dashed line) stellar data. The solid black line is the GC data presented in Figure 5.9 with 1σ errors (orange shaded region). The solid red and blue lines show the equivalent data for the red and blue subpopulations (split at g-i = 1.0 mag). The dashed black line shows the expected velocity dispersion profile for a constant M/L model. **Lower Panel** : $(M/L)_V$ versus projected radius for NGC 3923 stars (interior to vertical dashed line), GCs (solid black, red and blue lines) and X-ray data (black dot-dash line, Fukazawa et al. (2006)). The asterisks represent SSP model predictions for the M/L_V for the stellar population given the age and metallicity measured for the population either in Chapter 4 (larger radii point) or by Thomas et al. (2005a) (small radii point). The SSP models come from Maraston (2005) for Salpeter IMF (blue asterisks) and Kroupa IMF (green asterisks). Circles at the bottom of the panel present the radial distance of all 74 GCs split by colour.

even larger galactocentric radii would be able to determine if this is indeed the case. This would most likely prove impossible for all but the most massive galaxies with the richest GC systems, as smaller galaxies simply would not have enough GCs at large radii to make such a measurement possible. In the specific case of NGC 3923 the observed lack of rotation in the GC system, and the implied lack of angular momentum at large radii is consistent with the picture developed in Chapter 4 that the formation of at least the shell structures of this galaxy could not be due to a significant merger event. Such an event would be expected to create significant numbers of young clusters with considerable rotation at larger radii, neither of which is observed in this case.

The simple spherical isotropic model of the dynamics of NGC 3923 presented here supports the suggestion that this galaxy inhabits a DM halo. The observed M/L_V profile of NGC 3923 is found to be constant at a value of around 6-7 out to slightly beyond $1R_e$ (40-55 arcsec depending on the band), beyond which it then begins to rise sharply, reaching a value of close to M/L_V=20 at 5 R_e. The observed M/L_V in the outer parts is in good agreement with that determined from the X-ray observations of Fukazawa et al. (2006), adding this galaxy to the growing list in which X-ray and GC estimates of M/L both indicate the presence of significant quantities of DM. One caveat however is that without accurate GC number density profiles the derived values of the M/L profile are somewhat uncertain. The fact that the GC profiles determined for the inner regions of NGC 3923 from HST imaging by Sikkema et al. (2006) are significantly shallower than the galaxy surface brightness profile would indicate that the measured M/L may be systematically overestimated. As a test of the level of this effect the input surface brightness profile was adjusted in the outer regions, where the kinematics from the GCs are used, such that the surface brightness profile matched the shallower GC surface density profile seen by Sikkema et al. (2006). It was found that while the required DM in the inner regions was reduced, and the profile became inconsistent with the X-ray profile, significant amounts of DM were still required, but it was only at larger radii that the DM became significant (3 arcmin versus ~1arcmin). Overall the observed flat velocity dispersion profile found for the GC system of NGC 3923 makes it extremely difficult to produce a DM-free model which fits the data without invoking unusual density profiles and/or orbits for the GCs. Further work, described below will help to determine if such orbital structures are present in this galaxy.

A brief comparison with the results of similar studies into the M/L profiles of other

elliptical galaxies with GC kinematics measurements shows that NGC 3923 is in no way unusual. Similar studies carried out into the kinematics of NGC 3379 (Pierce et al., 2006a) and NGC 4649 (Bridges et al., 2006) GC systems implied very similar M/L profiles in these galaxies. It is possible that the M/L profile of NGC 3923 is slightly less steep than those observed in NGC 4649 and NGC 3379 but with the large uncertainties this is not conclusive. What can be stated for this small sample is that despite a wide range of absolute magnitudes (M_B= -19.93 (NGC 3379), -20.46 (NGC 3923 assuming D=17.9Mpc) and -21.38 (NGC 3379)), environment (small group to Virgo cluster) and globular cluster specific frequencies (S_N= 1.1 (NGC 3379), 4.1 (NGC 4649) and 5.6 (NGC 3923)) all three galaxies display robust evidence for a significant dark matter component. These three galaxies can be combined with the growing list of galaxies for which studies of GC dynamics indicate significant quantities of DM. This result appears to be in contradiction with the conclusions found using other dynamical tracers such as planetary nebulae (Romanowsky et al., 2003), with contradictory results found sometimes within the same galaxy for different tracers (see Pierce et al. (2006a) for the example of NGC 3379).

Future work with this dataset will add the accurate GC surface density profiles required to more accurately constrain the M/L profile of NGC 3923. This extra information will allow more complicated models to be implemented, in particular orbit-based models which will allow an examination of the degree of isotropy found in the orbits of the NGC 3923 GCs. Of particular interest will be an investigation of the similarities and differences of the orbital structure of the red and blue sub-populations. Most galaxies appear to have GC systems which are essentially isotropic but others exist where one or more sub-populations can be tangentially biased at some radii (Côté et al., 2003; Richtler et al., 2004). Differences in the orbital structure of GC subpopulations can provide powerful clues on the formation histories of the GC populations and hence the host galaxies. In the case of NGC 3923 the observed differences in velocity dispersion profiles between red and blue sub-populations already hint at differences in their kinematics and orbital parameters. Only more comprehensive modelling and an increase in sample size will confirm if this is indeed the case.

5.6. Conclusions

This Chapter has presented Gemini/GMOS spectra of 74 GCs associated with NGC 3923 measured using MOS and N&S techniques. Their radial velocities have been combined with stellar kinematics and used to constrain the DM content of the galaxy. The main conclusions are:

1. The GC velocity dispersion profile for the full sample is constant with radius; within the errors the red and blue subpopulations are also consistent with the same value of around 200 kms^{-1}.

2. The velocity dispersion of the integrated light of NGC 3923 at large radii is also consistent with the same velocity dispersion profile.

3. There is no significant evidence for rotation in any of the GC sub-samples studied here.

4. A simple spherical isotropic model strongly supports the presence of a massive DM halo in NGC 3923. The implied M/L profile determined from this analysis is also in excellent agreement with that found through the study of the X-ray emission from the hot gas halo surrounding the galaxy by Fukazawa et al. (2006).

Chapter 6

Conclusions

This thesis has presented a series of spectroscopic observations of the stellar populations and kinematics of S0 galaxies and the GC system of the shell elliptical galaxy NGC 3923. The main purpose of these observations is to draw inferences about the formation and evolution processes of these early-type galaxies.

The main conclusions of this thesis are listed in the following sections along with prospects for future work.

6.1. S0 Galaxies

Chapters 2 and 3 presented investigations of the kinematics and stellar populations of S0 galaxies. The main conclusions of these chapters were:

- The edge-on S0 galaxy NGC 3115 has a significant stellar disc component, which is both kinematically and chemically distinct from the spheroidal component of this galaxy. The disc is younger (~5-8 vs 10-11 Gyr), displays a shallower metallicity gradient and a lower value of [α/Fe] than the spheroid of NGC 3115.
- The age, metallicity and [α/Fe] of the spheroid of NGC 3115 at larger radii is entirely consistent with that displayed by the red GC sub-population, strongly hinting at a common origin for the two components.
- The GC system of NGC 3115 is observed to rotate in the same sense as both the disc and spheroidal components of NGC 3115.
- In the enlarged study of 18 nearby edge-on S0 galaxies (including NGC 3115) all 18 galaxies similarly displayed regular disc-like kinematics. The lack of any large-

scale counter rotation in the discs is evidence against the formation of these galaxies through major merger events.

- In all but two cases (NGC 3115 and NGC 3585) simple two component bulge+disc models provide acceptable fits to 2MASS NIR imaging of the galaxies. In the interesting cases of NGC 3115 and NGC 3585 an additional large-scale spheroidal component is required to fit the data. This additional component is perhaps indicative of a different formation history for these two galaxies; the kinematics of NGC 3585 in particular imply that this galaxy is composed of a rotating disc component embedded within a nonrotating elliptical as suggested by Scorza & Bender (1995) and Fisher (1997), this could be evidence of a merger origin for this galaxy.

- 72% of the S0 sample display some level of ionised gas emission. This emission is often kinematically complex and not simply due to rotation in the plane of the disc. In some cases this gas can be tied to material stripped from nearby companions, such as in the case of NGC 1596 and its companion NGC 1602 and perhaps in the case of NGC 7332 and its companion NGC 7339. This fraction (72%) is close to that seen in previous studies of S0-emission line gas in S0s such as the SAURON project (Sarzi et al., 2006) which found 83% of their 24 S0s displayed ionised gas emission.

- The stellar populations of the S0 sample broadly speaking exhibit one of two behaviours. In the first class, which is similar to that described for NGC 3115, the bulge is an old classical type bulge, with a strongly negative metallicity gradient. In this case the major and minor axes (disc-and-bulge dominated respectively) display very different stellar populations, with the major axis displaying a much shallower metallicity gradient and younger age. In the second class which appears to be the result of a younger pseudobulge component, the major and minor axes display broadly similar stellar populations.

- The frequency of disturbed ionised gas emission would seem to fit broadly into a hierarchical cosmological framework with the gas generally being the result of stripping from companions or the result of the disruption of smaller companions as is currently seen in the ongoing tidal disruption of Milky Way (MW) satellites by the MW itself.

- The S0 TFR relation of this sample of 18 S0s, plus an additional 5 Fornax cluster

S0s from the sample of Bedregal et al. (2006a,b), is found to be offset from that of the spiral TFR by ΔM_B=1.92 ±0.15 mag when assuming the spiral TFR slope from Tully & Pierce (2000). The scatter in the TFR for S0 galaxies is found to be 0.86 ±0.13 mag, of which the major component (0.7 mag) is found to be intrinsic and not due to observational errors. These conclusions are in excellent agreement with those of Bedregal et al. (2006a).

- The magnitude of the offset from the spiral TFR for individual S0s is found to strongly correlate with both disc and central (bulge) age, in the sense expected, and with approximately the right magnitude, if S0s represent a population of normal spirals which ceased forming stars at some time in the past and have since passively evolved to the present.

Taken together these observations strongly support the theory that S0 galaxies are the descendants of normal spiral galaxies in which star formation ceased at some point in the past. The magnitude of the scatter of the S0 TFR, and the wide variation in the SSP ages of the S0 discs, indicates that this conversion of spirals to S0s has been ongoing for a significant amount of time, a conclusion which is in agreement with the observation that there was an increase in the cluster S0 fraction since at least z=1 (Dressler et al., 1997; Smith et al., 2005; Postman et al., 2005). In the preliminary analysis presented here no obvious trends in galaxy structural properties or stellar populations with environment are apparent. This is somewhat unexpected given the observation that the fraction of early-types (and hence S0s) is observed to be relatively constant in field environments since z=1, while the fraction of S0s in groups and clusters is observed to increase (Smith et al., 2005). However, given the fact that the complete bulge-to-disc spectroscopic decomposition has not yet been completed, and given the small sample size, it is perhaps not surprising that no unambiguous signal of environmental dependence is detected.

The observation of a strong correspondence between the stellar populations of the red GC sub-population and that of the spheroid of NGC 3115 is also particularly striking. It has long been known that the distribution of red sub-population GCs more closely matches the diffuse stellar content of ETGs than does the blue GC sub-population. The observed correspondence between the stellar populations of the red GCs and that of the integrated light of NGC 3115 at large radii only serves to strengthen the belief that the GC populations of galaxies are closely related to the spheroids of galaxies.

6.1.1 Future Work

With the extremely rich data-set in hand (plus additional S0s currently being observed) several extensions of the work presented here are of immediate interest, both in the comparison of the GCs and the stellar populations of S0s, and in the study of the formation of S0 galaxies.

The deep i-band imaging could be combined with the spectroscopic observations of both axes to allow a full spectroscopic bulge-to-disc decomposition. This procedure is of particular importance in cases such as NGC 3115 and NGC 3585 where a significant spheroidal halo biases estimates of the disc parameters. This procedure will allow much more accurate estimations of stellar population parameters and their gradients within individual structures such as discs, bulges or halos. Such data will do much to constrain the formation processes responsible for building up these structures, and also the processes responsible for spiral to S0 transformation.

With the complete data set and more accurate estimates of the ages, metallicities and α-element abundances of the stellar structures of galaxies it will be possible to probe more deeply for any environmental dependence of either galaxy properties or of mechanisms for spiral to S0 transformation.The increased sample size combined with additional lower-luminosity S0s will allow an attempt to determine both the slope and zeropoint of the S0 TFR. Comparison of these values, determined in several bands (including the 2MASS NIR bands) will do much to determine the universality of the TFR slope. Any differences in observed slope for spiral and S0 TFRs would be of particular interest in constraining formation scenarios.

The correspondence between the kinematics and stellar populations of the spheroids of NGC 1380, NGC 3115 and NGC 3585 with their GC populations should also be examined. Spectroscopic observations of the GC system of NGC 1380, NGC 3115 and NGC 3585 have been published by Puzia et al. (2004, 2005), with additional GC spectroscopy of NGC 3115 GCs having been obtained recently by our group. By expanding the number of galaxies which have high S/N spectroscopic observations of both the integrated light and the GC population it will be possible to determine how common the close correspondence found for NGC 3115 actually is. In the case of NGC 3115 a significant library of GC spectroscopy now exists, so that more advanced analyses can be attempted which construct the observed spheroidal stellar population from the GC stellar populations - proving whether or not GCs really are the building blocks of galaxy spheroids.

6.2. Elliptical Galaxies

Chapters 4 and 5 presented observations of the isolated luminous elliptical NGC 3923. In the following section the observed properties from this study are combined with others from the literature to examine the constraints on formation models for elliptical galaxies.

- The GC system of the shell elliptical NGC 3923 is found to display old ages (>10 Gyr), metallicities in the range [Z/H] = -1.8 to +0.35 and a approximately constant [α/Fe] of 0.3. The data displays no evidence for a significant intermediate age population of GCs, and the GC sub-populations are coeval within the errors. The red GC sub-population is found to have ages, metallicities and α-element enhancements consistent with those of the integrated light of the galaxy beyond $2R_e$.

- These findings are consistent with other observations which demonstrate that the formation of ETGs is essentially completed at redshifts greater than 2. The fact that observations of the inner region of NGC 3923 suggest a younger age (Denicoló et al., 2005; Thomas et al., 2005a) is perhaps indicative of a minor merger event which led to gas accretion and star formation in the inner regions of this galaxy. This event may be related to the event which caused the formation of the shell system of NGC 3923. Only higher-S/N longslit observations of the galaxy will allow this theory to be examined.

- The observed strong correspondence between GC and spheroid stellar properties in this elliptical galaxy is further proof of the close connection between spheroid and GC formation.

- An examination of the kinematics of the GC system of NGC 3923 shows no statistically significant evidence of any rotation in either sub-population, a finding in line with the lack of significant rotation found in the integrated light of NGC 3923.

- The GC system and integrated light of NGC 3923 display consistent velocity dispersion profiles which are observed to remain constant with radius. The implementation of a simple spherical isotropic dynamical model demonstrates that significant amounts of Dark Matter are required to explain the observed constant velocity dispersions. The M/L profile produced is consistent with that determined from X-ray emission due to the hot halo gas surrounding NGC 3923.

These observations of the NGC 3923 GC system are in good agreement with the expectations of our current understanding of ETG formation. The stellar population of the GC system and the bulk of NGC 3923 at large radii is consistent with a formation event at early times (z>2). The observed high α-element enhancements of both the GCs and diffuse light also indicate that the formation event was fairly rapid. The complicating factor of the younger implied ages for the inner region of NGC 3923 can potentially be explained by the addition of a small frosting of younger stars formed in the inner regions after the hierarchical accretion of a small gas-rich companion. The observed M/L ratio determined from the GC kinematics is consistent with that found for several other ETGs using the same method and is strong evidence for the existence of a massive Dark Matter halo in this galaxy.

6.2.1 Future Work

Work still to be carried out with this data involves the comparison of the GC system of this galaxy with those of other ETGs and the improved dynamical modelling of the galaxy, its GC system and Dark Matter halo.

Our group has now compiled a reasonably large number (>100) of high-S/N GC spectra from a sample of 5 ETGs. Examination of the correlations between age, metallicity and [α/Fe] of this sample could potentially illuminate the early periods of galaxy formation.

The technique used to examine integrated light spectra at large radii at the same time as studying GC spectra could be used in several more galaxies. This method has the ability to study the integrated properties of galaxies to 4-5 R_e at the same time as carrying out in depth studies of the kinematics and stellar populations of GCs. The ability to compare the properties of GCs and integrated light at the same projected radii for the first time is potentially extremely useful in the study of the relationship between GCs and spheroidal components.

The NGC 3923 GC kinematics will be combined with improved GC density profiles to more accurately model the galaxy potential. Making use of either the X-ray mass profile, or one implied by the integrated light velocity dispersion profile to determine the galaxy potential, it will be possible to run more complex axisymmetric orbit-based models to place constraints on the GC orbital structure.

In recent years advances in instrumentation and the theoretical understanding of cosmol-

ogy have made possible great strides in the understanding of the formation and evolution of early-type galaxies, however the full picture remains incomplete. At present many important questions remain to be answered, such as determining the relative importance of various feedback mechanisms on the galaxy formation process, or in measuring the frequency and importance of mergers at more recent times. It is in answering such questions using techniques such as those utilised here that much room for significant advances in extragalactic astronomy are to be found.

Bibliography

Abadi, M. G., Moore, B., & Bower, R. G. 1999, MNRAS, 308, 947

Abraham, R. G., Glazebrook, K., McCarthy, P. J., Crampton, D., Murowinski, R., Jørgensen, I., Roth, K., Hook, I. M., Savaglio, S., Chen, H.-W., Marzke, R. O., & Carlberg, R. G. 2004, AJ, 127, 2455

Adelman-McCarthy, J. K., Agüeros, M. A., Allam, S. S., Allende Prieto, C., Anderson, K. S. J., Anderson, S. F., Annis, J., Bahcall, N. A., Bailer-Jones, C. A. L., Baldry, I. K., Barentine, J. C., Bassett, B. A., Becker, A. C., Beers, T. C., Bell, E. F., Berlind, A. A., Bernardi, M., Blanton, M. R., Bochanski, J. J., Boroski, W. N., Brinchmann, J., Brinkmann, J., Brunner, R. J., Budavári, T., Carliles, S., Carr, M. A., Castander, F. J., Cinabro, D., Cool, R. J., Covey, K. R., Csabai, I., Cunha, C. E., Davenport, J. R. A., Dilday, B., Doi, M., Eisenstein, D. J., Evans, M. L., Fan, X., Finkbeiner, D. P., Friedman, S. D., Frieman, J. A., Fukugita, M., Gänsicke, B. T., Gates, E., Gillespie, B., Glazebrook, K., Gray, J., Grebel, E. K., Gunn, J. E., Gurbani, V. K., Hall, P. B., Harding, P., Harvanek, M., Hawley, S. L., Hayes, J., Heckman, T. M., Hendry, J. S., Hindsley, R. B., Hirata, C. M., Hogan, C. J., Hogg, D. W., Hyde, J. B., Ichikawa, S.-i., Ivezić, Ž., Jester, S., Johnson, J. A., Jorgensen, A. M., Jurić, M., Kent, S. M., Kessler, R., Kleinman, S. J., Knapp, G. R., Kron, R. G., Krzesinski, J., Kuropatkin, N., Lamb, D. Q., Lampeitl, H., Lebedeva, S., Lee, Y. S., Leger, R. F., Lépine, S., Lima, M., Lin, H., Long, D. C., Loomis, C. P., Loveday, J., Lupton, R. H., Malanushenko, O., Malanushenko, V., Mandelbaum, R., Margon, B., Marriner, J. P., Martínez-Delgado, D., Matsubara, T., McGehee, P. M., McKay, T. A., Meiksin, A., Morrison, H. L., Munn, J. A., Nakajima, R., Neilsen, Jr., E. H., Newberg, H. J., Nichol, R. C., Nicinski, T., Nieto-Santisteban, M., Nitta, A., Okamura, S., Owen, R., Oyaizu, H., Padmanabhan, N., Pan, K., Park, C., Peoples, J. J., Pier, J. R., Pope, A. C., Purger, N., Raddick, M. J., Re Fiorentin, P., Richards, G. T., Richmond, M. W., Riess, A. G., Rix, H.-W., Rockosi, C. M., Sako, M., Schlegel, D. J., Schneider, D. P., Schreiber, M. R., Schwope,

A. D., Seljak, U., Sesar, B., Sheldon, E., Shimasaku, K., Sivarani, T., Smith, J. A., Snedden, S. A., Steinmetz, M., Strauss, M. A., SubbaRao, M., Suto, Y., Szalay, A. S., Szapudi, I., Szkody, P., Tegmark, M., Thakar, A. R., Tremonti, C. A., Tucker, D. L., Uomoto, A., Vanden Berk, D. E., Vandenberg, J., Vidrih, S., Vogeley, M. S., Voges, W., Vogt, N. P., Wadadekar, Y., Weinberg, D. H., West, A. A., White, S. D. M., Wilhite, B. C., Yanny, B., Yocum, D. R., York, D. G., Zehavi, I., & Zucker, D. B. 2008, ApJS, 175, 297

Aragón-Salamanca, A., Bedregal, A. G., & Merrifield, M. R. 2006, A&A, 458, 101

Arimoto, N. & Yoshii, Y. 1987, A&A, 173, 23

Armandroff, T. E. 1989, AJ, 97, 375

Armandroff, T. E. & Zinn, R. 1988, AJ, 96, 92

Ashman, K. M. & Zepf, S. E. 1992, ApJ, 384, 50

—. 1998, Globular Cluster Systems (Globular cluster systems / Keith M. Ashman, Stephen E. Zepf. Cambridge, U. K. ; New York : Cambridge University Press, 1998. (Cambridge astrophysics series ; 30) QB853.5 .A84 1998 ($69.95))

Baggett, W. E., Baggett, S. M., & Anderson, K. S. J. 1998, AJ, 116, 1626

Barr, J. M., Bedregal, A. G., Aragón-Salamanca, A., Merrifield, M. R., & Bamford, S. P. 2007, A&A, 470, 173

Baum, W. A. 1959, PASP, 71, 106

Beasley, M. A., Bridges, T., Peng, E., Harris, W. E., Harris, G. L. H., Forbes, D. A., & Mackie, G. 2008, MNRAS, 386, 1443

Beasley, M. A., Brodie, J. P., Strader, J., Forbes, D. A., Proctor, R. N., Barmby, P., & Huchra, J. P. 2004a, AJ, 128, 1623

Beasley, M. A., Forbes, D. A., Brodie, J. P., & Kissler-Patig, M. 2004b, MNRAS, 347, 1150

Beasley, M. A., Strader, J., Brodie, J. P., Cenarro, A. J., & Geha, M. 2006, AJ, 131, 814

Bedregal, A. G., Aragón-Salamanca, A., & Merrifield, M. R. 2006a, MNRAS, 373, 1125

Bedregal, A. G., Aragón-Salamanca, A., Merrifield, M. R., & Milvang-Jensen, B. 2006b, MNRAS, 371, 1912

Bekki, K. 1998, ApJ, 502, L133+

Bekki, K. & Couch, W. J. 2003, ApJ, 596, L13

Bekki, K., Couch, W. J., & Shioya, Y. 2002, ApJ, 577, 651

Bender, R. 1990, A&A, 229, 441

Bender, R., Burstein, D., & Faber, S. M. 1992, ApJ, 399, 462

Bender, R., Doebereiner, S., & Moellenhoff, C. 1988, A&AS, 74, 385

Bender, R., Saglia, R. P., & Gerhard, O. E. 1994, MNRAS, 269, 785

Bergond, G., Zepf, S. E., Romanowsky, A. J., Sharples, R. M., & Rhode, K. L. 2006, A&A, 448, 155

Bernardi, M., Nichol, R. C., Sheth, R. K., Miller, C. J., & Brinkmann, J. 2006, AJ, 131, 1288

Bernardi, M., Sheth, R. K., Annis, J., Burles, S., Eisenstein, D. J., Finkbeiner, D. P., Hogg, D. W., Lupton, R. H., Schlegel, D. J., SubbaRao, M., Bahcall, N. A., Blakeslee, J. P., Brinkmann, J., Castander, F. J., Connolly, A. J., Csabai, I., Doi, M., Fukugita, M., Frieman, J., Heckman, T., Hennessy, G. S., Ivezić, Ž., Knapp, G. R., Lamb, D. Q., McKay, T., Munn, J. A., Nichol, R., Okamura, S., Schneider, D. P., Thakar, A. R., & York, D. G. 2003, AJ, 125, 1866

Bertin, E. & Arnouts, S. 1996, A&AS, 117, 393

Beuing, J., Bender, R., Mendes de Oliveira, C., Thomas, D., & Maraston, C. 2002, A&A, 395, 431

Bower, G. A., Green, R. F., Bender, R., Gebhardt, K., Lauer, T. R., Magorrian, J., Richstone, D. O., Danks, A., Gull, T., Hutchings, J., Joseph, C., Kaiser, M. E., Weistrop, D., Woodgate, B., Nelson, C., & Malumuth, E. M. 2001, ApJ, 550, 75

Bower, R. G., Kodama, T., & Terlevich, A. 1998, MNRAS, 299, 1193

Bower, R. G., Lucey, J. R., & Ellis, R. S. 1992, MNRAS, 254, 601

Bower, R. G., Terlevich, A., Kodama, T., & Caldwell, N. 1999, in Astronomical Society of the Pacific Conference Series, Vol. 163, Star Formation in Early Type Galaxies, ed. P. Carral & J. Cepa, 211–+

Bridges, T., Gebhardt, K., Sharples, R., Faifer, F. R., Forte, J. C., Beasley, M. A., Zepf, S. E., Forbes, D. A., Hanes, D. A., & Pierce, M. 2006, MNRAS, 373, 157

Brough, S., Forbes, D. A., Kilborn, V. A., & Couch, W. 2006, MNRAS, 370, 1223

Brough, S., Proctor, R., Forbes, D. A., Couch, W. J., Collins, C. A., Burke, D. J., & Mann, R. G. 2007, MNRAS, 378, 1507

Bruzual, G. & Charlot, S. 2003, MNRAS, 344, 1000

Burstein, D., Faber, S. M., Gaskell, C. M., & Krumm, N. 1984, ApJ, 287, 586

Cantiello, M. & Blakeslee, J. P. 2007, ApJ, 669, 982

Capaccioli, M., Cappellaro, E., Held, E. V., & Vietri, M. 1993, A&A, 274, 69

Capaccioli, M., Vietri, M., & Held, E. V. 1988, MNRAS, 234, 335

Cappellari, M. & Emsellem, E. 2004, PASP, 116, 138

Carter, D., Thomson, R. C., & Hau, G. K. T. 1998, MNRAS, 294, 182

Cenarro, A. J., Beasley, M. A., Strader, J., Brodie, J. P., & Forbes, D. A. 2007, AJ, 134, 391

Chakrabarty, D. & Raychaudhury, S. 2008, AJ, 135, 2350

Chung, A. & Bureau, M. 2004, AJ, 127, 3192

Chung, A., Koribalski, B., Bureau, M., & van Gorkom, J. H. 2006, MNRAS, 370, 1565

Chung, A., van Gorkom, J. H., Kenney, J. D. P., & Vollmer, B. 2007, ApJ, 659, L115

Clem, J. L., Vanden Berg, D. A., & Stetson, P. B. 2008, AJ, 135, 682

Cole, S., Percival, W. J., Peacock, J. A., Norberg, P., Baugh, C. M., Frenk, C. S., Baldry, I., Bland-Hawthorn, J., Bridges, T., Cannon, R., Colless, M., Collins, C., Couch, W., Cross, N. J. G., Dalton, G., Eke, V. R., De Propris, R., Driver, S. P., Efstathiou, G., Ellis, R. S., Glazebrook, K., Jackson, C., Jenkins, A., Lahav, O., Lewis, I., Lumsden, S., Maddox, S., Madgwick, D., Peterson, B. A., Sutherland, W., & Taylor, K. 2005, MNRAS, 362, 505

Colless, M. 1999, Royal Society of London Philosophical Transactions Series A, 357, 105

Côté, P., Marzke, R. O., & West, M. J. 1998, ApJ, 501, 554

Côté, P., Marzke, R. O., West, M. J., & Minniti, D. 2000, ApJ, 533, 869

Côté, P., McLaughlin, D. E., Cohen, J. G., & Blakeslee, J. P. 2003, ApJ, 591, 850

Côté, P., McLaughlin, D. E., Hanes, D. A., Bridges, T. J., Geisler, D., Merritt, D., Hesser, J. E., Harris, G. L. H., & Lee, M. G. 2001, ApJ, 559, 828

Côté, P., West, M. J., & Marzke, R. O. 2002, ApJ, 567, 853

Cuillandre, J. C., Fort, B., Picat, J. P., Soucail, J. P., Altieri, B., Beigbeder, F., Duplin, J. P., Pourthie, T., & Ratier, G. 1994, A&A, 281, 603

D'Antona, F., Bellazzini, M., Caloi, V., Pecci, F. F., Galleti, S., & Rood, R. T. 2005, ApJ, 631, 868

de Vaucouleurs, G., de Vaucouleurs, A., Corwin, Jr., H. G., Buta, R. J., Paturel, G., & Fouque, P. 1991, Third Reference Catalogue of Bright Galaxies (Volume 1-3, XII, 2069 pp. 7 figs.. Springer-Verlag Berlin Heidelberg New York)

Debattista, V. P., Corsini, E. M., & Aguerri, J. A. L. 2002, MNRAS, 332, 65

Dekel, A., Stoehr, F., Mamon, G. A., Cox, T. J., Novak, G. S., & Primack, J. R. 2005, Nature, 437, 707

Denicoló, G., Terlevich, R., Terlevich, E., Forbes, D. A., & Terlevich, A. 2005, MNRAS, 358, 813

Djorgovski, S. & Davis, M. 1987, ApJ, 313, 59

D'Onofrio, M., Zaggia, S. R., Longo, G., Caon, N., & Capaccioli, M. 1995, A&A, 296, 319

Dressler, A. 1980, ApJ, 236, 351

Dressler, A., Faber, S. M., Burstein, D., Davies, R. L., Lynden-Bell, D., Terlevich, R. J., & Wegner, G. 1987, ApJ, 313, L37

Dressler, A., Oemler, A. J., Couch, W. J., Smail, I., Ellis, R. S., Barger, A., Butcher, H., Poggianti, B. M., & Sharples, R. M. 1997, ApJ, 490, 577

Eggen, O. J., Lynden-Bell, D., & Sandage, A. R. 1962, ApJ, 136, 748

Elson, R. A. W. 1997, MNRAS, 286, 771

Emsellem, E., Cappellari, M., Peletier, R. F., McDermid, R. M., Bacon, R., Bureau, M., Copin, Y., Davies, R. L., Krajnović, D., Kuntschner, H., Miller, B. W., & de Zeeuw, P. T. 2004, MNRAS, 352, 721

Emsellem, E., Dejonghe, H., & Bacon, R. 1999, MNRAS, 303, 495

Faber, S. M., Friel, E. D., Burstein, D., & Gaskell, C. M. 1985, ApJS, 57, 711

Faber, S. M. & Gallagher, J. S. 1976, ApJ, 204, 365

Faber, S. M. & Jackson, R. E. 1976, ApJ, 204, 668

Faber, S. M., Wegner, G., Burstein, D., Davies, R. L., Dressler, A., Lynden-Bell, D., & Terlevich, R. J. 1989, ApJS, 69, 763

Falcón-Barroso, J., Peletier, R. F., Emsellem, E., Kuntschner, H., Fathi, K., Bureau, M., Bacon, R., Cappellari, M., Copin, Y., Davies, R. L., & de Zeeuw, T. 2004, MNRAS, 350, 35

Fisher, D. 1997, AJ, 113, 950

Fisher, D., Franx, M., & Illingworth, G. 1996, ApJ, 459, 110

Forbes, D. A., Beasley, M. A., Brodie, J. P., & Kissler-Patig, M. 2001a, ApJ, 563, L143

Forbes, D. A., Brodie, J. P., & Grillmair, C. J. 1997, AJ, 113, 1652

Forbes, D. A., Brodie, J. P., & Larsen, S. S. 2001b, ApJ, 556, L83

Forbes, D. A., Raul Faifer, F., Carlos Forte, J., Bridges, T., Beasley, M. A., Gebhardt, K., Hanes, D. A., Sharples, R., & Zepf, S. E. 2004, MNRAS, 355, 608

Franx, M., Illingworth, G., & Heckman, T. 1989, AJ, 98, 538

Fukazawa, Y., Botoya-Nonesa, J. G., Pu, J., Ohto, A., & Kawano, N. 2006, ApJ, 636, 698

Fukugita, M., Hogan, C. J., & Peebles, P. J. E. 1998, ApJ, 503, 518

Gavazzi, G., Boselli, A., Scodeggio, M., Pierini, D., & Belsole, E. 1999, MNRAS, 304, 595

Gebhardt, K. & Fischer, P. 1995, AJ, 109, 209

Gebhardt, K., Pryor, C., Williams, T. B., & Hesser, J. E. 1994, AJ, 107, 2067

Gebhardt, K., Richstone, D., Tremaine, S., Lauer, T. R., Bender, R., Bower, G., Dressler, A., Faber, S. M., Filippenko, A. V., Green, R., Grillmair, C., Ho, L. C., Kormendy, J., Magorrian, J., & Pinkney, J. 2003, ApJ, 583, 92

González, J. J. 1993, Ph.D. Thesis, University of California, Santa Cruz

Gorgas, J., Efstathiou, G., & Aragon Salamanca, A. 1990, MNRAS, 245, 217

Goudfrooij, P., Hansen, L., Jorgensen, H. E., & Norgaard-Nielsen, H. U. 1994, A&AS, 105, 341

Goudfrooij, P., Strader, J., Brenneman, L., Kissler-Patig, M., Minniti, D., & Edwin Huizinga, J. 2003, MNRAS, 343, 665

Gunn, J. E. & Gott, J. R. I. 1972, ApJ, 176, 1

Harris, W. E. & van den Bergh, S. 1981, AJ, 86, 1627

Hinz, J. L., Rieke, G. H., & Caldwell, N. 2003, AJ, 126, 2622

Hinz, J. L., Rix, H.-W., & Bernstein, G. M. 2001, AJ, 121, 683

Hook, I. M., Jørgensen, I., Allington-Smith, J. R., Davies, R. L., Metcalfe, N., Murowinski, R. G., & Crampton, D. 2004, PASP, 116, 425

Hubble, E. P. 1936, Yale University Press

Illingworth, G. & Schechter, P. L. 1982, ApJ, 256, 481

Jarrett, T. H., Chester, T., Cutri, R., Schneider, S. E., & Huchra, J. P. 2003, AJ, 125, 525

Jedrzejewski, R. I. 1987, MNRAS, 226, 747

Jones, L. A. 1997, Ph.D thesis, Univ. North Carolina, Chapel Hill

Jordán, A., Blakeslee, J. P., Côté, P., Ferrarese, L., Infante, L., Mei, S., Merritt, D., Peng, E. W., Tonry, J. L., & West, M. J. 2007, ApJS, 169, 213

Kannappan, S. J., Fabricant, D. G., & Franx, M. 2002, AJ, 123, 2358

Kavelaars, J. J. 1998, PASP, 110, 758

Kawata, D. & Mulchaey, J. S. 2008, ApJ, 672, L103

Kissler-Patig, M., Brodie, J. P., Schroder, L. L., Forbes, D. A., Grillmair, C. J., & Huchra, J. P. 1998, AJ, 115, 105

Kobayashi, C. 2004, MNRAS, 347, 740

Koprolin, W. & Zeilinger, W. W. 2000, A&AS, 145, 71

Kormendy, J. 1977, ApJ, 218, 333

Kormendy, J. & Richstone, D. 1992, ApJ, 393, 559

Kuijken, K., Fisher, D., & Merrifield, M. R. 1996, MNRAS, 283, 543

Kundu, A. & Whitmore, B. C. 1998, AJ, 116, 2841

—. 2001a, AJ, 121, 2950

—. 2001b, AJ, 122, 1251

Kuntschner, H. 2000, MNRAS, 315, 184

—. 2004, A&A, 426, 737

Kuntschner, H., Lucey, J. R., Smith, R. J., Hudson, M. J., & Davies, R. L. 2001, MNRAS, 323, 615

Kuntschner, H., Ziegler, B. L., Sharples, R. M., Worthey, G., & Fricke, K. J. 2002, A&A, 395, 761

Larsen, S. S., Brodie, J. P., Beasley, M. A., & Forbes, D. A. 2002, AJ, 124, 828

Larsen, S. S., Brodie, J. P., Huchra, J. P., Forbes, D. A., & Grillmair, C. J. 2001, AJ, 121, 2974

Larsen, S. S. & Richtler, T. 2000, A&A, 354, 836

Larson, R. B. 1975, MNRAS, 173, 671

Laurikainen, E., Salo, H., Buta, R., & Knapen, J. H. 2007, MNRAS, 381, 401

Lee, H.-c. & Worthey, G. 2005, ApJS, 160, 176

Li, Z. & Han, Z. 2008, MNRAS, 385, 1270

Loubser, S. I., Sansom, A. E., & Soechting, I. K. 2007, in IAU Symposium, Vol. 241, IAU Symposium, ed. A. Vazdekis & R. F. Peletier, 422–423

Macchetto, F., Pastoriza, M., Caon, N., Sparks, W. B., Giavalisco, M., Bender, R., & Capaccioli, M. 1996, A&AS, 120, 463

Malin, D. F. & Carter, D. 1983, ApJ, 274, 534

Maraston, C. 1998, MNRAS, 300, 872

—. 2005, MNRAS, 362, 799

Martínez-Serrano, F. J., Serna, A., Domínguez-Tenreiro, R., & Mollá, M. 2008, MNRAS, 388, 39

Mathieu, A., Merrifield, M. R., & Kuijken, K. 2002, MNRAS, 330, 251

McCarthy, I. G., Frenk, C. S., Font, A. S., Lacey, C. G., Bower, R. G., Mitchell, N. L., Balogh, M. L., & Theuns, T. 2008, MNRAS, 383, 593

McLaughlin, D. E. 1999, AJ, 117, 2398

Mendel, J. T., Proctor, R. N., & Forbes, D. A. 2007, MNRAS, 379, 1618

Miley, G. K., Overzier, R. A., Zirm, A. W., Ford, H. C., Kurk, J., Pentericci, L., Blakeslee, J. P., Franx, M., Illingworth, G. D., Postman, M., Rosati, P., Röttgering, H. J. A., Venemans, B. P., & Helder, E. 2006, ApJ, 650, L29

Mobasher, B., Guzman, R., Aragon-Salamanca, A., & Zepf, S. 1999, MNRAS, 304, 225

Moore, B., Lake, G., & Katz, N. 1998, ApJ, 495, 139

Morganti, R., de Zeeuw, P. T., Oosterloo, T. A., McDermid, R. M., Krajnović, D., Cappellari, M., Kenn, F., Weijmans, A., & Sarzi, M. 2006, MNRAS, 371, 157

Mould, J. R., Huchra, J. P., Freedman, W. L., Kennicutt, Jr., R. C., Ferrarese, L., Ford, H. C., Gibson, B. K., Graham, J. A., Hughes, S. M. G., Illingworth, G. D., Kelson, D. D., Macri, L. M., Madore, B. F., Sakai, S., Sebo, K. M., Silbermann, N. A., & Stetson, P. B. 2000, ApJ, 529, 786

Neistein, E., Maoz, D., Rix, H.-W., & Tonry, J. L. 1999, AJ, 117, 2666

Nelan, J. E., Smith, R. J., Hudson, M. J., Wegner, G. A., Lucey, J. R., Moore, S. A. W., Quinney, S. J., & Suntzeff, N. B. 2005, ApJ, 632, 137

Norris, M. A., Sharples, R. M., & Kuntschner, H. 2006, MNRAS, 367, 815

O'Connell, R. W. 1976, ApJ, 206, 370

Pahre, M. A., de Carvalho, R. R., & Djorgovski, S. G. 1998, AJ, 116, 1606

Peletier, R. F. 1989, PhD thesis, , University of Groningen, The Netherlands, (1989)

Peletier, R. F., Davies, R. L., Illingworth, G. D., Davis, L. E., & Cawson, M. 1990, AJ, 100, 1091

Peng, C. Y., Ho, L. C., Impey, C. D., & Rix, H.-W. 2002, AJ, 124, 266

Peng, E. W., Jordán, A., Côté, P., Blakeslee, J. P., Ferrarese, L., Mei, S., West, M. J., Merritt, D., Milosavljević, M., & Tonry, J. L. 2006, ApJ, 639, 95

Persic, M., Salucci, P., & Stel, F. 1996, MNRAS, 281, 27

Pierce, M., Beasley, M. A., Forbes, D. A., Bridges, T., Gebhardt, K., Faifer, F. R., Forte, J. C., Zepf, S. E., Sharples, R., Hanes, D. A., & Proctor, R. 2006a, MNRAS, 366, 1253

Pierce, M., Bridges, T., Forbes, D. A., Proctor, R., Beasley, M. A., Gebhardt, K., Faifer, F. R., Forte, J. C., Zepf, S. E., Sharples, R., & Hanes, D. A. 2006b, MNRAS, 368, 325

Piotto, G., King, I. R., Djorgovski, S. G., Sosin, C., Zoccali, M., Saviane, I., De Angeli, F., Riello, M., Recio-Blanco, A., Rich, R. M., Meylan, G., & Renzini, A. 2002, A&A, 391, 945

Pipino, A., Puzia, T. H., & Matteucci, F. 2007, ApJ, 665, 295

Postman, M., Franx, M., Cross, N. J. G., Holden, B., Ford, H. C., Illingworth, G. D., Goto, T., Demarco, R., Rosati, P., Blakeslee, J. P., Tran, K.-V., Benítez, N., Clampin, M., Hartig, G. F., Homeier, N., Ardila, D. R., Bartko, F., Bouwens, R. J., Bradley, L. D., Broadhurst, T. J., Brown, R. A., Burrows, C. J., Cheng, E. S., Feldman, P. D., Golimowski, D. A., Gronwall, C., Infante, L., Kimble, R. A., Krist, J. E., Lesser, M. P., Martel, A. R., Mei, S., Menanteau, F., Meurer, G. R., Miley, G. K., Motta, V., Sirianni, M., Sparks, W. B., Tran, H. D., Tsvetanov, Z. I., White, R. L., & Zheng, W. 2005, ApJ, 623, 721

Proctor, R. N., Forbes, D. A., & Beasley, M. A. 2004, MNRAS, 355, 1327

Proctor, R. N., Forbes, D. A., Forestell, A., & Gebhardt, K. 2005, MNRAS, 362, 857

Proctor, R. N. & Sansom, A. E. 2002, MNRAS, 333, 517

Pulone, L., De Marchi, G., Covino, S., & Paresce, F. 2003, A&A, 399, 121

Puzia, T. H., Kissler-Patig, M., & Goudfrooij, P. 2006, ApJ, 648, 383

Puzia, T. H., Kissler-Patig, M., Thomas, D., Maraston, C., Saglia, R. P., Bender, R., Goudfrooij, P., & Hempel, M. 2005, A&A, 439, 997

Puzia, T. H., Kissler-Patig, M., Thomas, D., Maraston, C., Saglia, R. P., Bender, R., Richtler, T., Goudfrooij, P., & Hempel, M. 2004, A&A, 415, 123

Puzia, T. H. & Sharina, M. E. 2008, ApJ, 674, 909

Puzia, T. H., Zepf, S. E., Kissler-Patig, M., Hilker, M., Minniti, D., & Goudfrooij, P. 2002, A&A, 391, 453

Ramella, M., Geller, M. J., Pisani, A., & da Costa, L. N. 2002, AJ, 123, 2976

Reda, F. M., Proctor, R. N., Forbes, D. A., Hau, G. K. T., & Larsen, S. S. 2007, MNRAS, 377, 1772

Renzini, A. & Ciotti, L. 1993, ApJ, 416, L49+

Richtler, T. 2006, Bulletin of the Astronomical Society of India, 34, 83

Richtler, T., Dirsch, B., Gebhardt, K., Geisler, D., Hilker, M., Alonso, M. V., Forte, J. C., Grebel, E. K., Infante, L., Larsen, S., Minniti, D., & Rejkuba, M. 2004, AJ, 127, 2094

Richtler, T., Schuberth, Y., Hilker, M., Dirsch, B., Bassino, L., & Romanowsky, A. J. 2008, A&A, 478, L23

Romanowsky, A. J., Douglas, N. G., Arnaboldi, M., Kuijken, K., Merrifield, M. R., Napolitano, N. R., Capaccioli, M., & Freeman, K. C. 2003, Science, 301, 1696

Sakai, S., Mould, J. R., Hughes, S. M. G., Huchra, J. P., Macri, L. M., Kennicutt, Jr., R. C., Gibson, B. K., Ferrarese, L., Freedman, W. L., Han, M., Ford, H. C., Graham, J. A., Illingworth, G. D., Kelson, D. D., Madore, B. F., Sebo, K., Silbermann, N. A., & Stetson, P. B. 2000, ApJ, 529, 698

Sambhus, N., Gerhard, O., & Méndez, R. H. 2006, AJ, 131, 837

Sánchez-Blázquez, P., Forbes, D. A., Strader, J., Brodie, J., & Proctor, R. 2007, MNRAS, 377, 759

Sánchez-Blázquez, P., Peletier, R. F., Jiménez-Vicente, J., Cardiel, N., Cenarro, A. J., Falcón-Barroso, J., Gorgas, J., Selam, S., & Vazdekis, A. 2006, MNRAS, 371, 703

Sandage, A. & Visvanathan, N. 1978a, ApJ, 225, 742

—. 1978b, ApJ, 223, 707

Sarzi, M., Falcón-Barroso, J., Davies, R. L., Bacon, R., Bureau, M., Cappellari, M., de Zeeuw, P. T., Emsellem, E., Fathi, K., Krajnović, D., Kuntschner, H., McDermid, R. M., & Peletier, R. F. 2006, MNRAS, 366, 1151

Schlegel, D. J., Finkbeiner, D. P., & Davis, M. 1998, ApJ, 500, 525

Schuberth, Y., Richtler, T., Dirsch, B., Hilker, M., Larsen, S. S., Kissler-Patig, M., & Mebold, U. 2006, A&A, 459, 391

Scorza, C. & Bender, R. 1995, A&A, 293, 20

Serra, P. & Trager, S. C. 2007, MNRAS, 374, 769

Sharina, M. E., Afanasiev, V. L., & Puzia, T. H. 2006, MNRAS, 372, 1259

Sharples, R. M., Zepf, S. E., Bridges, T. J., Hanes, D. A., Carter, D., Ashman, K. M., & Geisler, D. 1998, AJ, 115, 2337

Sikkema, G., Carter, D., Peletier, R. F., Balcells, M., Del Burgo, C., & Valentijn, E. A. 2007, A&A, 467, 1011

Sikkema, G., Peletier, R. F., Carter, D., Valentijn, E. A., & Balcells, M. 2006, A&A, 458, 53

Sil'chenko, O. K. 1999, AJ, 117, 2725

Silva, D. R., Boroson, T. A., Thompson, I. B., & Jedrzejewski, R. I. 1989, AJ, 98, 131

Simard, L., Willmer, C. N. A., Vogt, N. P., Sarajedini, V. L., Phillips, A. C., Weiner, B. J., Koo, D. C., Im, M., Illingworth, G. D., & Faber, S. M. 2002, ApJS, 142, 1

Simien, F. & de Vaucouleurs, G. 1986, ApJ, 302, 564

Simien, F. & Prugniel, P. 1997a, A&AS, 126, 15

—. 1997b, A&AS, 126, 519

Smith, G. P., Treu, T., Ellis, R. S., Moran, S. M., & Dressler, A. 2005, ApJ, 620, 78

Spergel, D. N., Bean, R., Doré, O., Nolta, M. R., Bennett, C. L., Dunkley, J., Hinshaw, G., Jarosik, N., Komatsu, E., Page, L., Peiris, H. V., Verde, L., Halpern, M., Hill, R. S., Kogut, A., Limon, M., Meyer, S. S., Odegard, N., Tucker, G. S., Weiland, J. L., Wollack, E., & Wright, E. L. 2007, ApJS, 170, 377

Spolaor, M., Forbes, D. A., Proctor, R. N., Hau, G. K. T., & Brough, S. 2008, MNRAS, 385, 675

Springel, V., White, S. D. M., Jenkins, A., Frenk, C. S., Yoshida, N., Gao, L., Navarro, J., Thacker, R., Croton, D., Helly, J., Peacock, J. A., Cole, S., Thomas, P., Couchman, H., Evrard, A., Colberg, J., & Pearce, F. 2005, Nature, 435, 629

Strader, J., Beasley, M. A., & Brodie, J. P. 2007, AJ, 133, 2015

Strader, J., Brodie, J. P., Cenarro, A. J., Beasley, M. A., & Forbes, D. A. 2005, AJ, 130, 1315

Tamura, N., Sharples, R. M., Arimoto, N., Onodera, M., Ohta, K., & Yamada, Y. 2006, MNRAS, 373, 601

Tegmark, M., Eisenstein, D. J., Strauss, M. A., Weinberg, D. H., Blanton, M. R., Frieman, J. A., Fukugita, M., Gunn, J. E., Hamilton, A. J. S., Knapp, G. R., Nichol, R. C., Ostriker, J. P., Padmanabhan, N., Percival, W. J., Schlegel, D. J., Schneider, D. P., Scoccimarro, R., Seljak, U., Seo, H.-J., Swanson, M., Szalay, A. S., Vogeley, M. S., Yoo, J., Zehavi, I., Abazajian, K., Anderson, S. F., Annis, J., Bahcall, N. A., Bassett, B., Berlind, A., Brinkmann, J., Budavari, T., Castander, F., Connolly, A., Csabai, I., Doi, M., Finkbeiner, D. P., Gillespie, B., Glazebrook, K., Hennessy, G. S., Hogg, D. W., Ivezić, Ž., Jain, B., Johnston, D., Kent, S., Lamb, D. Q., Lee, B. C., Lin, H., Loveday, J., Lupton, R. H., Munn, J. A., Pan, K., Park, C., Peoples, J., Pier, J. R., Pope, A., Richmond, M., Rockosi, C., Scranton, R., Sheth, R. K., Stebbins, A., Stoughton, C., Szapudi, I., Tucker, D. L., Berk, D. E. V., Yanny, B., & York, D. G. 2006, Phys. Rev. D, 74, 123507

Terlevich, A. I., Kuntschner, H., Bower, R. G., Caldwell, N., & Sharples, R. M. 1999, MNRAS, 310, 445

Thomas, D., Maraston, C., & Bender, R. 2003, MNRAS, 339, 897

Thomas, D., Maraston, C., Bender, R., & Mendes de Oliveira, C. 2005a, ApJ, 621, 673

Thomas, D., Maraston, C., & Korn, A. 2004, MNRAS, 351, L19

Thomas, J., Saglia, R. P., Bender, R., Thomas, D., Gebhardt, K., Magorrian, J., Corsini, E. M., & Wegner, G. 2005b, MNRAS, 360, 1355

Tonry, J. L., Dressler, A., Blakeslee, J. P., Ajhar, E. A., Fletcher, A. B., Luppino, G. A., Metzger, M. R., & Moore, C. B. 2001, ApJ, 546, 681

Toomre, A. 1977, in Evolution of Galaxies and Stellar Populations, ed. B. M. Tinsley & R. B. Larson, 401–+

Trager, S. C., Faber, S. M., Worthey, G., & González, J. J. 2000, AJ, 120, 165

Trager, S. C., Worthey, G., Faber, S. M., Burstein, D., & Gonzalez, J. J. 1998, ApJS, 116, 1

Tran, H. D., Tsvetanov, Z., Ford, H. C., Davies, J., Jaffe, W., van den Bosch, F. C., & Rest, A. 2001, AJ, 121, 2928

Trujillo, I., Burkert, A., & Bell, E. F. 2004, ApJ, 600, L39

Tully, R. B. & Fisher, J. R. 1977, A&A, 54, 661

—. 1988, Annales de Geophysique

Tully, R. B. & Pierce, M. J. 2000, ApJ, 533, 744

Vazdekis, A. 1999, ApJ, 513, 224

Vazdekis, A, e. 2007, in prep

Visvanathan, N. & Sandage, A. 1977, ApJ, 216, 214

Vitvitska, M., Klypin, A. A., Kravtsov, A. V., Wechsler, R. H., Primack, J. R., & Bullock, J. S. 2002, ApJ, 581, 799

Vollmer, B. 2003, A&A, 398, 525

Vollmer, B., Braine, J., Balkowski, C., Cayatte, V., & Duschl, W. J. 2001, A&A, 374, 824

White, S. D. M. & Rees, M. J. 1978, MNRAS, 183, 341

Willick, J. A. 1994, ApJS, 92, 1

Woodley, K. A., Harris, W. E., Beasley, M. A., Peng, E. W., Bridges, T. J., Forbes, D. A., & Harris, G. L. H. 2007, AJ, 134, 494

Worthey, G. 1994, ApJS, 95, 107

Worthey, G., Faber, S. M., & Gonzalez, J. J. 1992, ApJ, 398, 69

Worthey, G. & Ottaviani, D. L. 1997, ApJS, 111, 377

Yoachim, P. & Dalcanton, J. J. 2008, ArXiv e-prints, 805

Yoon, S.-J., Yi, S. K., & Lee, Y.-W. 2006, Science, 311, 1129

Zepf, S. E. & Ashman, K. M. 1993, MNRAS, 264, 611

Zepf, S. E., Ashman, K. M., & Geisler, D. 1995, ApJ, 443, 570

Zepf, S. E., Beasley, M. A., Bridges, T. J., Hanes, D. A., Sharples, R. M., Ashman, K. M., & Geisler, D. 2000, AJ, 120, 2928

Zepf, S. E., Geisler, D., & Ashman, K. M. 1994, ApJ, 435, L117

Chapter 7

Appendix

7.1. Galaxy Kinematics

This section presents the measured absorption line kinematics for each of the sample galaxies, with comments on interesting features present in each galaxy given in the following section.

Notes On Individual Galaxies

NGC 148 : No previously published kinematics for this galaxy exist in the literature. The major axis rotation curve displayed in Figure 7.1 rises steeply out 5 arcsec before dipping slightly between 5 and 12 arcsec, the rotational velocity then begins to increase again before reaching a (relatively) constant plateau. Several interesting features of the rotation curve are immediately apparent, the first is that the observed dip in rotational velocity between 5 and 12 arcseconds is precisely the same point at which the luminosity along the major axis is observed to drop. The rotation velocity again begins to rise again at the same radius as "lobes" in the light profile appear. The behaviour of the h_3 term of the LOSVD as expected also displays similar behaviour in the same region. At larger radii (most clearly seen to the left of the galaxy centre), there is a noticeable bump in rotational velocity which begins to decrease again just as the luminosity provided by the "lobe" begins to drop. It appears that the "lobe" region is kinematicaly distinct from the material on either side and may in fact be the result of observing spiral arms edge on with the line of sight extending along their length.

NGC 1023 : As previously discussed in Section 3.4.1 the kinematics of NGC 1023 determined here are consistent within the errors with previously published values from Emsellem et al. (2004), Simien & Prugniel (1997b) and generally with Debattista et al. (2002). In particular the observed h_3 anti-correlation with velocity within a few arcsec is in excellent agreement (when disregarding a small zero point offset) with the findings of Emsellem et al. (2004). This behaviour appears consistent with the presence of a nuclear stellar disk, the existence of which has been hinted at by several other studies including Sil'chenko (1999) and Bower et al. (2001).

NGC 1380 : In common with NGC 148 the unsharp masked image of this galaxy displays lobes on either side of the galaxy nucleus, these lobes are again presumably the result of spiral arms being observed edge on. Unlike the case in NGC 148 however these features do not appear to have any significant influence on the kinematics measured here. The rotation curve of this galaxy is fairly regular, reaching an apparent plateau at around 70 arcsec, both the rotation curve and velocity dispersion profile are in excellent agreement with those of D'Onofrio et al. (1995). Unfortunately the data presented here does not extend far enough to examine the higher order LOSVD terms in the regions where the lobes are visible. Fortunately Bedregal et al. (2006b) present data which does extend to sufficient radii, they find that the h_3 profile is observed to plateau exactly as the lobes appear and that interestingly h_4 is observed to peak in the vicinity of the lobe structures.

ESO 358G006 : This small Fornax cluster galaxy is an almost edge on disc galaxy, with a compact nucleus visible both in the imaging presented here and ACS Fornax Cluster Survey (Jordán et al., 2007) observations. The rotation curve measured here is relatively smooth, albeit with increased errors due to the inability to measure σ, h_3 and h_4 due to σ being below the measurement threshold at all radii. The kinematics for this galaxy have also been measured by Bedregal et al. (2006b), who find that the velocity dispersion drops slightly in the nucleus, and observe some evidence for peaks in the h_4 profile coincident with the observed peaks in the disc light seen around 15 arcsec from the galaxy.

NGC 1527 : The unsharp mask image of this galaxy displays the existence of several components, most noticeably lobe structures and streams appearing to be associated with the lobes. The kinematics displayed in Figure 7.4 are very regular, with the commonly observed anticorrelation between velocity and h_3 visible in the inner regions, a feature likely to be associated with the slight change in rotation curve behaviour around 5-10

arcsec.

NGC 1596 : The imaging of this galaxy shows an edge on disc with a significant central bulge. The rotation curve again displays a rapid rise within the inner few arcsec, before undergoing a temporary dip similar to that seen in NGC 148, the observed h_3 profile also displays a marked anti-correlation with velocity in the same regions. The kinematics for measured for the major axis here match those presented in Chung & Bureau (2004) reasonably well. However the velocity dispersion measured for the minor axis peaks at a considerably higher value (200 kms^{-1} vs. 160 kms^{-1}) than the major axis. The reason for this is not entirely clear, though a difference in mean seeing between the observations of the major axis and those of the minor axis appears partly to blame.

NGC 3098 : A very similar example to NGC 1596, both in terms of the regular edge on disc, and the observation of a measured offset in central σ between the major and minor axes. The σ is too low to allow the measurement of the higher order LOSVD terms at essentially any radius.

NGC 3115 : The kinematics of this galaxy are discussed in detail in Chapter 2.4 .

NGC 3301 : The imaging this galaxy displays evidence for a disc component and a prominent peanut bulge. The rotation curve of this galaxy is very similar to those of NGC 1596 and NGC 3098, in that it rises rapidly in the inner region, before dropping off slightly, before rising again to reach a plateau at larger radii. The velocity dispersion of this galaxy is so low that higher order h_3 and h_4 terms are unmeasureable.

NGC 3585 : The kinematics of this galaxy are particularly fascinating, with clear evidence that the fast rotating disc component seen in the unsharp image is embedded in a larger non rotating spheroidal component. Previous observations by Scorza & Bender (1995) and Fisher (1997) demonstrated the existence of the turnover in the rotation curve and hinted at the observed σ drops on the major axes. However the observations presented here are the first to conclusively demonstrate that as the disc component disappears the rotation curve drops to zero. The major axis σ drops can also be understood as resulting from the fact that the disc component dominates the luminosity in these regions, hence dominating the measured kinematics. The higher order LOSVD terms are particularly extreme, reaching values close to ± 0.3, yet further evidence for the decoupled kinematics of the two components present.

NGC 4179 : Another example of the NGC 1596/NGC 3098 class, with a strong edge-on disc component and central bulge. The kinematics are likewise similar to NGC 1596, although without the prominent inflection points visble in the rotation curve of NGC 1596.

NGC 4281 : This galaxy does not display any obvious spiral features found prominently in other galaxies in this sample, similarly disc structure is not obvious in the unsharp mask image, perhaps indicating that this galaxy is viewed slightly above the disc, which is relatively smooth. NGC 4281 does however appear to contain a compact central light concentration. The major axis kinematics of this galaxy are fairly regular, with a quickly rising rotation curve which reaches a maximum velocity within 10 arcsec and then displays some evidence for a drop off beyond 40 arcsec. The velocity dispersion is centrally peaked at a relatively high value of 280 kms^{-1} which is presumably due to the observed nuclear light concentration. The rotation velocity is as usual anti-correlated with h_3, the strength of the h_3 feature and the relatively high value of σ seen at larger radii, may indicate that this galaxy is somewhat like NGC 3585, with a rotating disc surrounded by a none rotating spheroid.

NGC 4762 : This large edge-on galaxy displays regular disc dominated structure between 10 and 100 arcsec, beyond which the disc appears to flare and warp. The kinematics measured here are in excellent agreement with those published by Fisher (1997) apart from the measured h_4, where some disagreement between the values presented here and those of Fisher (1997) is apparent.

NGC 5854 : The kinematics of this almost edge-on galaxy are in excellent agreement with those published Simien & Prugniel (1997a), due to the low value of σ found throughout it is impossible to determine values for h_3 and h_4 for this galaxy.

NGC 5864 : The image of this galaxy displays clear evidence for spiral structure with some warping. The rotation curve is regular and well matched to the measurements made by Simien & Prugniel (1997a), the observations presented here extend far enough to reach the region where the rotation curved flattens. There is a systematic discrepancy of around 25 kms^{-1} between the measurement of velocity dispersion determined here and that of Simien & Prugniel (1997a).

NGC 6725 : This galaxy displays clear spiral structure with the viewing angle being somewhat above the plain of the disc. The rotation curve is regular, though displays a prominent step feature between ~2 to 8 arcsec. The complicated shape of the h_3 profile is

another indication of the complicated kinematics of the inner region of this galaxy, which are presumably due to the presence of a bar.

NGC 7041 : This galaxy appears to display a fairly significant spheroidal component, within which is the edge-on disc. The very obvious anti-correlation between rotation velocity and h_3 on the major axis may be an indication of this two component situation, similar to that seen in the case of NGC 3585. The rotation curve itself is extremely smooth and featureless, the data does not extend to large enough radii to begin to probe the region where the disc fades.

NGC 7332 : The kinematics of this edge-on and slightly warped galaxy are discussed fully in Section 3.4.1.

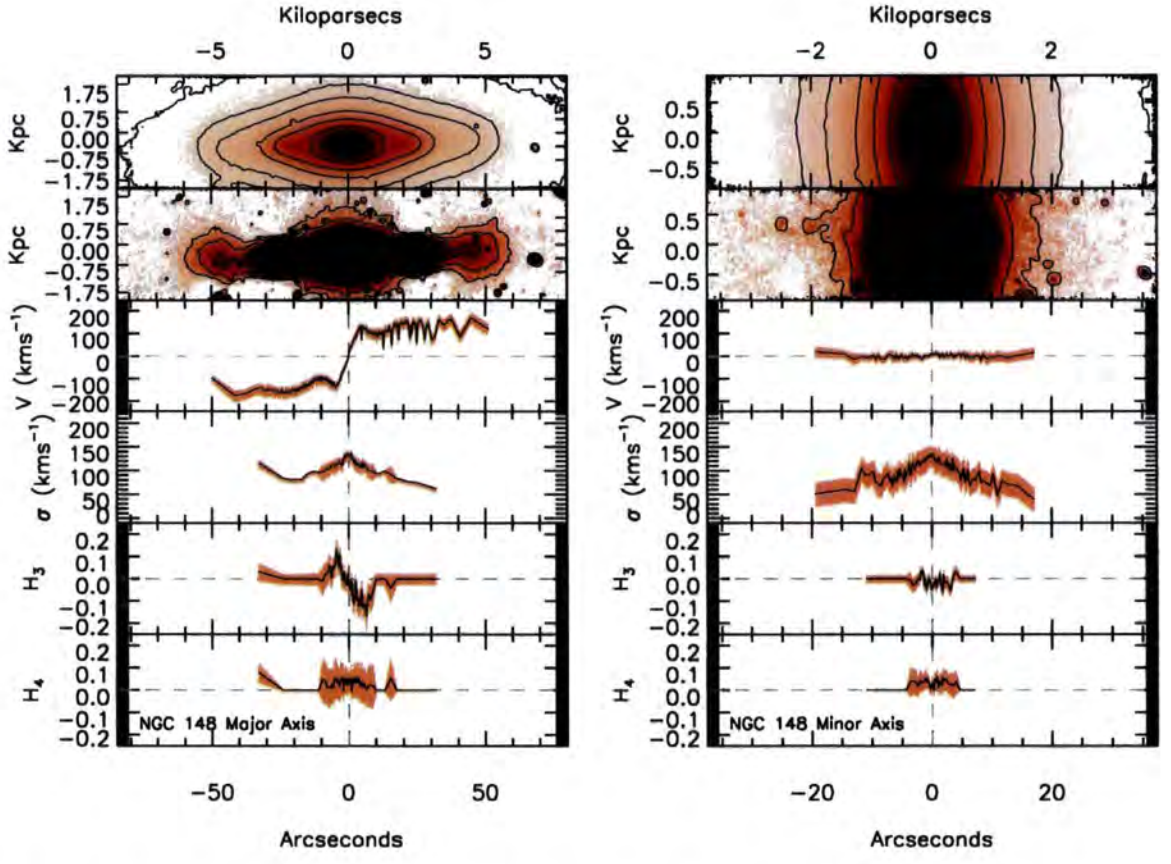

Figure 7.1: Measured kinematic parameters for NGC 148. In this case the major axis velocity dispersion displayed is that measured from the S/N=100 data due to problems with the S/N=30 data (visible as drops in the measured velocity to the right of the galaxy centre.

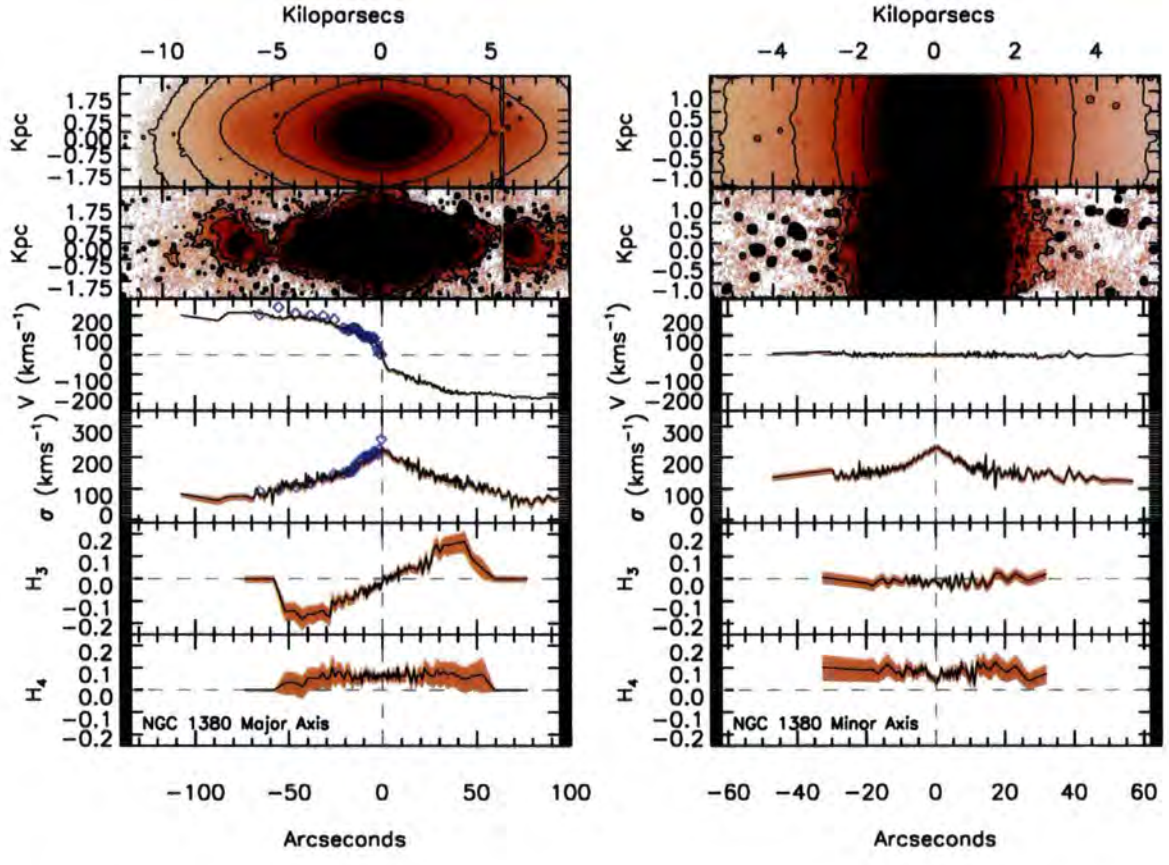

Figure 7.2: As in Figure 3.10 but for NGC 1380, blue diamonds in this case are from D'Onofrio et al. (1995).

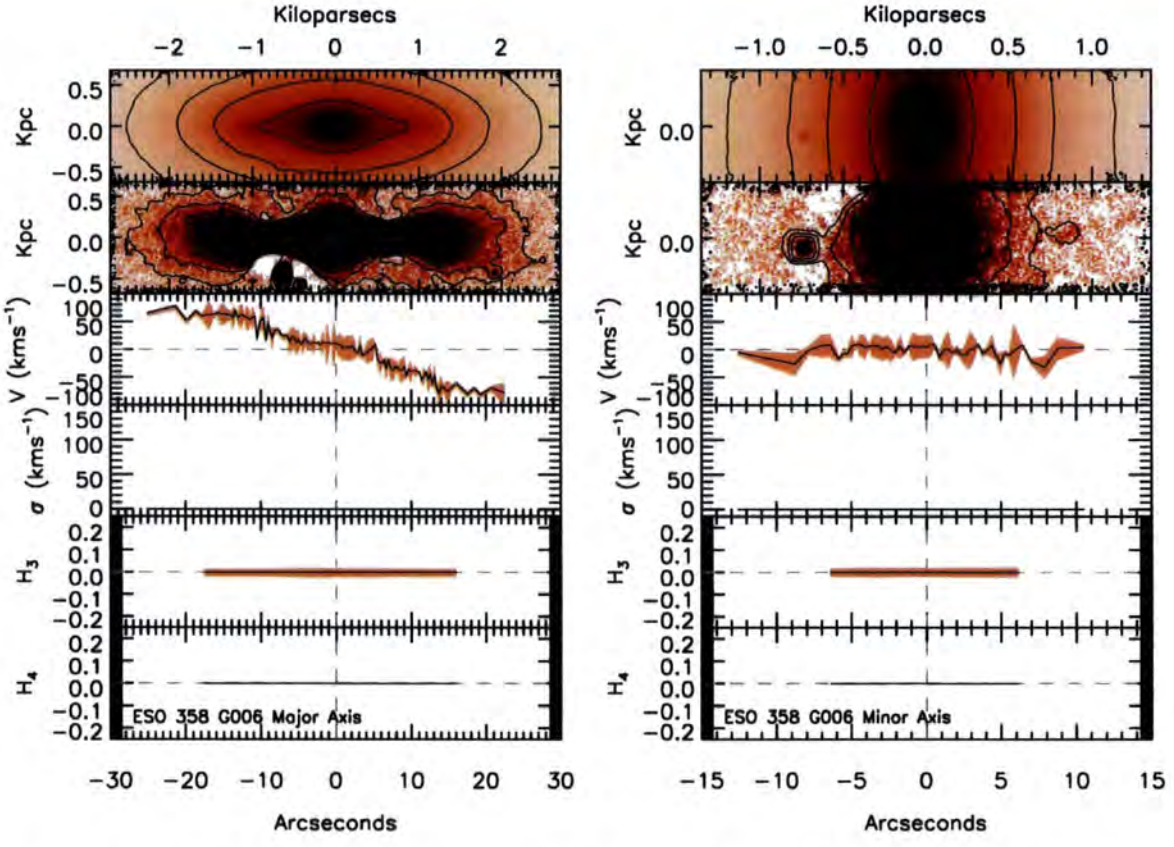

Figure 7.3: Measured kinematic parameters for ESO358-G006. In this case the velocity dispersion was below the measurement threshold of 50kms^{-1} at all radii.

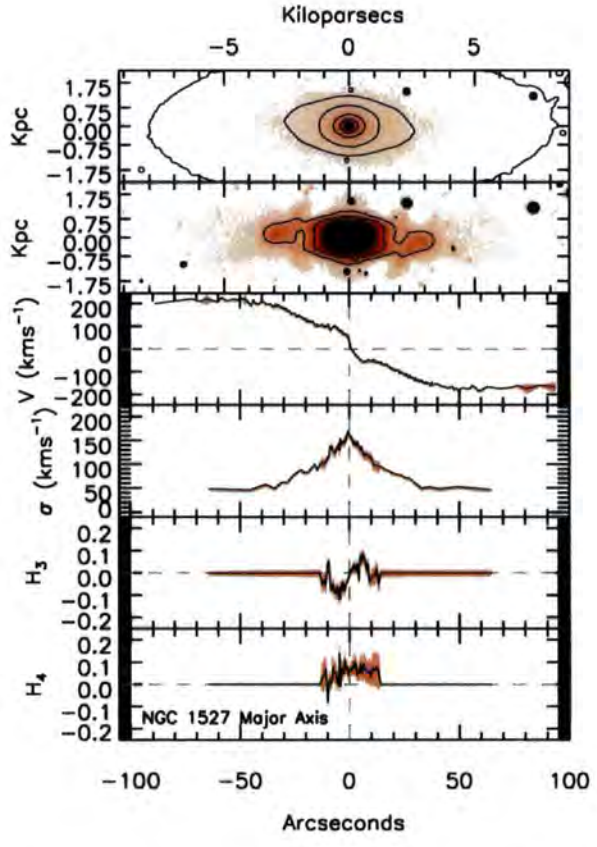

Figure 7.4: Measured kinematic parameters for NGC 1527. In this case no minor axis data is available, the velocity is measured from S/N=30 data, the other components of the LOSVD from S/N=100 data.

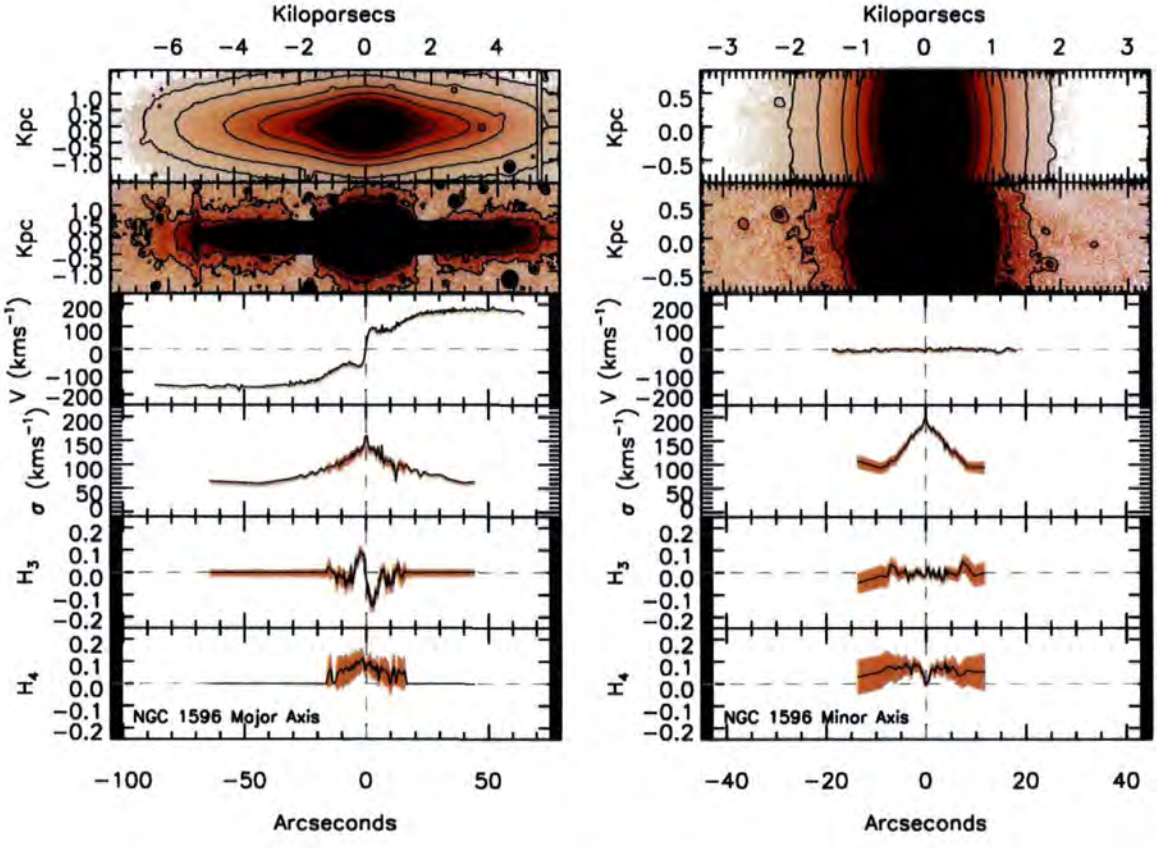

Figure 7.5: Measured kinematic parameters for NGC 1596. The velocity is measured from S/N=30 data, the other components of the LOSVD from S/N=100 data.

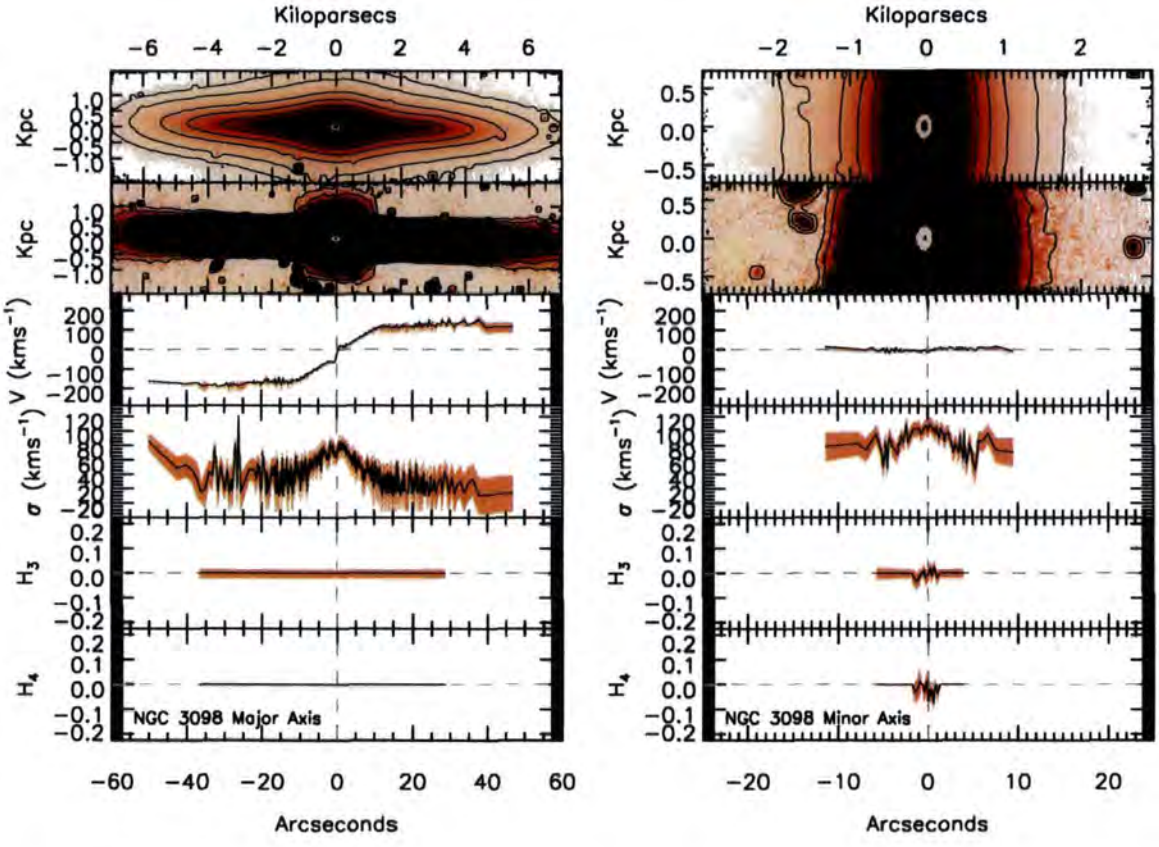

Figure 7.6: Measured kinematic parameters for NGC 3098. The velocity and σ is measured from S/N=30 data, the other components of the LOSVD from S/N=100 data.

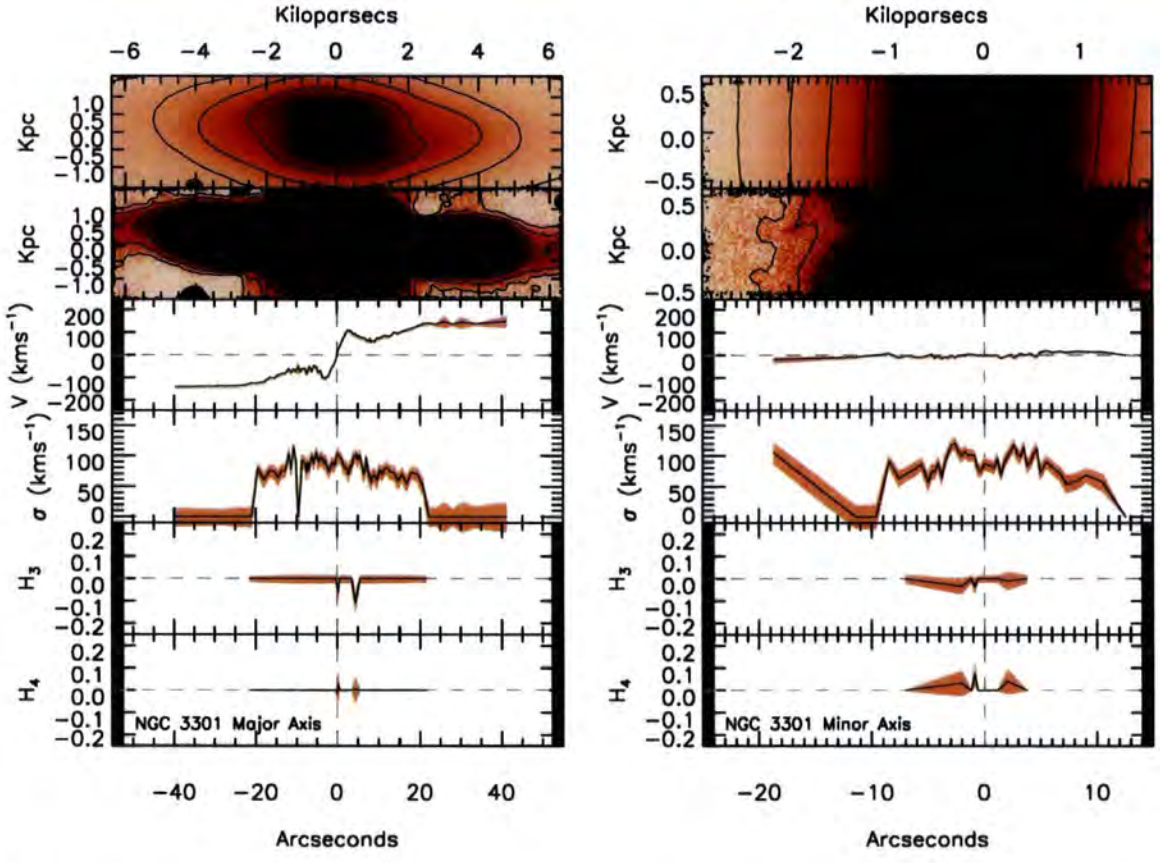

Figure 7.7: Measured kinematic parameters for NGC 3301. The velocity and σ is measured from S/N=30 data, the other components of the LOSVD from S/N=100 data.

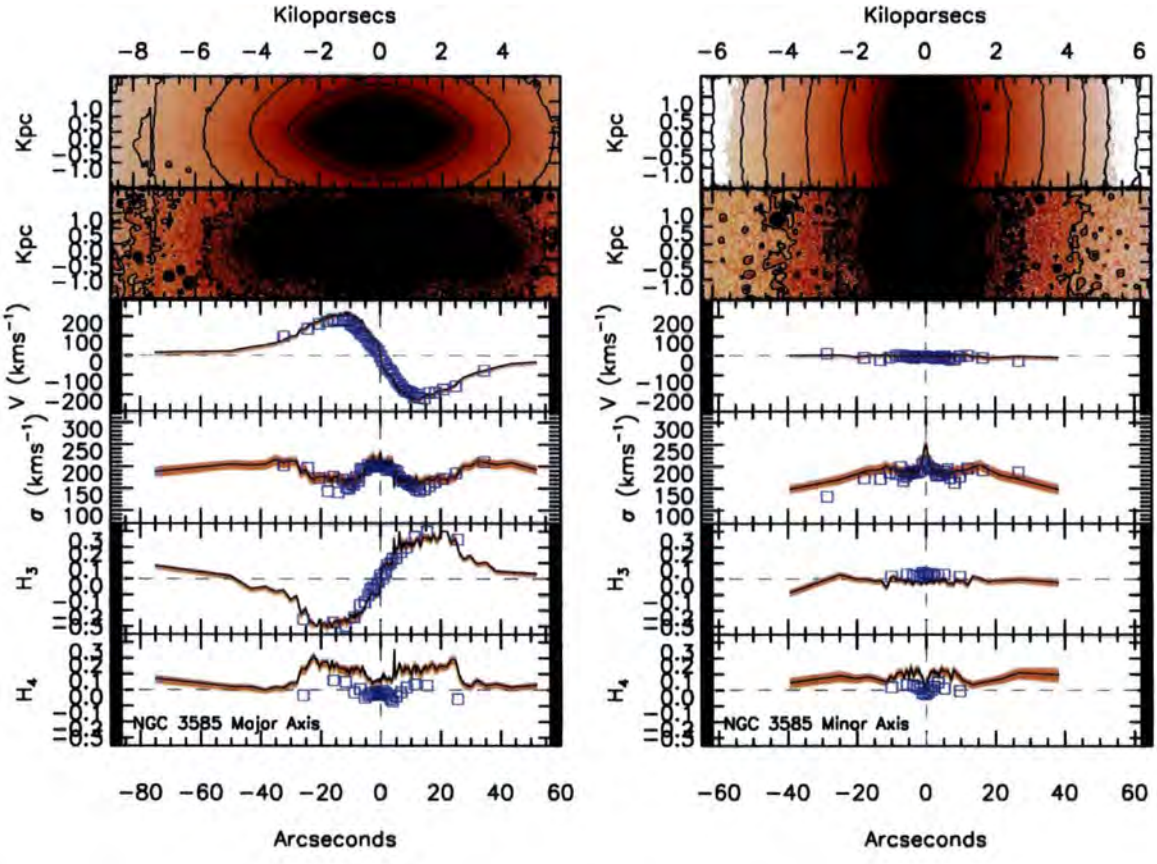

Figure 7.8: Measured kinematic parameters for NGC 3585, all measured from S/N=100 data, blue squares in this case are from Fisher (1997).

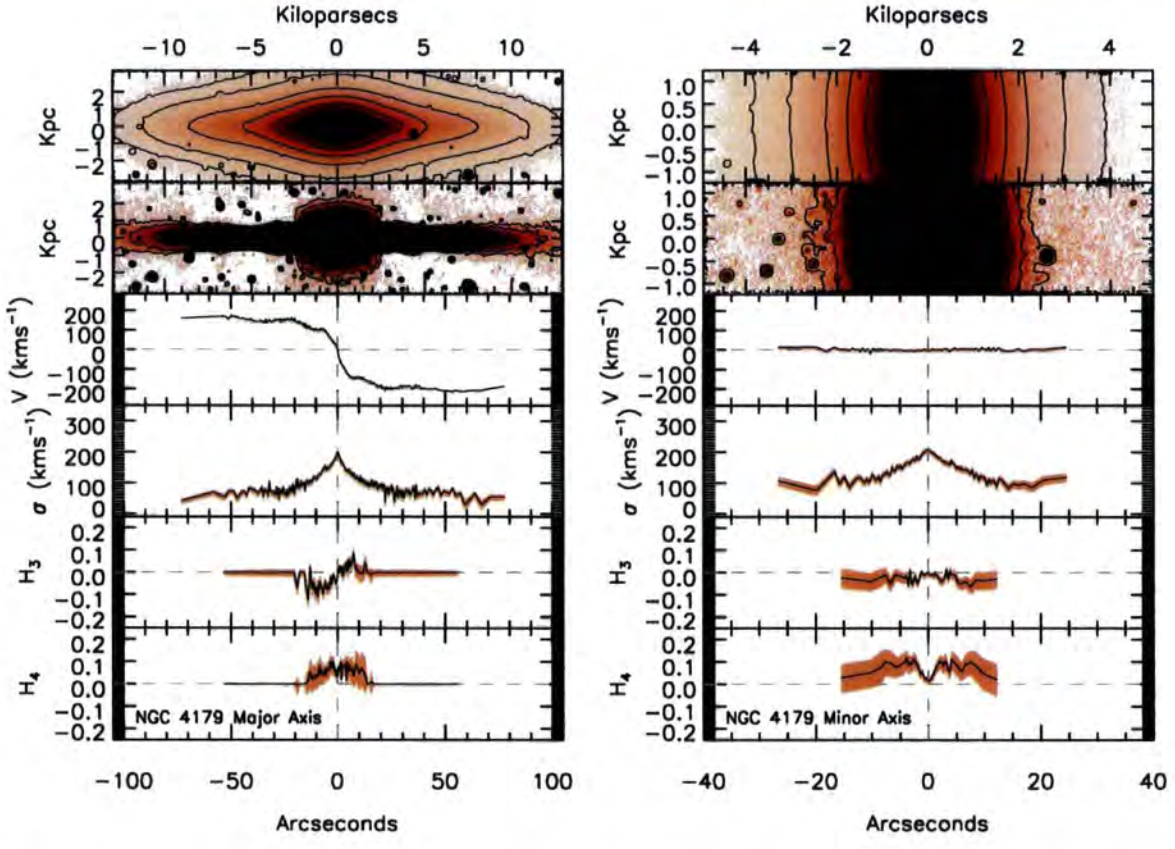

Figure 7.9: Measured kinematic parameters for NGC 4179. Rotation and σ were measured from S/N=30 data, h_3 and h_4 from S/N=100 spectra.

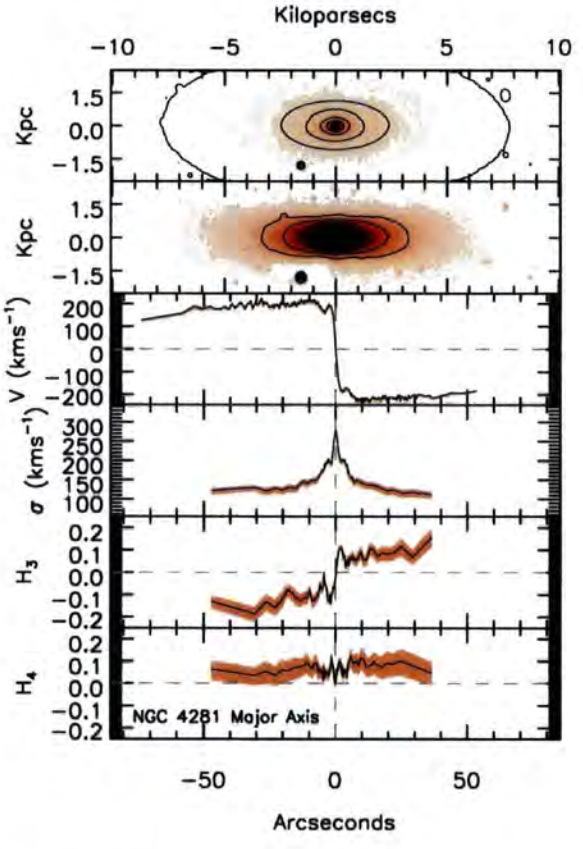

Figure 7.10: Measured kinematic parameters for NGC 4281. Rotation velocity was measured from S/N=30 data, σ, h_3 and h_4 from S/N=100 spectra.

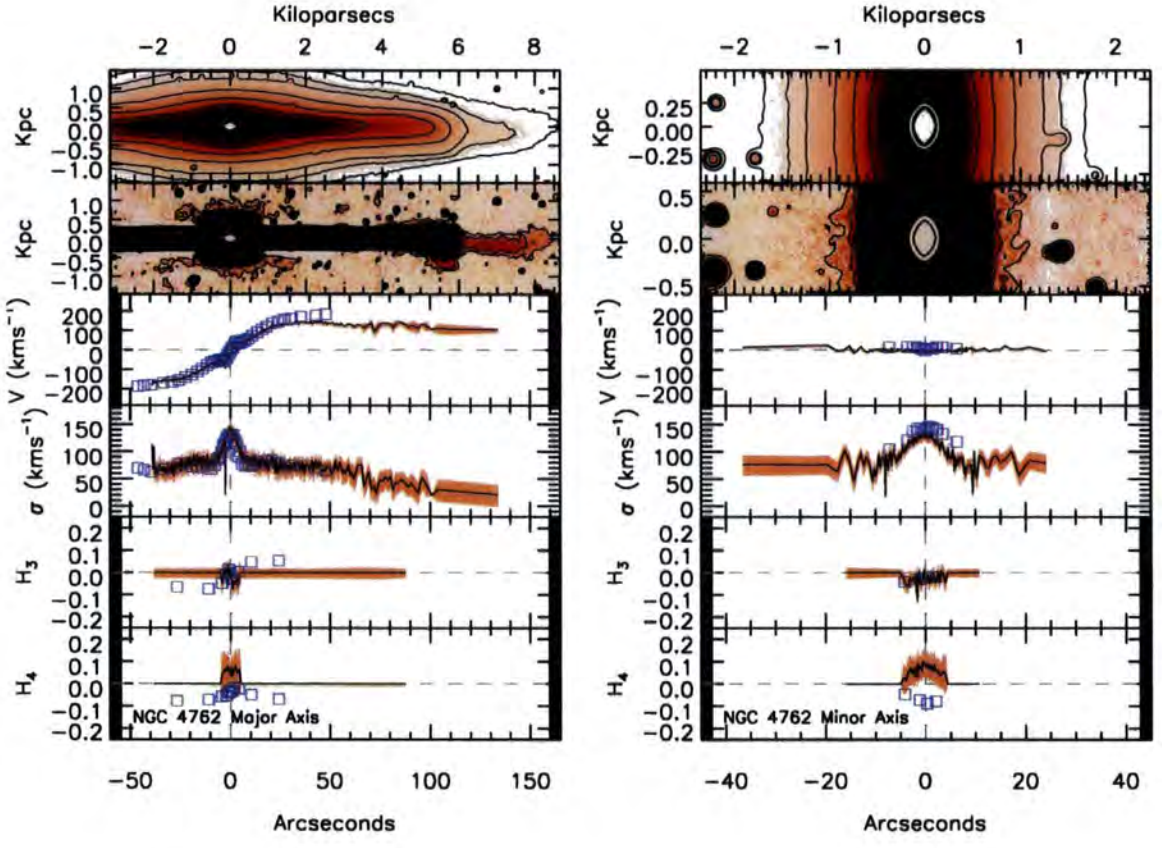

Figure 7.11: Measured kinematic parameters for NGC 4762. Rotation and σ were measured from S/N=30 data, h_3 and h_4 from S/N=100 spectra. Blue squares are the measurements of Fisher (1997).

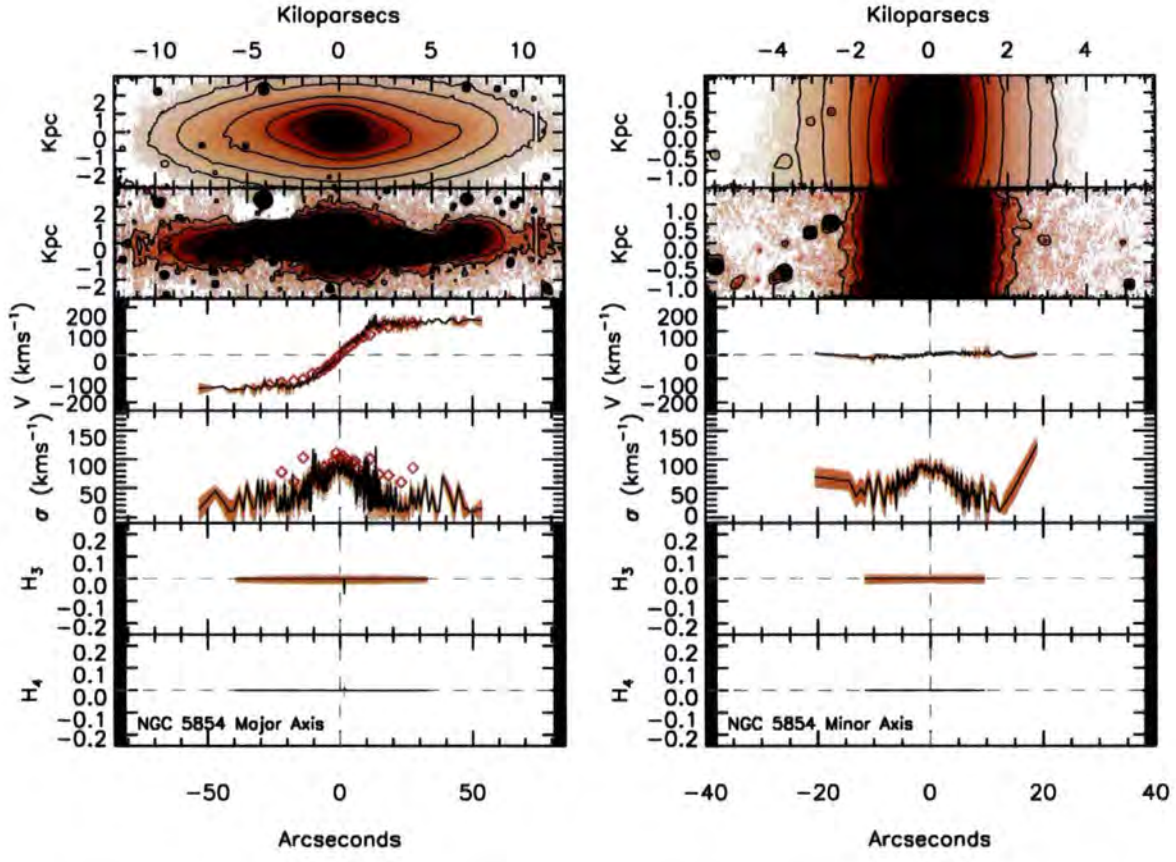

Figure 7.12: Measured kinematic parameters for NGC 5854. Rotation and σ were measured from S/N=30 data, h_3 and h_4 from S/N=100 spectra. Red diamonds are the measurements of Simien & Prugniel (1997a).

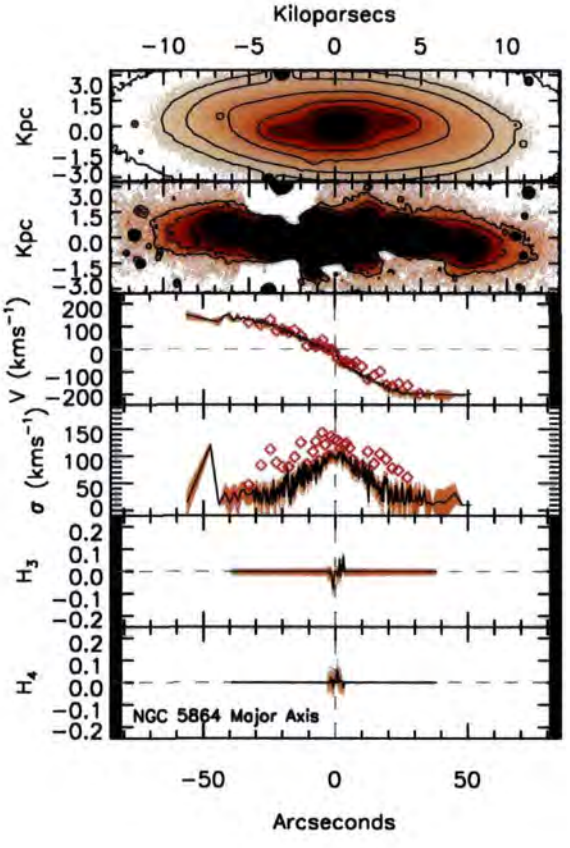

Figure 7.13: Measured kinematic parameters for NGC 5864. Rotation and σ were measured from S/N=30 data, h_3 and h_4 from S/N=100 spectra. Red diamonds are the measurements of Simien & Prugniel (1997a).

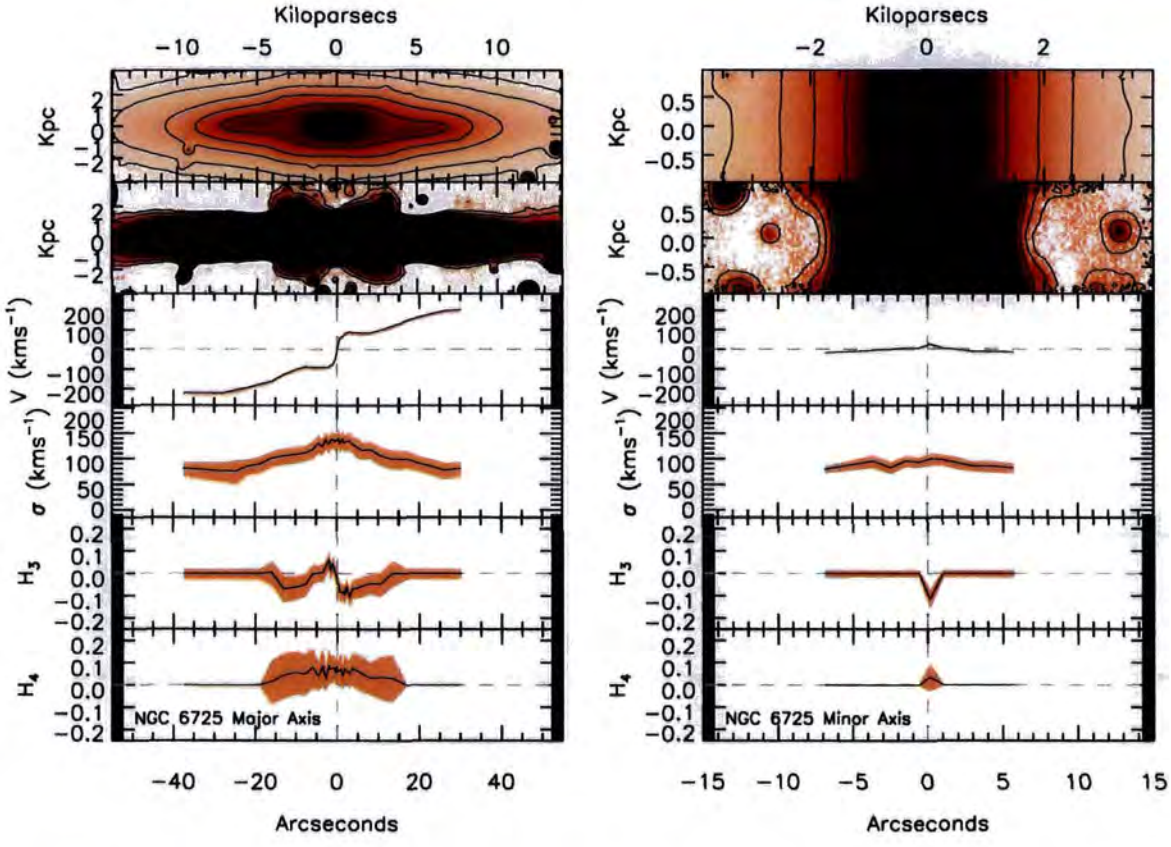

Figure 7.14: Measured kinematic parameters for NGC 6725. All values measured from S/N=100 data.

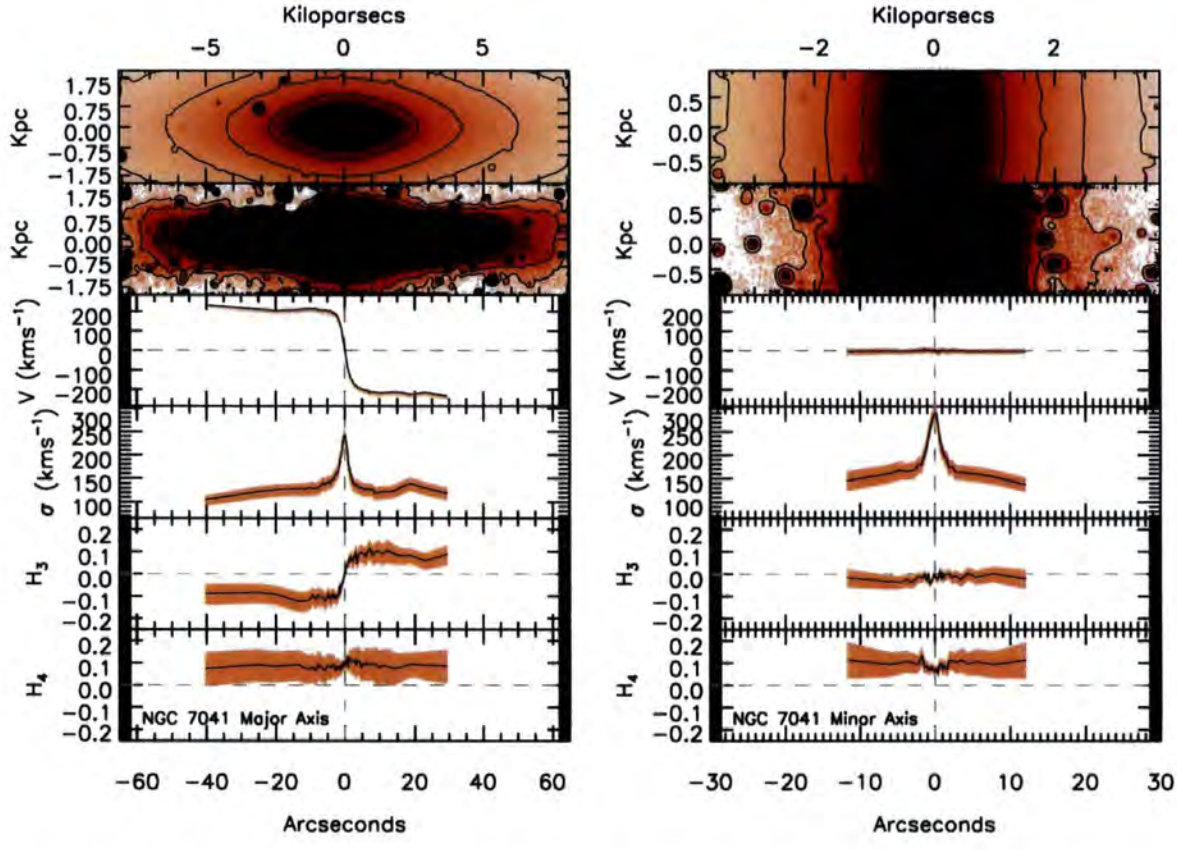

Figure 7.15: Measured kinematic parameters for NGC 7041. All values measured from S/N=100 data.

7.2. Sérsic + Exponential Models

This section presents the Sérsic + Exponential disc models produced by GALFIT as part of Section 3.4.2. Each panel presents the input 2MASS J band image, the best fit GALFIT Sérsic + Exponential disc model (Sérsic + Sérsic + Exponential disc in the case of NGC 3115 and NGC 3585) and the residuals when the model is subtracted from the input image. The middle panel of each group of three also displays the fitted field of view, ranging from 86"×86" in the case of ESO358-G006 to 531"×531" in the case of NGC 1023.

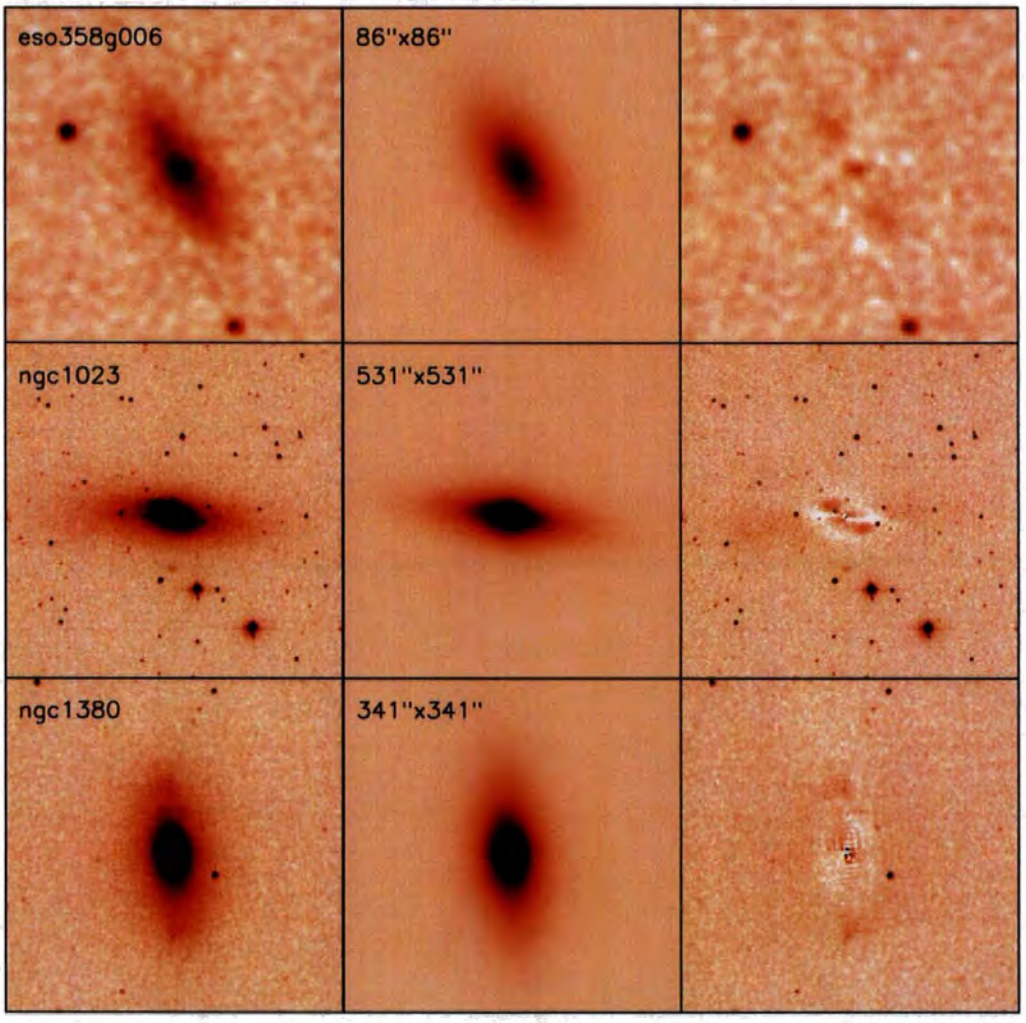

Figure 7.16: **Left Panel** : 2MASS J band images of 3 S0 galaxies. **Central Panel** : Best fit GALFIT Sérsic + Exponential disc model. Field of view of the fitting region is indicated. **Right Panel** : Residuals remaining after subtracting the model from the input image.

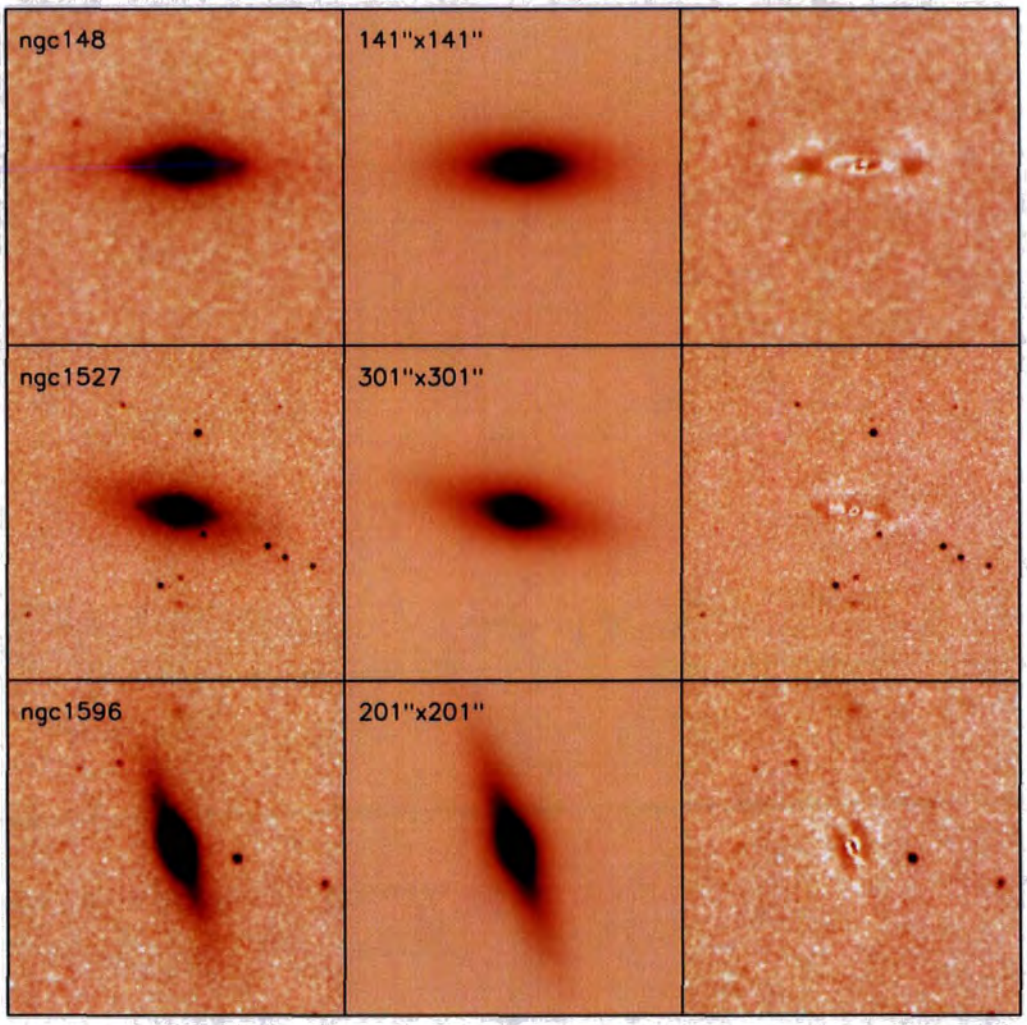

Figure 7.17: **Left Panel** : 2MASS J band images of 3 S0 galaxies. **Central Panel** : Best fit GALFIT Sérsic + Exponential disc model. Field of view of the fitting region is indicated. **Right Panel** : Residuals remaining after subtracting the model from the input image.

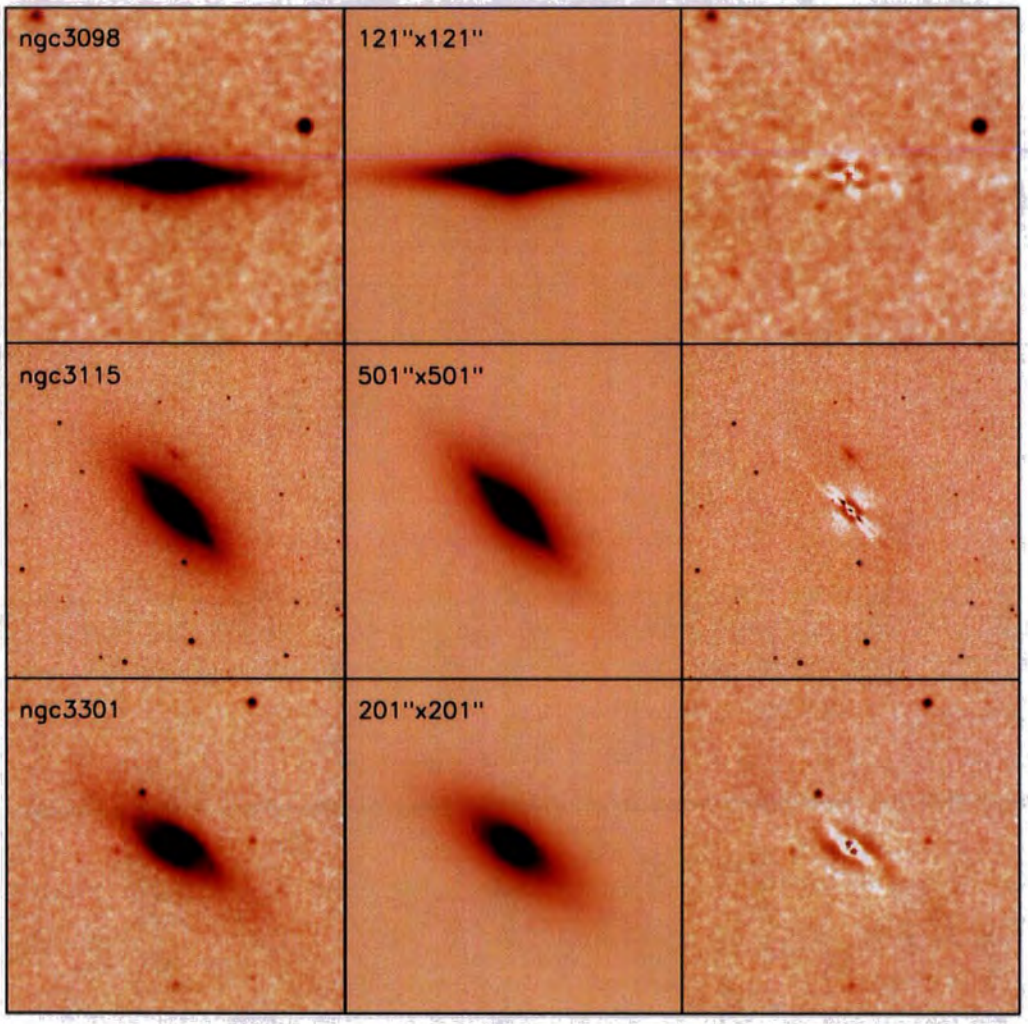

Figure 7.18: **Left Panel** : 2MASS J band images of 3 S0 galaxies. **Central Panel** : Best fit GALFIT Sérsic + Exponential disc model. Field of view of the fitting region is indicated. **Right Panel** : Residuals remaining after subtracting the model from the input image.

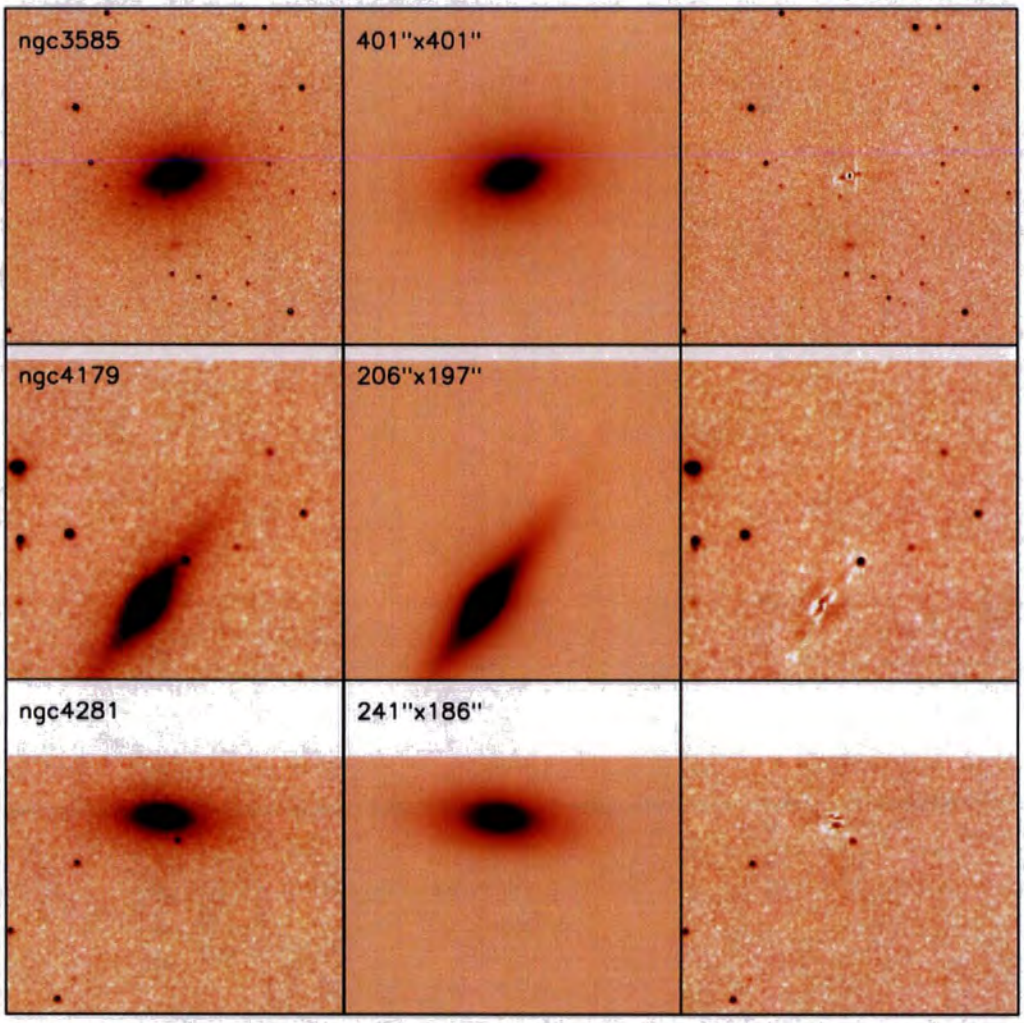

Figure 7.19: **Left Panel** : 2MASS J band images of 3 S0 galaxies. **Central Panel** : Best fit GALFIT Sérsic + Exponential disc model. Field of view of the fitting region is indicated. **Right Panel** : Residuals remaining after subtracting the model from the input image.

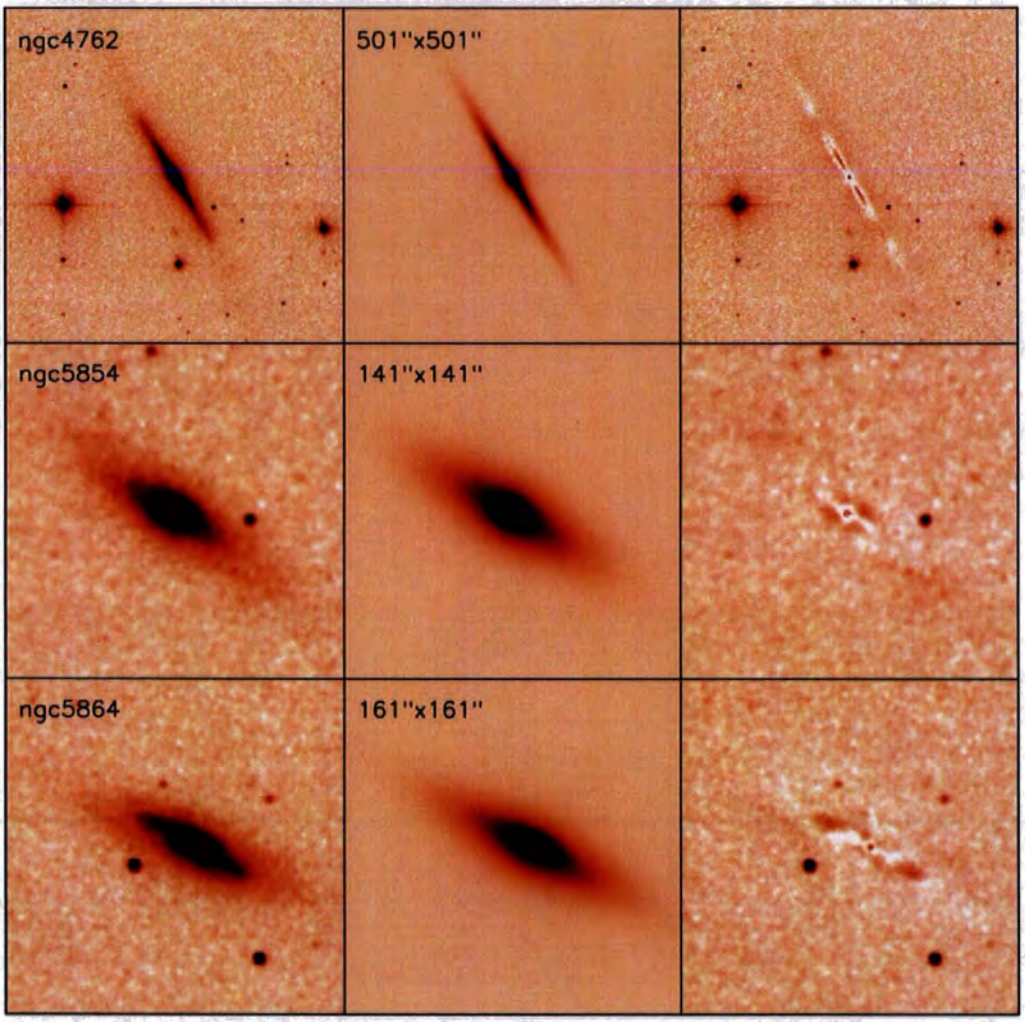

Figure 7.20: **Left Panel** : 2MASS J band images of 3 S0 galaxies. **Central Panel** : Best fit GALFIT Sérsic + Exponential disc model. Field of view of the fitting region is indicated. **Right Panel** : Residuals remaining after subtracting the model from the input image.

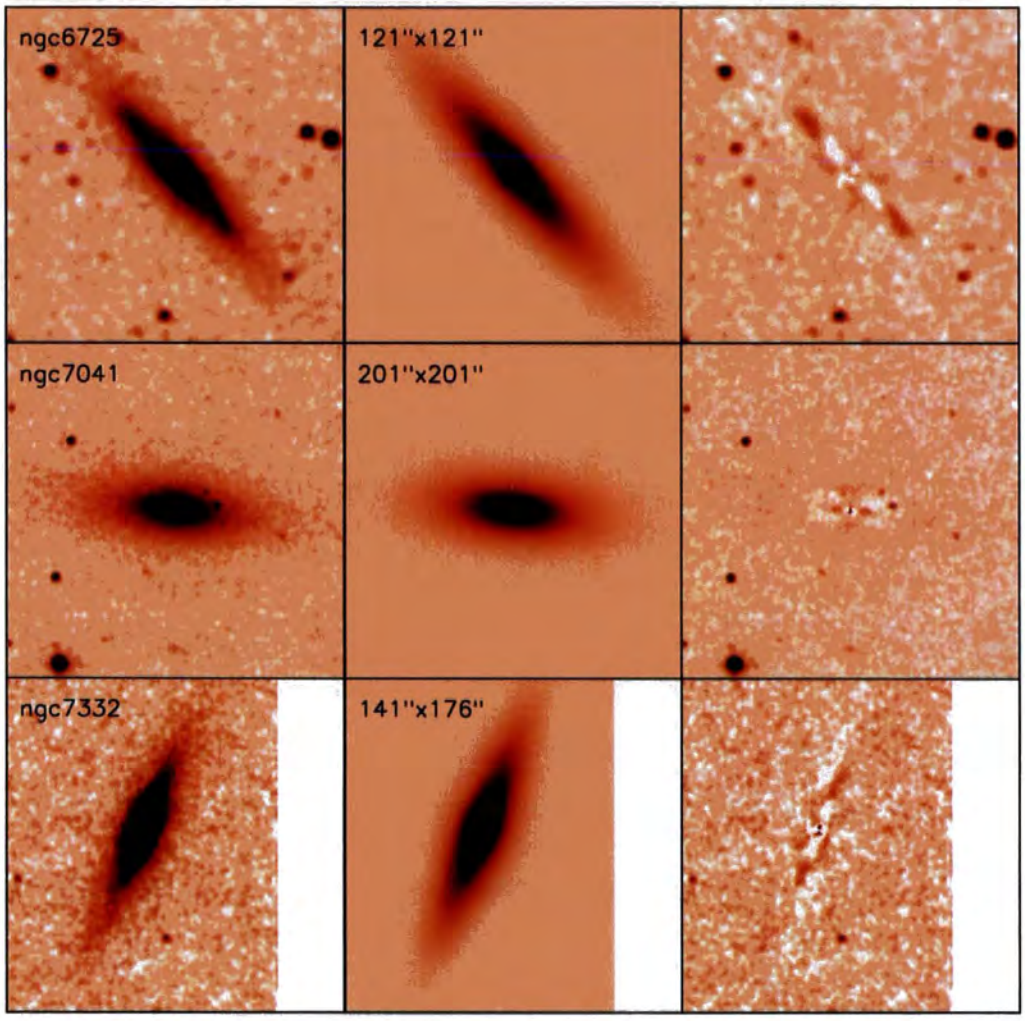

Figure 7.21: **Left Panel** : 2MASS J band images of 3 S0 galaxies. **Central Panel** : Best fit GALFIT Sérsic + Exponential disc model. Field of view of the fitting region is indicated. **Right Panel** : Residuals remaining after subtracting the model from the input image.

7.3. NGC 3923 GC Properties

This section provides tables of the properties of GCs studied in Chapter 4.

Table 7.1: Measured parameters for spectroscopically examined objects, both confirmed GCs around NGC 3923 as well as fore and background contaminants. In addition we provide the binned GC data and the measured indices for the spheroid of NGC 3923. For the GCs: ID (and number of objects per bin for the binned data in parentheses), coordinates, g magnitude, g–r and g–i colours are from our GMOS imaging and are instrumental magnitudes based on the standard Gemini/GMOS zeropoints. Heliocentric velocities are from the spectra presented in this work, as are the measured line strength indices. For the binned GC data the mean g–i colours of the binned data is provided, as is the error weighted mean line strength indices for each bin, the errors for the line strengths are the 1σ scatter in the individual line strengths in each bin. For the spheroid data the line strengths are provided as well as errors determined from a combination of the statistical uncertainty on the spectrum as well as the uncertainty in the velocity determination. Data are presented here only for the main indices; the complete table of measured indices is available on request.

ID	R.A. (J2000)	Dec. (J2000)	g' (mag)	g'–r' (mag)	g'–i' (mag)	V (km/s)	Hβ (Å)	Mgb (Å)	Fe5270 (Å)	Fe5335 (Å)
228	11:50:49.2	-28:46:58.0	22.92	0.57	0.79	1587±66	3.86±0.29	0.68±0.31	1.76±0.34	0.51±0.40
253	11:50:50.1	-28:50:19.0	23.08	0.64	0.82	2203±74	1.98±0.32	1.64±0.35	0.23±0.39	0.84±0.42
197	11:50:49.7	-28:48:55.5	22.75	0.77	1.08	1727±29	1.87±0.25	3.87±0.25	2.17±0.27	1.56±0.30
279	11:50:51.3	-28:50:38.1	23.10	0.83	1.20	1807±41	1.40±0.32	4.00±0.33	2.77±0.35	3.03±0.36
112	11:50:52.0	-28:48:32.2	22.27	0.71	0.97	1763±26	2.26±0.18	2.59±0.19	1.80±0.21	1.57±0.23
394	11:50:50.7	-28:46:47.9	23.48	0.58	0.84	1851±69	1.71±0.47	0.79±0.49	1.95±0.52	0.55±0.61
106	11:50:53.6	-28:46:07.1	22.13	0.69	0.99	1733±26	1.96±0.16	1.96±0.17	1.36±0.18	1.50±0.21
64	11:50:54.1	-28:48:15.8	21.75	0.68	0.93	1770±27	2.05±0.13	1.50±0.13	1.27±0.15	1.17±0.17
86	11:50:56.3	-28:45:59.3	22.02	0.70	1.02	1784±22	2.13±0.15	2.47±0.15	1.57±0.17	2.00±0.18
311	11:50:57.7	-28:46:42.1	23.19	0.70	0.98	1666±43	2.16±0.35	2.25±0.39	1.68±0.40	2.80±0.44
333	11:50:58.3	-28:50:51.0	23.25	0.82	1.15	1925±55	2.78±0.40	3.97±0.42	3.10±0.44	2.90±0.48
247	11:50:57.3	-28:50:13.5	23.01	0.66	0.86	1829±48	2.36±0.31	2.02±0.33	1.57±0.36	0.99±0.43
99	11:50:55.0	-28:48:00.3	22.12	0.75	1.07	1654±22	1.42±0.17	2.91±0.18	2.17±0.19	2.36±0.20

Table 7.2: Table 7.1 continued.

ID	R.A. (J2000)	Dec. (J2000)	g' (mag)	g'–r' (mag)	g'–i' (mag)	V (km/s)	Hβ (Å)	Mgb (Å)	Fe5270 (Å)	Fe5335 (Å)
99	11:50:55.0	-28:48:00.3	22.12	0.75	1.07	1654±22	1.42±0.17	2.91±0.18	2.17±0.19	2.36±0.20
322	11:50:55.4	-28:46:29.5	23.24	0.64	0.87	2099±50	1.86±0.40	1.17±0.41	1.11±0.44	1.08±0.49
498	11:50:55.8	-28:46:45.1	23.76	0.72	1.06	1600±49	-0.06±0.60	2.52±0.62	3.49±0.62	4.02±0.65
221	11:51:04.1	-28:45:45.6	22.89	0.59	0.79	1805±53	2.11±0.29	1.41±0.30	0.87±0.33	1.38±0.38
110	11:51:04.9	-28:45:48.5	22.24	0.72	1.07	1550±24	1.45±0.18	2.90±0.18	2.14±0.19	1.65±0.22
232	11:51:00.2	-28:46:55.0	22.96	0.71	1.10	1808±30	1.49±0.31	2.71±0.31	2.17±0.34	1.55±0.38
225	11:51:03.6	-28:49:53.0	22.92	0.81	1.17	1926±37	1.57±0.28	4.22±0.29	1.66±0.32	2.45±0.34
360	11:50:59.5	-28:50:05.8	23.37	0.80	1.20	1476±39	1.61±0.40	3.37±0.48	2.19±0.46	3.60±0.48
332	11:51:05.8	-28:49:51.3	23.28	0.85	1.30	1639±41	0.54±0.43	4.52±0.40	3.67±0.41	3.67±0.43
108	11:51:07.2	-28:50:11.9	22.20	0.77	1.14	2046±32	1.41±0.18	3.52±0.18	1.88±0.19	2.32±0.21
450	11:51:00.7	-28:45:40.3	23.66	0.71	1.01	2114±39	3.02±0.54	2.79±0.56	1.80±0.58	1.88±0.65
513	11:51:01.2	-28:45:52.5	23.86	0.71	1.15	1671±61	-1.10±0.73	3.86±0.63	1.53±0.71	1.81±0.76
492	11:50:59.2	-28:45:58.4	23.73	0.84	1.19	1746±50	1.99±0.53	3.43±0.54	2.13±0.58	1.45±0.64
167	11:51:08.0	-28:46:06.0	22.52	0.71	1.01	1806±22	1.65±0.22	2.74±0.22	1.41±0.24	0.88±0.28
65	11:51:07.6	-28:46:23.9	21.71	0.64	0.83	2295±30	1.77±0.13	1.20±0.14	0.70±0.15	1.09±0.17
104	11:51:08.6	-28:46:27.4	22.16	0.59	0.80	2152±45	2.41±0.17	1.05±0.18	0.94±0.20	0.85±0.22
93	11:51:09.1	-28:48:19.4	22.06	0.76	1.10	1754±25	1.93±0.16	3.82±0.16	0.98±0.18	2.01±0.20

Table 7.3: Table 7.1 continued.

ID	R.A. (J2000)	Dec. (J2000)	g' (mag)	g'–r' (mag)	g'–i' (mag)	V (km/s)	Hβ (Å)	Mgb (Å)	Fe5270 (Å)	Fe5335 (Å)
Bin 1 (8 GCs)			22.81	0.61	$0.82^{0.90}_{0.78}$		2.20±0.49	1.26±0.38	1.05±0.42	0.89±0.26
Bin 2 (7 GCs)			22.51	0.70	$0.99^{1.02}_{0.90}$		2.08±0.29	2.21±0.55	1.41±0.29	1.55±0.54
Bin 3 (7 GCs)			22.58	0.74	$1.09^{1.14}_{1.02}$		1.67±0.33	3.33±0.36	1.72±0.43	2.05±0.38
Bin 4 (7 GCs)			23.36	0.81	$1.19^{1.31}_{1.14}$		1.61±1.03	4.09±0.62	2.68±0.43	2.74±1.06
All GCs (29)			22.81	0.71	$1.02^{1.31}_{0.78}$		1.95±0.49	2.47±1.03	1.54±0.57	1.67±0.74
NGC 3923							1.52±0.36	3.04±0.37	1.79±0.42	2.00±0.46
30 (Star)	11:50:54.5	-28:50:19.5	21.17	0.76	1.03	91±34				
15 (Star)	11:50:56.9	-28:50:03.9	20.15	0.95	1.31	19±37				
118 (Star)	11:51:02.7	-28:45:54.1	22.28	0.90	1.22	92±34				
40 (QSO)	11:51:06.3	-28:46:46.6	21.45	0.50	0.46	z∼1.27				
56 (Star)	11:51:05.2	-28:46:50.3	21.55	0.40	0.47	289±59				
383 (Galaxy)	11:51:04.5	-28:50:38.2	23.47	0.90	1.14	z∼0.36				
113 (Galaxy)	11:51:10.7	-28:45:38.8	22.22	0.83	1.21	z∼0.29				
17 (Star)	11:51:09.9	-28:49:42.3	20.21	0.54	0.69	111±62				

Table 7.4: Derived stellar population parameters for the globular clusters and spheroid of NGC 3923. Age, [Fe/H], [α/Fe] and [Z/H] derived using the χ^2 minimization method described in Section 4.2.

ID	Age (Gyr)	[Fe/H] (dex)	[α/Fe] (dex)	[Z/H] (dex)	S/N	Comments
228	$10.0^{+3.0}_{-2.3}$	-2.25±0.37	0.48±0.40	-1.80±0.17	24.4	
253	$15.0^{+8.8}_{-5.5}$	-2.28±0.34	0.80±0.30	-1.53±0.29	22.5	
197	$6.0^{+2.7}_{-1.8}$	-0.49±0.17	0.44±0.10	-0.08±0.13	29.4	
279	$15.0^{+9.9}_{-5.9}$	-0.57±0.19	0.42±0.13	-0.18±0.16	22.2	
112	$7.9^{+3.4}_{-2.4}$	-0.88±0.13	0.30± 0.08	-0.60±0.15	39.4	
394	$11.9^{+4.9}_{-3.5}$	-1.31±0.27	0.38±0.41	-0.95±0.28	15.6	Fit unstable.
106	$11.9^{+1.9}_{-1.7}$	-1.19±0.12	0.15±0.12	-1.05±0.08	44.7	
64	$11.9^{+2.0}_{-1.7}$	-1.37±0.10	0.21±0.10	-1.18±0.06	56.1	
86	$15.0^{+6.3}_{-4.4}$	-1.15±0.15	0.34±0.11	-0.83±0.12	47.7	
311	$6.7^{+7.5}_{-3.5}$	-0.72±0.37	0.18±0.22	-0.55±0.27	20.0	
333	$15.0^{+28.0}_{-9.8}$	-0.27±0.26	0.21±0.16	-0.08±0.30	17.8	No Balmer lines in fit.
247	$14.1^{+8.6}_{-5.3}$	-1.35±0.28	0.32±0.24	-1.05±0.21	22.9	
99	$12.6^{+2.7}_{-2.2}$	-0.57±0.11	0.15±0.10	-0.43±0.08	43.4	
322	$11.2^{+4.5}_{-3.2}$	-1.25±0.26	0.24±0.30	-1.03±0.20	19.3	
498	$15.0^{+15.0}_{-7.5}$	0.13 ±0.25	-0.30±0.12	-0.15±0.29	12.4	Extremely poor fit
221	$10.6^{+2.7}_{-2.1}$	-1.45±0.25	0.24±0.26	-1.23±0.11	24.9	
110	$15.0^{+4.7}_{-3.6}$	-0.76±0.15	0.30±0.10	-0.48±0.11	40.6	
232	$11.9^{+4.2}_{-3.1}$	-0.78±0.18	0.24±0.15	-0.55±0.16	22.9	
225	$11.9^{+4.8}_{-3.4}$	-0.85±0.24	0.32±0.36	-0.55±0.24	25.7	
360	$10.6^{+5.9}_{-3.8}$	-0.77±0.24	0.53±0.20	-0.28±0.14	17.0	
332	$15.0^{+8.6}_{-5.5}$	0.15±0.16	0.03 ±0.12	0.18±0.18	18.7	Fit unstable.
108	$14.1^{+2.2}_{-1.9}$	-0.45±0.07	0.24±0.05	-0.23±0.05	41.9	
450	$10.0^{+6.2}_{-3.8}$	-0.61±0.28	0.38±0.19	-0.25±0.22	13.2	
513	$13.3^{+12.0}_{-6.3}$	-0.58±0.28	0.40±0.22	-0.20±0.23	11.4	
492	$8.9^{+7.9}_{-4.2}$	-0.23±0.24	0.62±0.18	0.35±0.25	13.0	
167	$12.6^{+3.7}_{-2.9}$	-1.30±0.15	0.50±0.13	-0.83±0.12	33.3	
65	$11.9^{+2.1}_{-1.8}$	-1.60±0.15	0.27±0.15	-1.35±0.07	53.5	
104	$11.9^{+1.8}_{-1.6}$	-1.73±0.17	0.38±0.17	-1.38±0.07	41.8	
93	$15.0^{+6.2}_{-4.4}$	-0.75±0.14	0.18±0.17	-0.58±0.19	45.6	
Bin 1 (8 GCs)	$11.9^{+2.9}_{-2.3}$	-1.60±0.29	0.24±0.30	-1.38±0.12		
Bin 2 (7 GCs)	$12.6^{+3.6}_{-2.8}$	-1.18±0.15	0.24±0.16	-0.95±0.10		
Bin 3 (7 GCs)	$15.0^{+5.6}_{-4.1}$	-0.70±0.16	0.27±0.12	-0.45±0.11		
Bin 4 (7 GCs)	$13.3^{+7.8}_{-4.9}$	-0.35±0.20	0.24±0.16	-0.13±0.15		
All GCs (29 GCs)	$15.0^{+15.4}_{-7.6}$	-1.00±0.37	0.21±0.29	-0.80±0.31		
NGC 3923	$15.0^{+5.5}_{-4.0}$	-0.65±0.17	0.34±0.13	-0.33±0.14		

Table 7.5: Measured velocities for GCs and NGC 3923 spheroid. ID, RA, DEC, target velocity (including fore and background objects) and velocity of NGC 3923 spheroid measured in the same slitlet.

ID	R.A. (J2000)	DEC. (J2000)	V_{target} (km/s)	$V_{NGC\ 3923}$ (km/s)
228	11:50:49.2	-28:46:58.0	1587±66	1866±72
253	11:50:50.1	-28:50:19.0	2203±74	1812±64
197	11:50:49.7	-28:48:55.5	1727±29	1859±37
279	11:50:51.3	-28:50:38.1	1807±41	1772±101
112	11:50:52.0	-28:48:32.2	1763±26	1815±34
394	11:50:50.7	-28:46:47.9	1851±69	1843±64
106	11:50:53.6	-28:46:07.1	1733±26	1972±106
30	11:50:54.5	-28:50:19.5	91±34	1750±90
64	11:50:54.1	-28:48:15.8	1770±27	1855±21
86	11:50:56.3	-28:45:59.3	1784±22	1830±50
311	11:50:57.7	-28:46:42.1	1666±43	1879±41
333	11:50:58.3	-28:50:51.0	1925±55	1952±48
15	11:50:56.9	-28:50:03.9	19±37	1917±33
247	11:50:57.3	-28:50:13.5	1829±48	1874±23
99	11:50:55.0	-28:48:00.3	1654±22	1874±32
322	11:50:55.4	-28:46:29.5	2099±50	1817±58
498	11:50:55.8	-28:46:45.1	1600±49	1867±32
221	11:51:04.1	-28:45:45.6	1805±53	1972±45
110	11:51:04.9	-28:45:48.5	1550±24	1910±54
118	11:51:02.7	-28:45:54.1	92±34	1909±45
232	11:51:00.2	-28:46:55.0	1808±30	1853±27
225	11:51:03.6	-28:49:53.0	1926±37	1878±29
360	11:50:59.5	-28:50:05.8	1476±39	1848±22
332	11:51:05.8	-28:49:51.3	1639±41	1881±37
108	11:51:07.2	-28:50:11.9	2046±32	1984±84
40	11:51:06.3	-28:46:46.6	z∼1.27	1843±24
56	11:51:05.2	-28:46:50.3	289±59	1858±25
450	11:51:00.7	-28:45:40.3	2114±39	1923±75
513	11:51:01.2	-28:45:52.5	1671±61	1913±49
492	11:50:59.8	-28:45:58.4	1746±50	1911±59
383	11:51:04.5	-28:50:38.2	z∼0.36	1822±45
167	11:51:08.0	-28:46:06.0	1806±22	1907±42
65	11:51:07.6	-28:46:23.9	2295±30	1860±38
104	11:51:08.6	-28:46:27.4	2152±45	1900±42
113	11:51:10.7	-28:45:38.8	z∼0.29	1872±91
93	11:51:09.1	-28:48:19.4	1754±25	1878±29
17	11:51:09.9	-28:49:42.8	111±62	1929±51

7.4. NGC 3923 GC Kinematics

This section provides tables of the position, magnitudes in g,r, and i, and velocities of the 74 GCs confirmed as members of the NGC 3923 GC system. The measurement of the provided quantities is described in detail in Chapter 5.

Table 7.6: Confirmed NGC 3923 GCs. RA, Dec, X, Y, g, r, i, velocity and velocity errors for all 74 confirmed NGC 3923 GCs. The X and Y positions refer to positions relative to the galaxy centre.

RA (J2000)	Dec. (J2000)	X (arcmin)	Y (arcmin)	g (mag)	r (mag)	i (mag)	V (kms^{-1})	V_{err} (kms^{-1})
177.705	-28.784	2.73	1.35	22.92	22.35	22.13	1586.53	66.00
177.709	-28.840	2.54	-2.00	23.08	22.44	22.26	2203.25	74.20
177.707	-28.816	2.62	-0.61	22.75	21.98	21.67	1726.61	28.91
177.714	-28.845	2.28	-2.32	23.10	22.27	21.90	1777.78	58.27
177.716	-28.810	2.13	-0.22	22.27	21.57	21.30	1762.72	26.22
177.711	-28.781	2.42	1.52	23.48	22.90	22.64	1851.21	69.24
177.723	-28.770	1.77	2.19	22.13	21.43	21.13	1733.16	26.34
177.725	-28.805	1.67	0.05	21.75	21.07	20.81	1764.20	29.61
177.734	-28.767	1.20	2.32	22.02	21.32	21.01	1784.69	37.02
177.740	-28.779	0.87	1.61	23.19	22.49	22.21	1666.38	42.50
177.743	-28.848	0.75	-2.54	23.25	22.43	22.10	1925.21	54.98
177.739	-28.838	0.97	-1.91	23.01	22.35	22.14	1839.62	42.97
177.729	-28.801	1.47	0.31	22.12	21.37	21.06	1673.22	23.52
177.730	-28.776	1.39	1.82	23.24	22.59	22.36	2008.47	69.15
177.732	-28.780	1.29	1.56	23.76	23.04	22.70	1623.86	46.51
177.767	-28.764	-0.52	2.55	22.89	22.30	22.10	1805.38	53.11
177.770	-28.764	-0.69	2.50	22.24	21.52	21.17	1556.56	29.82
177.751	-28.783	0.33	1.40	22.96	22.25	21.86	1807.94	29.60
177.765	-28.832	-0.41	-1.57	22.92	22.11	21.75	1938.98	46.49
177.748	-28.836	0.48	-1.78	23.37	22.57	22.17	1447.54	54.93
177.774	-28.832	-0.89	-1.54	23.28	22.43	21.98	1638.89	40.93
177.780	-28.838	-1.19	-1.89	22.20	21.43	21.06	2045.96	32.45
177.753	-28.762	0.23	2.64	23.66	22.95	22.65	2114.44	38.89
177.755	-28.766	0.11	2.44	23.86	23.15	22.71	1628.31	44.76
177.746	-28.767	0.56	2.34	23.73	22.89	22.54	1749.91	62.26

Table 7.7: Table 7.6 continued.

RA (J2000)	Dec. (J2000)	X (arcmin)	Y (arcmin)	g (mag)	r (mag)	i (mag)	V (kms^{-1})	V_{err} (kms^{-1})
177.783	-28.769	-1.37	2.21	22.52	21.81	21.51	1811.63	24.25
177.782	-28.774	-1.29	1.91	21.71	21.07	20.88	2295.48	30.40
177.786	-28.775	-1.51	1.85	22.16	21.57	21.36	2151.99	45.03
177.788	-28.806	-1.63	-0.01	22.06	21.29	20.95	1749.02	44.30
177.741	-28.780	0.82	1.59	23.24	22.39	22.02	1796.23	55.61
177.724	-28.791	1.72	0.94	21.82	21.15	20.90	1845.32	56.04
177.728	-28.798	1.52	0.51	22.81	22.17	21.90	1659.48	67.36
177.761	-28.780	-0.22	1.55	23.10	22.39	22.09	1190.82	44.52
177.774	-28.828	-0.88	-1.32	23.08	22.31	21.96	1944.99	64.24
177.746	-28.831	0.58	-1.49	23.43	22.65	22.35	1680.13	29.59
177.782	-28.779	-1.29	1.62	21.62	20.90	20.61	1996.67	44.70
177.783	-28.811	-1.39	-0.28	23.09	22.28	21.91	1809.02	31.71
177.779	-28.830	-1.15	-1.41	23.13	22.50	22.27	1752.73	45.44
177.795	-28.764	-2.02	2.52	22.75	22.11	21.92	2214.71	104.05
177.667	-28.825	4.71	-1.13	21.17	20.52	20.26	1517.02	32.15
177.658	-28.810	5.18	-0.23	21.94	21.27	21.03	1782.82	69.31
177.660	-28.864	5.10	-3.46	21.89	21.26	21.04	1354.71	62.02
177.695	-28.826	3.25	-1.20	20.92	20.20	19.92	1714.41	26.28
177.698	-28.841	3.09	-2.08	21.68	20.97	20.69	2109.27	23.53
177.700	-28.781	2.98	1.54	22.63	21.87	21.54	1922.90	24.35
177.697	-28.784	3.13	1.31	22.66	21.80	21.39	1989.01	31.72
177.693	-28.814	3.34	-0.48	22.42	21.66	21.35	1903.52	39.97
177.671	-28.834	4.53	-1.67	22.72	22.11	21.90	1305.67	31.05
177.682	-28.842	3.92	-2.16	21.93	21.28	20.97	1847.53	23.15
177.685	-28.856	3.78	-2.99	22.29	21.75	21.34	2024.47	68.07

Table 7.8: Table 7.6 continued.

RA (J2000)	Dec. (J2000)	X (arcmin)	Y (arcmin)	g (mag)	r (mag)	i (mag)	V (kms^{-1})	V_{err} (kms^{-1})
177.669	-28.791	4.63	0.93	23.22	22.38	22.01	1739.84	31.65
177.707	-28.824	2.64	-1.05	21.84	21.11	20.82	1590.80	35.88
177.720	-28.789	1.95	1.04	21.81	21.21	20.92	1227.46	86.35
177.718	-28.833	2.06	-1.64	22.06	21.30	20.97	1971.08	60.09
177.735	-28.844	1.14	-2.26	22.68	21.69	21.48	1769.91	20.76
177.824	-28.788	-3.53	1.12	22.37	21.66	21.45	1731.12	27.11
177.829	-28.752	-3.77	3.24	22.18	21.49	21.20	1733.96	40.10
177.812	-28.799	-2.87	0.42	23.64	22.83	22.49	1975.54	39.05
177.820	-28.779	-3.31	1.61	22.73	21.92	21.57	2064.39	15.75
177.801	-28.804	-2.32	0.12	21.66	21.03	20.83	1494.66	14.27
177.793	-28.803	-1.89	0.21	22.02	21.32	21.07	1761.02	20.02
177.794	-28.793	-1.97	0.78	22.44	21.70	21.41	1809.72	45.30
177.778	-28.731	-1.11	4.50	22.23	21.47	21.18	2039.05	33.30
177.775	-28.728	-0.96	4.69	23.50	22.70	22.41	1993.87	62.38
177.768	-28.747	-0.58	3.54	22.42	21.75	21.53	1635.22	52.23
177.770	-28.786	-0.68	1.19	23.43	22.69	22.35	1555.81	38.97
177.766	-28.727	-0.45	4.77	23.62	22.83	22.53	1805.65	51.17
177.738	-28.800	0.98	0.37	22.27	21.48	21.15	1937.61	24.18
177.741	-28.793	0.86	0.81	22.27	21.56	21.27	2114.59	53.87
177.752	-28.780	0.28	1.57	22.62	21.85	21.50	1760.62	15.24
177.752	-28.729	0.26	4.61	22.66	21.89	21.65	2167.89	39.86
177.755	-28.782	0.10	1.47	23.76	23.10	22.88	1628.05	80.35
177.758	-28.759	-0.06	2.81	23.58	22.91	22.70	2095.25	78.59
177.733	-28.773	1.28	1.99	23.20	22.38	21.96	1756.72	55.31